Theory of Electronic and Structural Transitions in Layered Materials and 2D Heterostructures: Properties Tunable with Pressure, Electric field and Twist

A Thesis
Submitted For the Degree of
DOCTOR OF PHILOSOPHY
in the Faculty of Science

by
Koyendrila Debnath

THEORETICAL SCIENCES UNIT
JAWAHARLAL NEHRU CENTRE FOR ADVANCED SCIENTIFIC RESEARCH
Bangalore - 560 064
JULY 2022

To my Parents

DECLARATION

I hereby declare that the matter embodied in the thesis entitled "**Theory of Electronic and Structural Transitions in Layered Materials and 2D Heterostructures: Properties Tunable with Pressure, Electric field and Twist**" is the result of investigations carried out by me at the Theoretical Sciences Unit, Jawaharlal Nehru Centre for Advanced Scientific Research, Bangalore, India under the supervision of Prof. Umesh V. Waghmare and that it has not been submitted elsewhere for the award of any degree or diploma.

In keeping with the general practice in reporting scientific observations, due acknowledgement has been made whenever the work described is based on the findings of other investigators.

Koyendrila Debnath

Koyendrila Debnath

CERTIFICATE

I hereby certify that the matter embodied in this thesis entitled "**Theory of Electronic and Structural Transitions in Layered Materials and 2D Heterostructures: Properties Tunable with Pressure, Electric field and Twist**" has been carried out by Ms. Koyendrila Debnath at the Theoretical Sciences Unit, Jawaharlal Nehru Centre for Advanced Scientific Research, Bangalore, India under my supervision and that it has not been submitted elsewhere for the award of any degree or diploma.

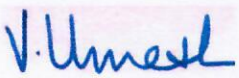

Prof. Umesh V. Waghmare
(Research Supervisor)

Acknowledgements

First and foremost, I would like to express my deepest gratitude towards my advisor, Prof. Umesh V. Waghmare, for his constant motivation and guidance. It wouldn't be an exaggeration to say that this thesis wouldn't have been possible without his supervision and constant support. I take this opportunity to thank him. He has been a big influence in shaping my ideas and also kept me motivated at my endeavours. I am grateful to him for his constructive feedbacks that pushed me to strengthen my concepts and theories. It is a learning and an experience that will always color my work from here-on. I also thank him for being patient and always willing to step in whenever the work needed him to. With his experience and enthusiasm, I have been able to match the persuasion that this thesis required.

I thank my collaborators, Prof. C. N. R. Rao, Prof. A. K. Sood, Prof. Kanishka Biswas, Prof. Mandar Deshmukh, Prof. Amit Agarwal, Dr. Pramoda, Dr. Subhadip, Dr. Srishti, Dr. Prabir, Dr. Atasi, Subhajit, Pratap, Swaraj, Aditi, Sushmita, Ivy, Paribesh for fruitful collaborations. I thank them for engaging me in fascinating and rigorous scientific interactions.

I thank all the TSU faculty, Prof. Umesh. V. Waghmare, Prof. S. Narasimhan, Prof. Vidhyadhiraja N. S., Prof. Subir K. Das, Prof. Swapan K. Pati, Prof. Kavita Jain and Prof. Srikanth Sastry for their instructive courses and scientific interactions.

It is my pleasure to thank the present and past members of Materials Theory Group for the co-operative and cheerful environment. I would like to sincerely thank Dr. Pawan

Kumar, Dr. Koushik Pal, Dr. Sharmila Shirodkar, Dr. Anjali Singh, and Dr. Lakshay Dheer for all the insightful discussions which helped me immensely.

I also thank the Complab, Academic, Admin, Library, Dhanvantari, Utility store, Dining Hall and Hostel mess staff and TSU secretary for all their help.

I would like to thank JNCASR for the research fellowship.

I am thankful to Aruna Ma'am and Kruti for their warm hospitality and making us feel like a family.

I am grateful to all my friends in JNC: Soumen, Souvik, Sumukh, Sanchita, Sushmita, Paribesh, Saif, Ankit, Abhishek, Swarna, Arijit, Souradip, Deepam, Sarbajit, Saptarshi for the good times. I would like to acknowledge my friends and cousins Sayantani, Aaheli, Moumita, Anweshak, Sarthak, Pranjal who have always been by my side.

I am also thankful to my friend Robi for all the wonderful times and his support.

Last but not the least, my parents who have been my pillars of strength, my lifelines, my backbone for their endless support and encouragement. Maa and baba this journey wouldn't have been possible without you both. I am grateful for all the love you have showered on me and I dedicate this thesis to you. I hope to make you proud one day.

Synopsis

Materials have been central and intimately related to advances of human civilization and have had a singular influence on our lifestyle. From Stone Age, through Bronze to Iron Age, every major advance in human kind and epoch of civilization have been influenced by a notable discovery of a material or its processing, which acted as key enablers to technological revolutions. Development of quantum physics in 1920's was crucial to opening of material technologies involving electrons. Rapid and continued advances in computational power, algorithms and techniques of simulations have enabled theoretical design of new materials with new functionalities. To this end, first-principles Density Functional Theory-based simulations have emerged as a powerful tool in computational materials science providing insights into structure-property relationship of materials and their applications depending on the arrangement of nuclei and electrons in space and time. These simulations can be effectively used to understand electronic and dynamical properties of materials in terms of mechanisms at the atomic-scale, and predict their behavior under varied conditions, bridging the gap between theory and experiments which are limited by expensive and time-intensive synthesis and characterization.

Our focus here is on the theoretical analysis of layered and 2-dimensional materials. We have used a combination of first-principles simulations and modelling to determine the effect of twist, electric field and pressure on the properties of layered materials and 2-dimensional heterostructures. The thesis is divided into three parts based on the external fields involved in functionality of materials investigated. **The first part** consisting of chapters 3 and 4, focuses on the theoretical analysis of how the angle of twist between atomic layers of 2-D heterostructures influences electronic and topological properties of graphene-hexagonal boron nitride (h-BN) bi and trilayers. We provide understanding of a chemical route to generation of interlayer twist through cross-linking by organic molecules

in graphene-h-BN bilayer in chapter 3. In chapter 4, we develop a rigid band model of frontier electronic states of trilayers of twisted double bilayer graphene (tDBG) to determine polarization as a function of electric field. We show that there exist two metastable states with distinct polarization states in tDBG, that can be accessed with electric field. Furthermore, distinctive coupling of top and bottom gates of a device induce inhomogeneity in doping in a multi-layer channel contributing to hysteresis in longitudinal voltage response upon doping as seen in our experiments.

The second part consisting of chapters 5 and 6 involves analysis of phonon renormalization of Raman modes upon hole doping and mechanical response to applied electric field in bulk and two-dimensional group-VI transition metal dichalcogenides (TMDs). In chapter 5, we show that while E_{2g} and B_{2g} phonon modes exhibit significant frequency softening with hole doping, A_{1g} mode shows relatively small frequency softening in bilayer *2H*-$MoTe_2$ and use group theory analysis to understand these results. In chapter 6, we calculate the electrostrictive coefficients of *2H*-MoS_2 and *1T*-HfS_2 and investigate the dependence of their electronic and phononic contributions on composition of atoms (chemistry), structure and the number of layers.

In the third part consisting of chapters 7, 8 and 9, we explore pressure or CDW-induced structural transitions in bulk VSe_2, $GdTe_3$ and $(TaSe_4)_2I$. Our first-principles calculations presented in chapter 7 reveal an iso-structural transition in *1T* polytype of VSe_2 at $P =$ 6 GPa and another structural phase transition from *1T* to 3R (Space group $R\bar{3}m$) phase at $P = 9$ GPa. While we show that Fermi surface nesting (FSN) is at the origin of charge density wave (CDW) in $GdTe_3$ (chapter 8), the CDW in $(TaSe_4)_2I$ is driven by strong electron-phonon coupling (chapter 9). We demonstrate how CDW-driven strong electron-phonon coupling and associated anharmonic interactions phonons result in low thermal conductivity of $GdTe_3$ and $(TaSe_4)_2I$.

List of Figures

List of Tables

Contents

Chapter 1

Introduction

Materials have been central and intimately related to historical advances of human civilization and have fueled technological growth. From Stone Age, through Bronze to Iron Age, every major advance of human kind and epoch of civilization have been influenced by a notable discovery of a material or its processing, which acted as key enablers to technological revolutions. Development of quantum physics in 1920's was crucial to opening of material technologies involving electrons. There are 98 naturally occurring elements in the periodic table giving rise to 4,753 potential binary compounds, 152,096 ternary compounds and 3,612,280 quaternary compounds, assuming equal amounts of each element in a single phase [2, 3]. Variety in possible materials grows exponentially with variation in concentration of constituent elements.

Rapid and continued advances in computational power, algorithms and techniques of simulations have enabled theoretical design of new materials with targeted properties and functionalities [4]. To this end, first-principles Density Functional Theory-based simulations [5] have emerged as a powerful tool in computational materials science providing

insights into structure-property relationship of materials and their applications depending on the arrangement of nuclei and electrons in space and time [6, 7]. These simulations can be effectively used to understand electronic and dynamical properties of materials in terms of mechanisms at the atomic-scale, and predict their behavior under varied conditions, bridging the gap between theory and experiments which are limited by expensive and time-intensive synthesis and characterization [8, 9].

In 1929, the physicist Paul Dirac wrote, "The underlying physical laws necessary for the mathematical theory of a large part of physics and the whole of chemistry are thus completely known, and the difficulty is only that the exact application of these laws leads to equations much too complicated to be soluble" [10]. At the fundamental level, arrangement of atoms and electrons in materials and their motions determine the macroscopic properties of a material. Since, the motion of electrons (atoms) is governed by quantum mechanical laws (Newtonian mechanics), most physical properties of materials can in principle be determined from these laws. However, quantum motion of constituent atoms and electrons affected by their Coulomb interactions, combined with their kinetic energies, form a many-body problem. A direct solution to the many-body Schrödinger equation describing a material is extremely challenging [11,12]. The development of theories to describe the electronic motion and solve the many-body problem is the foundation of first-principles or *ab initio* density functional theory.

A breakthrough in first-principles computational techniques was achieved in 1964 when Hohenberg and Kohn laid the foundations of density functional theory (DFT) [13], a theory based on electronic charge density which is a function of just three spatial coordinates of the system. Another seminal work was by Kohn and Sham showing that for the ground state, the many-electron problem can be mapped onto a system of one-electron equations, known as Kohn-Sham equations [14]. Owing to the burgeoning computational power and efficiency of first-principles simulations, it is now not only possible to determine and explain properties of a material (electronic structure, stress, polarization, elastic constants,

vibrational frequencies, forces and bulk modulii, etc.) but also the use of these in 'high-throughput' computational materials design enables the discovery of novel materials with desired properties for specific applications [15].

Macroscopic behaviour of a material is determined by many processes involving couplings between electronic charge, twist and lattice degrees of freedom. A study of effects of reduction in dimensionality combined with coupled degrees of freedom can be quite interesting. We have used a combination of first-principles simulations and modelling to determine the effect of twist, electric field and pressure on the properties of layered materials and 2D heterostructures. The thesis is divided into three parts based on the external fields involved in the functionalities of materials investigated. The first part consisting of chapters 3 and 4, focuses on the theoretical analysis of how the angle of twist between atomic layers of 2D heterostructures influences their electronic and topological properties, with examples of graphene-hexagonal boron nitride bi and trilayers. The second part consisting of chapters 5 and 6 involves analysis of phonon renormalization of Raman modes upon hole doping and mechanical response of bulk and two-dimensional group-VI transition metal dichalcogenides (TMDs) to applied electric field. In the third part consisting of chapters 7, 8 and 9, we explore pressure and CDW-driven structural transitions in bulk VSe_2, $GdTe_3$ and $(TaSe_4)_2I$. Here, we uncover the mechanism of low thermal conductivity of $GdTe_3$ and $(TaSe_4)_2I$, in terms of their charge density waves.

1.1 Layered materials

"What could we do with layered structures with just the right layers?" asked Richard Feynman in his famous 1959 lecture, "There's plenty of room at the bottom". With technological growth and advances in computational power, we are increasingly engaged in addressing this question. Layered materials are characterized by extended planar crystalline structures which are held together by strong in-plane covalent bonds and typically

weak out-of-plane van der Waals (vdW) forces [16]. Individual layers can be easily isolated by breaking the out-of-plane vdW bonds without notable damage to the rest of the structure [17, 18]. Successful isolation of graphene, a one-atom thick sheet of carbon atoms arranged in a honeycomb lattice, in 2004 by Geim *et al.* at the University of Manchester [19] has given birth to a new era of atomically thin materials, which has ultimately stimulated an enormous activity of research and interest in 2D systems in the last two decades [20]. Graphene is the thinnest known material in the universe and also the strongest. It is one of the most alluring 2D materials because of its unique and peculiar electronic structure which gives rise to exceptionally high carrier mobility, and provides a platform to study several charming properties like massless Dirac fermions and anamalous room-temperature quantum Hall effect [21]. Despite being a promising 2D material, absence of a gap in its electronic spectrum adversely limits its application in electronic devices (switching devices) [22]. This partly drove the scientific community to fabricate other 2D materials with a finite band gap and high mobility which are suitable for applications in nanoelectronics. The last decade has seen the rise of a cornucopia of layered and 2D materials (Fig. 1.1) spanning the entire spectrum of electronic properties: metals, superconductors, charge density wave (CDW) systems, Mott insulators and semiconductors [23–25].

Semiconducting transition-metal dichalcogenides (TMDs) with chemical formula MX_2, where M represents the transition metal (Mo, W) and X is a chalcogen (S, Se or Te), form another interesting class of 2D materials with a wide range of properties and applications [26, 27]. Their crystal structure consists of covalently bonded layers of $X-M-X$ layers stacked along the c-axis *via* weak vdW interactions. An interesting feature of TMDs is their characterization into different polytypes based on the coordination of transition metal atom and the stacking sequence of the three atomic plane (X, M, X) forming the individual $X-M-X$ layers [28]. The common structural phases are *1T* with octahe-

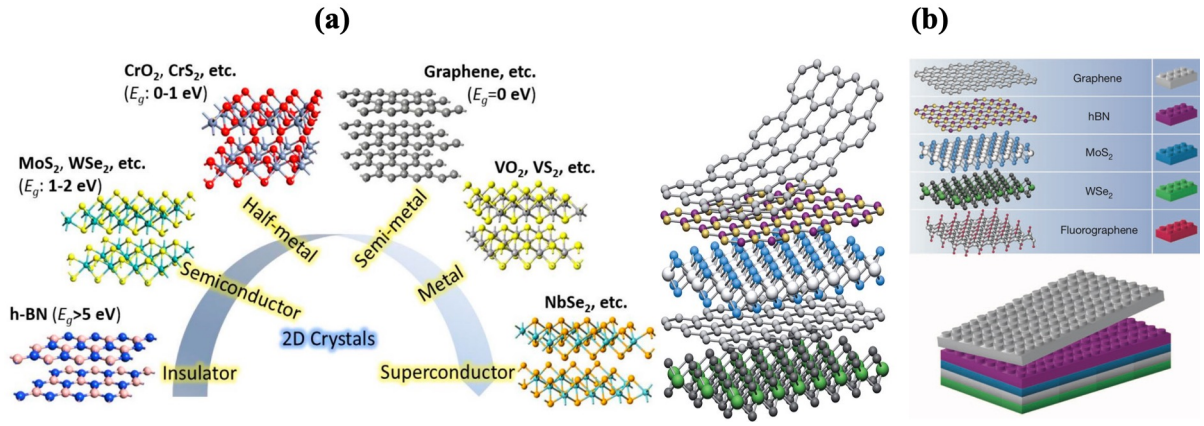

Figure 1.1: (a) The world of layered and 2D materials includes graphene and its analogues, such as hexagonal boron nitride; the III–VI family of semiconductors; and the transition-metal dichalcogenides (TMDs) spanning the full range of electronic properties. (b) Building vdW heterostructures analogous to Lego blocks (right panel). Reprinted by permission from Springer Nature Customer Service Centre GmbH: Springer Nature, Van der Waals heterostructures by A. K. Geim and and I. V. Grigorieva Ref. [18] Copyright © 2013, Nature Publishing Group.

dral metal coordination, *2H* and *3R* with trigonal prismatic coordination of metal atom (Fig. 1.2). Unlike graphene, TMDs exhibit sizeable electronic band gaps making them suitable for building active electronic devices. Many bulk TMDs have indirect band gaps, but reduction in number of layers results in a transition from indirect to direct band gap in materials, leading to stronger optical absorption [29]. Additionally, tuning of band gaps of these materials through application of strain, electric field, pressure, doping and alloying [30] has triggered a plethora of novel technological applications in electrochemical, optoelectronic devices [23, 25, 31, 32] and lasers [33]. Inversion symmetry breaking provides the prerequisite for a large portfolio of fascinating physical phenomena, such as valley-contrasting physics enabling development of new spintronics and valleytronics devices [34, 35].

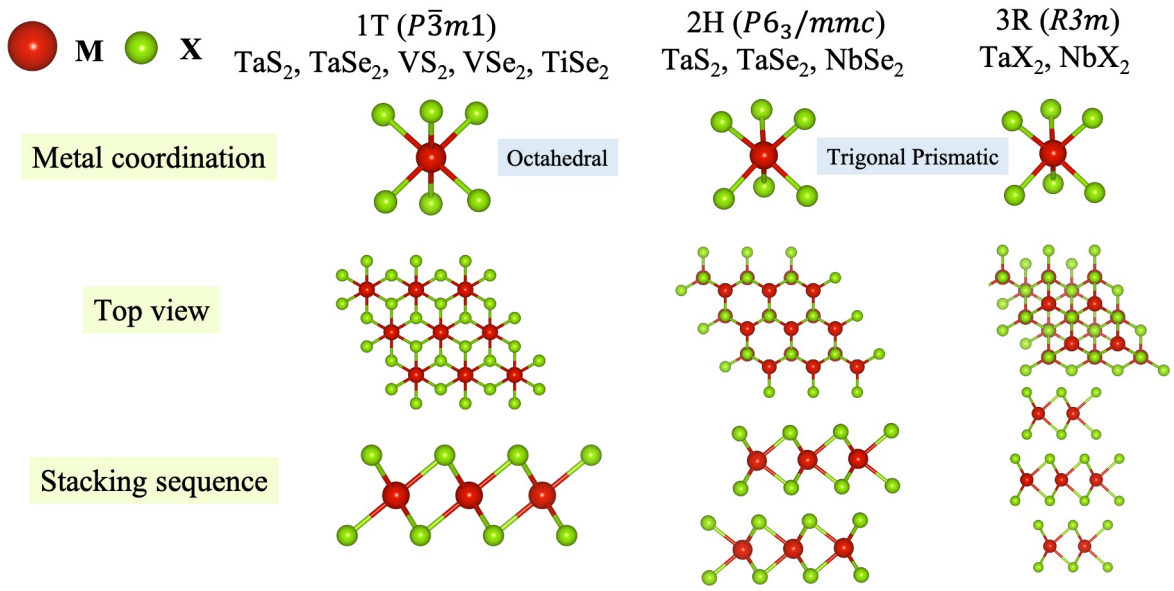

Figure 1.2: Structural polytypes of TMDs (*1T*, *2H* and *3R*) based on different coordination of transition metal atom and stacking sequence.

1.2 Stacking and interlayer twisting

Although bulk layered materials have several intriguing properties, there has also been a lot of interest in developing and understanding heterostructures (similar to building blocks of Lego), where atomic layers of different 2D materials are vertically stacked through weak vdW forces, offering unprecedented freedom of combining different crystals from the ever expanding catalogue of layered materials and opening new avenues for band engineered materials [18]. Furthermore, stacking graphene, TMDs, 2D magnets into heterostructures not only combines their respective functionalities but also imprints properties through proximity interactions across the interface [36, 37]. First reports on TMD heterostructures made of stacked monolayers of a $MoSe_2$ and WSe_2 revealed a new type of bound electron–hole (exciton) state [38, 39]. In contrast to the readily observed intralayer excitons fully confined within one layer of a TMD, the newly discovered interlayer exciton had the electron and hole located in the adjacent monolayers. Interlayer excitons are strongly bound (> 100 meV) and long-lived, with the radiative life times in the nanosecond range,

three orders of magnitude longer than the intralayer excitons. Proximity between magnetic 2D crystals and other layered materials may serve as a sensitive tool to study the details of magnetic structure. The first investigations demonstrating pronounced magnetic phenomena at vdW heterostructures were focused on CrI_3/WSe_2 structures [40].

Modulation of the relative twist angle between adjacent layers of 2D layered materials (twistronics) provides a rotational degree of freedom and acts as a new design parameter unveiling exotic electronic and topological properties [41–45]. When two single layers of graphene are stacked and twisted to an angle 1.1°, hybridization between the lowest lying energy bands gives rise to moiré superlattice bands with flat dispersion, which greatly enhances the local density of states and are impacted strongly by electron-electron interactions. Manipulation of the inversion symmetry breaking by the interlayer twist angle leads to the observation of fascinating new phenomena, such as highly tunable second-order nonlinear optical responses [46], ferroelectricity [47] and non-trivial valley polarization of both intralayer and interlayer excitons [42, 48, 49]. The 'tear-and-stack' technique [50, 51] is used to control the interlayer twist angle to 0.1° accuracy. Specifically, the atomic force microscope tip manipulation technique provides an in situ approach to dynamically control the interlayer twist angle in a single device. This can avoid extrinsic effects, which can affect interlayer coupling strength, from device processing (twist-angle inhomogeneity and cleanliness of the interface) and open up opportunities to study the intrinsic twist-angle-dependence of properties and solve the nature of the existing puzzles, such as the band gap size in a graphene/h-BN heterostructure [52, 53]. The atomic arrangement of the two lattices stacked with a twist has periodicity only for particular values of the twist angle, θ [54]. Other fascinating results on twisted bilayer graphene (TBLG) include demonstration of Hofstadter's Butterfly in its energy spectrum in a magnetic field [55], and neutrino-like oscillations as a result of coupling between Dirac cones of the two rotated layers [56].

1.3 Charge-density wave

The concept of charge-density wave (CDW) originates from Peierls' description of a fundamental instability that exists in a 1D metallic chain of atoms equally spaced by a distance, a [57].

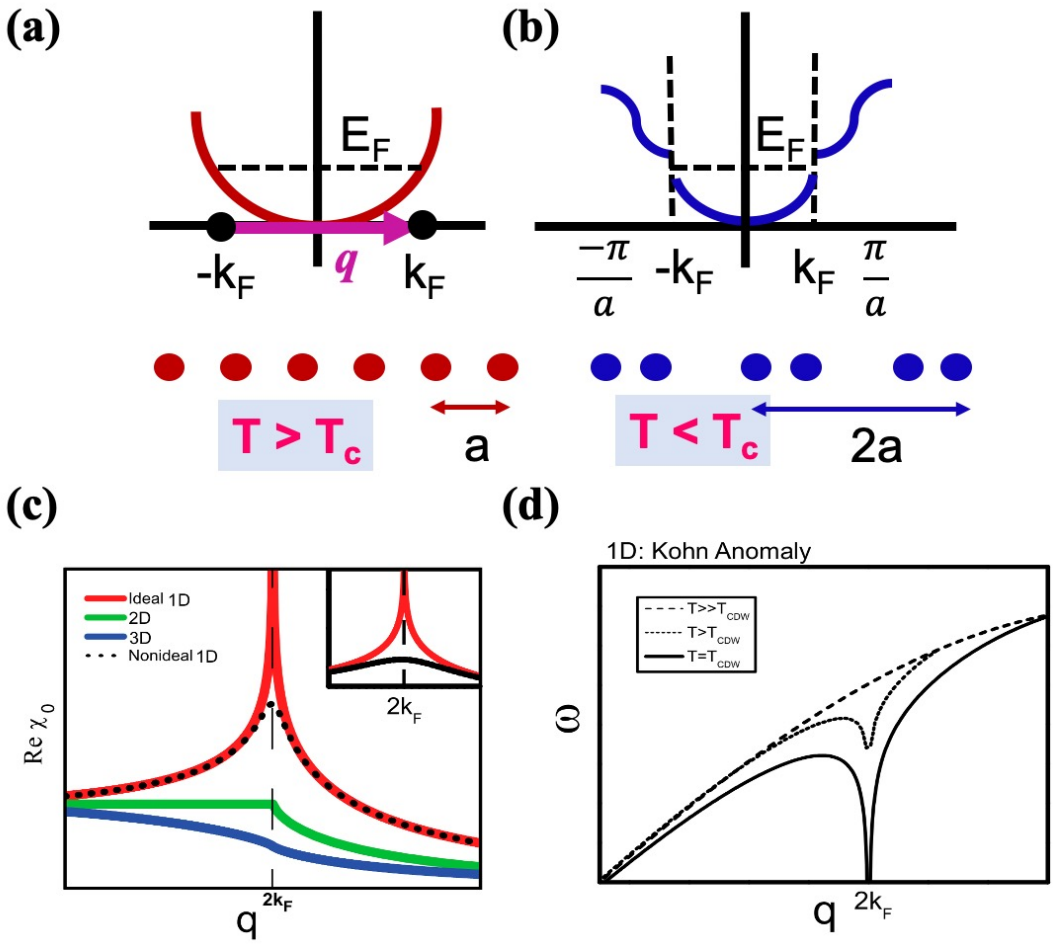

Figure 1.3: Illustration of the Peierls distortion in 1D chain of atoms. (a) Undistorted 1D chain with lattice constant, a above T_c, (b) distorted or charge density wave state with lattice constant changing to $2a$ below T_c and the corresponding free electron band of the 1D chain. (c) Real part of Lindhard response function as a function of dimensionality (d) Acoustic phonon dispersion relation of a 1D metal at various temperatures above the mean field transition temperature. Fig. (c) and (d) are reproduced with permission from ref. [78] © 2015 National Academy of Sciences.

In its free electronic structure, the Fermi surface (FS) consists of two points connected by

the wavevector $q = 2k_{\mathrm{F}}$ (Fig. 1.3). Peierls' asserted that a 1D chain of atoms is intrinsically unstable with respect to an electronic disturbance with the wavevector $q = 2k_{\mathrm{F}}$ that may change its periodicity of the lattice to $2a$ and opening up a gap at $k = \frac{\pi}{2a}$ of the new unit cell [58]. This amounts to a metal to an insulator phase transition, and accompanying lattice reconstruction called Peierls distortion. This also results in modulation of electronic charge density or CDW. The conjecture is that the gain in electronic energy due to opening up of a gap will always be able to overcome the cost of restructuring of the lattice. In the free electron model, response of an electron gas to an external perturbation is described by Lindhard's response function, $\chi(q)$. For a 1D electron gas, the real part of $\chi(q)$ has a divergent singularity at $q = 2k_{\mathrm{F}}$, indicating its instability with respect to formation of periodically varying electron density. In a response, phonons with wavevectors close to $q = 2k_{\mathrm{F}}$ undergoes renormalization to lower energy. This strong renormalization of the phonon due to interaction with electron is known as the Kohn anomaly (Fig. 1.3). Kohn described this as there is an image of Fermi surface in the vibrational spectrum [59].

Extension of the concept of CDW to reduced dimensional systems (D $>$ 1) has led to the concept of Fermi surface nesting (FSN), where non-zero measure of electronic states on the FS being scattered by the nesting wavevector (q_{CDW}) to other parts of the FS [60]. The structure is unstable w.r.t a perturbation of q_{CDW} wavevector, e.g. a phonon drives the structure to a lower energy. CDW order is most commonly found in metals with highly anisotropic crystal and electronic structure. These are known as "quasi-one-dimensional (quasi-1D)" or "low-dimensional" crystals. In real systems (with quasi-1D crystal structure), perfect nesting is reduced only to certain parts of the FS. In these cases, the CDW gap is expected to open only at the strongly nested parts of FS, and the system may remain metallic in its new ground state. Prototypical examples include quasi-1D $K_2Pt(CN)_4$ [61], blue bronzes [62], TMDs [63, 64], and as well as quasi-2D transition metal trichalcogenides [65] and rare-earth tritellurides [66]. The family of layered rare-

earth tritellurides $R\text{Te}_3$ (R = La − Nd, Sm, Gd − Tm, and Y) are metals and form a prime example of CDW systems [67–71]. These materials have an orthorhombic structure (*Cmcm* space group) consisting of two structural motiffs: corrugated RTe slabs and square planar Te sheets giving rise to two different types of 2D and 3D Brillouin zones (BZ). Strong nesting in the FS of these structures by q_{CDW} results in effective screening of phonons inducing Kohn anomalies in the phonon dispersion at q_{CDW}, driving a lattice reconstruction at low temperatures. However, the role of FSN in CDW has been widely debated, particularly in $NbSe_2$ [72] and the related dichalcogenides [73]. If FSN is the origin of CDW as in the Peierls picture, both real and imaginary part of the susceptibility, $\chi(q, \omega)$ should show strong peaks at q_{CDW} and phonon renormalization at each q_{CDW} inducing a lattice distortion [74]. However, in $NbSe_2$, the real part of $\chi(q, \omega)$ shows a broad peak and the imaginary part (which directly reflects FSN) does not peak at q_{CDW} at all. Mazin and coworkers used the classic CDW materials, $NbSe_2$ [72], $TaSe_2$ [60], to show that CDW in these systems is driven by enhancement of the electron-phonon coupling at q_{CDW} and not quite FSN. Thus, either FSN or strong electron-phonon coupling can be the origin of CDW in a material [75]. The CDW and superconductivity phases can either coexist or compete as seen in *2H*-$NbSe_2$. The interplay between the two can be tuned with chemical doping, electrostatic doping and pressure. In *1T* polytype of TMDs like semi-metallic $TiSe_2$ and TiS_2, the superconductivity state emerges while the CDW quenches under applied pressure or copper intercalation [76–78].

1.4 Effect of External Field

External field (electric field, doping and pressure) can be used to couple with a material and also tune its properties of a material which affects its performance in devices like transistors and sensors. The ability to control electronic properties of a material under externally applied voltage is at the heart of modern electronics. In experiments, this can

also be used as a knob to control carrier concentration in semiconductor devices [79, 80]. Equivalence of the two layers in a Bernal-stacked (AB-stacked) bilayer graphene is broken in the presence of an out-of-plane magnetic or electric field [81–83]. The band gap of bilayer graphene opens up with a perpendicular electric field making it suitable for devices such as field effect transistors [84, 85]. Experimental discovery of intrinsic magnetism in atomically thin films of CrI_3 [86], $Cr_2Ge_2Te_6$ [87], and Fe_3GeTe_2 [88] and other 2D vdW magents has attracted much attention and opened new opportunities for electrical control of magnetism [89]. Mak and co-workers demonstrated control of magnetism in CrI_3, an antiferromagnetic (AFM) semiconductor in its ground state, by application of gate voltages [90]. Applied electric field creates an interlayer potential difference, which results in a large linear magnetoelectric effect, whose sign depends on the interlayer AFM order. External electric field can also be used to control macroscopic electric polarization arising from spontaneous ordering of electric dipoles in ferroelectrics. Doping provides a feasible way to control phase transitions in low-dimensional TMDs. Wang *et al.* reported a phase transition from non-centrosymmetric *1H* phase to centrosymmetric *1T'* polytype in atomically thin $MoTe_2$ through electrostatic doping [91]. Electron doping in monolayer of MoS_2 results in softening of A_{1g} phonon, while the E^1_{2g} phonon mode is insensitive to electron doping [92]. This work opened up a new avenue for use of Raman spectroscopy in probing the level of doping in single-layer MoS_2-based FETs, which have a high on-off ratio and are of technological significance. Pressure is another effective field triggering phase transitions between various polytypes of TMDs (which exists in different structural polytypes) and electronic phases. According to high pressure Raman studies on *2H*-MoS_2, a first-order phase transition from $2H_a$ to $2H_c$ structure is observed at $P_c = 20$ GPa through layer sliding. This is a mixed phase with dominant contribution from $2H_c$ structure and once the phase transition (characterized by a collapse in the c-parameter and volume and also by changes in interlayer bonding) is complete at 40 GPa, MoS_2 becomes metallic [93]. A recent study not only reveals the pressure-induced structural

transformations and semiconductor-semimetal-superconductor transitions in PdSSe but also provides insights into the metallization and topological superconducting properties of the TMD compounds under high pressure [94]. So, we conclude that pressure can be used as an effective parameter to analyze changes in band structures, as it is a variable amenable to both experimental and first-principles study.

1.5 Overview of the Thesis

The objective of this thesis is to explicate extraordinary physical properties of layered materials and 2D heterostructures with particular attention to electronic properties, structural stability, topological and charge density wave phases using first-principles calculations and corroborating experimental observations (Fig. 1.4). Materials studied in this thesis have functionalities with a wide array of applications in electronics and optoelectronics making them not only technologically important but also fundamentally interesting as they exhibit novel phenomena involving physics of coupled electrons and phonons.

In chapter 2, we briefly describe the computational methods employed in our calculations within the framework of density functional theory (DFT) mentioning various approximations entering in the calculations. We begin with the central theorem of DFT, proven by Hohenberg and Kohn, which states that for any system of interacting particles in an external potential $V_{ext}(\mathbf{r})$, the potential $V_{ext}(\mathbf{r})$ is uniquely determined by the ground state electronic density $\rho_0(\mathbf{r})$ of the system within the ambiguity of an additive constant and the second theorem which states that the ground state energy of an electronic system is a unique functional of its charge density and is a minimum with respect to the charge density. We then proceed to discuss the formalism by Kohn-Sham that mapped a given many body interacting system to an auxiliary system which is a fictitious non-interacting system with exactly the same ground state density. Thus, ground state solution of non-

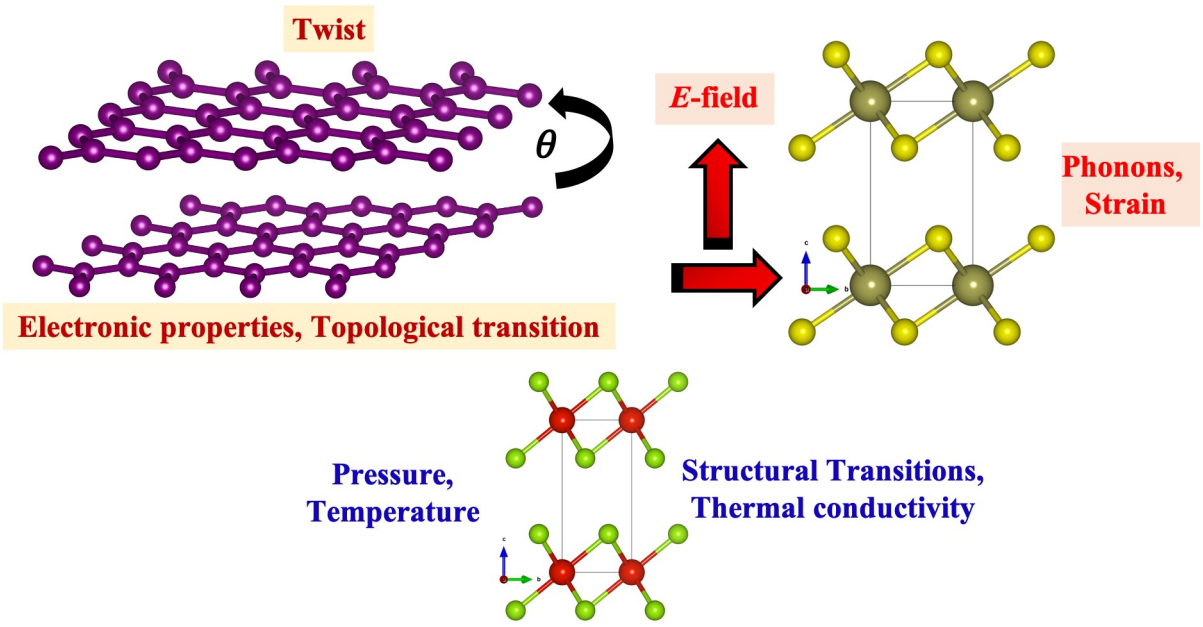

Figure 1.4: Schematic of the main theme of the thesis depicting the effect of twist, electric field, pressure and temperature (CDW) on the properties of layered materials and 2D heterostructures through couplings between various degrees of freedom.

interacting problem gives the ground state charge density of the real system, which can be used to determine its total energy and hence its physical properties. Lastly, we discuss in detail the methodologies to include dispersive interactions in DFT calculations since vdW interactions generally play an important role in layered systems.

Part I: Twisted heterostructures based on Graphene and h-BN

The first part (chapters 3 and 4) focuses on the theoretical analysis of how the angle of twist between atomic layers of 2-D heterostructures influences electronic and topological properties of graphene-hexagonal boron nitride bi and trilayers. In chapter 3, I will provide an understanding of a chemical route to generation of interlayer twist through cross-linking with organic molecules in graphene-h-BN bilayer. Our first-principles calculations throw light on the structure and interaction of amine-containing linkers L_1 = trans-1,4-diaminocyclohexane and L_2 = 1,5-diaminonaphthalene by cross-linking in exfoliated graphene containing surface carboxyl groups and L_3 = Oxalic acid in hexagonal

boron nitride (h-BN). As a result of the structure of the cross-linking, the second layer gets placed at an angle with respect to the first layer, manifesting itself in the form of moiré pattern. The complex geometry of the twisted graphene-h-BN bilayer significantly affects its electronic properties. The Dirac cones otherwise present in single layer graphene (G) at the K-point is missing in the graphene complexes (G$-$L$_1-$G and G$-$L$_2-$G). The band gap of h-BN complex is 0.3 eV which is much lower than that of pristine h-BN monolayer of 6.08 eV.

In chapter 4, our central result is change of Berry curvature dipole as the valley Chern number of bands changes in twisted double bilayer graphene (TDBG) with a small twist angle 1.1^o. In this work, we elucidate the origin of hysteresis in longitudinal voltage V^{ω}_{xx} governed by dopings near charge neutrality point (CNP) as observed in experiments. We develop a rigid band model of frontier electronic states of trilayers of TDBG to determine its out-of-plane polarization as a function electric field. We show that there exists two metastable states with distinct polarization states in TDBG, that can be accessed with electric field. Furthermore, distinctive coupling of top and bottom gates of a device induce inhomogeneity in doping in the multi-layer channel contributing to hysteresis in longitudinal voltage response upon doping as observed in experiments.

Part II: Layer dependence of response of MX_2 (M = Mo, Hf and X = Te, S) to electric field

The second part (chapters 5 and 6) involves analysis of renormalization of Raman modes upon hole doping and mechanical response to applied electric field in bulk and two-dimensional group-VI transition metal di chalcogenides (TMDs). In chapter 5, we study symmetry-induced phonon renormalization in bilayer *2H*-$MoTe_2$ upon hole doping. Experiments show that while E_{2g} and B_{2g} phonon modes exhibit significant frequency softening with hole doping, A_{1g} mode shows relatively small frequency hardening in few layers

of *2H*-$MoTe_2$. In our theoretical analysis, we have considered bilayer *2H*-$MoTe_2$ since the dependence of phonon renormalization of E_{2g} mode on the number of layers is negligible, indicating that the doping primarily occurs in the top two layers. We simulated hole doping in *2H*-$MoTe_2$ bilayer by adding a small fraction of holes (close to the experimental doping concentration) to its unit cell. From the changes in calculated frequencies we observe significant softening of E_{2g} and B_{2g} phonon modes and small frequency softening in A_{1g} mode upon hole doping. It is interesting to compare these trends with the phonon renormalization seen in n-doped monolayer MoS_2. Electron doping in monolayer MoS_2 has contrasting effects on the frequencies of A_{1g} and E^1_{2g} optical modes. While A_{1g} mode softens significantly, E^1_{2g} remains unaffected. The contrasting effects of electron and hole doping on phonon renormalization are explained with symmetry arguments, and have been estimated quantitatively with first-principles calculations.

In chapter 6, we present analysis of electrostrictive coefficients for the $1T$ and $2H$ polytypes of MoS_2 and HfS_2, and investigate the dependence of their electronic (M^{elec}) and phononic (M^{ionic}) contributions on composition of atoms (chemistry), structure and the number of layers. We show that the composition of constituent atoms or chemistry is crucial to the electronic part of electrostriction, M^{elec}. While M^{elec} is positive for MoS_2, it is negative for HfS_2. For the $2H$ polytype, electrostriction is dominated by electronic contribution, while in $1T$ electrostriction is largely phononic with weak electronic contributions. Lastly, we demonstrate that the phononic part, M^{ionic}, shows weak sensitivity to reduction in dimensionality, whereas M^{elec} decreases with decrease in the number of layers (as the band gap increases) in the stable polymorphs of TMS_2. Furthermore, we also analyze contributions of IR-modes with non-zero mode effective charge and the corresponding oscillator strength to understand the phononic contribution of IR-modes to electrostriction in stable $2H$-MoS_2 and $1T$-HfS_2.

Part III: Electronic and structural transitions in layered materials

In the third part (chapters 7, 8 and 9), we explore pressure and CDW-induced structural transitions in bulk VSe_2, $GdTe_3$ and $(TaSe_4)_2I$. Here, we uncover the CDW-mechanism and the origin of low thermal conductivity of $GdTe_3$ and $(TaSe_4)_2I$. In chapter 7, we study pressure-induced structural evolution of VSe_2. Our experimental collaborators find a transition from *1T* to *3R* phase at 12 GPa. An interesting feature of bulk VSe_2 is its characterization into different polytypes based on the coordination of the transition metal atom and various stacking sequences. The *1T* phase with CdI_2 crystal structure and space group $P\bar{3}m1$ is the ground state structure of VSe_2. Lattice parameters of *1T*-VSe_2 vary smoothly with pressure with a notable change in the slope of c/a ratio suggesting an isostructural transition at 6 GPa. We obtain the change in enthalpy with pressure from first-principles to understand the experimental results and find that the *1T* to *3R* transition is captured using spin-polarized calculations with Hubbard correction ($U_{eff} = U - J = 8$ eV), at ~ 9 GPa, close to the experimental transition pressure.

In chapter 8, we present analysis of effects of CDW on thermal conductivity in $GdTe_3$. We establish charge transfer from GdTe layer to Te sheets of $GdTe_3$. Strong nesting of its Fermi surface leads to instabilities and Kohn anomalies at the nesting wavevectors in phonon dispersion of metallic $GdTe_3$. Unstable phonon modes involve displacements of Te atoms only in Te-bilayers and constitute the origin of CDW. We establish strong anharmonicity in terms of anomalously high Grüneisen parameters of the CDW-coupled phonon modes along Γ - S direction. Such high value of Grüneisen parameters indeed reflects strong anharmonic phonon-phonon interactions making acoustic phonons ineffective of heat-transport, resulting in low thermal conductivity in $GdTe_3$, observed experimentally.

In chapter 9, we employ first-principles calculations to show that quasi-one-dimensional

material $(TaSe_4)_2I$ is a Weyl semimetal that hosts CDW. It is interesting to note that there exists two sets of Weyl points in its electronic structure, one along Γ to Z and the other along N to P directions in the Brillouin Zone. The linearly dispersed bands are more dispersive along Γ to Z compared to N to P direction, displaying highly anisotropic behaviour and is understandable because Γ to Z is the $TaSe_4$ chain direction (c-axis) in the crystal structure. Phonon dispersion of $(TaSe_4)_2I$ reveals weakly unstable modes with imaginary frequencies ($\omega^2 < 0$) at the Γ (22i cm^{-1}), Σ (13i cm^{-1}) and X (9i cm^{-1}) points of the BZ. Unstable modes at Γ involve displacements of Ta atoms along the chain direction (c-axis) leading to tetramerization of Ta atoms, analogous to Peierls distortion in one-dimension metal. With only weak nesting of the Fermi surface, we trace the origin of CDW to strong electron-phonon coupling. High Grüneisen parameters of the unstable mode at Γ indicate strong anharmonic vibration of Ta atoms along c-axis, scattering off the heat-carrying acoustic phonons, leading to low thermal conductivity of $(TaSe_4)_2I$.

Chapter 2

Methods and Formalism

Materials are composed of fundamental particles, electrons and nuclei, which determine the properties of materials and processes at the atomistic level. The interactions between nuclei and electrons is described by quantum mechanical laws and hence, development of efficient techniques to solve the many-body system is crucial. However, exact analytical solution of full, many-body Schrödinger equation (SE) describing the system is impossible. So, one can make approximations for the ground state to deal with the complexity of the problem. Density functional theory (DFT) is the a highly accurate and most widely used state-of-the-art method for *ab initio* calculations of the structure and properties of atoms, molecules, crystals, surfaces and nanosystems and discovery of materials for science and technology. Nearly all physical properties of a material can be determined from the derivatives of energy as a function of an external perturbation. The first derivatives of energy w.r.t strain, magnetic field and atomic positions give stress, magnetization and forces respectively and elastic constants, magnetic susceptibility and interatomic force constants are second derivatives of energy w.r.t. strain, magnetic fields and atomic positions.

2.1 Introduction

In this chapter, we briefly describe the computational methods employed in our calculations within the framework of density functional theory (DFT) mentioning various approximations entering in the calculations. DFT is primarily a theory of electronic ground state structure. The many-body Hamiltonian of a system of electrons and nuclei is defined as [4]:

$$\begin{aligned} \hat{H} &= -\frac{\hbar^2}{2m_e}\sum_i \nabla_i^2 + \frac{1}{2}\sum_{i\neq j}\frac{e^2}{|\mathbf{r}_i-\mathbf{r}_j|} - \sum_{i,I}\frac{Z_I e^2}{|\mathbf{r}_i-\mathbf{R}_I|} \\ &- \sum_I \frac{\hbar^2}{2M_I}\nabla_I^2 + \frac{1}{2}\sum_{I\neq J}\frac{Z_I Z_J e^2}{|\mathbf{R}_I-\mathbf{R}_J|}, \end{aligned} \tag{2.1}$$

where m_e and M_I are the masses of electron and I^{th} ion respectively, e is the charge of an electron, $\hbar$ is the Planck's constant and Z_I is the charge of the I^{th} ion. $\mathbf{r}_i$ and $\mathbf{R}_I$ are the position vectors of i^{th} electron and I^{th} ion respectively. The first and fourth terms in Eq. (2.1) are the kinetic energy of electrons and nuclei respectively. Second, third and fifth terms represent electron-electron, electron-nuclei and nuclei-nuclei Coulomb interactions, respectively. As the mass of the nuclei is significantly larger than that of electron, $M_I \sim 1836 * m_e$, the kinetic energies of ions are small and can be ignored. This approximation is known as Born-Oppenheimer or adiabatic approximation. The electronic time scales are small enough that the electrons can relax to their instantaneous ground states in the time scale required for the nuclear motion. As the motion of electrons and nuclei are decoupled within the adiabatic approximation,, the many body wavefunction can be written as a product of electronic and nuclear wavefunctions given as:

$$\Psi(\mathbf{R},\mathbf{r},t) = \sum_{n,n'} \phi_n(\mathbf{R},t)\psi_{n'}(\mathbf{R},\mathbf{r}). \tag{2.2}$$

$\psi_{n'}(\mathbf{R},\mathbf{r})$ are the electronic wavefunctions, which depend on the nuclear or ionic positions $\mathbf{R}$. $\phi_n(\mathbf{R})$ are nuclear wavefunctions but are independent of electronic positions $\mathbf{r}$. Electronic many-body wavefunctions are determined by the solution of time independent Schrödinger equation:

$$\hat{H}\Psi(\mathbf{R},\mathbf{r}) = \epsilon\Psi(\mathbf{R},\mathbf{r}). \tag{2.3}$$

Substituting Eq. 2.1 and Eq. 2.2 in Eq. 2.3 we get

$$\begin{aligned}\left[-\frac{\hbar^2}{2m_e}\sum_i \nabla_i^2 - \sum_{i,I}\frac{Z_I e^2}{|\mathbf{r}_i - \mathbf{R}_I|} + \frac{1}{2}\sum_{i\neq j}\frac{e^2}{|\mathbf{r}_i - \mathbf{r}_j|} + \frac{1}{2}\sum_{I\neq J}\frac{Z_I Z_J e^2}{|\mathbf{R}_I - \mathbf{R}_J|}\right]\psi_n(\mathbf{R},\mathbf{r}) \\ = E_n(\mathbf{R})\psi_n(\mathbf{R},\mathbf{r})\end{aligned} \tag{2.4}$$

and

$$\left[-\frac{\hbar^2}{2M_I}\sum_{I=1}^{P}\nabla_I^2 + E_n(\mathbf{R})\right]\phi_n(\mathbf{R}) = \epsilon_n\phi_n(\mathbf{R}). \tag{2.5}$$

The ground state or the lowest energy state ψ_0(r) is determined by finding the minimum of total energy (Eq. 2.6) with respect to all the parameters defining ψ(r).

$$\begin{aligned}E_{tot}[\psi] &= \frac{\left\langle \psi \left| \hat{H}_e \right| \psi \right\rangle}{\langle \psi \mid \psi \rangle}, \text{ where} \\ \hat{H}_e &= \hat{T} + \hat{V}_{ee} + \hat{V}_{ext}.\end{aligned} \tag{2.6}$$

Electronic wavefunctions have to be antisymmetric as electrons are Fermions. While Born-Oppenheimer approximation partially resolves the difficulty in determining the quantum mechanical ground state for a given set of atomic positions (R_I), ψ_i is still a function of $3N$ number of variables (N=number of electrons) and hence determination of the ground state still remains quite hard and requires additional approximations.

2.2 Density Functional Theory

Density functional theory (DFT) is a standard method of calculation providing insight into electronic and structural properties of materials. The main idea behind density functional theory is that it casts the interacting many-body problem into a set of single particle problems via the charge density of the electrons, where many-body effects are included through the exchange-correlation energy functional. The foundation of DFT lies on the basis of two powerful theorems given by Hohenberg & Kohn [95] in 1964, followed by their practical implementation by Kohn & Sham [14] in 1965 which became effective in prediction and explanation of the properties of materials through computations using only atomic numbers as the input.

The modern electronic structure calculation began with the idea of L. H. Thomas and E. Fermi [96], who around the same time of Hartree, thought that the full electronic density can be used as a fundamental variable in many body problems rather than the complicated many-body wave function itself. Their approximation is known as *Thomas-Fermi* approximation.

2.2.1 Thomas-Fermi model

Thomas and Fermi wrote the total electronic energy of an inhomogeneous system as a functional of electron density n as given below,

$$E_\alpha[n] = \int n(\mathbf{r})\epsilon_\alpha[n(\mathbf{r})]d\mathbf{r}, \tag{2.7}$$

where $\epsilon_\alpha[n(\mathbf{r})]$ is the energy density which consists of the contributions coming from the kinetic, exchange and correlation energies of a homogeneous electron gas for which good approximations already exist. This energy density is calculated locally in terms of $n(\mathbf{r})$ at every point and integrated over whole space to get the total energy. This is known as *local density approximation* (LDA). The above expression in the square bracket of Eq.

(2.7) is called a functional as it is a function of another function (*i.e.* electron density $n(\mathbf{r})$).

The exchange and correlation effects were introduced in the same *local* spirit by Dirac [97] and Wigner [98] respectively and are given by,

$$E_X[n] = -C_X \int n(\mathbf{r})^{4/3} d\mathbf{r} \tag{2.8}$$

$$E_C[n] = -a \int \frac{n(\mathbf{r})^{4/3} d\mathbf{r}}{b + n(\mathbf{r})^{1/3}}, \tag{2.9}$$

where $C_X = \frac{3}{4}(3/\pi)^{1/3}$. a, b are numerical constants. When exchange interaction is included, the theory is called *Thomas-Fermi-Dirac* approximation. Finally the total electronic energy according to the Thomas-Fermi-Dirac theory as a functional of electron density can be written as,

$$\begin{aligned} E_{TFD}[n] = C_k \int n(\mathbf{r})^{5/3} d\mathbf{r} + \int n(\mathbf{r}) \nu_{ext}(\mathbf{r}) d\mathbf{r} \\ + \frac{1}{2} \iint \frac{n(\mathbf{r}) n(\mathbf{r'})}{|\mathbf{r} - \mathbf{r'}|} d\mathbf{r} d\mathbf{r'} - C_X \int n(\mathbf{r})^{4/3} d\mathbf{r} + E_C[n], \end{aligned} \tag{2.10}$$

where $\int n(\mathbf{r}) \nu_{ext}(\mathbf{r}) d\mathbf{r} = V_{ext}$ is the external field arising from the electron-ion interactions and $C_k = \frac{3}{10}(3\pi^2)^{2/3}$.

2.2.2 Hohenberg-Kohn Theorems

The foundations of DFT were laid by Hohenberg and Kohn who showed that the electronic ground-state total energy can be expressed as a functional of the ground-state charge density, and another theorem by Kohn and Sham, which states that the ground-state charge density can be determined by a set of self-consistent one-body equations including many-body effects in the exchange-correlation energy functional of density. The two landmark theorems can be stated as follows:

Theorem I: *For any system of interacting particles in an external potential $V_{ext}(\boldsymbol{r})$, the potential $V_{ext}(\boldsymbol{r})$ is uniquely determined by the ground state electronic density $n_0(\boldsymbol{r})$ of the system within the ambiguity of an additive constant.*

Theorem II: *A universal functional of energy $E[n]$ can be defined for any external potential $V_{ext}(\boldsymbol{r})$. The ground state energy of a system is the global minimum of this functional. The electronic density $n(\boldsymbol{r})$ which minimizes the functional is called ground state density $n_0(\boldsymbol{r})$ of the system.*

These two theorems reduce the number of variables of a function from 3N (in equation 2.4) to 3 (in $n(\mathbf{r})$). As the total energy is a function of ground state electron density, the theory is known as density functional theory. The total energy functional is given by,

$$\begin{aligned} E_{HK}[n] =& T[n] + E_{ee}[n] + \int d\mathbf{r} V_{ext}(\mathbf{r}) n(\mathbf{r}) + E_{ion-ion} \\ =& F_{HK}[n] + \int d\mathbf{r} V_{ext}(\mathbf{r}) n(\mathbf{r}) + E_{ion-ion}. \end{aligned} \tag{2.11}$$

$T[n]$ and $E_{ee}[n]$ are the kinetic and potential energies of interacting electron system. E_{II} represents the coulomb interaction energy of nuclei.

These theorems do not provide a practical scheme for determining the ground state electron density or energy of an interacting electron system. Kohn and Sham in 1965 proposed a method for determining ground state electron density $n_0(\mathbf{r})$.

2.2.3 Kohn-Sham ansatz

The Hohenberg-Kohn theorem is not complete since it cannot provide information about the exact form of the functional $F[n]$. For a system of interacting electrons, all the particles repel each other, and exchange leads to a lowering of the energy. The interactions between the electrons make the motion of the particles to be correlated which can further

reduce the energy of the mutual interaction. A very useful and effective approximation for the universal energy functional $F[n]$ was proposed by Kohn and Sham in 1965 [14]. The idea of Kohn-Sham is that if one can find any non-interacting electronic system that produces the same electronic density as that of the interacting system, then the kinetic energy of the electrons can be approximated through one electron orbitals. The kinetic energy calculated in this way is not exactly the same as that of the kinetic energy obtained from the many-body wave functions. The missing fraction in the energy comes due to the *correlation* among the electrons which can be included in correlation effects in the exchange-correlation energy functional. Thus, calculations of an original system can be performed on an auxiliary non-interacting particles system with the total energy functional given by,

$$E_{KS} = T_s[n] + \int d\mathbf{r} V_{ext}(\mathbf{r}) n(\mathbf{r}) + E_{XC}[n] + E_H[n] + E_{II}. \tag{2.12}$$

Terms in Eq. (2.12) are described below:

$n(\mathbf{r})$ is charge density of auxiliary system determined by the sum of square of N_e non-interacting electrons′ wavefuctions ($\psi_i(\mathbf{r})$):

$$n(\mathbf{r}) = \sum_{i=1}^{N_e} |\psi_i(\mathbf{r})|^2, \; and \; N_e = \int d\mathbf{r} \; n(\mathbf{r}). \tag{2.13}$$

$T_s[n]$ is the kinetic energy of N_e non-interacting electrons, and given by,

$$T_s[n] = -\frac{\hbar^2}{2m_e} \sum_{i=1}^{N_e} \langle \psi_i(\mathbf{r}) | \nabla^2 | \psi_i(\mathbf{r}) \rangle. \tag{2.14}$$

$E_H[n]$ is the Hartree energy, classical interaction energy of the electron density interacting

with itself, and define as,

$$E_H[n] = \frac{e^2}{2} \int \frac{n(\mathbf{r})n(\mathbf{r}')}{|\mathbf{r} - \mathbf{r}'|} d\mathbf{r} d\mathbf{r}'. \tag{2.15}$$

$E_{XC}[n]$ is the exchange-correlation energy of electrons that takes into account of (i) difference in kinetic energy of the many-body interacting system and set of non-interacting system, and (ii) residual energy contributions due to the exchange asymmetry and correlations. E_{XC} is given by,

$$E_{XC}[n] = (T[n] - T_s[n]) + (E_{int}[n] - E_H[n]), \tag{2.16}$$

where $[n]$ denotes a functional of the electron density $n(\mathbf{r})$. The exact form of $E_{XC}[n]$ is unknown, and will be discussed shortly. In this approch, the Hamiltonian of an auxiliary non-interacting particles is called Kohn-Sham Hamiltonian (H_{KS}), and written as,

$$H_{KS} = -\frac{\hbar^2}{2m_e}\nabla^2 + V_{KS}(\mathbf{r}), \tag{2.17}$$

where $V_{KS}(\mathbf{r})$ is Kohn-Sham potential expressed as,

$$V_{KS}(\mathbf{r}) = V_{ext}(\mathbf{r}) + V_H(\mathbf{r}) + V_{XC}(\mathbf{r}), \tag{2.18}$$

where $V_{ext}(\mathbf{r})$, $V_H(\mathbf{r})$ and $V_{XC}(\mathbf{r}) = \frac{\partial E_{XC}[n]}{\partial n(\mathbf{r})}$ are external, Hartree and exchange-correlation potentials, respectively. Now, one can write single-particle Kohn-Sham equations as,

$$H_{KS}\psi_i(\mathbf{r}) = \epsilon_i \psi_i(\mathbf{r}), \tag{2.19}$$

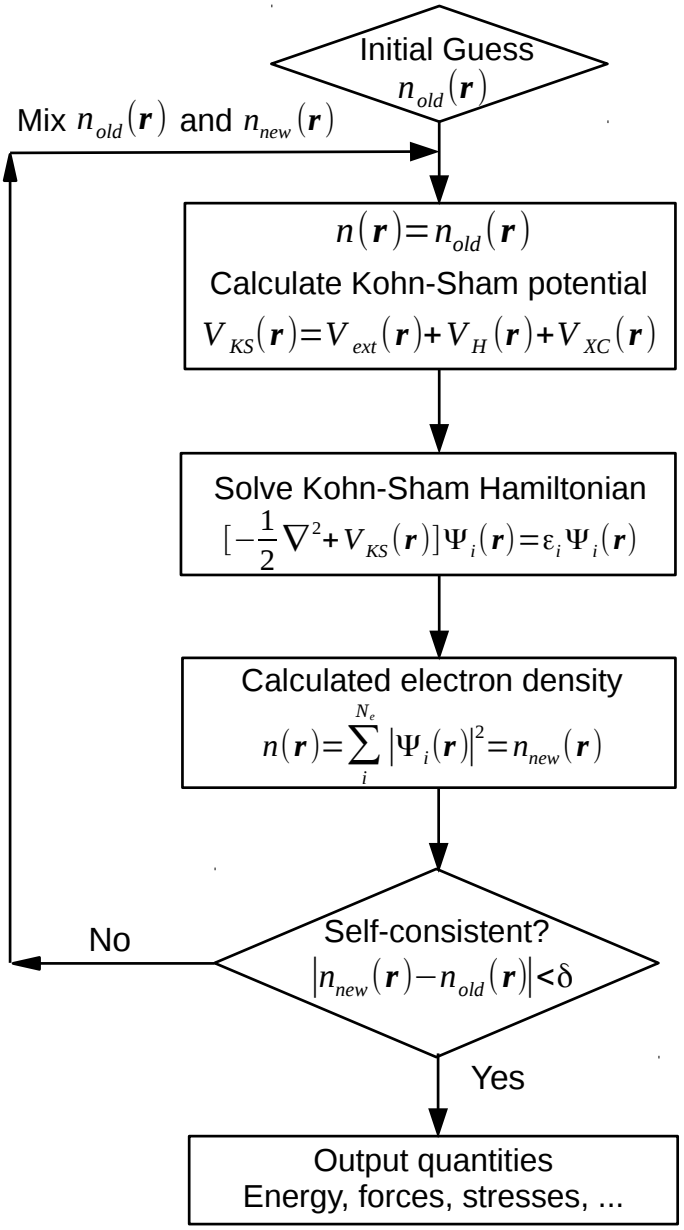

Figure 2.1: Flow chart for the iterative solution of Kohn-Sham equations.

the solution of Eq. (2.19) is a self-consistent iterative method, and illustrated in Fig. 2.1.

2.2.4 Basis sets

There are three basic approaches to the calculate the Kohn-Sham wavefunctions in materials, which are equally accurate provided they are applied carefully and taken to comparable convergence. In Kohn-Sham formalism, the independent-particle wavefunctions are expanded using basis sets and these methods are classified based on their basis sets. The commonly used basis sets are plane waves, atomic orbitals and a combination of both known as mixed basis.

Plane wave basis is used widely due to their simplicity and absence of Pulley forces. Since plane wave are eigenfunctions of the Schrödinger equation with constant potential, they are the natural basis for description of band structure of many materials including sp-bonded metals and semiconductors. The Kohn-sham wavefunction in the plane basis can be expanded as,

$$\psi_{i,\mathbf{k}}(\mathbf{r}) = \sum_{|\mathbf{G}|} C_{i,(\mathbf{k}+\mathbf{G})} e^{i(\mathbf{k}+\mathbf{G}).\mathbf{r}}, \tag{2.20}$$

where G is the reciprocal lattice vector and k is Bloch wavevector at which Kohn-Sham equations are solved [99, 100]. This expansion is infinite and is truncated to make it computationally feasible. To truncate the set of G vectors, a kinetic energy cutoff is used. The number of reciprocal lattice vectors in the sum is limited by including all those vectors which satisfy the condition,

$$\frac{\hbar^2}{2m_e}|\mathbf{k}+\mathbf{G}|^2 \leq E_{cut}. \tag{2.21}$$

The cutoff energy (E_{cut}) is increased until the calculated energy converges.

Atomic orbital basis [101] captures the essence of atomic-like features of wave- functions of molecules and solids. Mixed basis is a more general basis where the atomic-like features

are incorporated near the core, and smoothly varying (plane waves) away from the nucleus [102]. We have used plane wave basis in all our calculations here.

2.2.5 Exchange-Correlation Energy Functional

Electrons are Fermions, hence the wavefunction of many electron system should be asymmetric under exchange of any two electrons. This produces a spatial separation between the electrons that have the same spin causing a reduction in the Coulomb energy of the electronic system. This reduction in energy due to antisymmetric nature of wavefunction is known as the exchange energy, and this is referred to as the Hartree-Fock approximation. Coulomb energy of the system is also reduced at the cost of an increase in kinetic energy when the electrons of the same spin are spatially separated. The difference between the many body energy of an electronic system and that calculated in the Hartree-Fock approximation is called the correlation energy. Formulation of a correct exchange-correlation functional is one of the bottlenecks in DFT due to electron-electron interactions involved. Kohn Sham replaces many electron problem by single electron equation. The exchange-correlation energy functional Kohn Sham approach can be defined as:

$$E_{XC}[n(\mathbf{r})] = T[n(\mathbf{r})] - T_{\circ}[n(\mathbf{r})] + E_{ee}[n(\mathbf{r})] - E_H[n(\mathbf{r})] \tag{2.22}$$

where, $\mathrm{T}_{\circ}[n(\mathbf{r})]$ and $\mathrm{E}_{ee}[n(\mathbf{r})]$ are exact kinetic and electron-electron interaction energies respectively. Since, exact value of E_{xc} is not known; so various approximations based on electron density have been introduced to describe it.

Local density approximation (LDA): In LDA, the exchange-correlation energy of an electronic system is constructed by assuming that the exchange-correlation energy per electron ($\epsilon_{XC}(\mathbf{r})$) at a point $\mathbf{r}$ in the electron gas is equal to the exchange-correlation energy per electron of a homogeneous electron gas that has the same density as the

electron density at a point **r**. Thus,

$$E_{XC}^{LDA}[n(\mathbf{r})] = \int \epsilon_{XC}(\mathbf{r}) n(\mathbf{r}) d^3\mathbf{r} \tag{2.23}$$

and

$$\frac{\delta E_{XC}[n(\mathbf{r})]}{\delta n(\mathbf{r})} = \frac{\partial [n(\mathbf{r})\epsilon_{XC}]}{\partial n(\mathbf{r})} \tag{2.24}$$

where

$$\epsilon_{XC}^{LDA}(\mathbf{r}) = \epsilon_{XC}^{hom}[n(\mathbf{r})] \tag{2.25}$$

The LDA approximation proves to be very successful for many systems especially for those whose electron density is quite uniform such as bulk metals, ionic crystals etc. But it fails to produce some properties (e.g. band gap) in semiconductors, strongly correlated systems due to fact that the excitation spectrum of homogeneous electron gas is gapless and exchange-correlation energy is regular [103]. LDA also fails to capture weak intermolecular bonds, hydrogen bonds etc. The Perdew-Zunger (PZ) [104], Perdew-Wang (PW) [105], and Vosko-Wilk-Nusair (VWN) [106] functionals are the LDA functionals used commonly in calculations, which interpolate between exact results available at high and low densities n.

Generalized gradient approximation (GAA): GGA is an improved version of the LDA in which several aspects which were not present in LDA like inhomogeneity of electrons, non-local exchange correlation effect, complete cancellation of self-energies of electrons are taken into account. The exchange correlation energy in GGA [4] can be written as:

$$E_{XC}^{GGA}[n(\mathbf{r})] = \int d^3\mathbf{r} n(\mathbf{r}) \epsilon_{XC}[n(\mathbf{r}), |\nabla n|, |\nabla^2 n|, \cdots] \tag{2.26}$$

GGA method turns out to be better than LDA in the sense that it improves binding energies, bond lengths and also improves the band gap of semiconductors over LDA. Perdew and Wang (PW91) [107] and Perdew, Burke and Ernzerhof (PBE) [108] are some of the functional within GGA.

2.2.6 Pseudopotential approximation

The wavefunctions of a given atom are the eigenstates of the atomic Hamiltonian. The electronic states of an atom fall into three main categories. (i) Core states: which are highly localized and do not take part in chemical bonding, (ii) valence states: which are located far from the nucleus, hence extended and responsible for chemical bonding, and (iii) semi-core states: these states are in between the core and valence states. They are localized and polarisable, but usually do not contribute directly to chemical bonding.

The core states are localized in the vicinity of the nucleus. In an atom, the core electrons are tightly bound to the nucleus, and their wavefunctions are highly peaked in the region close to the nucleus. Therefore, a large number of plane-wave components are required for the plane-wave expansion of the wavefunctions to represent such steep wavefunctions. The valence states are oscillating in nature near the core region to maintain orthogonality with the core electrons. This rapid oscillation of the valence electrons causes large kinetic energy in the core region, which roughly cancels the large potential energy due to the strong Coulomb potential. The valence electrons are much more weakly bound to the nucleus than the core electrons.

Therefore, it is convenient to replace the strong Coulomb potential and the core electrons by an effective pseudopotential. The rapidly oscillating valence electron wave-functions in the core region can be replaced by the pseudo-wave-functions, which shows smooth variation in the core region instead of rapid oscillation. The pseudopotential approximation has to be developed carefully in order to reproduce the properties of the true potential. To formulate pseudopotentials one has to follow two main steps. At the first step the core

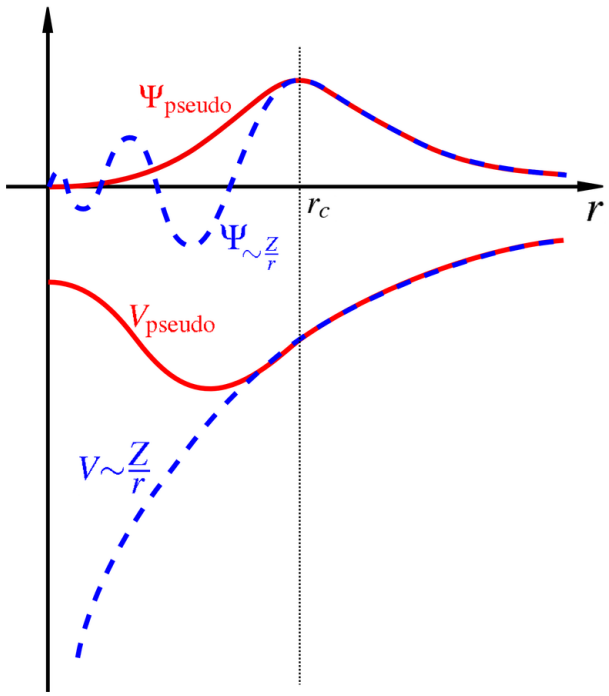

Figure 2.2: Schematic representation of an all electron potential (dotted line) and pseudopotential (solid line) along with corresponding wavefunction. Images by Sassospicco is licensed under CC BY-SA 1.0.

electrons are removed from the calculation, and the interaction of the valence electrons with the nucleus plus the core states (including orthogonalization) is replaced by an effective, screened potential. The effective potential depends on the angular momentum of the valence electrons.

In the second step, the interaction between the core electrons and the ions, which is known as the ion-electron interaction that includes the orthogonality of the valence wavefunctions to the core states, is replaced by a softer pseudopotential. The solution of the atomic Schr odinger equation using the pseudopotential gives a pseudo-wavefunction which is different from the true wavefunction.

The pseudopotential, however, is constructed in such a way it should keep certain features the same as for the all-electron potential, e.g., the scattering properties, phase shifts, etc. The main concept behind developing a pseudopotential is that the pseudo wavefunctions should have the scattering properties identical to the valence and core electrons. The pseu-

dopotential will be angular momentum dependent since the scattering properties depend on the angular momentum component of the valence wavefunction. Pseudopotentials with an angular momentum dependence are called non-local pseudopotentials.

The behavior of pseudopotential in different regions of radius r (see Fig. 2.2) is defined by a cut-off radius (r_c). For $r \geq r_c$, all-electron and pseudo wavefunctions of valence electrons are identical. For $r < r_c$, energy eigenvalues and scattering properties are conserved by the pseudo-wavefunctions. If the charge density of each pseudo wavefunction is equal to the charge density of the actual wavefunction inside the region r $< r_c$, the pseudopotential is known as a norm-conserving pseudopotential [109]. This is generalized in ultrasoft pseudopotentials [110], where the total charge in $r < r_c$ region is conserved along with augmented charge density.

2.2.7 Norm-conserving pseudopotentials

The most important and necessary condition to obtain the exchange-correlation energy accurately is that the real and pseudo wavefunctions should be identical outside the core region, so that both wavefunctions should give the same charge densities. The norm-conserving pseudopotentials should satisfy:

$$\int_0^{r_c} \psi^*_{AE}(\mathbf{r})\psi^*_{AE}(\mathbf{r})d\mathbf{r} = \int_0^{r_c} \psi^*_{ps}(\mathbf{r})\psi^*_{ps}(\mathbf{r})d\mathbf{r}, \tag{2.27}$$

where $_{AE}$ and $_{AE}$ are the all-electron and pseudo wavefunctions, respectively. The condition in Eq. (2.27) ensures that the all-electron and pseudo wavefunctions are equal outside the core region [109]. In practice, this can be achieved by using a non-local pseudopotential which uses a different potential for each angular momentum component of the pseudopotential. This kind of pseudopotential can describe the scattering properties from the ion core very well. The non-local norm-conserving pseudopotentials can describe the scattering properties of an ion in a variety of atomic environments which makes them

highly transferable.

2.2.8 Ultrasoft pseudopotentials

One more step forward in the field of electronic structure calculations was the introduction of ultrasoft pseudopotentials, suggested by D. Vanderbilt [110]. The devel- opment of ultrasoft pseudopotentials reduces the limitations of norm-conservation, and lowers the computational cost. That portion of the electronic charge which is not conserved in the pseudo wavefunction is included by adding an 'augmentation' charge in the core region of the pseudo wavefunction. To deal with this augmented charge, in addition to the plane wave energy cutoff, one has to introduce a larger cut off for the electronic charge density. The value of this charge density cut off should typically be 8 to 12 times the value of the energy cutoff for the plane wave basis sets.

2.2.9 Projector Augmented Wave method (PAW)

The principle of the Projector Augmented Wave (PAW) method is to represent the electronic wave functions in a system using a set of projectors that are centered on the atomic nuclei. The PAW method is based on the idea of a pseudopotential, where the effects of the core electrons in a system are approximated and the valence electrons are treated explicitly in the calculations. The projectors in the PAW method are used to describe the core electrons, which are not treated explicitly in the calculations. The projectors are chosen such that they accurately represent the core-valence interactions in the system. The valence electrons are treated explicitly in the calculations and are described by a wave function that is orthogonal to the wave functions described by the projectors. The PAW method allows for the calculation of the electronic structure of a system while reducing the computational cost compared to fully treating both the core and valence electrons. This is because the core electrons are not explicitly treated, but their effects are included

through the use of the projectors.

2.2.10 Dispersive interaction

GGA functionals including hybrid schemes have a general drawback that they can not describe long-range electron correlations that are responsible for van der Waals (vdW, dispersive) forces [111,112] as they replace part of the local HF exchange by nonlocal HF exchange. The vdW interactions between atoms and molecules play an important role in many chemical problems [113]. In recent years, to include these dispersive interactions in DFT calculations, several methods have been developed. These interactions are divided into two classes, (1) treatment of dispersion interaction as semi-empirical corrections on top of existing local functionals, and (2) to develop non-local exchange-correlation energy functionals that can incorporate the London interactions [114,115]. To account for such weak interactions between layers of materials such as graphene/h-BN heterostructures, $MoTe_2$, MoS_2, VSe_2, $GdTe_3$ and $(TaSe_4)_2I$ we have used parametrized DFT-D2 scheme of Grimme [114]. This gives a fairly accurate treatment of London dispersion interactions at relatively low computational cost, and we briefly describe the formulation below. The total energy with dispersion correction is given as,

$$E_{DFT-D2} = E_{KS-DFT} + E_{disp} \tag{2.28}$$

where E_{KS-DFT} is the self-consistent Kohn-Sham energy and E_{disp} is the empirical dispersion correction given as,

$$E_{disp} = -s_6 \sum_{i=1}^{N_{at}-1} \sum_{j=i+1}^{N_{at}} \frac{C_6^{ij}}{R_{ij}^6} f_{dmp}(R_{ij}) \tag{2.29}$$

Here, N_{at} is the number of atoms in the system, C_6 denotes the dispersion coefficient for atom pair (i, j), s_6 is a global scaling factor that depends only on the approximate

functional used in $KS-DFT$, and R_{ij} is an interatomic distance. In order to avoid near-singularities at small R, a damping function f_{dmp} must is used:

$$f_{dmp}(R_{ij}) = \frac{1}{1+e^{-d(R_{ij}/R_r-1)}} \tag{2.30}$$

Here, R_r is the sum of atomic van der Waals radii and the parameter d determines the dispersion corrections to the total energy and is fixed to 20 by Grimme to give accurate dispersion energies, but still maintaining negligible energies for typical covalent bonding situations. The dispersion coefficient C_6^{ij} for a given pair of atoms i and j, is taken as a geometric mean of the individual coefficients,

$$C_6^{ij} = \sqrt{C_6^i C_6^j} \tag{2.31}$$

2.3 Phonons

Phonon is a quasiparticle and quantum of vibrational energy associated with collective motion of atoms in materials. The concept of phonons provides a powerful tool to study the properties of materials which are governed by atomic displacements. Phonon-dispersion, behavior of vibrational frequency (ω) versus wave-vector ($\mathbf{q}$), reveals interesting physics of materials that governs stability of structures, thermodynamic properties and structural phase transformation of crystalline materials. There are two types of phonons: (i) stable phonons ($\omega^2 > 0$) and (ii) unstable phonons ($\omega^2 < 0$). Frozen-phonon and linear-response methods are the two methods which are commonly used to calculate phonons from first-principles.

2.3.1 Frozen-phonon method

Within Born-Oppenheimer approximation, electrons remain in their ground state and total energy is only a function of ionic positions ($\mathbf{R}_I$). The adiabatic motion of ions is governed by this Born-Oppenheimer surface ($E(\mathbf{R}_I)$). The amplitude of atomic vibration is typically small compared to the interatomic distance. The position of the I^{th} atom is $\mathbf{R}_I = \mathbf{R} + \mathbf{u}_I$, $\mathbf{u}_I$ is vibrating displacement of the I^{th} atom from its equilibrium position ($\mathbf{R}$).

The potential energy is expressed as a Taylor expansion in $\mathbf{u}$:

$$V = V_0 + \sum_{I,\alpha} \frac{\partial E}{\partial R_{I,\alpha}} \mid_{u=0} u_{I\alpha} + \frac{1}{2} \sum_{I,J,\alpha,\beta} \frac{\partial^2 E}{\partial \mathbf{R}_{I,\alpha} \partial \mathbf{R}_{J,\beta}} \mid_{u=0} u_{I\alpha} u_{J\beta} + O(u^3). \tag{2.32}$$

At the equilibrium atomic positions, forces acting on the atoms are zero, and hence the second term of Equation 2.32 is zero. Ignoring the terms V_0 and $O(u^3)$, force constant matrix $K_{IJ,\alpha\beta}$ from the quadratic term in $\mathbf{u}$ is given by,

$$\begin{aligned} V &= \frac{1}{2} \sum_{I,J} \sum_{\alpha,\beta} \frac{\partial^2 E}{\partial \mathbf{R}_{I,\alpha} \partial \mathbf{R}_{J,\beta}} \mid_{u=0} u_{I\alpha} u_{J\beta} \\ &= \frac{1}{2} \sum_{I,J} \sum_{\alpha,\beta} K_{I\alpha,J\beta} u_{I\alpha} u_{J\beta}. \end{aligned} \tag{2.33}$$

Solving the equation of motion of these harmonic oscillators, we get,

$$M_I \frac{\partial^2 u_{I\alpha}}{\partial t^2} = - \sum_{J,\beta} K_{I\alpha,J\beta} u_{J\beta}. \tag{2.34}$$

Assuming the time dependence of $u_{I\alpha}$ to be,

$$\mathbf{u}_I(t) = u_I e^{i\omega t}, \tag{2.35}$$

equation 2.34 reduces to,

$$\omega^2 M_I u_{I\alpha} = \sum_{J,\beta} K_{I\alpha,J\beta} u_{J\beta}. \tag{2.36}$$

We can get phonon frequencies (ω: eigenvalue) and eigenvectors (u) by solving the above eigenvalue equation. For the atomic system, the force constant matrix is ($3N \times 3N$) dimensional and there will be 3 normal mode frequencies. Phonon frequencies determine the thermal stability of the structure. When $\omega^2 > 0$ (stable system), the excitation of any phonon mode with frequency ω increases the energy of the system. In an unstable system ($\omega^2 < 0$), a finite amplitude of unstable phonon mode results in lowering of the total energy of the structure.

In the frozen phonon method, we calculate total energy and forces (within the framework of density functional theory) by displacing the atoms by small amount ($\pm$d). The force constant matrix is obtained with:

$$K_{I\alpha,J\beta} \approx -\frac{\Delta F_{I,\alpha}}{\Delta \mathbf{R}_{J,\beta}} \approx -\frac{\Delta F_{I,\alpha}}{2\ d}, \tag{2.37}$$

where d is the amplitude of atomic displacement that is frozen in each direction. We can determine phonons at $q \neq 0$ using frozen phonon method by considering supercells (commensurate with the q-vector) and obtain the full phonon dispersion. Thus, it is computationally expensive and time consuming to calculate phonons at $q \neq 0$ with frozen phonon method. Density functional perturbation theory overcomes this drawback of frozen phonon method.

2.3.2 Density functional perturbation theory

Density functional perturbation theory is a linear response theory used to calculate response functions (physical property such as phonons, force, stress, dielectric constant and

Born effective charges) as the second derivatives of total energy with respect to external perturbation (λ_i). The first and second derivatives of energy are,

$$\begin{aligned}\frac{\partial E}{\partial \lambda_i} =& \frac{\partial E_{ion-ion}}{\partial \lambda_i} + \int d\mathbf{r} \frac{\partial V_{ext}(\mathbf{r})}{\partial \lambda_i} n(\mathbf{r}), \\ \frac{\partial^2 E}{\partial \lambda_i \lambda_j} =& \frac{\partial^2 E_{ion-ion}}{\partial \lambda_i \lambda_j} + \int d\mathbf{r} \frac{\partial^2 V_{ext}(\mathbf{r})}{\partial \lambda_i \partial \lambda_j} n(\mathbf{r}) + \int d\mathbf{r} \frac{\partial n(\mathbf{r})}{\partial \lambda_i} \frac{\partial V_{ext}(\mathbf{r})}{\partial \lambda_j}.\end{aligned} \tag{2.38}$$

The first-order change in electron density with respect to λ_i is determined by linearizing equation 2.13 as

$$\Delta n(\mathbf{r}) = 2Re \sum_{i=1}^{N_e/2} \psi_i^*(\mathbf{r}) \Delta\psi_i(\mathbf{r}). \tag{2.39}$$

The variation in Kohn-Sham wavefunctions can be evaluated by solving first-order perturbation theory:

$$(H_{KS} - \epsilon_i)|\Delta\psi_i\rangle = -(\Delta V_{KS} - \Delta\epsilon_i)|\psi_i\rangle. \tag{2.40}$$

$\Delta\epsilon_i$ ($= \langle\psi_i|\Delta V_{KS}|\psi_i\rangle$) is the first-order variation in Kohn-Sham eigenvalues. The change in Kohn-Sham effective potential (ΔV_{KS}) is given as:

$$\Delta V_{KS}(\mathbf{r}) = \Delta V_{ext}(\mathbf{r}) + e^2 \int d\mathbf{r}' \frac{\Delta n(\mathbf{r}')}{|\mathbf{r} - \mathbf{r}'|} + \int d\mathbf{r}' \frac{\partial^2 V_{XC}(\mathbf{r})}{\partial n(\mathbf{r}) \partial n(\mathbf{r}')} \Delta n(\mathbf{r}'). \tag{2.41}$$

The response of electron density to external perturbation depends on the coupling between occupied and empty electronic states, and $\Delta\psi_i$ is projected onto empty states manifold (of gapped systems) and given by,

$$(H_{KS} - \epsilon_i)|\Delta\psi_i\rangle = -\hat{P}_{empty}\ \Delta V_{KS}|\psi_i\rangle, \tag{2.42}$$

where $\hat{P}_{empty}$ is the projection onto the empty states manifold and is defined as,

$$\hat{P}_{empty} = 1 - \hat{P}_{occ};\ \hat{P}_{occ} = \sum_{i=1}^{N_e} |\psi_i\rangle\langle\psi_i|. \tag{2.43}$$

From the solution of (Eq. 2.42) this set of linear equations, the response properties of a system can be obtained accurately and efficiently.

$K_{I\alpha,J\beta}$ can be evaluated using DFPT by calculating the second derivative of total energy with respect to atomic displacements. Born effective charges (Z^*) can be estimated using DFPT as the mixed derivative of total energy with respect to electric field and atomic displacements. The dielectric constant (ϵ^∞) can be determined from the second derivative of total energy with respect to the electric field.

As the responses to phonon perturbations with different wavelengths are decoupled, linear perturbation theory is beneficial over the non-perturbative approaches like frozen phonon methods, and the calculation of phonon frequencies at arbitrary q-vectors can be performed using DFPT without introducing supercells.

Part I

Twisted heterostructures based on Graphene and h-BN

Chapter 3

Chemical route to twisted graphene, graphene oxide and boron nitride [†]

3.1 Introduction

Two-dimensional (2D) layered materials have become an important area of research [117–121]. An important development in this area is the generation of van der Waals heterostructures formed by depositing a monolayer or a few layers of a 2D material on a monolayer or few layers of the same or another 2D material [122, 123]. As an alternative to van der Waals heterostructures, superlattices of 2D materials have been generated by covalent cross-linking. These materials exhibit several novel properties [124–126]. An exciting recent discovery is that of 2D superlattices of graphene formed by twisted bilayers [127–134]. Twisted bilayer graphene (tBLG) superlattice is reported to be superconducting. The tBLG superlattice has been fabricated using dry-transfer technique. A

[†]This work has been published in Chem. Eur. J. **26**, 6499-6503 (2020) [116]. Reproduced with permission from John Wiley & Sons, Inc.

"tear-and-stack" technique was developed by Cao *et al.* to enable subdegree control of the twist angle in twisted bilayer graphene [135]. Mogera *et al.* have synthesized superlattices of twisted multilayer graphene (tMLG) by drop coating solution of a hydrocarbon such as naphthalene on a Ni foil followed by Joule heating [136]. Selected area electron diffraction (SAED) patterns reveal angular relations between the twisted layers of graphene. Twisted multilayer graphene exhibits split spots with definite angular spacings in SAED pattern unlike graphite, which shows hexagonal diffraction spots, suggesting angular deviations from AB packing. Most of the methods reported for the synthesis of twisted graphene require the use of substrates and are not amenable for large-scale synthesis.

Our experimental collaborators (Aditi Saraswat from Prof. C. N. R. Rao's group at Jawaharlal Nehru Centre for Advanced Scientific Research) have generated twisted multilayer graphene/h-BN superlattices chemically using trans-1,4-diaminocyclohexane (DACH) and oxalic acid as the linkers. We have simulated twisted graphene and h-BN structures using first-principles density functional theory (DFT) calculations, as implemented in the QUANTUM ESPRESSO package [137]. To simulate the interaction of linker molecules (L_1=trans-1,4-diaminocyclohexane, L_2 = 1,5-diaminonaphthalene, L_3 = Oxalic acid), we have used (3×3, 5×5, 3×3) periodic supercells of graphene and h-BN. A vacuum of 15 Å was introduced along the z-direction to avoid interaction between the system and its periodic image.

3.2 Experimental observations

Our experimental collaborators (Aditi Saraswat from Prof. C. N. R. Rao's group at Jawaharlal Nehru Centre for Advanced Scientific Research) have prepared twisted multilayer graphene oxide (tMLGO) superlattices by cross-linking graphene oxide (GO) layers with the DACH linker by the carbodimide method. The SAED patterns of tMLGO shows a set of diffraction spots spread out with angular spacings varying in the range 8–14^o, directly

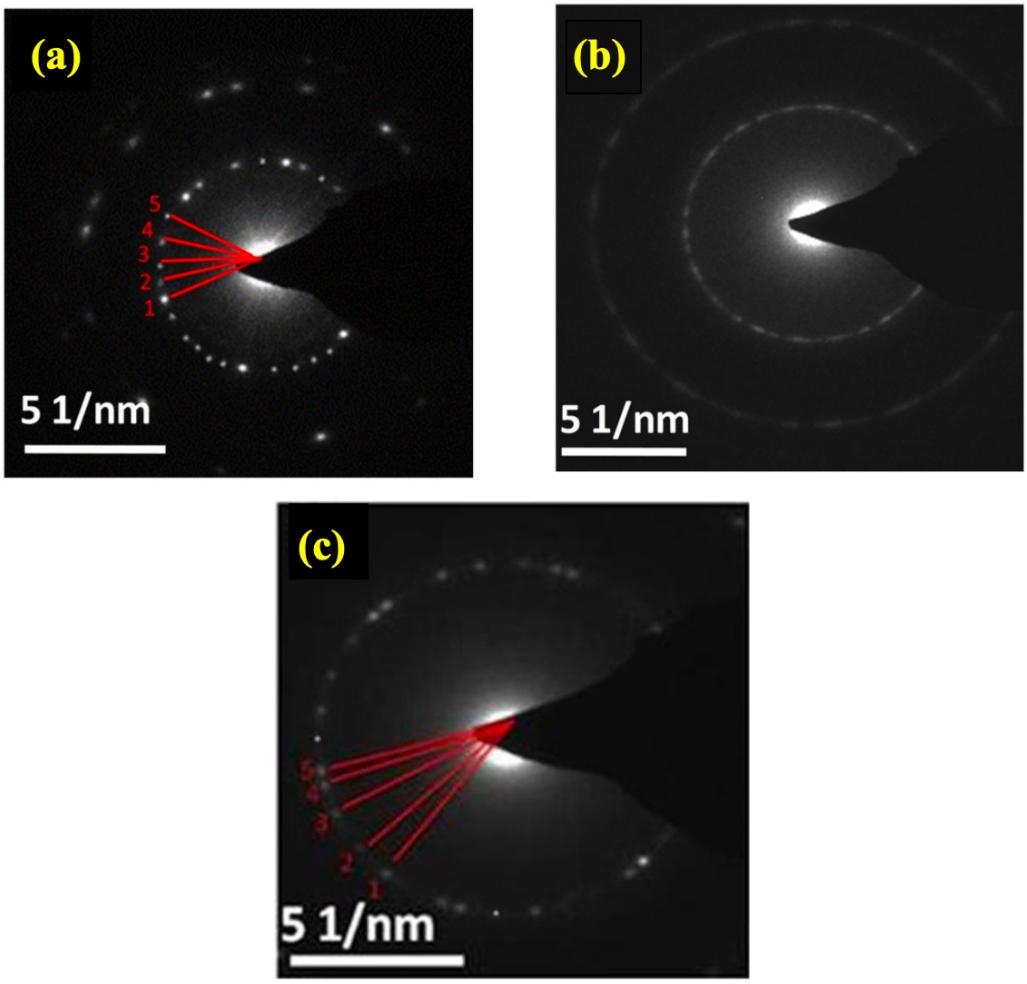

Figure 3.1: SAED pattern (obtained by Aditi Saraswat from Prof. C. N. R. Rao's group at Jawaharlal Nehru Centre for Advanced Scientific Research) of twisted multilayer graphene prepared using (a) trans-1,4-diaminocyclohexane and (b) 1,5-diaminonapthalene linker and twisted multilayer hexagonal boron nitride using (c) Oxalic acid.

related to the angular rotations between individual GO sheets (Fig. 3.1(a)). Superlattice of tMLGO was also obtained by using 1,5-diaminonapthalene as the linker (Fig. 3.1(b)). Encouraged by the success in preparing twisted multilayer graphene, twisted superlattices of h-BN have been prepared. The procedure involves dispersing amine-functionalized h-BN, prepared by the reaction of boric acid and urea at a high temperature, and cross-linking it with the oxalic acid linker in the presence of 1-ethyl-3-(3-dimethylaminopropyl)-carbodiimide (EDC). Superlattices of tMLBN show split spots in SAED pattern, indicating angular deviation from the AB packing responsible for keeping layers decoupled

(Fig. 3.1(c)).

3.3 Computational details

We have employed the Quantum ESPRESSO package [137], in which we treat only the valence electron by replacing the potential of iconic cores with ultrasoft pseudopotentials. The exchange-correlation energy of the electrons is treated within a generalized gradient approximation (GGA) [138] with a functional form parametrized by Perdew, Burke, and Ernzerhof (PBE) [139]. The electronic wave functions and charge density are represented in plane wave basis sets truncated at energy cut-offs of 40 Ry and 320 Ry respectively. Brillouin zone (BZ) integrations were sampled on a uniform 3×3×1 mesh of **k**-points. The discontinuity in occupation numbers of electronic states was smeared using a Fermi-Dirac distribution function with broadening temperature of $k_{\mathrm{B}}\mathrm{T} = 0.003$ Ry. As the PBE functional does not capture long range van der Waals interaction, we include van der Waals (vdW) interaction using PBE+D2 method of Grimme [140]. The electronic spectrum was calculated at Bloch wave vectors along the high symmetry lines (Γ−K−M−Γ) in the Brillouin Zone.

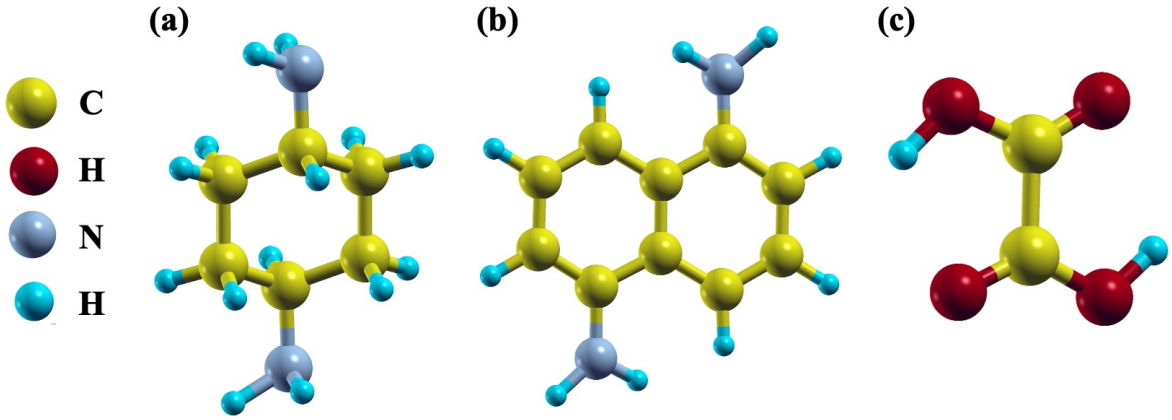

Figure 3.2: Structure of organic linkers (a) trans-1,4-diaminocyclohexane, (b) 1,5-diaminonaphthalene and (c) oxalic acid.

3.4 Results and Discussion

Our first-principles based DFT calculations throw light on the structure and interactions at the interface of linker and 2D monolayer: graphene–trans-1,4-diaminocyclohexane−graphene (G−L_1−G), graphene–1,5-diaminonaphthalene–graphene (G−L_2−G) and h-BN−Oxalic acid−h-BN (h-BN−L_3−h-BN). In relaxation of structure, we start with a single layer of graphene/h-BN and a linker molecule attached to it (Fig. 3.3). Using bond lengths, bond angles and orientation of the linker with respect to the monolayer of graphene/h-BN in the optimized structure, another layer of graphene/h-BN is attached to the other side of the linker. As a result, the second layer gets placed with a twist by an angle with respect to the first monolayer. We then simulate the chemically twisted bilayer graphene/h-BN by stacking two layers of graphene such that one layer is rotated with respect to the other by an angle θ. We start with a graphene layer with the superperiodicity defined by (N, M) and $(\text{-}M, N + M)$ vectors and rotate it by $+\theta/2$. The second graphene layer with periodicity (M, N) and $(\text{-}N, M + N)$ vectors is rotated by $-\theta/2$. The commensurate tBLG is labelled by integers (N, M) (Fig. 3.4). These integers (N, M) are related to the twist angle θ and the number of atoms N_{atom} in the supercell of size L_{cell} using Eq. 3.1, Eq. 3.2 and Eq. 3.3 [141]:

$$cos\theta = \frac{N^2 + 4NM + M^2}{2(N^2 + NM + M^2)}, \tag{3.1}$$

$$L_{cell} = d\sqrt{3(N^2 + NM + M^2)}, \tag{3.2}$$

$$N_{atom} = 4(N^2 + NM + M^2), \tag{3.3}$$

where d is the C−C distance in the graphene layer.

Commensurate tBLG has the hexagonal symmetry because of C_3 rotational symmetry of

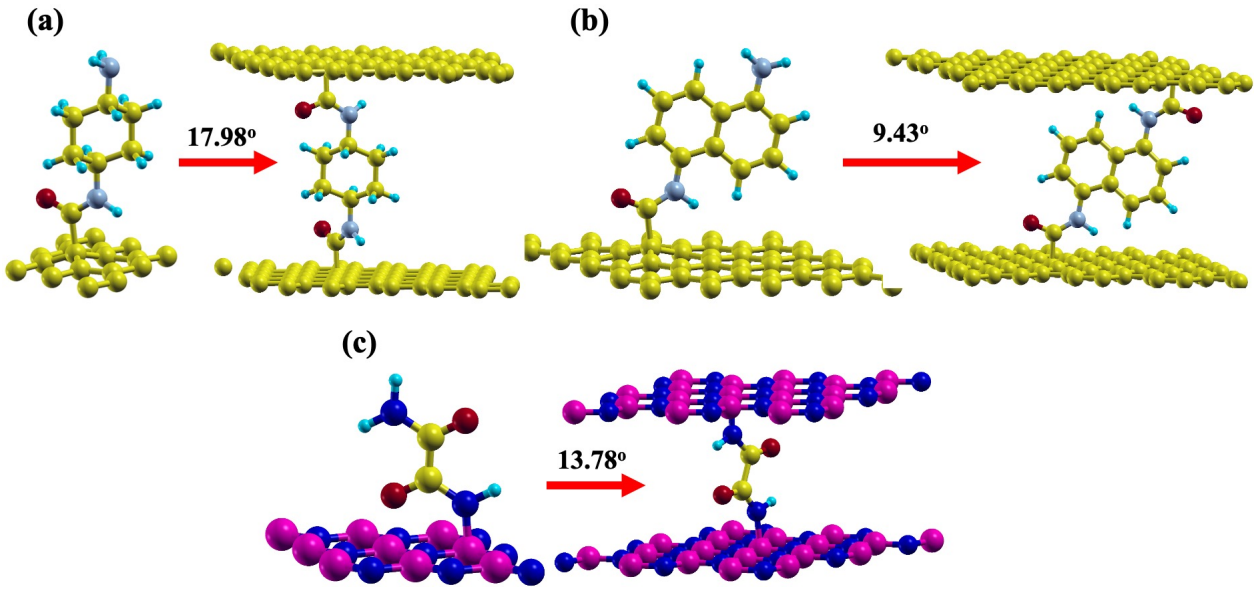

Figure 3.3: Optimized structures of (a) graphene–trans-1,4-diaminocyclohexane−graphene (G−L_1−G), (b) graphene–1,5-diaminonaphthalene–graphene (G−L_2−G) and (c) h-BN−Oxalic acid−h-BN (h-BN−L_3−h-BN).

graphene. Fig. 3.5 shows moiré patterns of graphene/h-BN for various twist angles and exhibit interesting patterns. The smaller the rotation angle, the bigger the periodicity and the discrete the moiré pattern.

The calculated C−C bond length at the interface of G–L_1 is 1.56 Å. In G–L_2 and h-BN–L_3, the C−C and B−N bond lengths are 1.66 Å and 1.62 Å respectively. The theoretical twist angles in G–L_1–G, G–L_2–G and h-BN–L_3–h-BN are 17.98^o, 9.438^o and 13.78^o, respectively. Electronic density of states (DOS) (Fig. 3.6) of these chemically linked bilayers show a peak at E_F associated with the covalent bond between the linker and the graphene/h-BN sheet. This can be understood from the orbital-projected density of states (Fig. 3.6(d-f)), in which we see an overlap between the $2p$ orbitals of carbon atom of the linker molecule and $2p$ orbitals of carbon atom in graphene sheet in G–L_1 and G–L_2 and $2p$ orbitals of boron in boron nitride and N-$2p$ of linker in h-BN–L_3. In the optimized geometries of linker-monolayer complexes shown in (Fig. 3.3), we note an out-of-plane

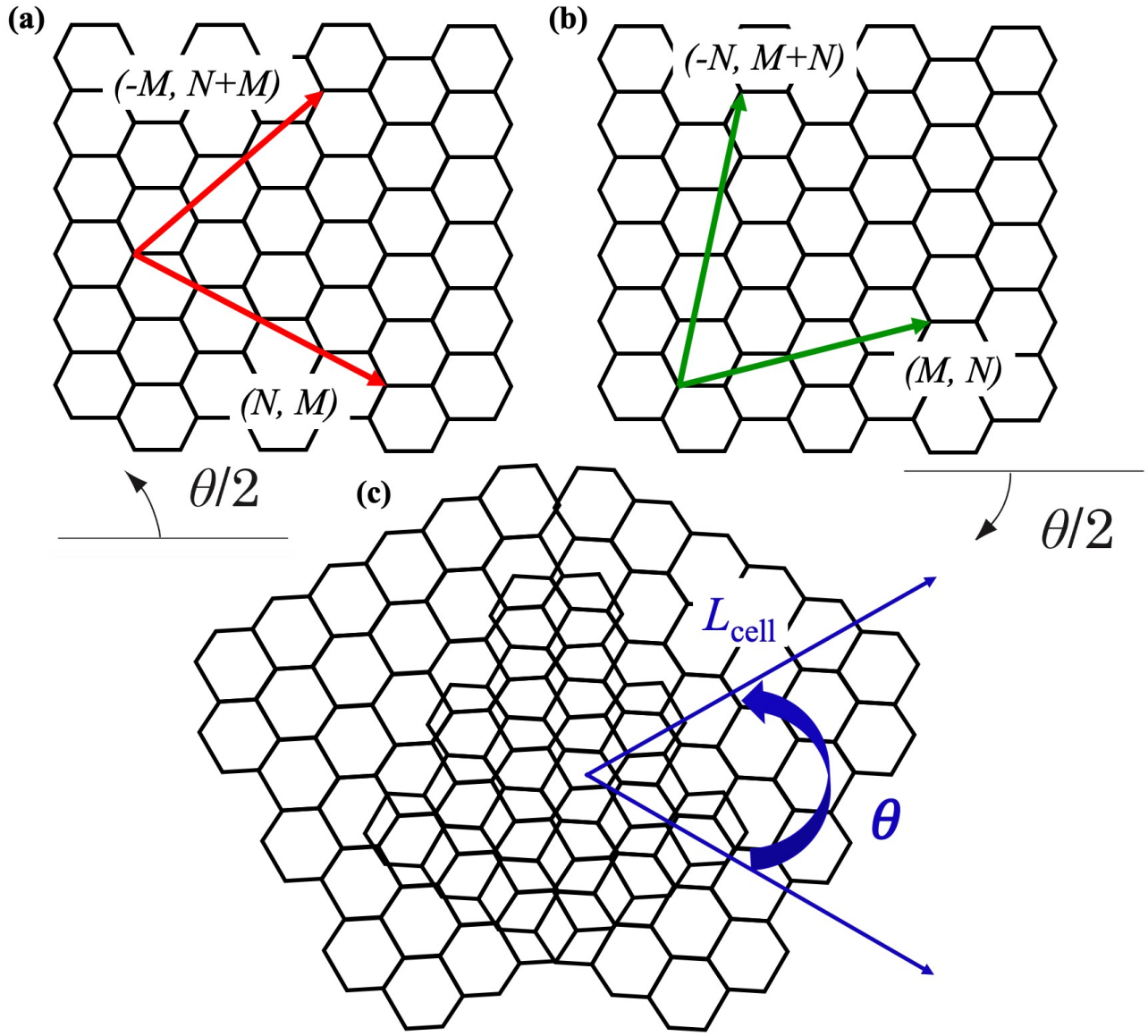

Figure 3.4: (a) Graphene sheet with a superperiodicity defined by the two (N, M) and $(-M, N + M)$ vectors and rotate it by $+\theta/2$. (b) Similarly, take a graphene sheet with periodicity defined by the (M, N) and $(-N, M + N)$ vectors and rotate it by $-\theta/2$. (c). The commensurate tBLG with the twist angle θ and the periodicity L_{cell} is obtained by stacking rotated graphene sheets as shown in (a) and (b).

displacement of the carbon atom of graphene in response to bonding interaction with L_1 and L_2 (and boron of boron nitride due to bonding with L_3), suggesting a change in hybridization from sp^2 to sp^3.

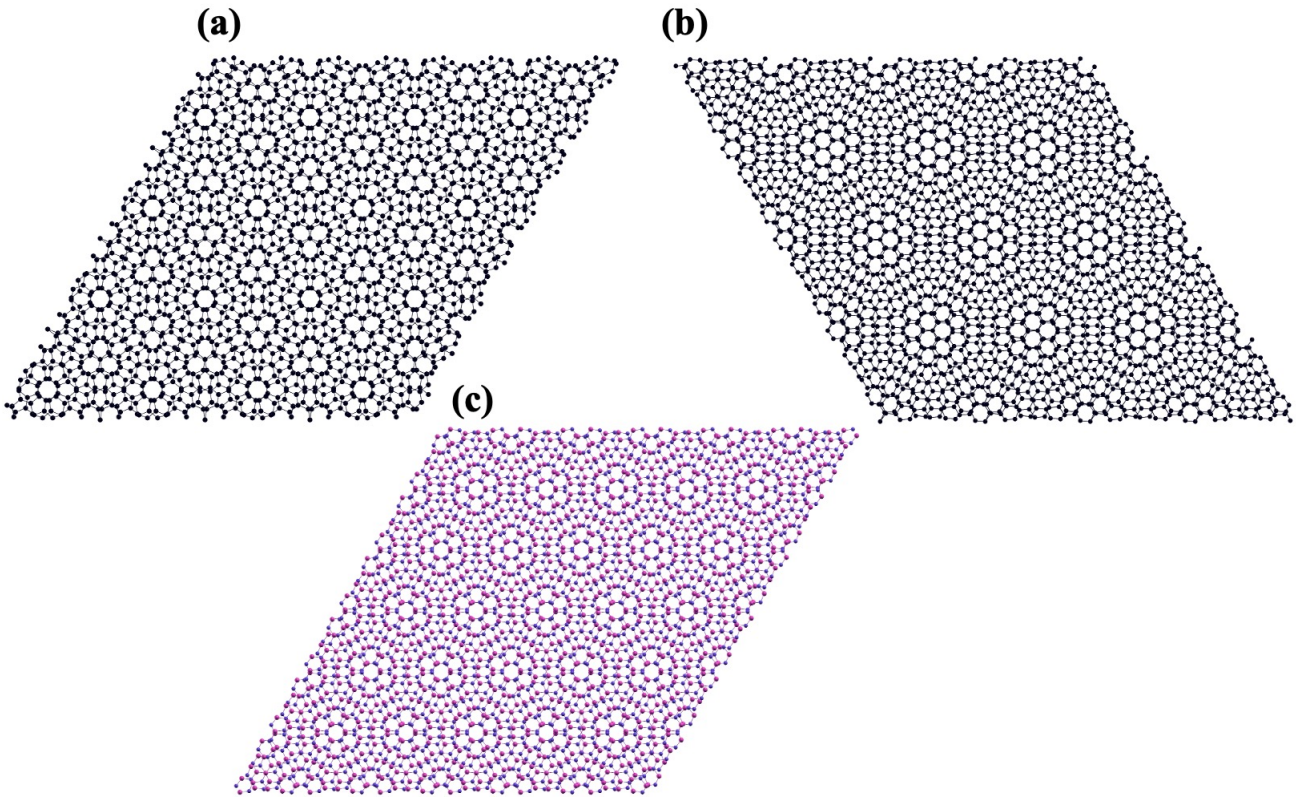

Figure 3.5: Moiré patterns for twist angles θ of (a) 17.98^o, (b) 9.43^o in graphene and (c) 13.78^o in boron nitride, which arise from the chemical linkers L_1 = trans-1,4-diaminocyclohexane, L_2 = 1,5-diaminonaphthalene, L_3 = oxalic acid.

In contrast to the electronic structure of monolayered graphene which exhibits Dirac cones [142] at K-point, the chemically twisted graphene exhibits energy bands with a gap at K-point (Fig. 3.6(a, b)). Electronic structure of chemically twisted boron nitride shows a smaller bandgap of 0.3 eV compared to a band gap of 6.08 eV in monolayered h-BN (Fig. 3.6(c)). Boron nitride sheets form N−C bonds with the linker as seen from the overlap of the corresponding orbitals in (Fig. 3.6(f)). An interesting feature common to twisted graphene and h-BN is the appearance of a nearly flat band near E_F (Fig. 3.6(a-c)). Visualization of wavefunctions of the flat band at E_F at the Γ-point shows that the band has contributions from the $2p$ orbitals of both linker and graphene/h-BN and the charge distribution is confined only up to the graphene/h-BN and the carbon/nitrogen of the linker bonded to the layers (Fig. 3.7). The red and blue colors denote sign of

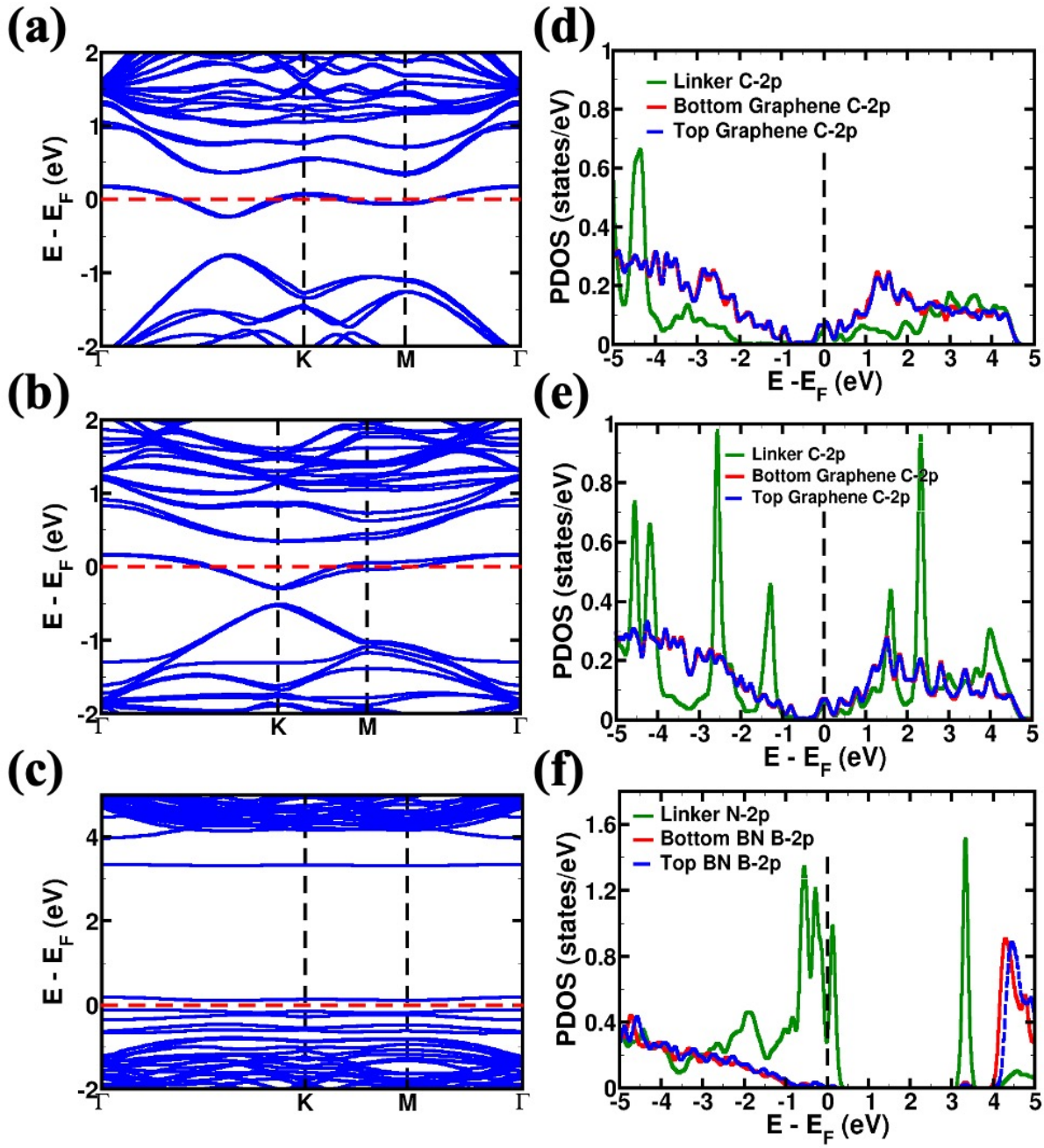

Figure 3.6: Electronic structure and projected density of states for G−L_1−G (a,d), G−L_2−G (b,e) and h-BN−L_3−h-BN (c,f) complexes.

the wavefunction (indicative of polarity) at the Gamma point. These bands are different from the flat bands observed at the Fermi level in tBLG (AA-stacking) when the twist angle $\theta = 1.08^o$ [143]. The Fermi velocity for $\theta = 1.087^o$ is close to zero and these nearly

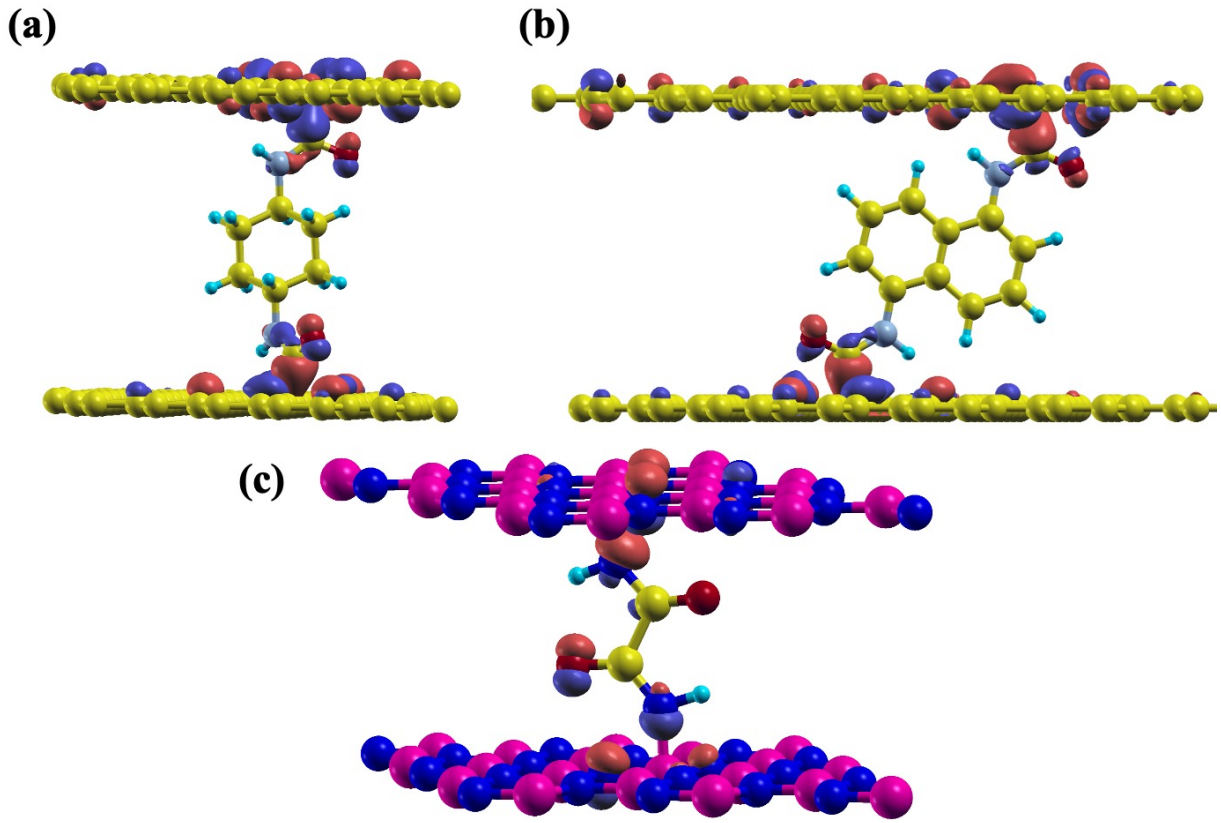

Figure 3.7: Visualization of wavefunctions of the flat band at E_F at Γ-point of (a) G−L_1−G, (b) G−L_2−G and (c) h-BN−L_3−h-BN. The red and blue colors denote sign of the wavefunction (indicative of polarity) at the Gamma point.

dispersion-less bands show highly localized charge density.

3.5 Conclusions

In conclusion, we have been able to prepare twisted graphene, graphene oxide and h-BN by covalent linking of the layers. First-principles calculations corroborate the experimental observations that covalent cross-linking of carboxylic groups of graphene (graphene oxide), through amine functional groups of the linker as well as of amine groups of boron nitride with carboxylic groups of the linker, leads to generation of interlayer twist in multilayer graphene/h-BN.

Chapter 4

Berry curvature dipole senses topological transition in a moiré superlattice [†]

4.1 Introduction

Tailoring properties of two-dimensional materials by tuning the relative twist angle between successive layers has enormously increased the study and understanding of electron correlation physics, such as superconductivity [145,146], orbital ferromagnetism [147,148] and Mott insulator states [149, 150]. Twistronics has emerged as a new field where the twist angle is a degree of freedom that can be exploited to obtain fascinating and novel phenomena in materials [151, 152]. Bilayer graphene (TBG) is obtained by stacking two

[†]This work has been published in Nat. Phys. **18**, 765-770 (2022) [144]. Reproduced with permission from Springer Nature.

single layers of graphene on top of each other where the typical interlayer distance is 3.35 Å. It can exist in different lattice orientations such as 'Bernal' or 'AB' which is energetically more favourable than 'AA' arrangement. The rotational misorientation between the two layers results in twisted bilayer graphene (TBG) with moiré superlattices containing stacking domains related to the twist angle. Recently, magic-angle ($\theta = 1.1^o$) TBG has attracted attention due to observation of several novel pheneomena in these moiré systems [145, 150]. In particular, the observation of anomalous Hall effect, orbital ferromagnetism and Chern insulating states point to the rich topology of these twisted systems [147, 148, 153].

Exploring materials with new topological phases and probing their symmetries has been at the forefront of modern research. Topology is often characterized by Berry curvature that manifests as the quantum Hall effect [154] or anomalous Hall effect in magnetic materials [154, 155]. Berry curvature is a mathematical concept that arises in the context of the quantum mechanics of systems with degenerate energy levels. It is a measure of the geometric phase acquired by a quantum state when it adiabatically evolves along a closed loop in parameter space. The Berry curvature is defined as a vector field on the parameter space, and its integral over a closed loop is known as the Berry phase. Although these effects have led to many breakthroughs in physics, these linear responses vanish in systems that preserve time-reversal symmetry and inversion symmetry. However, even in time-reversal-symmetry-protected systems, broken inversion symmetry can lead to the first moment of Berry curvature, namely, a Berry curvature dipole (BCD), when further spatial symmetries are reduced [156]. In the presence of an a.c. current (of frequency ω) in such a system, the BCD can drive a second-order electrical response, namely, the nonlinear Hall (NLH) voltage with zero (d.c.) and second-harmonic (2ω) frequencies. Aligned with the recent interest in various nonlinear phenomena such as nonlinear optics, there is a rapidly growing interest to look for quantum materials that host the NLH effect. In this work, we use twisted double bilayer graphene (TDBG), in which two copies

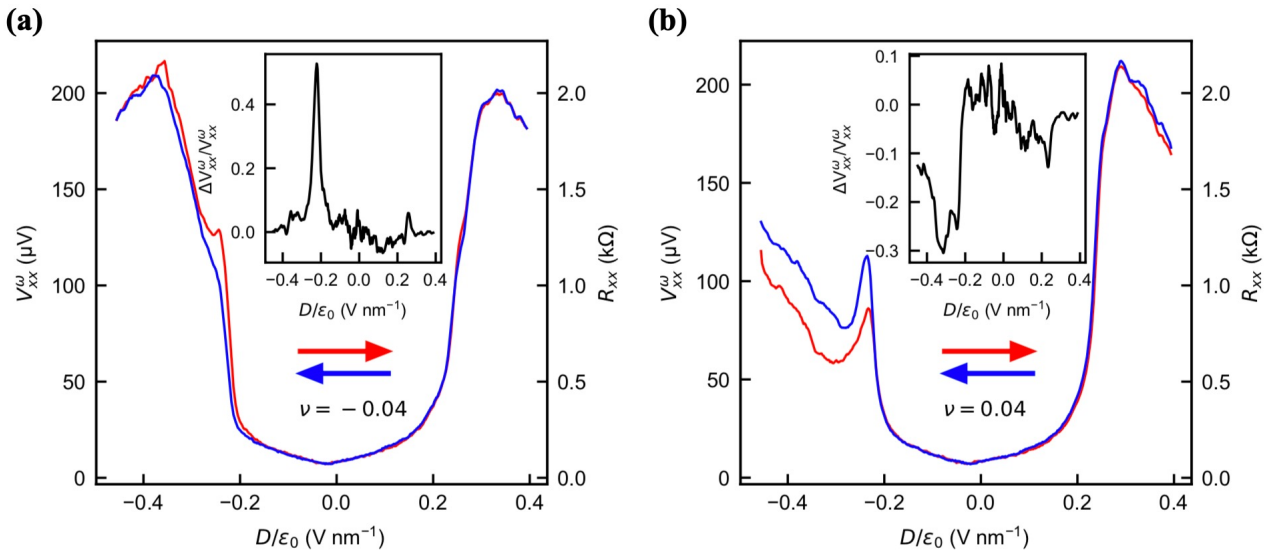

Figure 4.1: Hysteresis in longitudinal resistance R_{xx} with displacement field (D/ϵ_0) for a doping below CNP at $\nu = -0.04$ (a) and above CNP at $\nu = 0.04$ (b). The arrows indicate direction of sweeping D. On the negative D side, the red curve leads the blue curve in (a), while it lags in (b). Such a change in hysteretic response due to doping cannot be accounted for via charge traps in dielectric. The insets show the relative difference in V^{ω}_{xx} of up and down sweep. The relative difference is maximum around $D/\epsilon_0 \sim 0.23$ Vnm^1, where a topological transition takes place. Experiments by Subhajit Sinha and Pratap Chandra Adak from Prof. Mandar Deshmukh's group at Tata Institute of Fundamental Research, Mumbai.

of bilayer graphene are stacked together with a small twist angle of approximately 1.1°, as a candidate system to study topological transitions using the NLH effect. Our central result is change of Berry curvature dipole as the valley Chern number (Chern number is a topological index that characterizes the total Berry curvature contained in a closed two-dimensional surface in the Brillouin zone. It is an integer value that can take on positive or negative values, and it is a measure of the Berry curvature polarization of the bands enclosed by the surface) of these bands changes in twisted double bilayer graphene (TDBG) with a small twist angle 1.1^o. However in this chapter, we elucidate the origin of hysteresis in longitudinal voltage V^{ω}_{xx} governed by dopings near charge neutrality point (CNP) as a function of the electric field suggesting switching between the metastable states.

4.2 Experimental observations

Our experimental collaborators (Subhajit Sinha, Pratap Chandra Adak and Prof. Mandar Deshmukh at Tata Institute of Fundamental Research, Mumbai) show hysteresis in longitudinal voltage V_{xx}^{ω} with displacement field (D/ϵ_0) for dopings near charge neutrality point (CNP) (Fig. 4.1). The CNP gap opens up at a nonzero electric field in twisted double bilayer graphene, as a result of which we see an increasing trend in V_{xx}^{ω} after a nonzero electric field $D/\epsilon_0 \sim 0.2$ Vnm^1 is applied. The red (blue) curve indicates the data taken while increasing (decreasing) the electric field. The insets in (Fig. 4.1(a) and Fig. 4.1(b)) show the difference in V_{xx}^{ω} between the forward and backward sweep of the electric field, normalized with measured V_{xx}^{ω} in the forward direction. In figure 4.1, towards negative electric field side, the red plot leads (lags) the blue plot. This shows a change in sense of hysteresis governed by doping. We try to understand these results with our first-principles calculations and modelling.

4.3 Computational details

Our first-principles calculations are based on density functional theory (DFT) as implemented in Quantum ESPRESSO (QE) package [137]. We use ultrasoft pseudopotentials to represent the interaction between ionic cores and valence electrons. The exchange-correlation energy of electrons is treated within a generalized gradient approximation (GGA) [138] with a functional form parametrized by Perdew, Burke, and Ernzerhof [139]. We truncated the plane wave basis used in expansion of Kohn-Sham wave functions and charge density with energy cut-offs of 45 Ry and 360 Ry respectively. We used $18 \times 18 \times 1$ uniform grid of k-points for sampling the Brillouin zone (BZ) integrations. The discontinuity in occupation numbers of electronic states was smeared with broadening temperature of $k_{\mathrm{B}}T = 0.005$ Ry using a Fermi-Dirac distribution function. We include van der Waals (vdW) interaction using PBE + D2 method of Grimme [140]. The 2D system is simu-

lated using a periodic supercell, with a vacuum layer of 12 Å separating adjacent periodic images of the sheet. To simulate response to electric field, we add a saw-tooth potential as a function z.

4.4 Results and Discussion

Twisted double bilayer graphene, TDBG, in our experiments is composed of two AB-stacked bilayers of graphene rotated by an θ [157] and encapsulated from top and bottom by hexagonal boron nitride (h-BN-TDBG-h-BN) (Fig. 4.2(b)). Thus, parallelly stacked one atomic plane of hexagonal boron nitride and two layers of graphene (Gr-Gr-h-BN) is a building block making a half of h-BN-TDBG-h-BN (upper trilayer) (Fig. 4.2(a)). Interestingly, a single Gr-Gr-h-BN unit is noncentrosymmetric and lacks the horizontal mirror symmetry. Hence, it is expected to have a non-vanishing polarization (dipole moment perpendicular to the plane). We consider two different configurations of Gr-Gr-h-BN which have been obtained by changing stacking sequences of Gr-Gr-h-BN (i) stacking of h-BN same as bottom graphene and (ii) stacking sqeuence of h-BN not matching with either of the two graphene layers. However, the energies of the two configurations are comparable (0.1 meV) and we carry out our theoretical analysis with the first configuration as a model.

We first examine the electronic structure of Gr-Gr-h-BN and find a band gap of $\sim$ 26 meV at K point (h-BN breaks sublattice symmetry of AB-stacked bilayer graphene, (Fig. 4.3(a)). From the slope of macroscopic average electrostatic potential in vacuum, our estimate of polarization of Gr-Gr-h-BN is $P_z \approx$ -0.34 μC/cm^2 (Fig. 4.4(b)). Thus, Gr-Gr-h-BN has a nonzero polarization due to the broken inversion and horizontal reflection symmetries. This mechanism is similar to ferroelectricity in bilayer h-BN [158]. The lower trilayer of TDBG is h-BN-Gr-Gr (Fig. 4.2(c)) and has exactly the same polarization

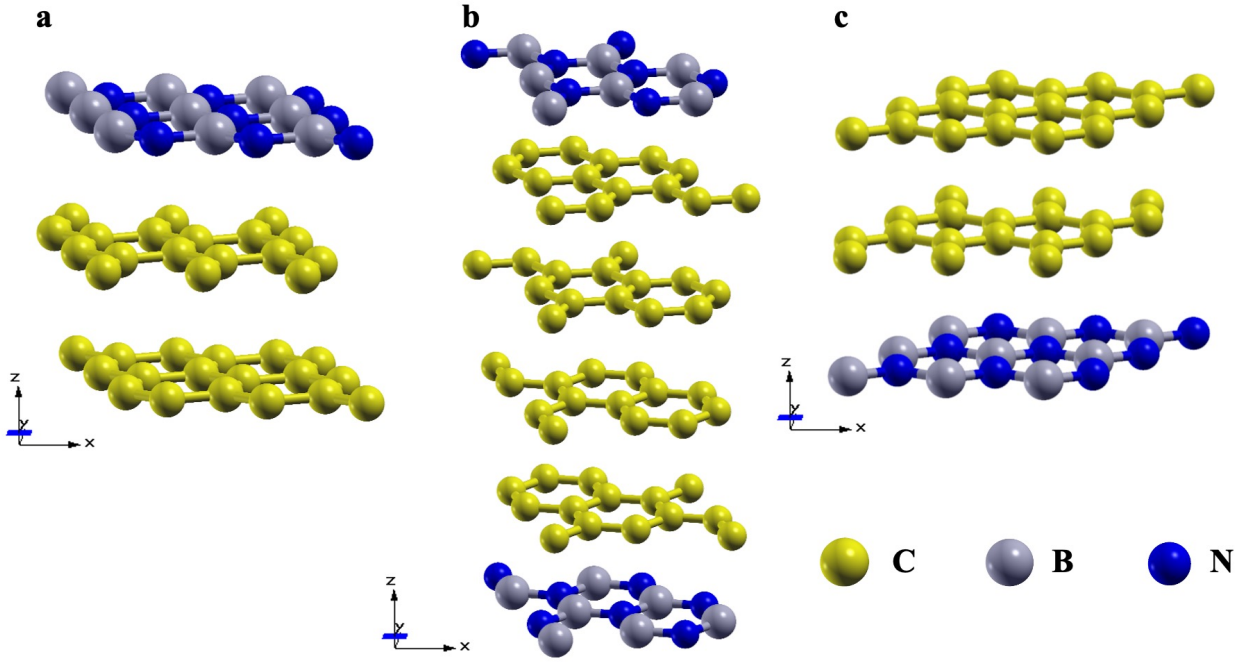

Figure 4.2: (a) Structure of Gr-Gr-h-BN, (b) unit cell of twisted double bilayer graphene encapsulated between hexagonal boron nitride (h-BN-TDBG-h-BN) with a rotation angle of 21.78° and (c) structure of h-BN-Gr-Gr. The building blocks of h-BN-TDBG-h-BN are Gr-Gr-h-BN and h-BN-Gr-Gr. The atomic species C, B and N are displayed in yellow, grey and blue colors, respectively.

with opposite sign.

The sense of hysteresis in longitudinal and nonlinear Hall voltage for doping just below charge neutrality point (CNP) is flipped on changing the doping to a point just above CNP. To understand the metastable states governing this hysteresis, we present a rigid band model for h-BN-Gr-Gr (lower trilayer) and Gr-Gr-h-BN (upper trilayer) of electronic states coupling with electric field and determine polarization as a function of electric field. Evolution of band energies with perpendicular electric field is modelled as

$$H_i = \epsilon_i + eE\langle Z_i \rangle \tag{4.1}$$

where i is the band index ($i = 1$ to 4 for the four bands close to Fermi at K point), ϵ_i is energy of i^{th} band, e is charge of an electron, E is electric field, $\langle Z \rangle$ is the average

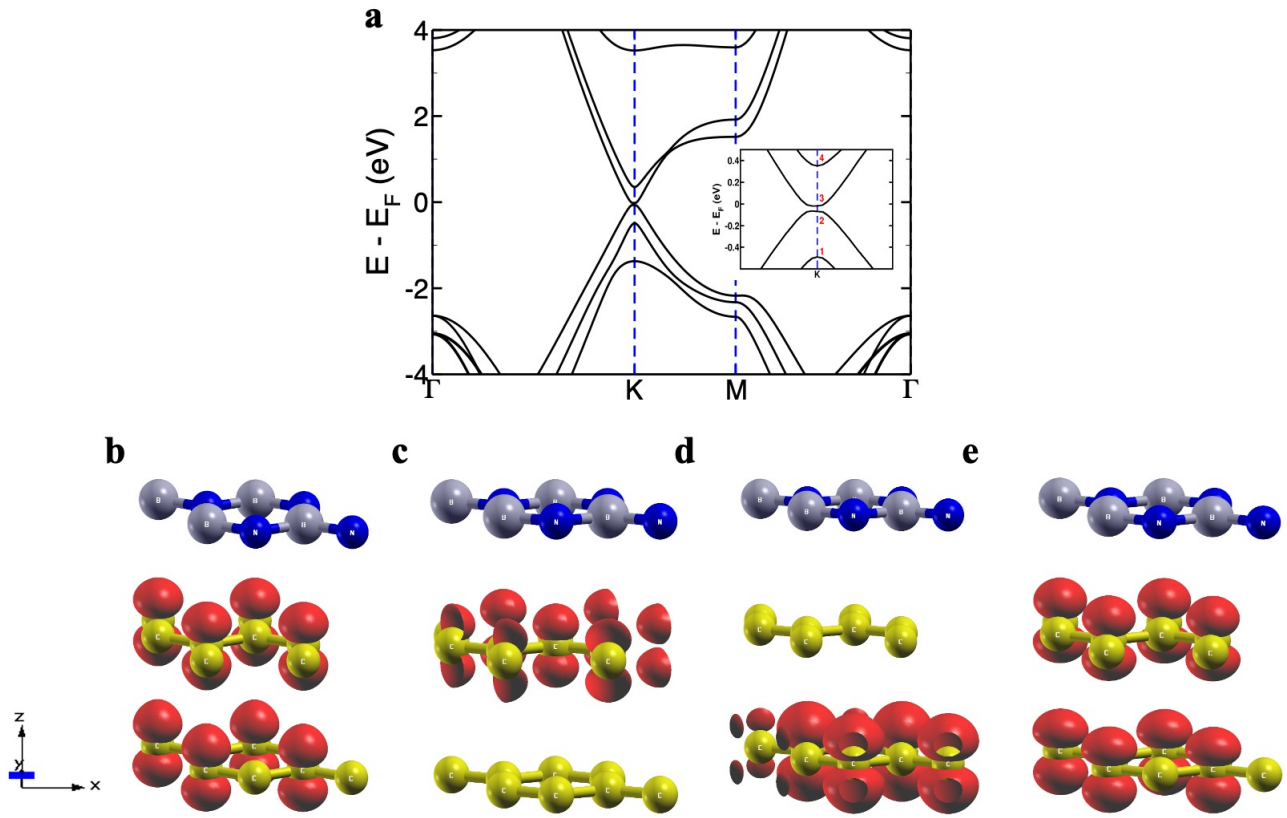

Figure 4.3: (a) Electronic structure of Gr-Gr-h-BN shows a band gap of 26 meV at K point. Visualization of wavefunctions of four states near Fermi energy at K point of (b) Band 1, (c) Band 2, (d) Band 3 and (e) Band 4 of Gr-Gr-h-BN shows contribution from p_z orbitals of carbon of graphene. The average position, $\langle Z \rangle$ in terms of interlayer distance d = 3.2 Å for bands 2 and 3 is 3/2d, and 1/2d, respectively.

position of each state (Fig. 4.3(b-e)). $\langle Z \rangle$ is minus (-) for h-BN-Gr-Gr (lower trilayer) and plus (+) for Gr-Gr-h-BN (upper trilayer), respectively. Band 2 of the lower trilayer and band 3 of upper trilayer cross at E = -0.0039 V/Å (band 3 of lower trilayer and band 2 of upper trilayer cross at E = 0.0039 V/Å), resulting in redistribution of charges among these bands (Fig. 4.4(c)). We show that there exists two metastable states for (i) E < -0.0039 V/Å and (ii) E > 0.0039 V/Å, with distinct polarization states in h-BN-TDBG-h-BN, that can be accessed with electric field within our rigid band model (Fig. 4.4(d)). However, the resistance associated with the two metastable states remains the same. While the metastable states in h-BN-TDBG-h-BN are explained using the rigid

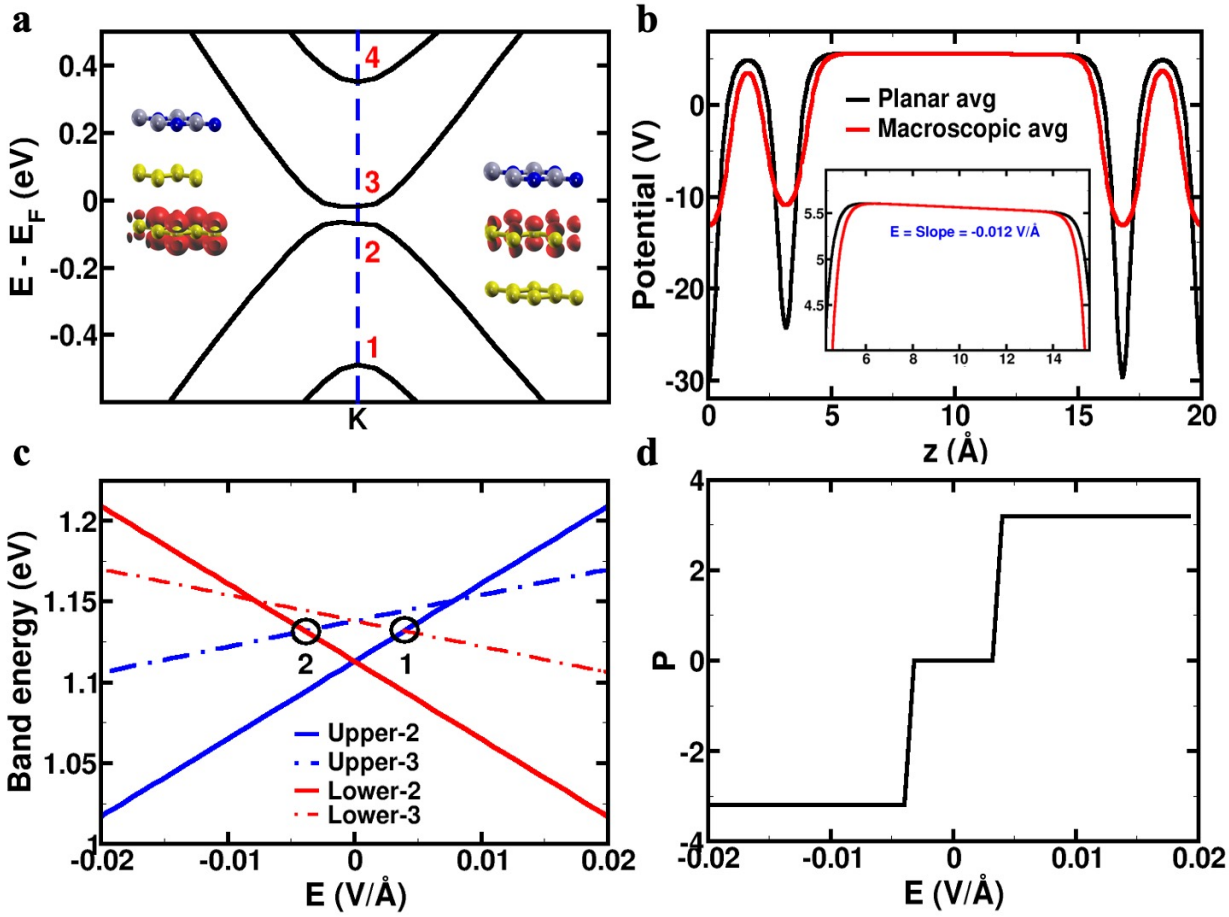

Figure 4.4: (a) Electronic structure of Gr-Gr-h-BN shows a band gap of 26 meV at K point. The inset shows spatial distribution of the wave functions of bands labelled 2 and 3. (b) Electric field (E) calculated from slope of average macroscopic potential of Gr-Gr-h-BN in vacuum. (c) Evolution and crossing of band 2 and 3 at E = -0.0039 V/Å and E = 0.0039 V/Å of upper and lower trilayer of h-BN-TDBG-h-BN as a function of electric field using our rigid band model and (d) metastable states for (i) E < -0.0039 V/Å and (ii) E > 0.0039 V/Å, with nonzero polarization in h-BN-TDBG-h-BN that are accessible with electric field.

band model, the hysteresis in resistance seen in experiments can originate from the broken symmetry, which can possibly arise from the distinction in coupling of top and bottom gates inducing inhomogenous doping in the channel or by a twist between two trilayers.

To understand the role of a gate electrode, we obtain the difference in planar-averaged electron charge density, $\bar{\rho}(z)$ for $n = 4 \times 10^{12}/\mathrm{cm}^2$, E = 0.00625 V/Å and $n = 4 \times 10^{12}/\mathrm{cm}^2$,

E = 0 V/Å with and without electric boundary conditions of a gate (Fig. 4.5(b) and Fig. 4.5(c)) in h-BN-TDBG-h-BN with a twist angle $\theta = 21.78^{o}$. Asymmetry in $\Delta\bar{\rho}(z)$ at the atomic planes (red dashed lines in Fig. 4.5(b) and Fig. 4.5(c)) indicate accumulation and depletion of electronic charge and local polarization arising from polarizability of p_z orbitals and a transfer of a tiny amount of charge. In the presence of gate, a positive electric field (along $\hat{z}$) pushes the electrons to the bottom gate (the scale of y-axis in Fig. 4.5(c) is higher than Fig. 4.5(b)), highlighting the inhomogenity in doping. We note that a spontaneous electric dipole p_z can also arise from the restructuring of the regions with AA, AB, BA and BB stacking upon application of electric field [158] and contribute to the observed hysteresis.

4.5 Conclusions

A periodic supercell to model boron nitride encapsulated TDBG with magic angle (θ) = 1.1^{o} is rather large 31,332 atoms and first-principles theoretical analysis of its response to gating electric field is computationally extremely expensive. To tackle this in realistic way, we have used a combination of modeling and first-principles density functional theoretical calculations. We note that the encapsulating h-BN sheets do impact properties of TDBG and have not been included in any analysis so far. We have determined the effects of gate electrodes and consequent doping in TDBG on its polarization with suitable electrostatic boundary conditions in our first-principles calculations, using TDBG with a twist angle $\sim 21.8^{o}$ consisting of 84 atoms as a model system, noting that it too has a broken inversion symmetry. We analyze effects of perpendicular electric field on the TDBG in two steps, focusing first on the coupling of field with the DBG (twist angle = 0) and then discuss the effect of twist in terms of variation in stacking between the DBGs. Using a rigid band model of frontier electronic states of DBG, we demonstrate that electric field permits switching to two metastable states with opposite polarization arising from the inversion

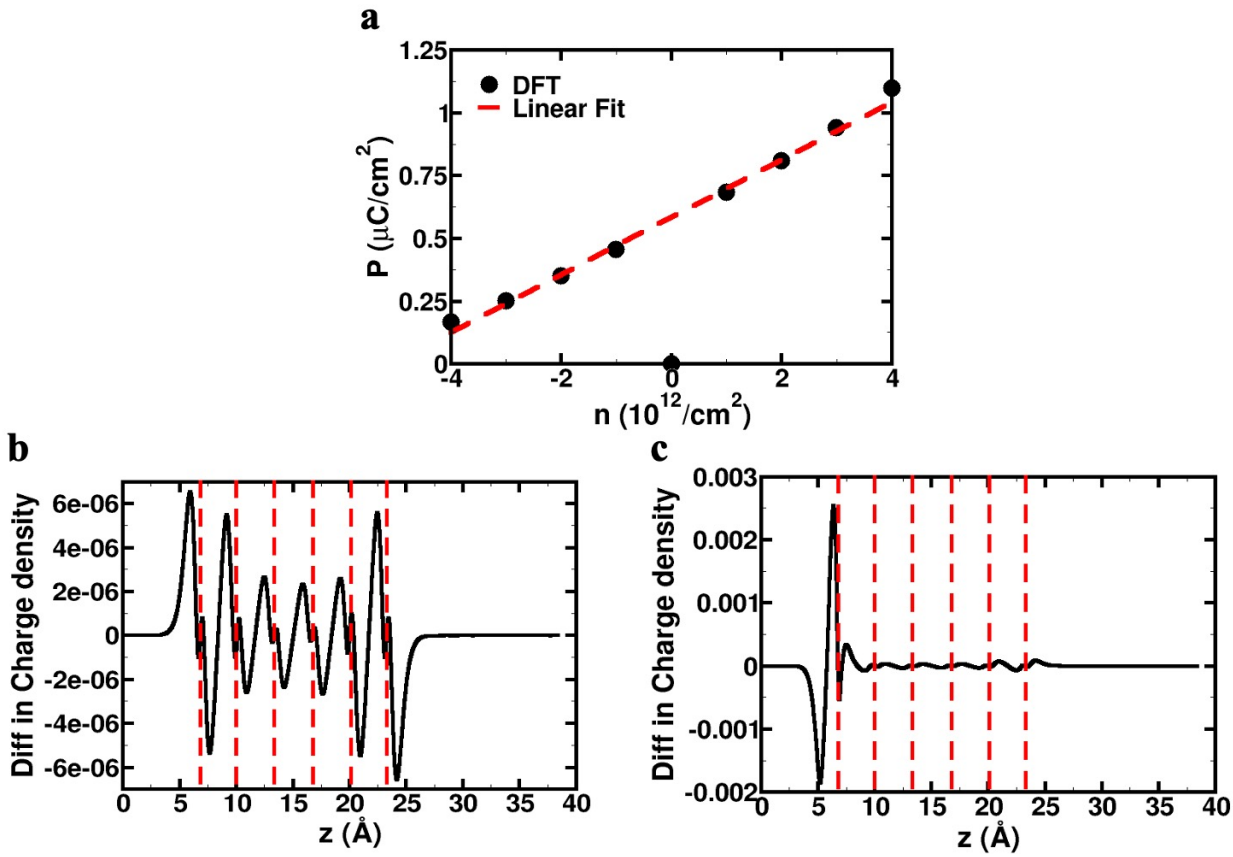

Figure 4.5: (a) Polarization in TDBG calculated as a function of doping in the presence of a bottom gate. The difference in planar-averaged electron charge density, $\bar{\rho}(z)$ for n = 4 $\times 10^{12}$/cm^2, E = 0.00625 V/Å and n = 4 $\times 10^{12}$/cm^2, E = 0 V/Å (b) without and (c) with gate set-up in h-BN-TDBG-h-BN with a twist angle $\theta = 21.78^{o}$. In the presence of gate, a positively oriented electric field pushes the electrons at the bottom gate (the scale of y-axis in Fig. 4d is higher than Fig. 4c).

of frontier electronic states in one of the DBGs. We clearly establish inhomogeneous doping across the layers due to differences in the top and bottom gate electrodes, which is also expected in TDBG with magic angle of twisting. The difference in planar averaged charge densities, $\bar{\rho}(z)$ for n = 4 $\times 10^{12}$/cm^2, E = 0.00625 V/Å and n = 4 $\times 10^{12}$/cm^2, E = 0 V/Å with and without electric boundary conditions of a gate clearly reveal the asymmetry in $\bar{\rho}(z)$ about the atomic planes in terms of accumulation and depletion of electronic charge and also a transfer of charge between the layers. Such inhomogeneity is relevant to coupling of the TDBG sheets (at all angles) with perpendicular electric

field. We note that the periodic supercell of TDBG twisted by magic angle consists of AAAA, BBBB, ABBA and ABAB stacking regions in the moiré pattern. The balance between spontaneous polarization in opposite directions in ABAB and ABBA regions will be altered due to reconstruction on application of electric field, and give rise to ferroelectric properties like switching and hysteresis [158]. Thus, the observed hysteresis has possible contributions from inhomogeneous stacking as well as inhomogeneous layer-dependent carrier concentration.

Part II

Layer dependence of response of MX_2 (M = Mo, Hf and X = Te, S) to electric field

Chapter 5

Symmetry induced phonon renormalization in bilayer 2H-$MoTe_2$ †

5.1 Introduction

The discovery of unique and remarkable properties of graphene has sparked unprecedented interest in other classes of two dimensional (2D) materials like transition metal dichalcogenides (TMDs, MX_2, where M = transition metals (Mo, W, Ti, Nb, Ta) and X = chalcogens (S, Se, Te)) for their potential applications in nano and opto-electronics [28]. Optical and electrical properties of these TMDs can be easily manipulated by changing the layer number and carrier doping. $MoTe_2$ is a member of the group-VI TMD family that crystallizes into three stable phases: Hexagonal (α or *2H*) [160], monoclinic (β or *1T′*) [161]

†This work has been published in Nanotechnology **32**, 045202 (2021) [159]. Reproduced with permission from the IOP Publishing.

and orthorhombic (γ or T_d) [162]. The *2H* phase is semiconducting [163], whereas the *1T′* phase is a narrow band gap semiconductor [164]. Similar to other group-VI dichalcogenides, *2H*-$MoTe_2$ has a trigonal-prismatic coordinated crystal structure [165], consisting of weakly coupled sandwich layers of Te-Mo-Te units, where Mo-atom layer is enclosed between two Te layers (Fig. 5.1) [160]. Unlike other TMDs, energy difference between the *2H* and *1T′* phase is very small ($\sim$ 31 meV per formula unit [79]). This enables easy tuning of the two phases by strain [166,167], laser irradiation [168,169] and electron doping [91,170], making this material an ideal candidate for next generation homojunction devices [171]. From electron doping (n) induced transition from *2H* to *1T′* phase in multilayer $MoTe_2$, Zakhidov *et al.* recently suggested that doped electrons by ionic liquid (IL) gating are localized on the top few layers of the nanocrystal [170], consistent with previous theoretical calculations [172].

Bulk $MoTe_2$ has an indirect band gap of $\sim$ 1.0 eV [173,174] which becomes a direct band

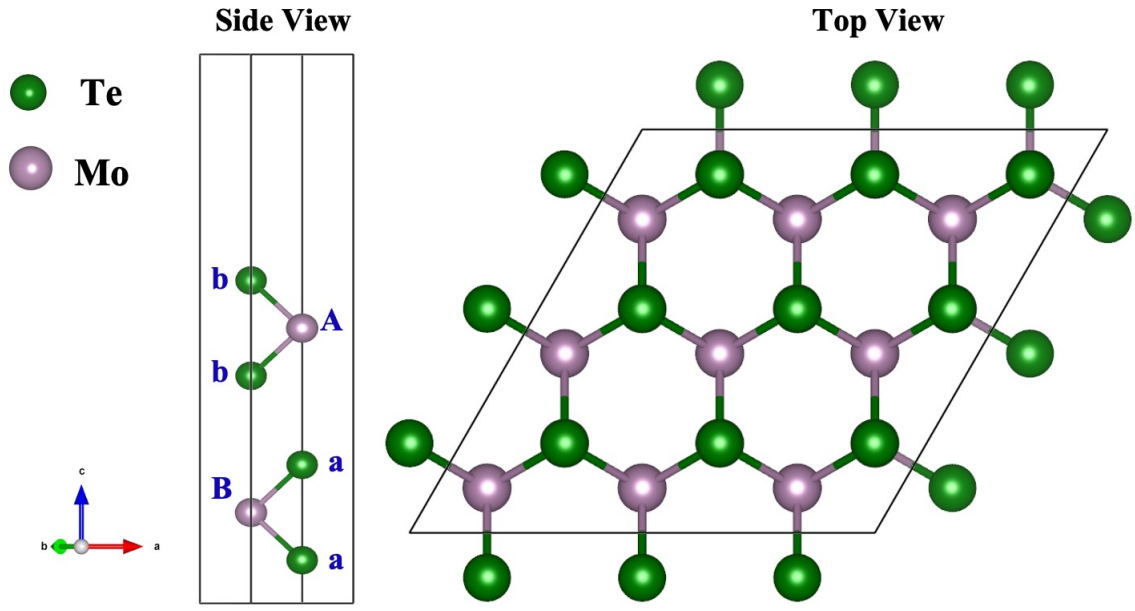

Figure 5.1: Top and side view of the crystal structure of bilayer *2H*-$MoTe_2$. The periodic unit cell of bilayer *2H*-$MoTe_2$ is characterized by a stacking sequence of *aBa bAb*. Violet and green spheres denote Mo and Te atoms respectively.

gap semiconductor in a monolayer with an emission peak of excitonic photoluminescence

(PL) spectrum in the near-infrared range ($\sim$ 1.1 eV) [163]. This enables the material to be a highly sensitive photodetector [175, 176] and light-emitting diode [177, 178]. With device performance at par with its sister compounds MoS_2 and $MoSe_2$ [179], $MoTe_2$ shows ambipolar transport properties [180], which has been recently implemented as a p-n homojunction rectifier device with low charge trapping at the junction interface [181]. Since the exploration of these properties has been mostly carried out in monolayer regime, investigation of the charge localization at high gate bias in few layers of the nanocrystal can open up new possibilities in the field of opto-electronics.

Carrier concentration in a semiconductor can be modulated by injecting resonant photons from light emitting diode [182–184], substitutional doping during growth process [185] and application of an electrostatic field on the channel of a FET [186–189]. Electrolyte gating has gained immense interest recently for electrostatic modulation of carrier density up to $\sim 10^{15}/\text{cm}^2$ [190] owing to their large dielectric capacitance. On application of gate voltage, ions move inside the electrolyte to screen the applied electric field to form few Angstroms [191] thick double layers of ions near the device and gate electrode [192, 193]. However electrolyte gating is well known source of electrostatic disorders [194, 195] and is best suited for disorder robust systems such as superconductors [196, 197].

As Raman spectroscopy does not require any sample preparation, it has been extensively used as a non-invasive, contact-less, fast and accurate tool to determine strain [198], doping effects [91], layer number [199, 200], crystal orientation [201], structural transitions between different polytypes [91, 166, 168–170, 202–204] in fewlayer $MoTe_2$ devices in ambient as well as different sample environments. Furthermore, Raman scattering has been employed in various 2D materials to measure electron-phonon coupling (EPC) that governs electronic transport properties [186, 187]. For n-type semiconducting MoS_2, symmetry of the conduction band minimum (CBM) determines EPC of the A_{1g} and E^1_{2g} modes [188]. In ambipolar phosphorene transistor, electrons and holes couple differently to phonons as CBM and valence band maximum (VBM) possess different orbital symmetries [189].

Although the electronic band structure of monolayer $MoTe_2$ is similar to MoS_2 [172], the VBM of the former remains at the K-point from single to three layers [172, 205]. Thus a study of the EPC in few layer $MoTe_2$, an intrinsic p-type semiconductor [206, 207], will reveal asymmetry of phonon coupling with holes and electrons in these hexagonal polytypes of TMDs.

Bulk $MoTe_2$ belongs to D_{6h} point-group [208] with six Raman active modes (A_{1g}+ $2B_{2g}$+ E_{1g}+ $2E_{2g}$) [200]. A_{1g} and E_{2g} modes have vibrations perpendicular to and along the basal plane of the lattice, respectively [200]. The in-plane E_{1g} mode is absent in backscattering configuration [200]. Notably, the translation symmetry along the z-direction is broken in a few layer nanocrystal, reducing the symmetry to D_{3h} and D_{3d} for odd and even layers of $MoTe_2$, respectively [208]. Thus, the out-of-plane inactive mode B_{2g} in bulk becomes Raman active in few layers and shows highest intensity in a bilayer nanocrystal [209]. For odd layer nanocrystal, the inversion symmetry breaks, making some modes both Raman and infrared active [200]. For simplicity, the Raman modes of even and odd layers of $MoTe_2$ in this paper are represented by the bulk phonon symmetry group of equivalent atomic displacements (Table 5.1).

Table 5.1: Irreducible representation of the Raman modes at Γ-point for N-layer and bulk $MoTe_2$ [1]. The dagger symbols (†) represent silent modes. The E_{1g} mode is absent in backscattering configuration [1]. The modes with $E^{'}$ symmetry are both Raman and infrared active [1].

Layer number	Zone-center phonon representation of the Raman modes					
	≤ 30 cm^{-1}	≤ 40 cm^{-1}	$\sim$120 cm^{-1}	~ 170 cm^{-1}	~ 235 cm^{-1}	~ 290 cm^{-1}
Odd Layer	$\frac{N-1}{2}E'$	$\frac{N-1}{2}A_1'$	$\frac{N-1}{2}E'$	$\frac{N+1}{2}A_1'$	$\frac{N+1}{2}E'$	$\frac{N-1}{2}A_1'$
Even layers	$\frac{N}{2}E_g$	$\frac{N}{2}A_{1g}$	$\frac{N}{2}E_g$	$\frac{N}{2}A_{1g}$	$\frac{N}{2}E_g$	$\frac{N}{2}A_{1g}$
Bulk	E_{2g}	$B_{2g}^{\dagger}$	E_{1g}	A_{1g}	E_{2g}	$B_{2g}^{\dagger}$

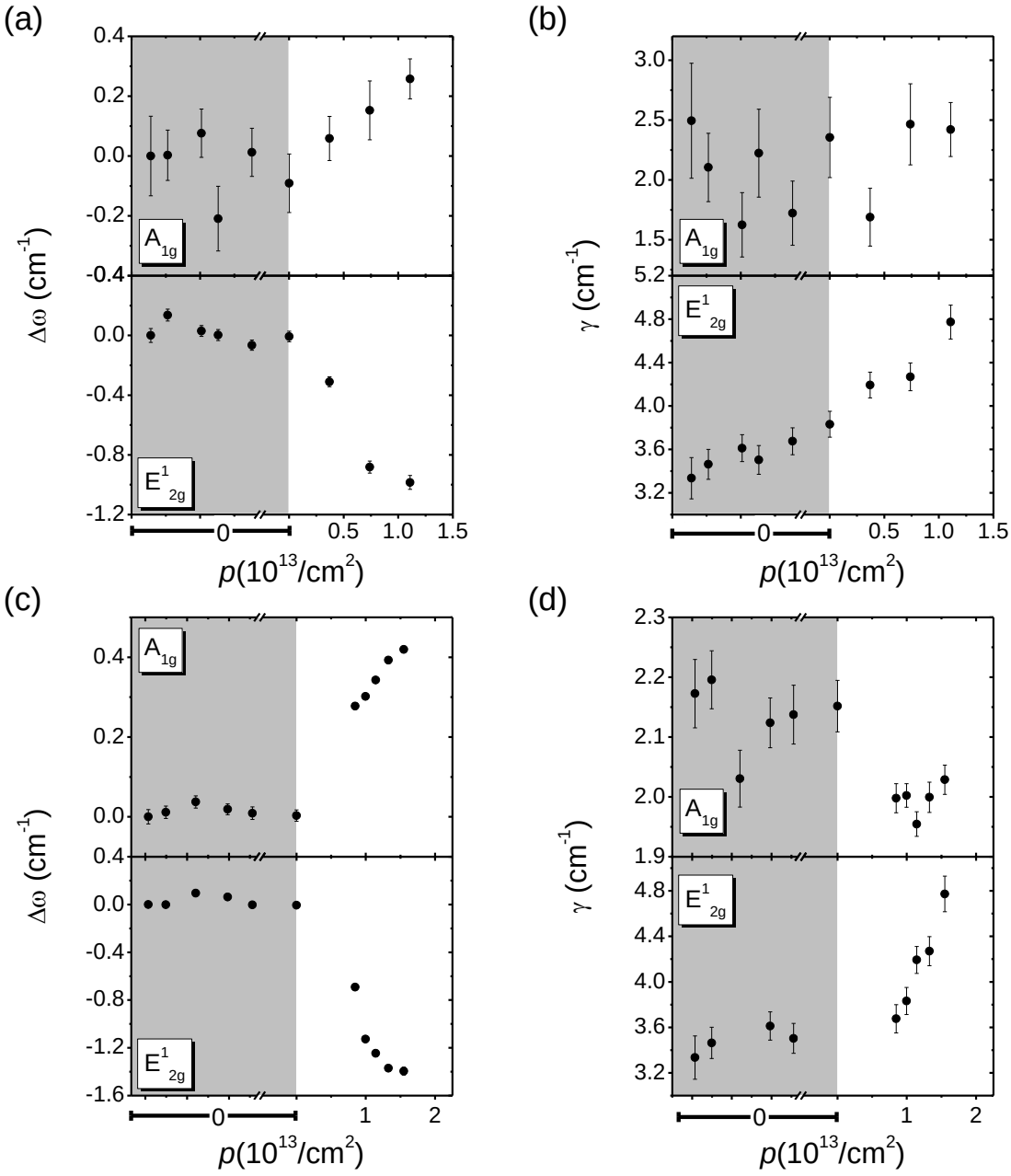

Figure 5.2: Experimentally observed (obtained by Dr. Subhajit Das from Prof. A. K. Sood's group at IISc) change in the frequency ($\Delta\omega$=$\omega_{n\neq0}$-$\omega_{n=0}$) and linewidth (γ) of the Raman modes with hole doping concentration (p) for (a and b) trilayer and (c and d) bilayer nanocrystal, respectively. Gray regions represent the zero doped state ($V_g \leq V_{Th}$). Change in the horizontal axis increments below zero doping is represented by the break symbol.

In this chapter, we have carried out first-principles density functional theory (DFT) calculations to understand phonon renormalization with hole-doping in bilayer $MoTe_2$. We

show that the holes couple weakly with the A_{1g} mode as compared to E^1_{2g} and B_{2g} modes and demonstrate that different orbital symmetries of the VBM and CBM at the K-point of $MoTe_2$ and MoS_2, respectively, contribute to their contrasting EPC.

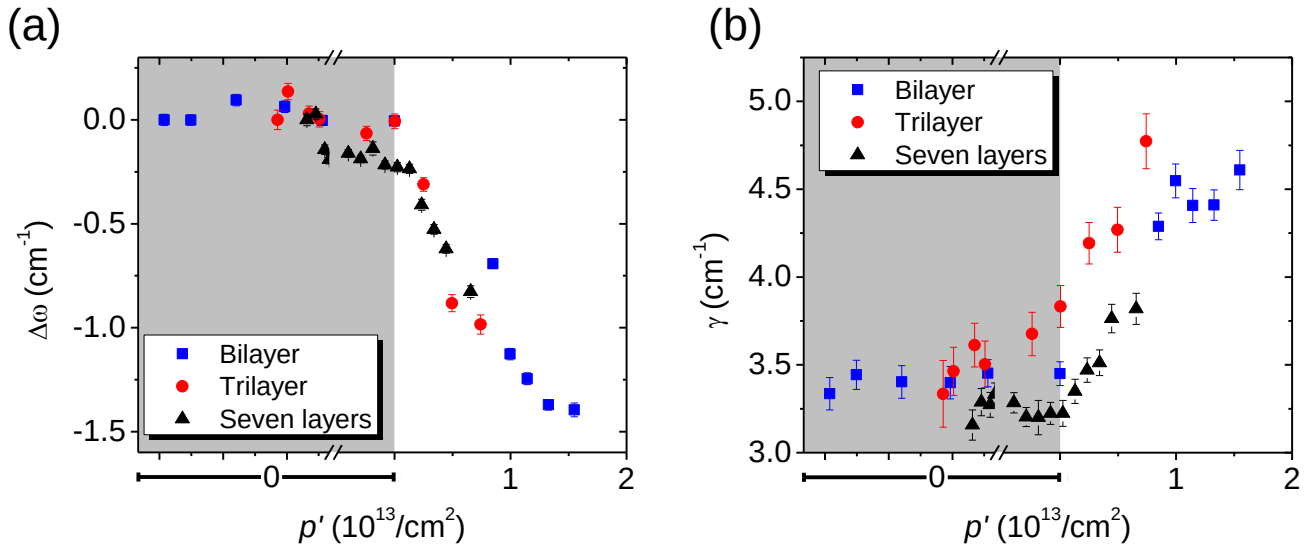

Figure 5.3: Experimental (obtained by Dr. Subhajit Das from Prof. A. K. Sood's group at IISc) (a) $\Delta\omega$ and (b) γ with average doping concentration (p') of the E^1_{2g} mode in 2, 3 and 7 layer nanocrystal.

5.2 Experimental observations

Our experimental collaborators (Dr. Subhadip Das from Prof. A. K. Sood'd group at Indian Institute of Science) have measure in-operando optical phonons in a few layers of *2H*-$MoTe_2$ based field-effect transistors (FETs) as a function of hole doping concentration (p) up to $\sim 2.3\times10^{13}$ cm^{-2}. The modes involving both metal and chalcogen atom vibrations, E^1_{2g} and B_{2g} [200] show phonon softening and linewidth broadening while the A_{1g} mode with out-of-plane vibrations of only the chalcogen atoms [200], shows in contrast, relatively smaller phonon hardening and linewidth sharpening (Fig. 5.2). The frequency renormalization comparison of E^1_{2g} mode from 2, 3 and 7 layer devices indicate that the doping is confined to only two top layers of the nanocrystal (Fig. 5.3).

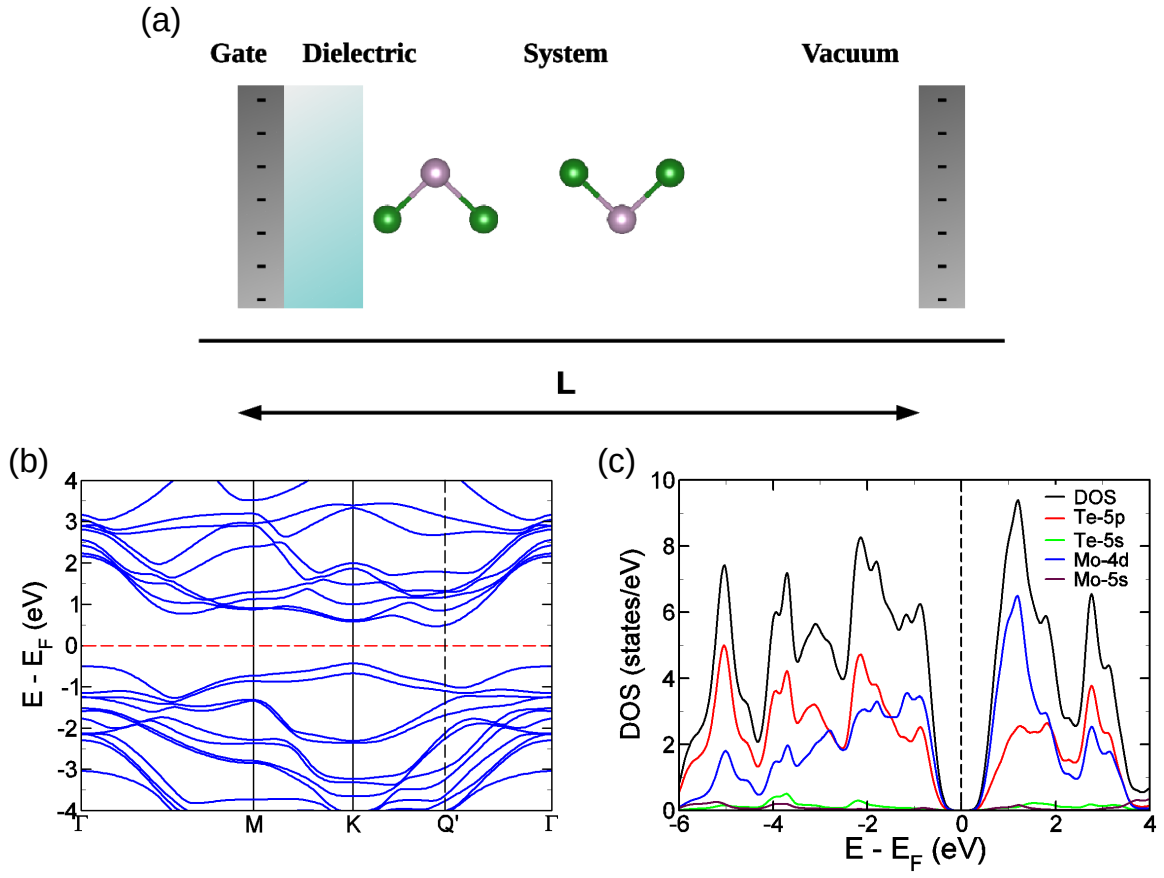

Figure 5.4: (a) Schematic illustration of an FET setup simulated in a periodically repeated unit cell where the layers of *2H*-$MoTe_2$ is placed in front of a charged plane mimicking the metallic gate (shown with gray color plate). The layers are doped with holes, such that the charged plane is charged with the same magnitude of opposite charges. To mimic the dielectric separation layer, we include a potential barrier (shown in blue). The length of the unit cell along the z-direction is given by L. (b) Electronic structure of bilayer *2H*-$MoTe_2$ calculated including the effect of spin-orbit coupling, shows it to be an indirect band gap semiconductor with VBM at K and CBM at Q′ point (Q′ point is along Γ-K direction) with a band gap of 0.88 eV. (c) Projected density of states of bilayer *2H*-$MoTe_2$ shows a strong coupling between the Mo d orbitals and Te p orbitals evident in their joint contributions to states near the gap.

5.3 Computational details

Our first-principles DFT calculations of the bilayer were carried out with Quantum ESPRESSO (QE) package [137], in which we treat only the valence electrons by effectively replacing the potential of ionic cores with pseudopotentials. Exchange-correlation energy of electrons is included within a generalized gradient approximation (GGA) [138] in the

functional form parametrized by Perdew, Burke, and Ernzerhof [139]. We include spin-orbit coupling (SOC) through use of relativistic pseudopotentials and a second variational procedure [210]. Kohn-Sham wave functions and charge density were represented in plane wave basis sets truncated at energy cut-offs of 40 Ry and 320 Ry respectively. A vacuum layer of 10 Å has been introduced parallel to $MoTe_2$ layer (perpendicular to z-direction) to weaken the interaction between the layer and its periodic images. Brillouin zone (BZ) integrations were sampled on uniform $24 \times 24 \times 1$ mesh of **k**-points. The discontinuity in occupation numbers of electronic states was smeared using a Fermi-Dirac distribution function with broadening temperature of $k_{\mathrm{B}}\mathrm{T} = 0.003$ Ry. We include van der Waals (vdW) interaction using PBE+D2 parametrized scheme of Grimme [140].

We have used the FET setup [211] as implemented in QE package to treat gating electric field. A 2D charged plate modeling the gate electrode is placed at z= 0.019 L. A potential barrier with a height of $V_0 = 0.09$ Ry and a width of $d_b = 0.1$ L is used to model the dielectric layer, preventing ions from moving too close to the gate electrode (Fig. 5.4(a)). Dynamical matrices were calculated within the Density Functional Perturbation Theory (DFPT) [212] on a $3 \times 3 \times 1$ mesh of q-vectors in the Brillouin zone. Fourier interpolation of these dynamical matrices was done to obtain phonon frequencies at arbitrary wavevectors and dispersion along the high symmetry lines in the Brillouin zone.

5.4 Results and Discussion

Bilayer *2H*-$MoTe_2$ has a hexagonal structure, where covalently bonded layers of Te-Mo-Te atomic planes are stacked along c-axis interacting via weak vdW interaction. The periodic unit cell of bilayer *2H*-$MoTe_2$ is characterized by a stacking sequence *aBa bAb*, where Wyckoff positions *A*, *B* label basal Te atomic planes and *a*,*b* label Mo atomic planes of the hexagonal lattice (Fig. 5.1). Our estimate of the lattice parameter a (= b) is 3.53 Å which matches well with previous experimental value [213]. Bilayer *2H*-$MoTe_2$

is an indirect band gap semiconductor with VBM at K and CBM at Q′ point (along Γ-K direction) separated by a gap of 0.88 eV (Fig. 5.4(b)). From the projected electronic density of states (DOS) (calculated without SOC) (Fig. 5.4(c)), it is evident that there is a rather strong coupling between the Mo d orbitals and Te p orbitals, contributing to states near the gap. Visualization of wavefunctions of states at VBM and CBM at Γ and K-points confirms the contribution of specific d-orbitals of Mo and p-orbitals of Te (Fig. 5.5(a-d)). The doped holes occupy the states at the K-point. With increasing hole-doping, holes continue to accumulate in states at K-point because energy separation between valence band of Q′ valley and valence band states at K-point is rather large ($\sim$ 490 meV) (Fig. 5.4(b)). We find that inclusion of SOC in our calculations leads to notable reduction in the indirect band gap by 60 meV and hence we have included SOC in further calculations.

We simulated hole doping in *2H*-$MoTe_2$ bilayer by adding a small fraction of holes (close to the experimental doping concentration) to its unit cell. From the changes in calculated frequencies with their linear fits (Fig. 5.5(e)), it can be seen that $\Delta\omega$ for A_{1g} mode is ~ -5.1 cm $^{-1}$ for $p = 4.1 \times 10^{13}/cm^2$, in contrast to corresponding higher softening of E^1_{2g} mode by 10.2 cm^{-1} and B_{2g} mode by 11.4 cm^{-1}. The magnitude of the slope S $(= |d(\Delta\omega)/dp|)$ for the A_{1g} mode is least, indicating smallest change of this mode frequency (compared to E^1_{2g} and B_{2g}) with doping. Although DFT analysis qualitatively captures the experimental trend of $\Delta\omega$ versus p for E^1_{2g} and B_{2g}, the relatively smaller phonon hardening observed in experiments for the A_{1g} mode (as compared to E^1_{2g} and B_{2g} modes) is not captured in our DFT analysis.

In order to understand why A_{1g} and B_{2g} are affected differently, we have calculated the EPC of pristine bilayer without inclusion of SOC to understand these trends, as estimation of EPC with doping in FET geometry is not currently implemented in the QE code. The

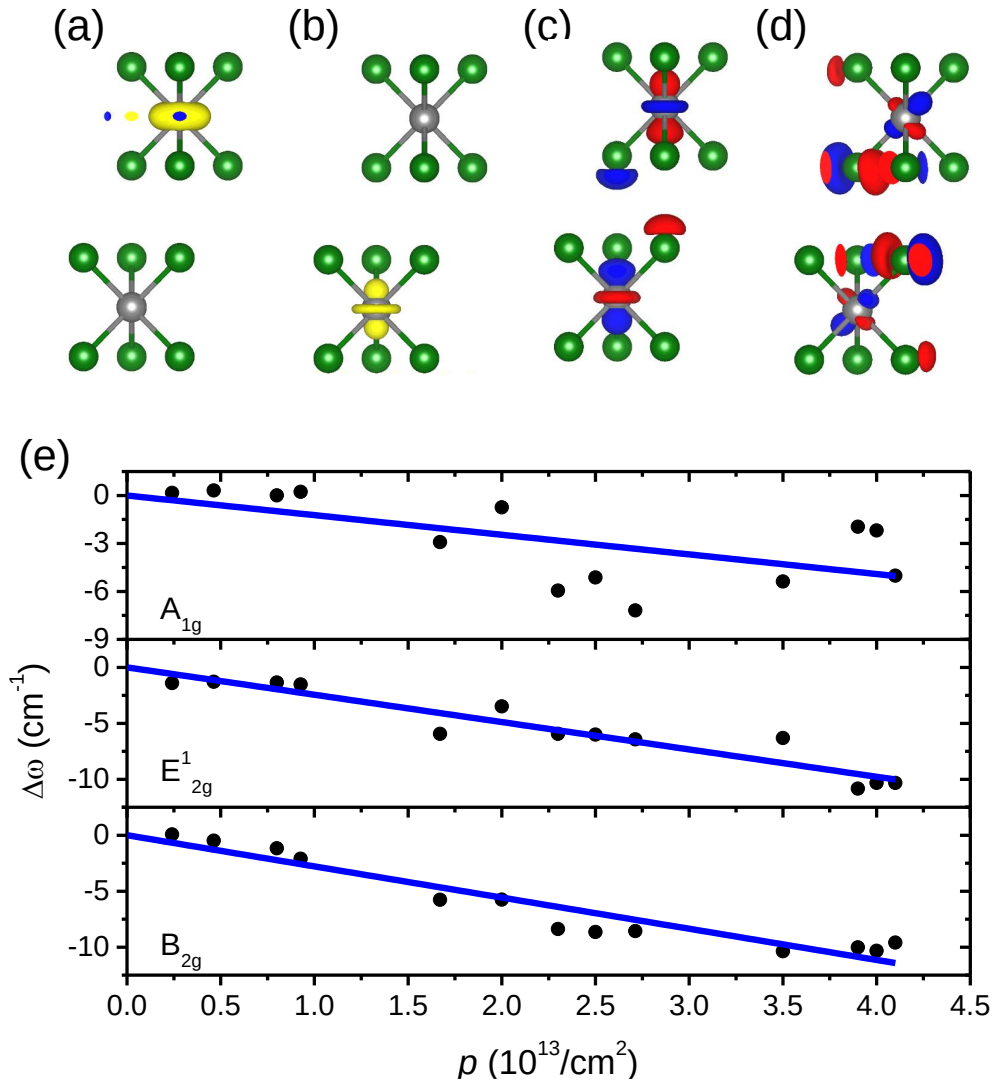

Figure 5.5: Isosurfaces of wavefunctions of states at (a) VBM and (b) CBM at K-point showing in-plane d_{xy} and out-of-plane d_{z^2} orbital (Mo) character respectively. Isosurfaces of wavefunctions of states at (c) VBM and (d) CBM at Γ-point. Clearly, VBM at Γ-point is formed of out-of-plane (Mo d_{z^2} and Te p_z) orbitals and CBM has contributions mainly from out-of-plane Mo and in-plane Te states (Mo d_{z^2} and Te $p_{x/y}$). (e) Changes in frequencies of A_{1g}, E^1_{2g} and B_{2g} modes as a function of hole concentration p. E^1_{2g} and B_{2g} modes soften more significantly with hole doping than the A_{1g} mode. Blue lines represent linear fit to the data with slope of -1.23, -2.44 and -2.78 $cm^{-1}/(10^{13}cm^{-2})$ for A_{1g}, E^1_{2g} and B_{2g} modes, respectively.

EPC of a mode ν at momentum $\boldsymbol{q}$ (with frequency $\omega_{\boldsymbol{q}\nu}$) is calculated as [188]

$$\lambda_{\boldsymbol{q}\nu} = \frac{2}{\hbar\omega_{\boldsymbol{q}\nu}N(\epsilon_f)}\sum_k\sum_{mn}|g^{q\nu\,,\,ij}_{k+q,k}|^2 \times \delta(\epsilon_{\boldsymbol{k+q},\boldsymbol{i}} - \epsilon_f) \times \delta(\epsilon_{\boldsymbol{k},\boldsymbol{j}} - \epsilon_f), \tag{5.1}$$

where ω and $N(\epsilon_f)$ are the phonon frequency and electronic density of states at the Fermi energy, respectively. The EPC matrix element is given by

$$g^{q\nu\,,\,ij}_{k+q,k} = (\frac{\hbar}{2M\omega_{\boldsymbol{q\nu}}})^{\frac{1}{2}} < \psi_{\boldsymbol{k+q,i}}|\Delta V_{\boldsymbol{q\nu}}|\psi_{\boldsymbol{k},j} >, \tag{5.2}$$

where $\psi_{\boldsymbol{k},j}$ is the electronic wave function with wave vector $\boldsymbol{k}$ and energy eigenvalue $\epsilon_{k,j}$ for band j, and M is the ionic mass. $\Delta \mathrm{V}_{\boldsymbol{q\nu}}$ is the change in the self-consistent potential induced by atomic displacements of phonon $\boldsymbol{q\nu}$. The calculated values of EPC of B_{2g} and A_{1g} modes are 0.016 and 0.011 respectively, consistent with the experimental observation that B_{2g} phonon is renormalized more with the hole doping.

It is interesting to compare these trends with the phonon renormalization seen in n-doped monolayer MoS_2 [188]. Electron doping in monolayer MoS_2 has contrasting effects on the frequencies of A_{1g} and E^1_{2g} optic modes [188]. While A_{1g} mode softens significantly (~ 7 cm^{-1} at $\sim 1.8{\times}10^{13}/\mathrm{cm}^2$), E^1_{2g} remains unaffected [188]. We can understand this contrast as follows: monolayer MoS_2 is a direct band-gap semiconductor with a gap of ~ 1.8 eV with the VBM and CBM at the K-point [205]. The CBM at the K-point of MoS_2 has contribution from the out-of-plane d_{z^2} orbital of Mo atoms [188]. The A_{1g} mode has the symmetry of the lattice, hence matrix element $< \psi_{\boldsymbol{k+q,i}}|\Delta V_{\boldsymbol{q\nu}}|\psi_{\boldsymbol{k},j} >$ is non zero [188]. In contrast, matrix element $< \psi_{\boldsymbol{k+q,i}}|\Delta V_{\boldsymbol{q\nu}}|\psi_{\boldsymbol{k},j} >$ of in-plane vibrational mode E^1_{2g} vanishes as it is orthogonal to A_{1g} irreducible representation [188]. In comparison, hole doping in bilayer *2H*-$MoTe_2$ leads to occupation of states at the top of the valence band at the K-point, having dominance of in-plane d_{xy} orbitals (odd symmetry states) of Mo. The crystal symmetry at K-point is point group C_2 which is a nontrivial subgroup of D_{3d} and the symmetry of the valence band is A_{2u}. The matrix element $<\psi_{\boldsymbol{f}}|\Delta\ \mathrm{V}_{\boldsymbol{q\nu}}|\psi\ _{\boldsymbol{i}}>$ (where i and f are the initial and final electronic wavefunctions) for $\nu = \mathrm{A}_{1g}$, E^1_{2g} and B_{2g} modes are non-zero as calculated using direct product table for C_2. Hence, changes in occupancy

of these states as a function of doping result in renormalization of these modes. Though A_{1g} and B_{2g} modes have different symmetries in bulk, the modes reduce to the same symmetry, A_{1g} in the case of bilayer (symmetry in even layer, odd layer, and bulk $MoTe_2$ has been listed in Table 5.1), softening is stronger for B_{2g} mode as compared to A_{1g}. This is consistent with the EPC being slightly higher for the B_{2g} (0.016) than the A_{1g} (0.011) mode and is also evident in frequency versus hole doping concentration plot (Fig. 5.5(e)).

5.5 Conclusions

We have demonstrated through our first-principles calculations that hole doping in bilayer *2H*-$MoTe_2$ results in softening of Raman-active phonons E_g^1 and A_{1g}^1, whereas A_{1g}^2 remains relatively unaffected. Our DFT analysis captures the experimental trend of $\Delta\omega$ versus p for E_{2g}^1 and B_{2g}, however, the experimentally observed relatively smaller phonon hardening of the A_{1g} mode on hole doping (as compared to E_{2g}^1 and B_{2g} modes) is not captured in our DFT analysis. Interestingly, this behavior is in sharp contrast to the trends obtained in electron doped monolayer MoS_2. We have argued that the contrast between behaviors of MoS_2 and $MoTe_2$ arises from the difference in symmetry of their frontier states relevant to electron and hole doping. In addition to being relevant to use Raman spectroscopy as a non-invasive tool for characterization of $MoTe_2$-FET devices, our study will be useful in understanding the role of relevant phonon interaction with charge carriers in determining carrier mobility in $MoTe_2$ devices.

Chapter 6

Electrostriction in *1T* and *2H* polymorphs of $TM\mathbf{S}_2$ (TM = Mo, Hf)

6.1 Introduction

Experimental isolation of graphene, a one-atom thick sheet of carbon atoms arranged in a honeycomb lattice, by mechanical exfoliation of graphite by Geim *et al.* [214] in 2004 marked the emergence of intense research on layered materials in the last decade due to their fascinating properties [215, 216]. Graphene does not have a band gap, and is not suitable for applications in digital electronics [217]. This has directed significant research on other 2D semiconducting materials, such as hexagonal boron nitride (h-BN), phosphorene, transition-metal oxides (TMO_2) and transition metal dichalcogenides (TMDs) opening up a plethora of possibilities of electrnic devices. TMDs with the chemical fromula TMX_2 (where TM represents the transition metal Mo, Hf, V and W and X is a chalcogen like S, Se or Te) have emerged as a class of materials for wide range of

applications [218, 219]. These layered materials are characterized by covalently bonded $X - TM - X$ planar atomic layers that are stacked *via* weak van der Waals (vdW) interactions analogous to graphite. Bulk TMDs (MoS_2, WS_2) are indirect band gap semiconductors with band gaps in the range of 1.0 – 1.35 eV [220]. On reducing the number of layers, their band gap typically increases and transforms into an direct gap for a monolayer TMD [221]. A variety of polymorphs achieved through variations of stacking sequences, constituent atoms and coordination of transition metal atom, effectively tune its electronic, mechanical and thermal properties [222]. Modification of band gap of these materials (for applications in nanoelectronics) can be achieved not only by varying the number of layers, but also by doping [223], intercalation [224], pressure and application of strain and electric field [225, 226]. Most materials experience stresses and electric field when used in a device, and their stability is impacted by piezoelectric and electrostrictive strains.

Tunability of electronic structure through strain engineering has been an important strategy to achieve promising properties of TMDs. It has been highlighted that strain can be used in MoS_2 to enhance its carrier mobility, to create tunable photonic devices and solar cells [227], and even to control its magnetic properties [228, 229]. While strains perturb electronic structure of these materials, MoS_2 can withstand strains greater than 11% without rupture owing to its two-dimensional nature [230–232]. Piezoelectricity is observed in gapped *2H-TM*Ds with odd number of layers, due to lack of inversion symmetry. Wu *et al.* observed piezoelectricity in monolayered MoS_2 flake strained by 0.53 %, generating a peak output of 15 mV and mechanical-to-electrical conversion efficiency of 5.08 % [233]. In piezoelectric materials, strain (ϵ) is directly proportional to electric field and changes its sign with applied electric field ($\epsilon = P \times E$) [234]. Electrostriction, on the other hand involves a non-linear electromechanical coupling allowed by all crystal symmetries, which describes second-order strain/stress response induced by an

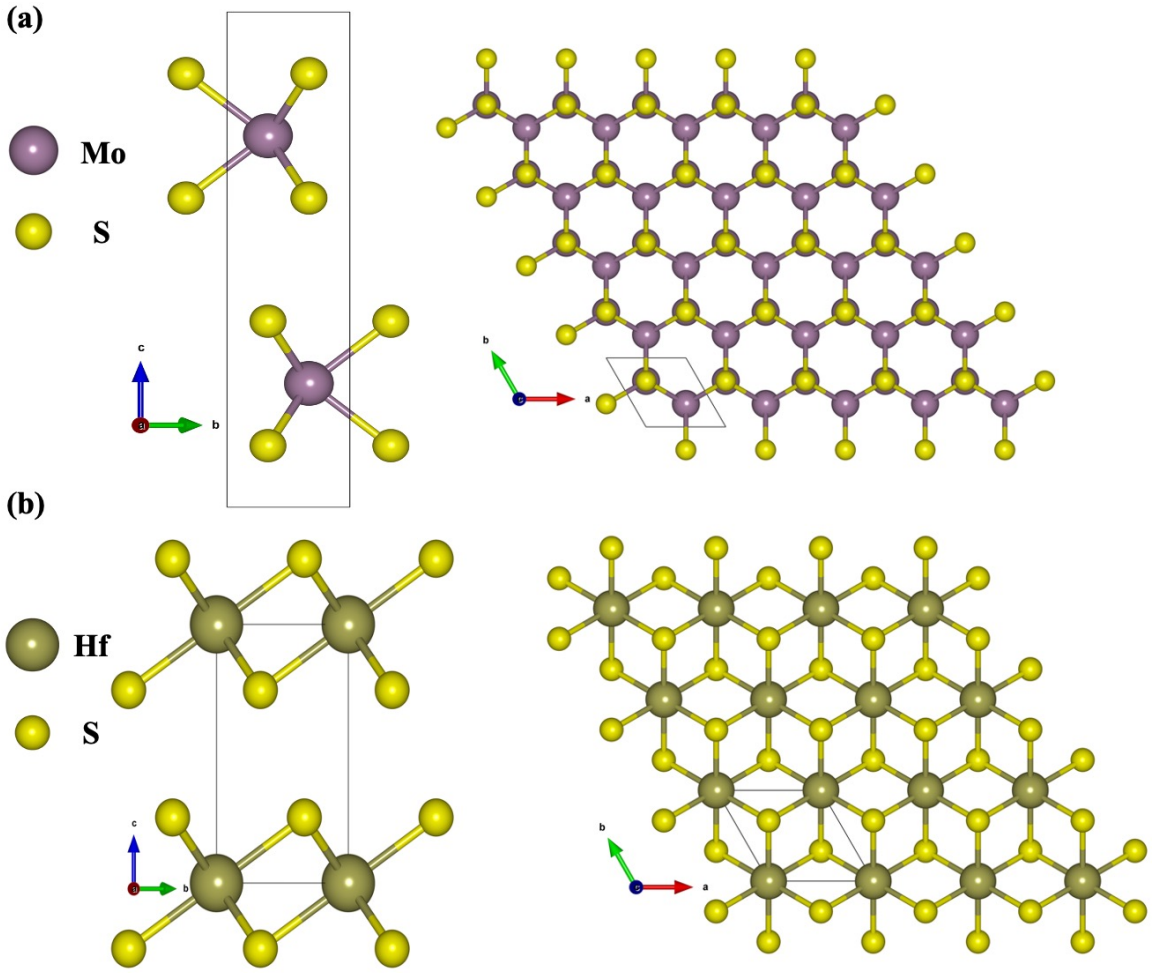

Figure 6.1: Side and top view of crystal structure of (a) *2H* phase of MoS_2 with trigonal prismatic coordination of metal atom, Mo and (b) *1T* phase of HfS_2 with octahedral coordination of Hf atom.

electric field/polarization field. The electrostrictive strain (ϵ) being proportional to the square of electric field, it is independent of the sign of the applied field ($\epsilon = M \times E^2$). Popular examples exhibiting strong electrostriction are relaxor ferroelectrics with perovskite structures, such as $Pb(Mg_{1/3}Nb_{2/3})O_3$ (PMN), $Pb(Zn_{1/3}Nb_{2/3})O_3$ (PZN), and $0.9Pb(Mg_{1/3}Nb_{2/3})O_3{-}0.1PbTiO_3$ (PMN−0.1PT) single crystals/ceramics, in which a high electrostrictive strain has been observed along with their high dielectric response. These are suitable for applications in sonars, actuators, and other tunable electromechanical systems [235–240].

In this paper, we discuss the electrostrictive effects in the monolayer (ML), bilayer (BL) and bulk forms of $TM\mathrm{S}_2$ (TM = Mo and Hf) using a robust method proposed by Tanner *et al.* [241] based on calculation of susceptibility at different stresses, avoiding the limitations related to finite D method. We consider *2H* and *1T* polymorphs of MoS_2 and HfS_2 and determine dependence of electronic (M^{elec}) and phononic (M^{ionic}) contributions to their electrostriction properties on composition (chemistry), structure and the number of layers. Furthermore, we analyze the contributions of IR-active modes (with non-zero mode effective charge) and the corresponding oscillator strength to understand phononic contribution of IR-active modes to electrostriction in stable structures: *2H*-MoS_2 and *1T*-HfS_2. To the best of our knowledge, this is the first report of electrostrictive response in MoS_2 and HfS_2 using first-principles calculations.

6.2 Computational Details

Our first-principles calculations are based on density functional theory (DFT) employing Quantum ESPRESSO (QE) package [242], with interactions between valence electrons and ionic cores are represented with projector augmented wave (PAW) potentials. The exchange-correlation energy of electrons is treated within a generalized gradient approximation (GGA) [243] with a functional form parametrized by Perdew, Burke, and Ernzerhof [244]. Plane wave basis used in expansion of Kohn-Sham wave functions and charge density were truncated at energy cut-offs of 55 Ry and 440 Ry respectively. Integrations over the Brillouin zone (BZ) were sampled on uniform $24\times24\times6$, $24\times24\times1$ and $24\times24\times1$ meshes of k-points in calculations of bulk, bilayer and monolayer forms of $TM\mathrm{S}_2$ (TM = Mo, Hf), respectively. The discontinuity in occupation numbers of electronic states was smeared with a broadening temperature of $k_\mathrm{B}T = 0.003$ Ry in the Fermi-Dirac distribution function. We include van der Waals (vdW) interaction using PBE + D2 method of Grimme [140]. A 2D system is simulated using a periodic supercell, with a vacuum

layer of 20 Å separating adjacent periodic images of the sheet. Kohn-Sham DFT typically underestimates band gaps (a known limitation). We have also employed hybrid functionals based on Hartree-Fock-Exchange (HSE06) with screened Coulomb potential to estimate band gaps more accurately. Lattice-dynamical properties were determined within the framework of self-consistent density functional perturbation theory (DFPT) as implemented within the QE code [242]. We have used LOBSTER code [245] for crystal orbital overlap population (COOP) analysis of orbital interactions among different nearest neighbor pairs of atoms of MoS_2 [246, 247], for quantification of the role of atomic orbitals in chemical bonding.

Electrostrictive coefficients were calculated using the open-source ABINIT software package [248] (target stress cannot be applied in Qauntum ESPRESSO or VASP) adopting the PseudoDoJo [249] norm conserving pseudopotentials to represent the interaction between the frozen core and the valence electrons with a plane wave cutoff energy of 40 Ha. Linear-response calculations were analyzed using the ANADDB module of the ABINIT package.

In response to an electric field (E) applied to a material, strain (ϵ) is induced given by:

$$\epsilon_{ij} = d_{ijk}E_k + M_{ijkl}E_kE_l \tag{6.1}$$

where d_{ijk} denotes the piezoelectric tensor and M_{ijkl} is the electric-field related electrostriction tensor [250]. Piezoelectricity is exhibited by non-centrosymmetric materials while electrostriction is observed in all crystals including centrosymmetric ones where electrostrictive strain (ϵ) is proportional to the square of applied electric field and independent of the sign of electric field. The electrostrictive coefficient M is a rank four tensor

given by the derivative of susceptibility, χ, with respect to stress of the slab, X^{slab} [251]:

$$2M_{ijkl} = -\epsilon_0 \frac{\partial \chi_{ij}}{\partial X_{kl}^{slab}} \tag{6.2}$$

where ϵ_0 is vacuum permittivity. To remove the arbitrariness in thickness of the periodic supercell, in-plane dielectric constants are rescaled as [252]:

$$\epsilon_{2\mathrm{D},\,||} = 1 + \frac{c}{t}(\epsilon_{\mathrm{SC},\,||} - 1) \tag{6.3}$$

where $\epsilon_{2\mathrm{D},\,||}$ represents in-plane dielectric constant of the supercell, c is the thickness of the supercell and t is the effective thickness of the 2D material.

To benchmark our results, we have also determined the hydrostatic electrostriction coefficient (M_h) of MgO under applied hydrostatic stress. Our estimate of M_h^{ionic} is 883 $\mathrm{pm^2/V^2}$ which compares well with $M_\mathrm{h} = 883$ $\mathrm{pm^2/V^2}$ in a recent report [241]. We further calculated electronic and phononic contributions to hydrostatic electrostriction in MgO: $M_h^{elec} = 35$ $\mathrm{pm^2/V^2}$ and that of phonons is $M_h^{ionic} = 848$ $\mathrm{pm^2/V^2}$ (Table 6.1). Thus, we show that hydrostatic electrostriction of MgO is largely phononic in nature.

Table 6.1: Calculated hydrostatic electrostrictive coefficient, M_h of MgO.

Compound	**Structure**	$\boldsymbol{M_\mathrm{h}}$		
		M **($\mathbf{pm^2/V^2}$)**	M^{ionic} **($\mathbf{pm^2/V^2}$)**	M^{elec} **($\mathbf{pm^2/V^2}$)**
MgO	**Bulk**	883	848	35

6.3 Results and Discussion

6.3.1 Atomic and Electronic structure

TMX_2 (TM = Mo, Hf and X = S) compounds belong to the family of transition metal dichalcogenides (TMDs), where covalently bonded $X-TM-X$ are stacked *via* weak vdW interaction along c-axis. A single layer consists of TM atomic planes sandwiched between two atomic planes of X. At ambient conditions, MoS_2 exists in the *2H* polytype (H stands for hexagonal), where sulphur atoms are arranged in a trigonal prismatic coordination of Mo atoms (Fig. 6.1a). The stacking sequence of bilayer *2H*-MoS_2 is *AbA BaB*, Wyckoff positions A, B, C label basal S atomic planes and a, b, c label Mo atomic planes of the hexagonal unit cell. Bulk MoS_2 has a point group symmetry of D_{6h} [165, 253], ML (odd layer) has D_{3h} point group symmetry [253] due to the presence of the horizontal reflection plane (σ_{h}) passing through Mo atom. The point group of BL (even number of layers) MoS_2 is D_{3d} because of the presence of inversion symmetry [208]. Our estimate of the in-plane lattice parameters of bulk, BL and ML-MoS_2 are a = 3.189, 3.188 and 3.187 Å, respectively (within 1% of the respective experimental value) [254, 255]. *1T*-HfS_2, with *AbC* stacking sequence (Fig. 6.1b), crystallizes in the *1T*-CdI_2 structure with $P\bar{3}m1$ space group and D_{3d} point group symmetry. Optimized lattice parameters of bulk and ML-HfS_2 are a = 3.62 and 3.63 Å, respectively. These are in reasonable agreement with experimental lattice constants [256] and an earlier theoretical report [257].

It is clear from the atom-resolved electronic structures of *2H*-polytype of MoS_2 (bulk, BL and ML) and *1T*-HfS_2 (bulk and ML) shown in Fig. 6.2 and Fig. 6.3, respectively that the valence bands (VBs) of all three forms of *2H*-MoS_2 involve strong hybridization between S-3p and Mo-4d states whereas the conduction bands (CB) are primarily contributed by Mo-4d, with weaker contribution from S-3p orbitals. Band structures of bulk and BL-MoS_2 exhibit an indirect gap of 1.4 eV and 1.6 eV, respectively [215]. In contrast to

bulk MoS_2, with VBM at Γ and CBM at a point midway along Γ−K, VBM and CBM of BL-MoS_2 are at Γ and at K-points. In the case of ML-MoS_2, we find a direct band gap of 2.1 eV at K-point. We observe that reduction in dimensionality leads to an increase of band gap and a transformation from indirect to direct band gap.

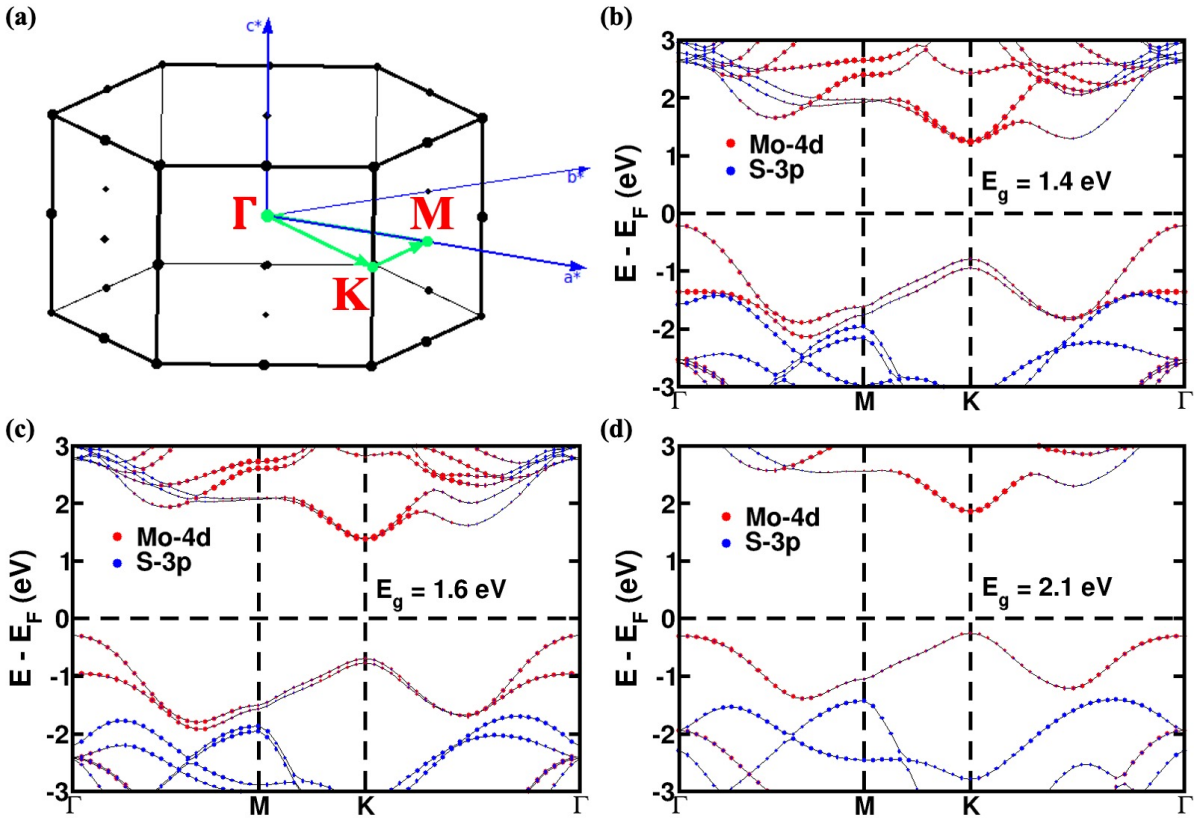

Figure 6.2: (a) Brillouin zone of hexagonal unit cell where the green lines mark the paths connecting the high symmetry points (in red) used in our calculations of electronic structure and phonon dispersion. Atom-resolved electronic structure of (b) bulk, (c) bilayer and (d) monolayer forms of *2H*-MoS_2.

As reported earlier by Colibaba *et al.* [257], both bulk and monolayered forms of *1T*-HfS_2 exhibit an indirect band gap with VBM at Γ and CBM at M with gaps of 1.7 eV and 2.3 eV, respectively. Its valence band is composed of S-p orbitals whereas conduction band states have predominantly Hf-d orbital character as seen in atom-resolved electronic structure, with very less hybridization revealing its ionic nature (Fig. 6.3). We note that electronic band gap of *1T*-HfS_2 (bulk and ML) is higher than that of bulk and ML forms

of *2H*-MoS_2.

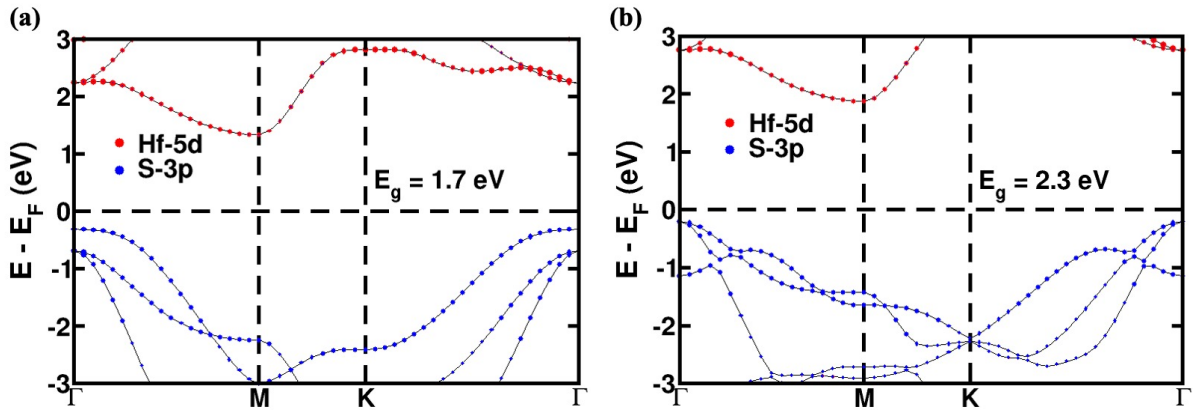

Figure 6.3: Atom-resolved electronic structure of (a) bulk and (b) monolayer forms of *1T*-HfS_2.

6.3.2 Phonons of MoS_2 and HfS_2

Phonon dispersion of *2H*-MoS_2 (bulk, BL and ML) exhibits no unstable modes ($\omega^2 < 0$), confirming their dynamic structural stability (Fig. 6.4(a,b,c)). Bulk MoS_2 has the symmetries of P63/*mmc* space group and D_{6h} point group. The irreducible representations of phonons at the Brillouin zone center (Γ) are: $A_{1g} \bigoplus 2A_{2u} \bigoplus 2B_{2g} \bigoplus B_{1u} \bigoplus E_{1g} \bigoplus 2E_{1u} \bigoplus 2E_{2g} \bigoplus E_{2u}$, where A_{1g}, E_{1g} and E_{2g} modes are Raman (R) active, and A_{2u} and E_{1u} modes are infrared (IR) active [165,253]. As the point symmetry group of BL-MoS_2 is D_{3d}, its lattice vibrations (18 phonon modes) at Γ are labelled with irreducible representations of D_{3d}: $3A_{1g} \bigoplus 3A_{2u} \bigoplus 3E_g \bigoplus 3E_u$, where A_{1g} and E_g are Raman active and A_{2u} and E_u are IR active [208]. Raman and infrared active modes are mutually exclusive in bulk and bilayer MoS_2 because of its inversion symmetry. Unit cell of ML-MoS_2 is composed of three atoms and its nine normal vibrational modes at Γ-point labelled with irreducible representations of D_{3h} point group: $2A_2'' \bigoplus A_1' \bigoplus 2E' \bigoplus E''$, where A_2'' is IR active , A_1' and E'' are R active [253]. Infrared active modes contribute to the lattice dielectric response and also electrostrictive response.

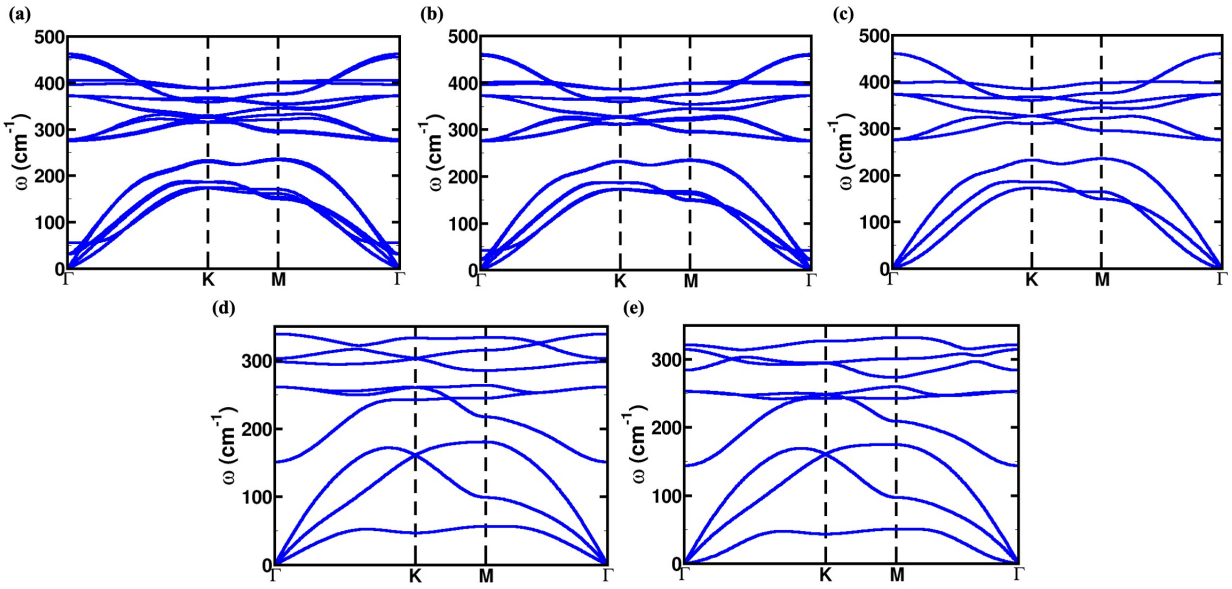

Figure 6.4: Calculated phonon dispersion for (a-c) bulk, bilayer and monolayer forms of *2H* polytype of MoS_2 and (d) bulk, and (e) monolayer forms of *1T*-HfS_2. We observe that all the phonon frequencies are real, implying a dynamically stable structure.

There are nine vibrational modes each of bulk and ML forms of *1T*-HfS_2, classified according to irreducible representation of D_{3d} point group: $A_{1g} \bigoplus 2A_{2u} \bigoplus E_g \bigoplus 2E_u$, where Raman and IR modes are mutually exclusive due to center of inversion [258, 259]. With no unstable modes ($\omega^2 < 0$) in their phonon dispersion, we conclude that both bulk and ML-HfS_2 are structurally stable (Fig. 6.4). We do note significantly lower frequencies of vibration of HfS_2 than of MoS_2.

6.3.3 Born effective charges

Born effective charge or dynamical charge ($Z^*_{i,\alpha,\beta}$) gives a force acting on an ion in the 'α' direction in response to an electric field is applied in the 'β' direction (E_β). An anomalously large Z^* is often an indicator of the tendency of a material to undergo a ferroelectric distortion, or its vicinity to metallicity of the compound. The in-plane Born effective charges of bulk TMS_2 (TM = Mo, Hf) are expected to be closer to their nominal charges (i.e. +4 for M and -2 for S). However, we find that values and even the

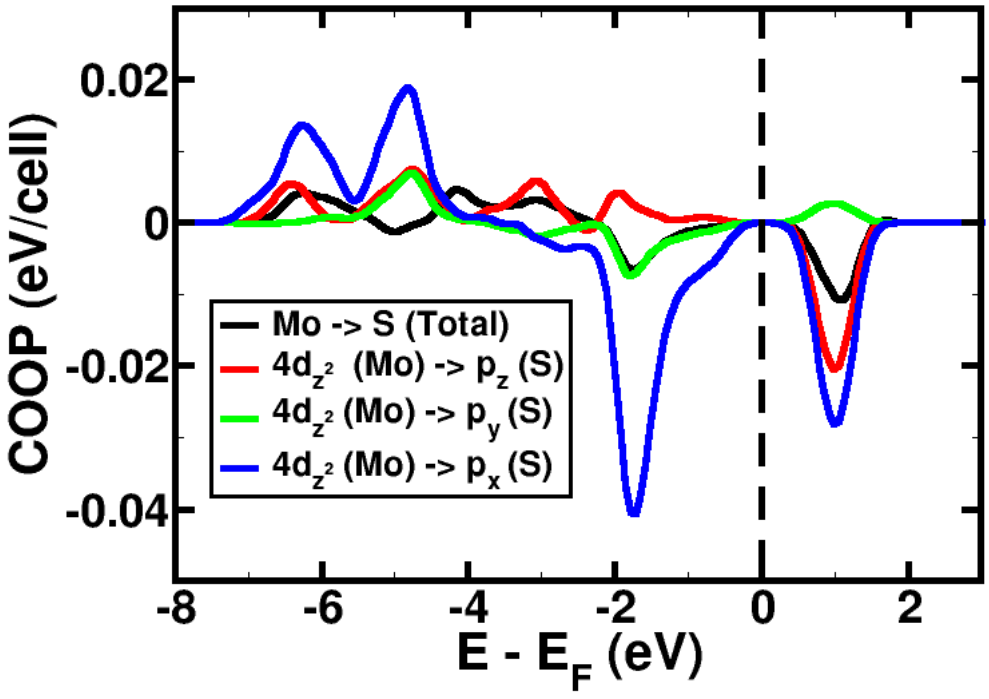

Figure 6.5: Crystal Orbital Overlap Population (COOP) analysis of bulk *2H*-MoS_2 showing antibonding $4d_{z^2} - p$ orbitals of Mo-S bonds near Fermi level.

sign of in-plane Born effective charge (Z^*_{xx}) of Mo and S ions in *2H*-MoS_2 are anomalous ($Z^*_{Mo} = -0.8$ and $Z^*_S = 0.7$) (Table 6.2). Highly anomalous Z^* suggests strong covalency or orbital interactions in these materials, and the opposite sign of Z^* arises from the contribution of the *d*-states of Mo atoms constituting the topmost valence band just below the Fermi level. In an ionic crystal like *1T*-HfS_2, Z^*_{xx} values of Hf and S ions are closer to nominal values ($Z^*_{Hf} = 6.6$ and Z^*_S = -3.3) (Table 6.2). The presence of antibonding $4d_{z^2} - p$ orbitals of Mo-S bonds near Fermi level (in accordance with our Crystal Orbital Overlap Population, COOP analysis) (Fig. 6.5) could result in an electron transfer and a change in local polarization around the transition metal atom.

Table 6.2: In-plane Born effective charges (Z^*_{xx}) of *1T* and *2H* polytypes of $TM\mathrm{S}_2$ (TM = Mo and Hf).

		$Z^*_{xx} = Z^*_{yy}$	
Compound	**Structure**	M	S
***2H*-$\mathbf{MoS_2}$**	**Bulk**	-0.8	0.7
***1T*-$\mathbf{HfS_2}$**	**Bulk**	6.6	-3.3

6.3.4 Electrostriction coefficient in MoS_2 and HfS_2

With ground state structures of bulk, BL and ML-$TM\mathrm{S}_2$ (TM = Mo and Hf) as the reference, we determine strain (ϵ) induced in response to applied stress (σ) by relaxing internal atomic positions and lattice parameters through minimization of enthalpy, $H = E - V\sigma\epsilon$, at target stresses (in the parameters range of -2 GPa to 2 GPa). For the structure optimized at a given stress, we use Density functional perturbation theory (DFPT) to determine dielectric susceptibility. The electrostrictive coefficient is then obtained by fitting dielectric susceptibility as a function of stress, using Eq. (6.2) e.g. to calculate M_{11}, we apply stress along a-axis, X_{11} (in Voight notation) and determine χ_{11} (Fig. 6.6). The electrostrictive coefficients of these compounds in bulk, bilayer, and monolayered structural forms have been tabulated in Table 6.3, where M_{11} represents the total (static) electrostrictive coefficient as an addition of electronic (M^{elec}_{11}) and phononic or ionic (M^{ionic}_{11}) parts. One of the key points to note is that the electronic part (M^{elec}) dominates the electrostrictive response in bulk, BL and ML forms of *2H*-MoS_2. Dominance of electronic contribution to static dielectric constant has been reported by Laturia *et al.* for *2H* polytypes of TMDs [252]. In contrast, electrostriction of *1T*-HfS_2 (bulk and ML) is largely phononic with weak electronic contributions ($M^{ionic} > M^{elec}$). In addition, we find that the sign of M_{11} in HfS_2 is negative and opposite to that of MoS_2, implying compression of its lattice (negative strain) on application of electric field.

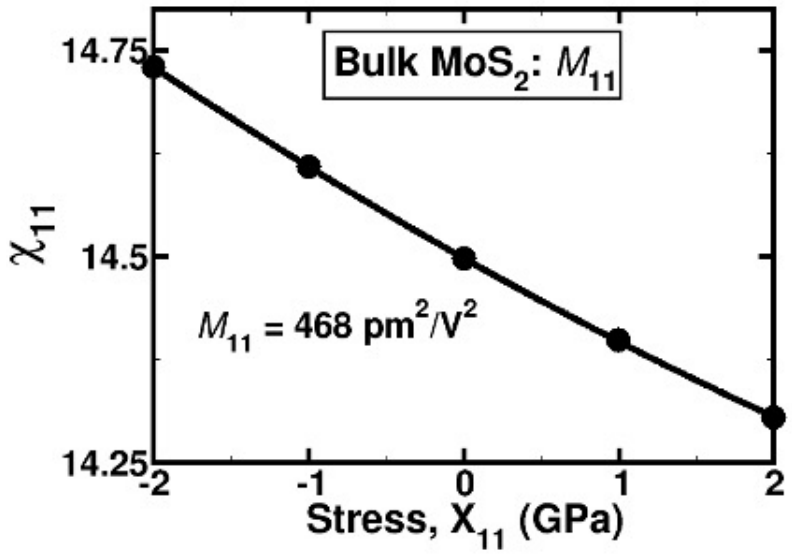

Figure 6.6: Fitting of dielectric susceptibility as a function of stress.

Table 6.3: Calculated electrostrictive coefficient, M_{11} of *1T* and *2H* polytypes of $TM\mathrm{S}_2$ (TM = Mo and Hf) and its dependence on chemistry and number of layers.

Compound	**Structure**	$\boldsymbol{M_{11}}$		
		M **(pm²/V²)**	M^{ionic} **(pm²/V²)**	M^{elec} **(pm²/V²)**
***2H*-$\mathbf{MoS_2}$**	**Bulk**	468	-55	523
	Bilayer	382	-55	437
	Monolayer	371	-54	425
***1T*-$\mathbf{HfS_2}$**	**Bulk**	-3080	-2135	-945
	Monolayer	-2139	-2027	-112
***1T*-$\mathbf{MoS_2}$**	**Bulk**	2410	1868	542
***2H*-$\mathbf{HfS_2}$**	**Bulk**	-1715	-800	-915

To establish whether the structure is crucial to electrostriction, we calculated electrostrictive responses of these materials in their metastable polytypic forms. The *1T* polymorph of MoS_2 has been shown to be locally unstable by Shirodkar *et al.* [260]. Strong nesting in

its Fermi surface and consequent instability in its vibrational spectrum lead to a structural phase transition, with emergence of improper ferroelectricity in the distorted structure. Hence, we have carried out our analysis on this distorted stable $\sqrt{3} \times \sqrt{3}$ *1T*-MoS_2 which results from trimerization of Mo atoms [260].

While the M^{ionic} of 2*H*-HfS_2 is weaker than that of its *1T* structure, M^{ionic} of *1T*-MoS_2 is higher than that of *2H*-MoS_2. The difference between ionic contributions of *2H* and*1T* polytypes can be attributed to the breaking of both rotational and inversion symmetry of 1*T* structure on application of in-plane field, unlike in *2H* structures where only the rotational symmetry is broken. Centrosymmetric 1*T*-structure potentially hosts ferroelectric state by breaking inversion symmetry, and hence exhibits soft IR-active phonons that cause giant dielectric and electrostrictive responses. In contrast, the non-centrosymmetric 2*H* structure exhibits relatively harder IR-active modes whose contribution to χ and M_{11} responses is weaker.

A careful comparison reveals that M^{elec} of MoS_2 (oxidation state of Mo^{+4} with $4d^2$ electronic configuration) is positive, while that of HfS_2 ($5d^0$ electronic configuration of Hf^{+4}) is negative. Clearly, chemistry or composition of atoms plays an important role in the electronic part of electrostriction. Noticeable variation in M^{ionic} of 2*H* is seen with composition of atoms, whereas corresponding changes in M^{ionic} of *1T* phase are much weaker. It must be noted here that electrostrictive coefficient, M_{11} of *1T*-HfS_2 is an order of magnitude higher than the corresponding values of *2H*-MoS_2.

Having established the relevance of structure and composition in determination of the electrostriction in TMS_2, we now investigate the dependence of M_{11} (electronic and ionic) on the number of layers (N). We note that variation of M^{ionic} with N is insignificant. This is consistent with their phonon dispersions of the stable polytypes of TMS_2 (bulk and

2D-forms) which show rather feeble changes with the number of layers, N. In contrast, M^{elec} decreases profoundly with reduction in dimensionality. This observed dependence of M^{elec} on N is in conformance with the trend of band gap, which increases with decrease in N.

6.3.5 Electronic and ionic contributions to dielectric and electrostrictive responses

The static dielectric tensor (ϵ^0) has contributions from electrons (ϵ^∞) and IR-active phonon modes [261]:

$$\epsilon^0_{\alpha\beta} = \epsilon^\infty_{\alpha\beta} + \frac{4\pi e^2}{M_0 V}\sum_\lambda \frac{\tilde{Z}^*_{\lambda\alpha}\tilde{Z}^*_{\lambda\beta}}{\omega^2_\lambda} = 1 + 4\pi(\chi^{elec} + \chi^{ionic}) \tag{6.4}$$

where α and β label Cartesian coordinates, e is the charge of an electron, M_0 is the reference mass that has been taken 1 amu, V is the volume of the unit cell, ω is the frequency of the IR-active phonon mode λ and the mode effective charges, $\tilde{Z}^*_{\lambda\alpha}$ are given by

$$\tilde{Z}^*_{\lambda\alpha} = \sum_{i\beta} Z^*_{i,\alpha\beta}(\frac{M_0}{M_\mathrm{i}})^{1/2}\xi_{i,\lambda,\beta} \tag{6.5}$$

where $\xi_{\mathrm{i},\lambda,\alpha}$ is the eigendisplacement of atom i in α direction in phonon mode λ. If we take trace of Eq. (6.4), we get

$$Tr[\epsilon^0] = Tr[\epsilon^\infty] + \sum_\lambda \epsilon_\lambda \tag{6.6}$$

where

$$\epsilon_\lambda = \frac{4e^2\pi}{M_0 V\omega^2_\lambda}\tilde{Z}^{*2}_\lambda \tag{6.7}$$

Table 6.4: Mode frequency, scalar mode effective charge, and contribution of each IR-active mode to the trace of the dielectric tensor (in a.u.).

Compound	**Structure**	**IR-Mode (cm^{-1})**	$\tilde{Z}^*_\lambda$	ϵ_λ ($\times 10^{-5}$)
***2H*-MoS_2**	**Bulk**	376 (E_{1u})	1.5	2.7
		455 (A_{2u})	0.9	1.1
	Bilayer	373 (E_u)	1.5	3.0
		459 (A_{2u})	0.2	0.1
	Monolayer	373 ($E^{'}$)	1.1	1.5
		460 ($A_2{''}$)	0.10	0.01
***1T*-HfS_2**	**Bulk**	151 (E_u)	6.4	54.5
		298 (A_{2u})	1.8	4.5
	Monolayer	144 (E_u)	6.8	62.4
		314 (A_{2u})	0.6	0.4

is the contribution of mode λ to the trace of the static dielectric tensor through scalar mode effective charge $\tilde{Z}^{*\,2}_\lambda = \sum_\alpha \tilde{Z}^{*}_{\lambda\alpha}{}^2$ [261].

We present in Table 6.4 frequencies and irreducible representations of IR-modes with non-zero scalar mode effective charge ($\tilde{Z}^*_\lambda$) and the corresponding oscillator strength (ϵ_λ). We find that IR modes of bulk, BL and ML-MoS_2 are not soft and have weak $\tilde{Z}^*_\lambda$ and ϵ_λ, while higher frequency IR-modes with largest $\tilde{Z}^*_\lambda$ do not contribute to the static dielectric constant since squared frequency in the denominator of Eq. (6.4) suppresses it. This is in direct contrast to *1T*-HfS_2, where the soft modes have rather high $\tilde{Z}^*_\lambda$ and ϵ_λ, contributing dominantly to dielectric response and thereby electrostriction.

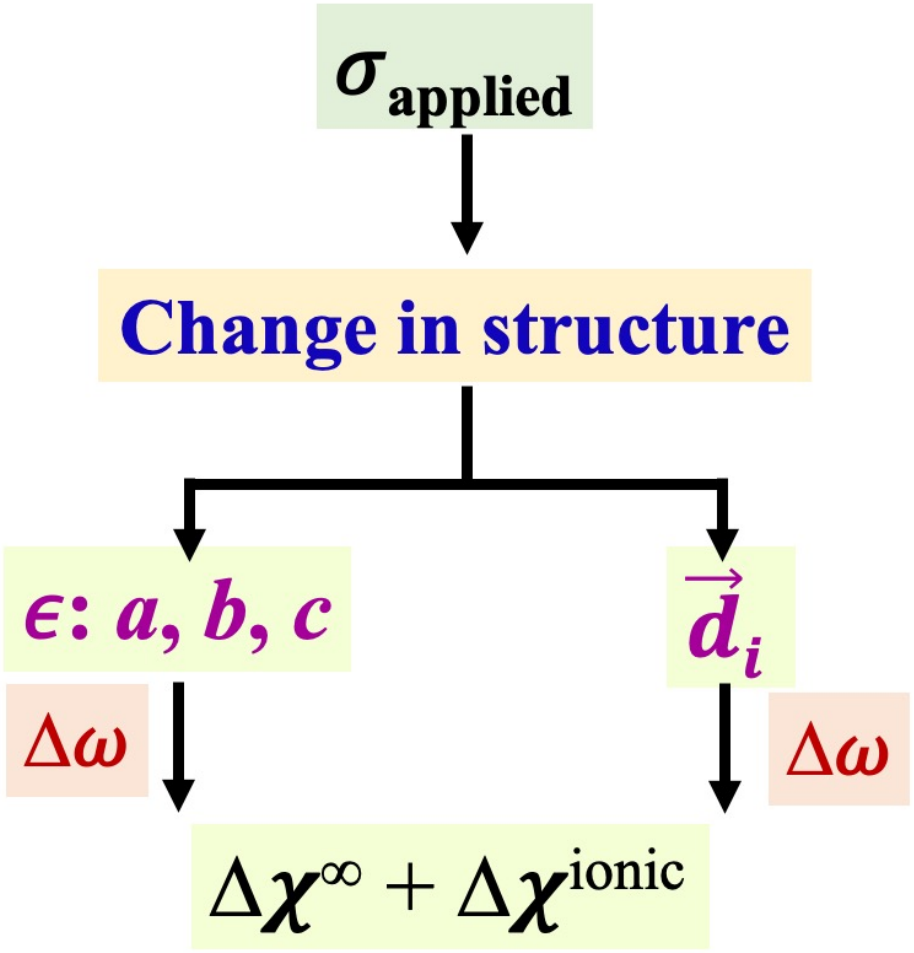

Figure 6.7: Schematic depicting the effect of stress on lattice parameters (ϵ) and atomic positions (d) in a crystal structure and the emergence of electrostrictive response.

6.4 Conclusion

Using first-principles density functional theoretical calculations, we identified the roles of structure and chemical composition in *1T* and *2H* polymorphs of bulk, bilayer and monolayer TMS_2 (TM = Mo, Hf) and their impact on electrostrictive coefficient, M_{11}. We uncover the precise mechanisms of electrostriction (electronic or phononic) in terms of electronic band gap, phonon normal modes, scalar mode effective charge and oscillator strengths of IR-active modes. Our calculations show that M^{elec} of transition metal with d^0 electronic configuration (Hf) is negative, while it is positive for transition metal with

d^2 configuration like Mo irrespective of $2H$ versus $1T$ structure. We find that the electronic contributions dominate the electrostrictive response of *2H*-TMDs, while phononic contributions dominate in $1T$ polytpe of TMDs which exhibit soft IR-active phonons. Lastly, we determined the effects of reduction in dimensionality on electrostrictive response (electronic and ionic) of TMS_2. Application of stress results in changes in the structure (a) lattice parameters (strain) and (b) position of atoms (contributing to electronic and phononic/ionic part of electrostriction), both of which impact phonons together and govern the ionic component of electrostriction.

Part III

Electronic and structural transitions in layered materials

Chapter 7

Pressure-induced structural phase transition in VSe_2[†]

7.1 Introduction

Layered quasi-2D transition metal dichalcogenides (TMDs; MX_2, M = transition metal = Mo, W, V, Ta, Ti, Mn etc., and X = chalcogen = S, Se, Te etc.) are being pursued intensely in recent years due to their emergent properties and significant applications [263–267]. One of the interesting features of the bulk MX_2 compounds is their crystallization into different polytypes (viz. *1T, 2H, 3R, 1T′, T_d* etc.) depending on the co-ordination of the nearest-neighbour chalcogen polyhedra around the transition metal and the various stacking sequences of the 2D layers in (001) direction [268–272]. A TMD monolayer is comprised of a sandwiched hexagonal layer of transition metal atoms between two hexagonal layers of chalcogens. These covalently bonded $X - M - X$ slabs are then

[†]This work has been published in Phys. Rev. B **104**, 014108 (2021) [262]. Reproduced with permission from the American Physical Society.

stacked in vertical c-direction with weak van der Waals bond between them, resulting in an anisotropic 3D structure. The trigonal *1T* polytype of VSe_2 with standard CdI_2 structure having space group $P\bar{3}m1$ [273–275], has a regular octahedral co-ordination of six Se atoms around the central vanadium and a stacking sequence *aBc* (where *a, b* and *c* label Se atomic layers and *A, B* and *C* label V atomic layers) of Se-V-Se monolayers without any lateral shift (Fig. 7.2(a)). The *3R* polytype has trigonal prismatic coordination of vanadium atom with a *aBc bCa cAb* stacking (Fig. 7.3(a) and Fig. 7.3(b)). Unlike the semiconducting *2H* polytypes, the *1T* bulk VSe_2 is metallic due to significant overlaps between vanadium d bands and selenium p bands and shows a charge density wave (CDW) state [276, 277]. *1T*-VSe_2 is unique in the formation of a 3D chiral CDW [274, 278, 279] due to the partial nesting of its Fermi surface [280, 281]. X-ray and electron diffraction studies [282, 283] have established periodic lattice deformation to be the key precursor to this CDW transition to an incommensurate phase below 110 K and to a $4a' \times 4a'$ commensurate superlattice structure below 80 K (still incommensurate along c-axis with $c' \approx 3c$). The CDW transition of *1T*-VSe_2 is very sensitive to any external perturbation that directly affects its electronic band structure. While the effects of reduced thickness down to monolayer limit [284–288] or intercalation by Na, K, Cs etc. [289–291] or interstitial vanadium itself [292] have been studied, there is limited work on its electronic and structural stability under external pressure. While a large number of TMD crystals like $2H_c$-MoS_2, $MoSe_2$, WSe_2 exhibit pressure induced metallization followed by an isostructural transformation of the crystal to $2H_a$ (except for $2H_c$-$MoSe_2$) [293–296], a few others show crystal symmetry change, e.g. transformation of trigonal *1T*-TiS_2 to an orthorhombic phase at 16.2 GPa [297], cubic to orthorhombic transition of MnS_2 [298], appearance of monoclinic phase in *1T*-$IrTe_2$ at 5 GPa followed by transition to a cubic phase at 20 GPa [299].

Friend *et al.* [300] have reported high pressure resistivity and Hall studies on bulk *1T*-VSe_2 up to 3 GPa which showed an increase of CDW transition temperature (T_C) with

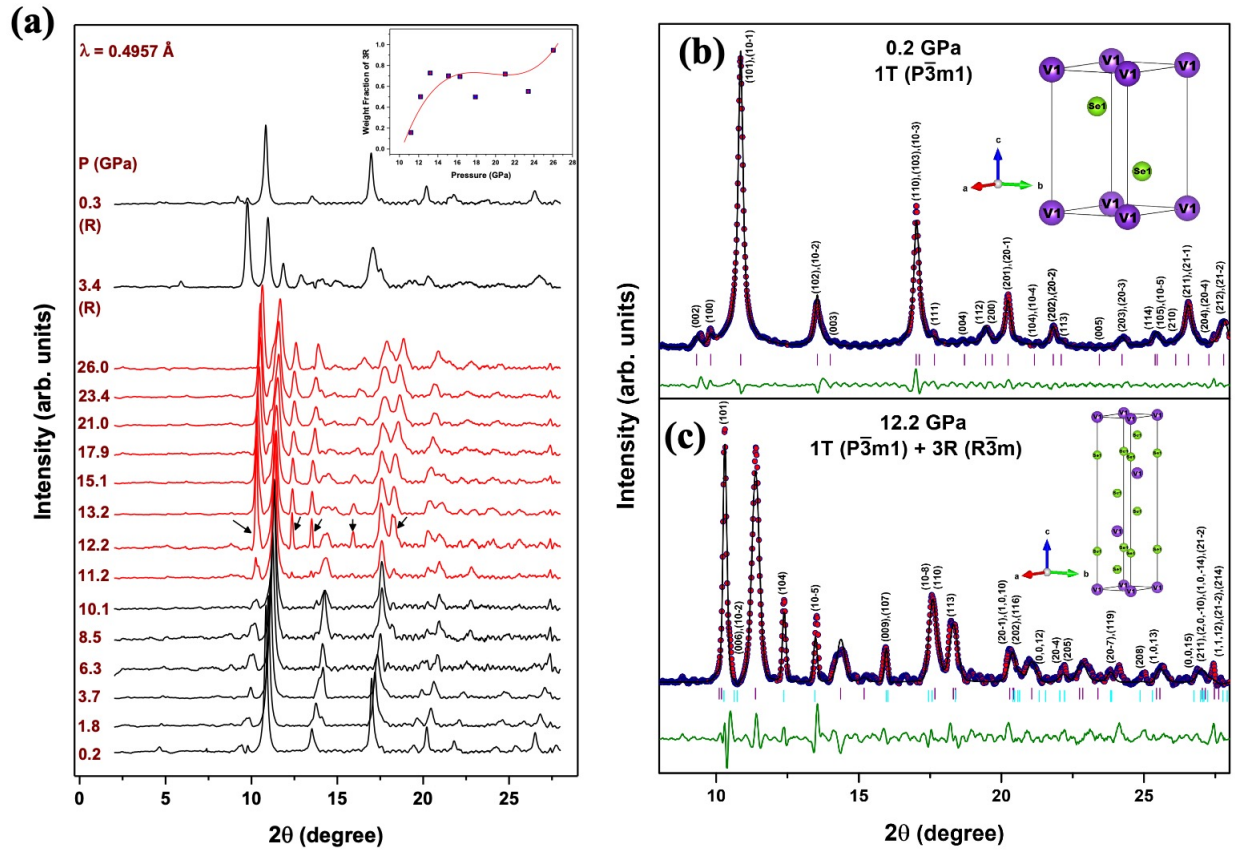

Figure 7.1: (a) Experimental angle dispersive XRD patterns (obtained by Dr. Srishti Pal from Prof. A. K. Sood's group at IISc) during pressurization from 0.2 to 26.0 GPa (two top-most patterns are after depressurizing to 0.3 GPa). Arrows indicate new peaks appearing at the onset of the first order structural transition. The evolution of wight fraction of the *3R* phase with increasing pressure is shown in the inset. (b) and (c) Rietveld refined XRD patterns at 0.2 GPa and 12.2 GPa, respectively matched with $P\bar{3}m1$ (#164) and a mixture of $P\bar{3}m1$ (#164) and $R\bar{3}m$ (#166). Experimental data are indicated by solid circles. Calculated pattern is drawn as black solid line. Reflection positions for *1T* phase are indicated by magenta vertical bars and those for *3R* by cyan ones. Lower dark green curve is the weighted difference between observed and calculated profile. The unit cells including atoms are shown in the inset.

$\frac{dT_C}{dP} \sim 0.8$ K.GPa^{-1} due to pressure broadening of vanadium *d*-conduction band. Recently, using the crystals from same batch as used in the present study, Sahoo et al. [301] showed pressure-enhancement of the CDW T_C in bulk *1T*-VSe_2 reaching 240 K at 12 GPa followed by quenching of the CDW state before finally evolving into a superconducting phase with $T_C \sim 4$ K after 15 GPa. While this manuscript was under preparation, a

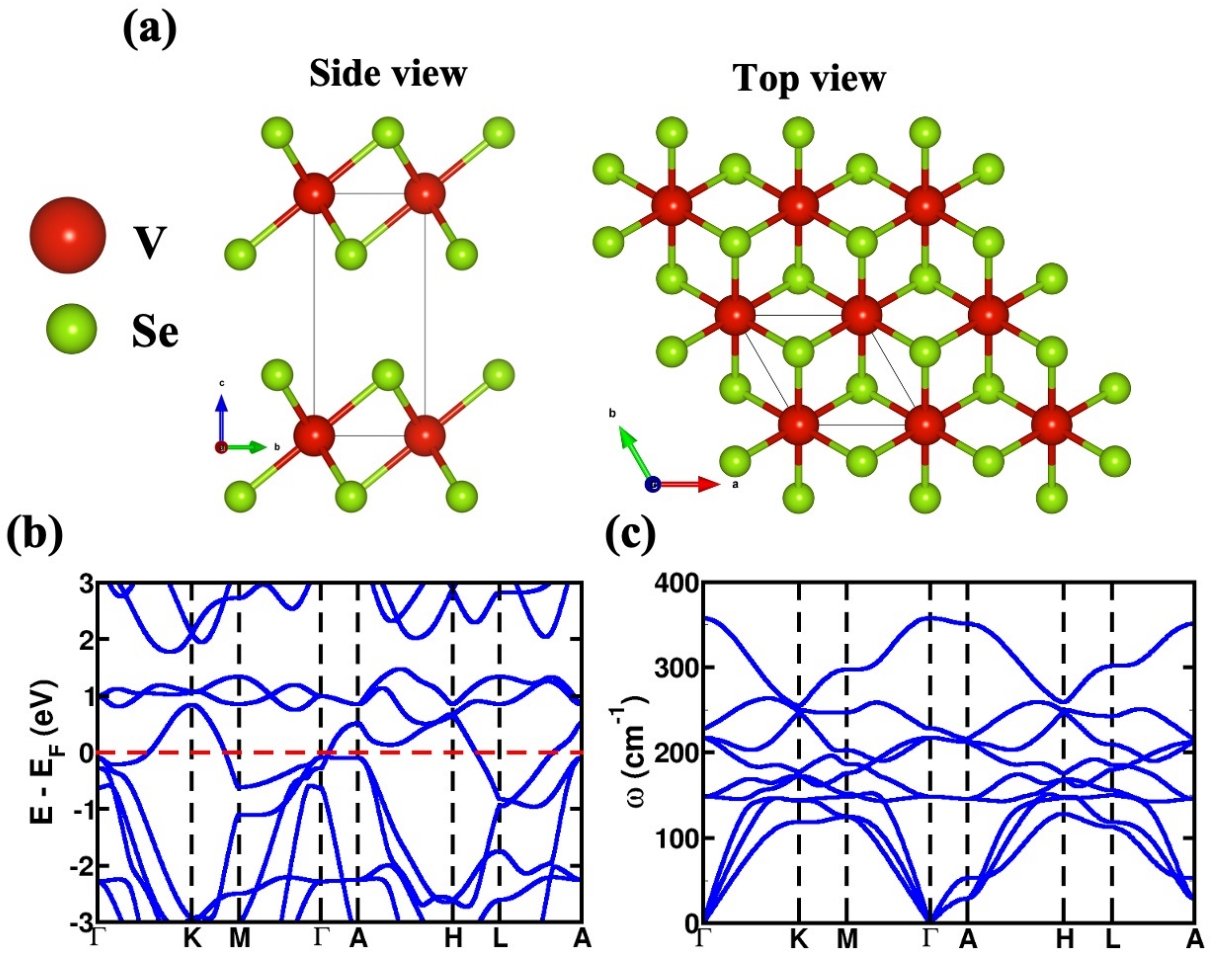

Figure 7.2: (a) Side and top view of *1T* (space group: $P\bar{3}m1$) crystal structure of VSe_2. (b) Electronic structure and (c) phonon dispersion of *1T*-VSe_2 at 0 GPa.

recent report on high pressure XRD and DFT studies [302] indicated the new phase of VSe_2 after 12 GPa to be a 3×3×1 supercell of monoclinic symmetry.

In this chapter, we report high pressure XRD and density functional theoretical (DFT) calculations which are at variance with the recent report [302]. Our XRD data shows a first order structural transition to a *3R* phase at $\sim$ 11 GPa (Fig. 7.1(a)). We also show an isostructural transition at $\sim$ 6 GPa, in agreement with recent reports [301,302], by the anomalous c/a ratio. Our XRD data and theoretical calculations are inconsistent with the monoclinic space group assignment of Ref. [302]. Our detailed DFT calculations shows a transition from *1T* to *3R* at $\sim$ 9 GPa, close to the experimental transition pressure of 11

GPa.

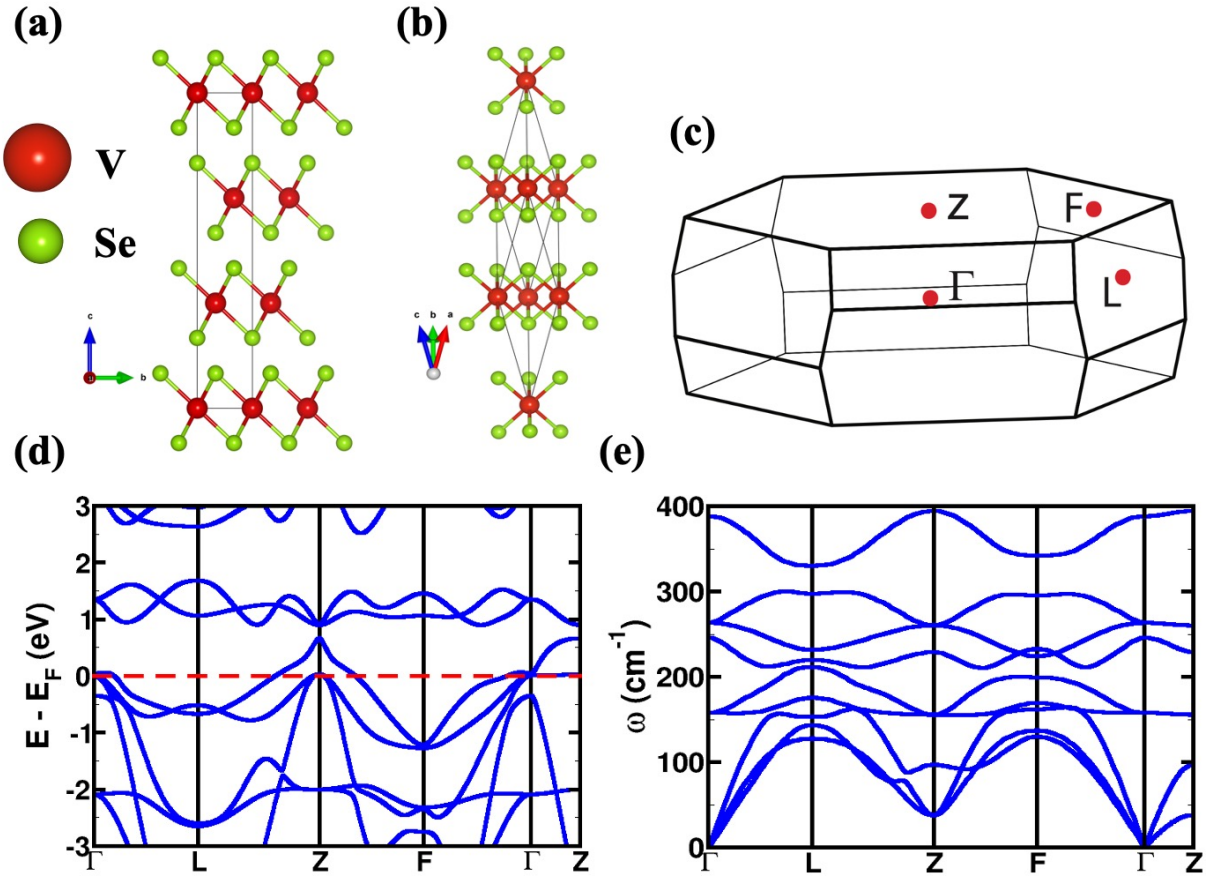

Figure 7.3: (a) Conventional hexagonal and (b) primitive rhombohedral unit cell of *3R* (space group: $R\bar{3}m$) polytype of VSe_2 and its (c) Brillouin zone with high symmetry points. (d) Electronic structure and (e) phonon dispersion of *3R*-VSe_2 at 12 GPa.

7.2 Experimental observations

Angle dispersive synchrotron XRD study on *1T*-VSe_2 (carried out at Elettra, Italy using the Xpress beamline by Dr. Srishti Pal from Prof. A. K. Sood's group at Indian Institute of Science) at room temperature at selected pressure values are stacked in (Fig. 7.1(a)). The ambient trigonal phase with space group $P\bar{3}m1(164)$, $z = 1$ exhibits stability up to $\sim$ 10.1 GPa above which new peaks start to appear in the diffraction pattern at $\sim$ 10.3°, 12.3°, 13.5°, 15.9°, 18.3°, 20.3°, 22.1° and 23.8° and are prominent in intensity from 12.2

GPa (marked by arrows in (Fig. 7.1(a))) onwards. Emergence of new Bragg reflections over the existing ones confirms the occurrence of new crystal symmetry coexisting with the previous 1T phase (weight fraction of the 3R phase with increasing pressure is shown in the inset of (Fig. 7.1(a)). Rietveld refined fitted patterns at 0.2 GPa and 12.2 GPa using $P\bar{3}m1$ (1T) and mixture of $P\bar{3}m1$ (1T) and $R\bar{3}m$ (3R), respectively has been shown in Fig. 7.1(b).

7.3 Computational Details

Our first-principles calculations are based on DFT as implemented in Quantum ESPRESSO (QE) package [137], in which we treat only the valence electrons by replacing the potential of ionic cores with pseudopotentials. The exchange-correlation energy of electrons is treated within a generalized gradient approximation (GGA) [138] with a functional form parametrized by Perdew, Burke, and Ernzerhof [139]. Electronic wave functions and charge density were represented in plane wave basis sets truncated at energy cutoffs of 60 Ry and 500 Ry respectively. Brillouin zone (BZ) integrations were sampled on uniform dense $24 \times 24 \times 12$ and $24 \times 24 \times 6$ meshes of $\boldsymbol{k}$-points for *1T* and *3R* structures of VSe_2, respectively. The discontinuity in occupation numbers of electronic states was smeared using a Fermi-Dirac distribution function with broadening temperature of $k_{\mathrm{B}}\mathrm{T} = 0.003$ Ry. We include van der Waals (vdW) interaction using PBE+D2 method of Grimme [140]. Dynamical matrices were calculated within the Density Functional Perturbation Theory (DFPT) [212] on a $2\times2\times2$ mesh in the Brillouin Zone. We Fourier interpolated these dynamical matrices to obtain the phonon frequencies at arbitrary wavevectors and dispersion along the high symmetry lines in the Brillouin zone. We have calculated the lattice parameters in ABINIT. We also performed first-principles calculations using projected augmented wave (PAW) method [303, 304] as implemented in Vienna *ab-nitio* simulation package VASP [305, 306]. Spin-polarized calculations were performed using

Perdew-Burke-Ernzerhof (PBE) functional for exchange-correlation term, with Hubbard parameter correction GGA+U introduced by Dudarev et al. [307, 308] in which the parameters U and J do not enter separately, only the difference ($U-J$) is relevant ($U_{\text{eff}} = U-J = 8.0$ eV). Plane wave basis was truncated at a kinetic energy cut-off of 36.75 Ry. Maximum Force on ions in relaxed structure was within a threshold of 10^{-4} eV/Å. BZ integrations were sampled on dense $24 \times 24 \times 12$, $24 \times 24 \times 24$, and $5 \times 24 \times 8$ meshes of $\boldsymbol{k}$-points for *1T*, *3R* (primitive unit cell considered), and recently reported [302] *C2/m* structures of VSe_2, respectively. Also, for the sake of comparison, a sparse $8 \times 8 \times 3$ mesh of $\boldsymbol{k}$-points was used in sampling Brillouin zone (BZ) integrations for enthalpy calculations of *1T* and *C2/m* structures, similar to the recent report [302] and $8 \times 8 \times 8$ mesh was used in calculation of *3R* structure (primitive unit cell considered).

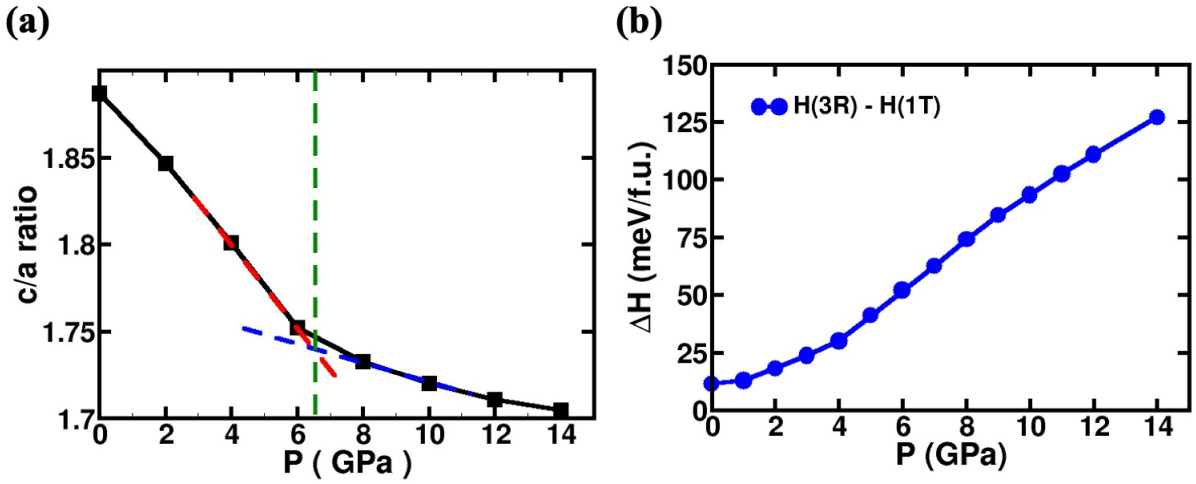

Figure 7.4: (a) Variation of c/a ratio in *1T*-VSe_2 with pressure. (b) Variation of difference in enthalpy between *3R* ($R\bar{3}m$) and *1T* ($P\bar{3}m1$) structures of VSe_2 with pressure.

7.4 Results and Discussion

Our first-principles calculations reproduce the metallic nature of ambient *1T*-VSe_2 ($P\bar{3}m1$) as shown in Fig. 7.2(b). Our estimates of the optimized lattice constants of *1T*-VSe_2 at 0 GPa are $a = 3.35$ Å and $c = 6.12$ Å, in close agreement with our experimental values

(a = 3.35 Å and c = 6.10 Å). The phonon-dispersion (Fig. 7.2(c)) of *1T*-VSe_2 at 0 GPa confirms its local stability as no imaginary frequencies were observed. *3R*-VSe_2 ($R\bar{3}m$) is metallic at 12 GPa since the valence band maxima and conduction band minima overlap (Fig. 7.3(d)). Optimized lattice parameters obtained from our first-principles calculation using Grimme-D2 van der Waals correction at 12 GPa are a = 3.16 Å and c = 17.39 Å, where c-value is overestimated as compared with the experimental values (a = 3.24 Å and c = 16.07 Å). The $R\bar{3}m$ phase is dynamically stable with no unstable phonon modes in its phonon dispersion (Fig. 7.3(e)). Lattice parameters of *1T*-VSe_2 vary smoothly as a function of hydrostatic pressure up to $P \sim 12$ GPa, with a notable change in the slope of c/a ratio with pressure at $P_C \sim 6$ GPa, (Fig. 7.4(a)) suggesting an isostructural phase transition, consistent with our experimental results and the recent report [302].

Table 7.1: Calculated lattice parameters (in Å) using Quantum ESPRESSO and ABINIT for *1T* and *3R* structures of VSe_2 at P = 0 and 12 GPa compared to experimental values.

***1T*-VSe_2**		**a (Å)**	**c (Å)**	**V (Å^3)**
0 GPa	QE	3.31	6.24	59.33
	ABINIT	3.32	6.27	60.02
0.2 GPa	Exp.	3.35	6.10	59.30
12 GPa	QE	3.21	5.49	48.96
	ABINIT	3.22	5.55	49.69
12.2 GPa	Exp.	3.23	5.63	50.74
***3R*-VSe_2**		**a (Å)**	**c (Å)**	**V (Å^3)**
0 GPa	QE	3.30	19.07	60.04
	ABINIT	3.32	19.07	60.53
12 GPa	QE	3.16	17.39	50.39
	ABINIT	3.18	17.45	50.83
12.2 GPa	Exp.	3.24	16.07	48.85

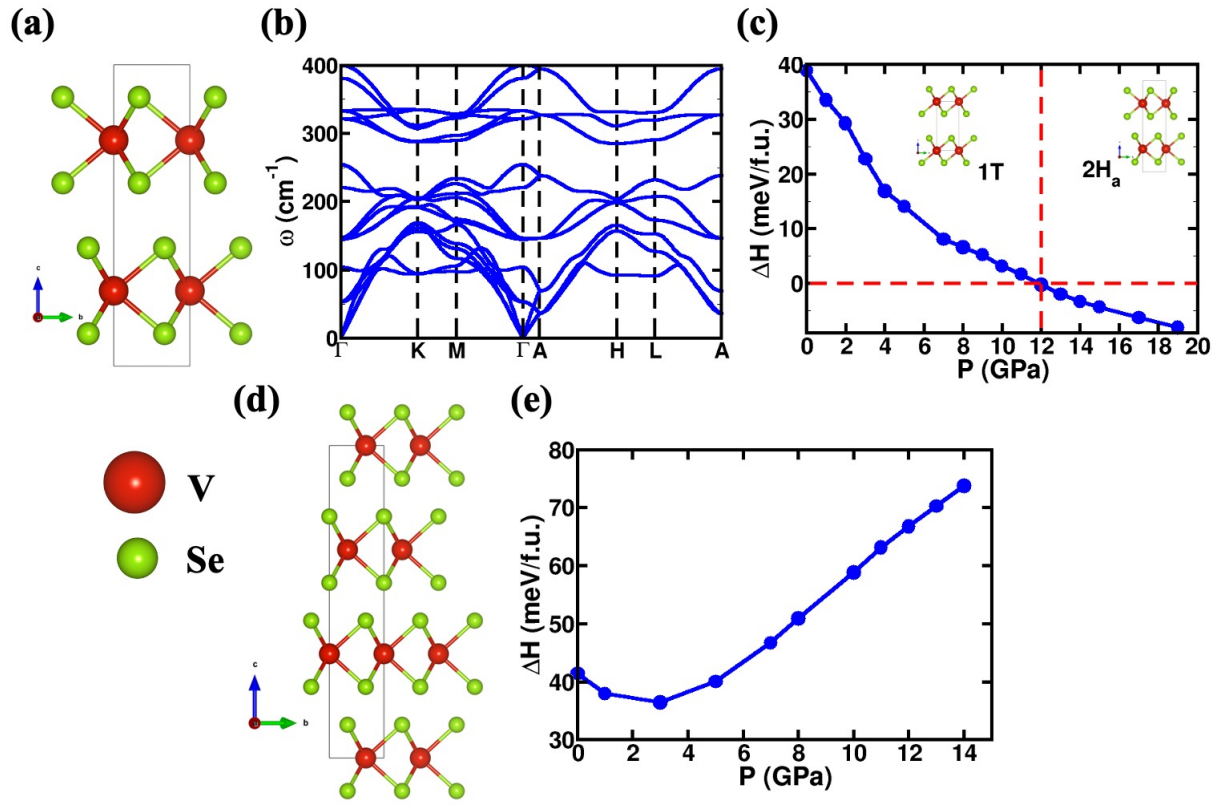

Figure 7.5: (a) $2H_a$ crystal structure of VSe_2, (b) its phonon dispersion at 12 GPa and (c) the difference in enthalpy of $2H_a$ and $1T$ structures of VSe_2. (d) $3R$ ($R3m$) VSe_2 and (e) the difference in enthalpy of $3R$ ($R3m$) and $1T$ structures of VSe_2.

To explore the possibility of a pressure dependent phase transition from $1T$ to $3R$ structure of VSe_2, we have determined the changes in enthalpy of these structures but did not observe any transition from the $1T$ to $3R$ phase (Fig. 7.4(b)). VSe_2 is a layered material which has a strong covalent bonding within the layer and weak van der Waals interaction between the layers. In this regard, we compared the lattice parameters of $3R$ with experiments obtained using different flavours of van der Waals correction, London-s6 forces and introduced Hubbard U parameter of 1 eV [307] to include on-site correlations of d electrons of the V atom. These results are presented in Table 7.2. As we did not find a phase transition from $1T$ to $3R$ structure under hydrostatic pressure, we investigated the stability of $2H_a$ (another polytype into which bulk dichalcogenides crystallize) having a hexagonal unit cell with $aBa\ cBc$ stacking and space group $P6_3/mmc$ [309, 310]

Table 7.2: Lattice parameters (in Å) of *3R* structure of VSe_2 (space group: $R\bar{3}m$) evaluated using different functionals compared to experiments at P = 12 GPa.

Method		**a (Å)**	**c (Å)**
van der Waals interaction	Grimme-D2	3.16	17.39
	Df-c09	3.15	17.46
	Df2-b86r	3.17	17.47
London-s6	0.65	3.17	17.41
	0.70	3.17	17.40
	0.75	3.17	17.39
	0.80	3.17	17.38
	0.85	3.17	17.34
	1.50	3.17	17.14
Hubbard-U	1 eV	3.18	17.39
Experiment	-	3.24	16.07

(Fig. 7.5(a)). Phonon dispersion at 12 GPa confirms that $2H_{\mathrm{a}}$ is stable and has soft modes indicating a possible phase transition (Fig. 7.5(b)). From estimated difference in enthalpy, we do find a transition from *1T* to $2H_{\mathrm{a}}$ near $P \sim$12 GPa (Fig. 7.5(c)). Though our theory predicts this phase transition, the $2H_a$ structure cannot be fitted to our XRD data at high pressures. We have also considered *3R* structure based on $2H_a$ stacking (*R3m* space group with *aBa bCb cAc* stacking) (Fig. 7.5(d)). The relative stability of this *3R* with respect to *1T* structure as seen from difference in enthalpy does not reveal a phase transition (Fig. 7.5(e)).

To examine if the finite-temperature effects contribute to the stability of the *3R* phase, we have evaluated temperature dependent vibrational free energies of *1T*, *3R* ($R\bar{3}m$) and *3R* (*R3m*) structures. The vibrational contributions to the free energies as a function of

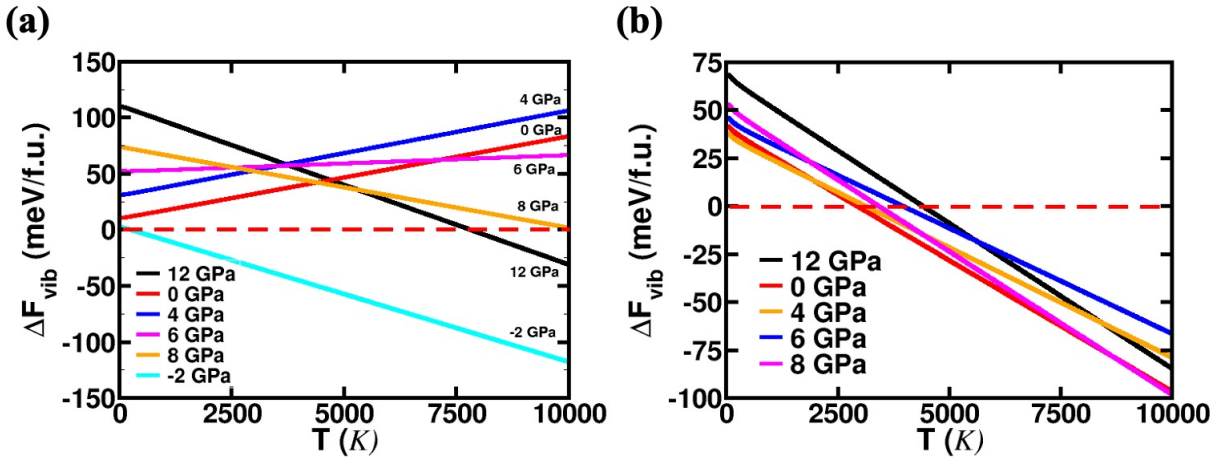

Figure 7.6: The difference in vibrational free energy of *3R* and *1T* structures of VSe_2 as a function of temperature in (a) *3R* ($R\bar{3}m$) and (b) *3R* ($R3m$).

temperature is estimated within a harmonic approximation [267]:

$$F_{\text{vib}} = E_{\text{total}} + \frac{k_{\text{B}}T}{N_{\text{q}}} \sum_{q,i} \log \left[2 \sinh \left(\frac{\hbar \omega_{\text{iq}}}{2k_{\text{B}}T} \right) \right] \tag{7.1}$$

where N_q is the number of **q**-points on a $24 \times 24 \times 12$ mesh in the BZ and ω_{iq} is the frequency of mode i at a wave vector **q**. As evident in the transition temperatures at various hydrostatic pressure (Fig. 7.6(a) and Fig. 7.6(b)), the temperature that stabilizes *3R* polytypes is not realistic, ruling out temperature effects.

Having examined all the above possibilities to stabilize the *3R* phase established unambiguously in our XRD experiments, we obtain the energetics of *1T* and *3R* structures of VSe_2 with spin-polarized calculations using VASP including Hubbard parameter correction GGA+U, ($U_{\text{eff}} = U$ - J = 8.0 eV). Sampling of Brillouin zone (BZ) integrations was carried out on dense uniform $24 \times 24 \times 12$, $24 \times 24 \times 24$, and $5 \times 24 \times 8$ meshes of $\boldsymbol{k}$-points for *1T*, *3R* (primitive unit cell considered), and *C2/m* structures of VSe_2, respectively. Calculated enthalpies of *1T*, *3R*, and *C2/m* phases as a function of pressure are plotted in (Fig. 7.7(b)). Surprisingly, the present DFT calculations predict the monoclinic *C2/m*

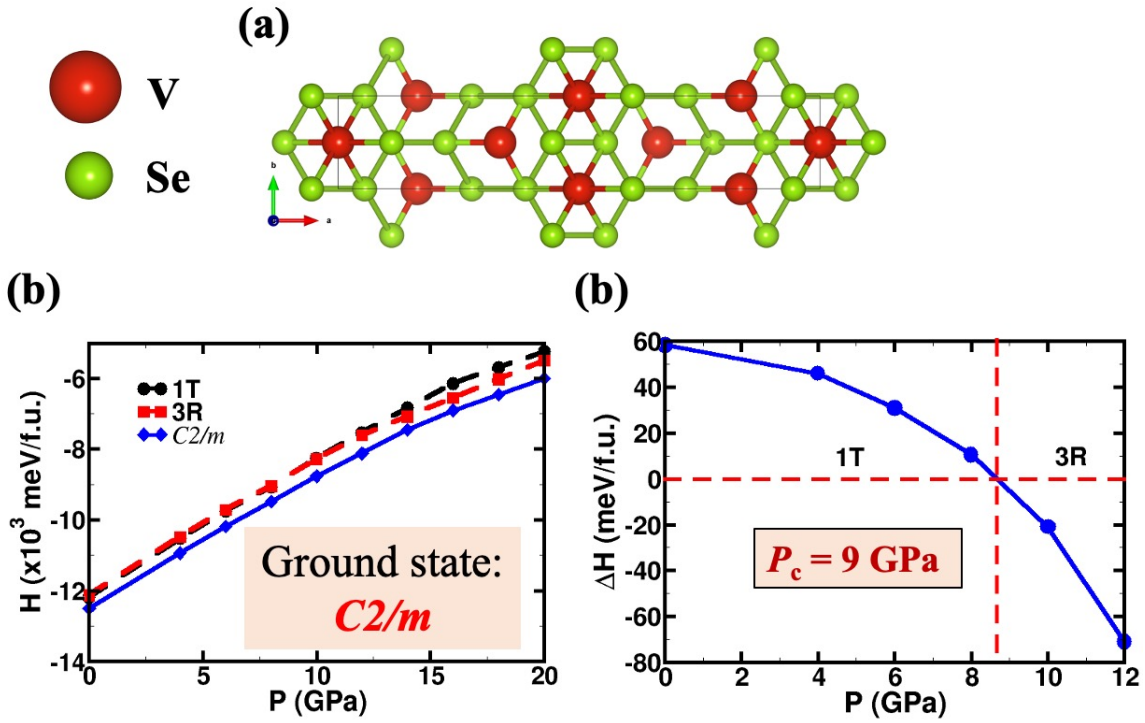

Figure 7.7: (a) *C2/m* structure of VSe_2, (b) pressure dependence of enthalpies of the *1T*, *3R*, and *C2/m* structures of VSe_2. (c) The difference in enthalpy between *3R* (space group: $R\bar{3}m$) and *1T* structures, indicating a phase transition from *1T* to *3R* structure of VSe_2 at $P \sim$9 GPa.

structure to be the ground state of the VSe_2 system at $P = 0$ GPa compared to the experimentally established ambient *1T* phase. The *C2/m* structure remains the lowest-energy structure of the system up to $P = 20$ GPa. Also, the absence of any crossover between the *1T* and the *C2/m* phases is at variance with the claim of Ref. [302] of obtaining *1T* to *C2/m* transition at $\sim$ 15.5 GPa. Fig. 7.7(c) represents the difference in enthalpy between the *3R* (space group: $R\bar{3}m$) and *1T* (space group: $P\bar{3}m1$) structures of VSe_2 revealing a phase transition from *1T* to *3R* structure at $P \sim 9$ GPa.

The $\boldsymbol{k}$-meshes in the present study have been chosen appropriately to satisfy the inverse proportionality to the lattice constants in real space. Also, metallic systems require a dense set of $\boldsymbol{k}$-points due to the presence of a Fermi surface where the occupation of the bands changes rapidly from zero to one and thereby implying a very high Fourier compo-

Table 7.3: Transition temperatures from *1T* to *3R* structures ($R\bar{3}m$ and $R3m$) at $P = 0$, 4, 8 and 12 GPa.

Pressure (GPa)	**T (*K*)**	
	R$\bar{3}$m	**R3m**
0	-	2950
4	-	3140
8	10300	3430
12	7820	4420

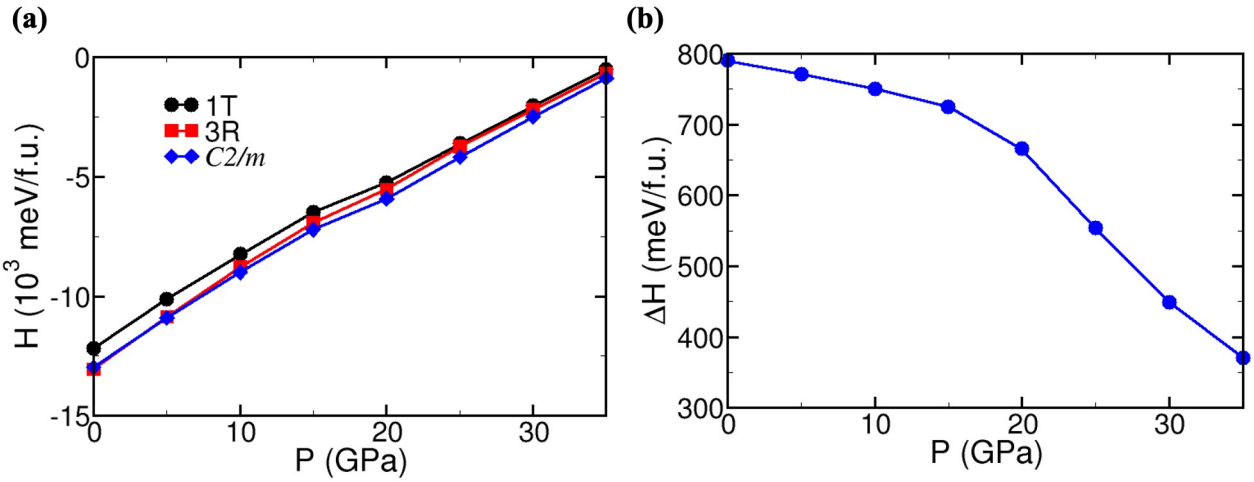

Figure 7.8: (a) Pressure dependence of enthalpies of the *1T*, *3R*, and *C2/m* structures of VSe_2. (b) The differences in enthalpies of *1T* and *C2/m* calculated using VASP using the same computational parameters as used by Sereika *et al.*

nents in $F(\boldsymbol{k})$, whereas the chosen $\boldsymbol{k}$-mesh of $8 \times 8 \times 3$ for the *1T* and *C2/m* structures in Ref. [302] is less-dense. We now present our theoretical analysis on the stability of the monoclinic structure *C2/m* predicted in Ref. [302] using the same computational parameters (and the same code) as used by Sereika *et al.* ([302]) to obtain the energies (and enthalpies) of 1T and *C2/m* phases of VSe_2. For the sake of comparison, we have also performed the enthalpy calculation for the *3R* phase using a sparse $\boldsymbol{k}$-mesh of $8 \times 8 \times 8$. The monoclinic structure (Fig. 7.7(a)) has lattice parameters $a = 18.68$ Å, $b = 2.76$ Å, $c = 5.63$ Å, $V = 287.41$ Å^3, and $\beta = 97.458^o$ at $P = 35$ GPa. Fig. 7.8(a) represents the pressure evolution of enthalpies for the *1T*, *3R*, and *C2/m* structures. *3R* comes out to

be the lowest energy structure at $P = 0$ GPa and a *3R* to *C2/m* transition is indicated at ∼3 GPa Fig. 7.8(a). The pressure evolution of difference in enthalpy of *1T* and *C2/m* shown in Fig. 7.8(b) (VASP calculation) reveals robust stability of *C2/m* phase of VSe_2 relative to its *1T* structure as a function of pressure. This contradicts the *1T* to *C2/m* phase transition at $P = 15.5$ GPa reported in Ref. [302].

7.5 Conclusions

To conclude, we address two pressure driven transitions in bulk *1T*-VSe_2 using X-ray diffraction and DFT studies. The first transition around 4 GPa is isostructural with distinctive anomalies in bond length, bond angle, c/a ratio. The second transition around 11 GPa is from *1T* ($P\bar{3}m1$) to *3R* ($R\bar{3}m$) structure due to the sliding of Se-V-Se tri-layer leading to a contraction of unit cell volume per formula unit by $\sim 3\%$. Similar layer sliding mechanism has also been seen in other TMD materials like MoS_2, [293, 294] and WSe_2 [296]. Our high-pressure XRD data is inconsistent with the *C2/m* monoclinic space group assignment by a recent report [302]. The possible reasons behind this discrepancy are the differences in the pressure mediums and quality of the samples used in two studies. Hence, further exploration of the system, preferably using different pressure transmitting mediums, sets up for potential future scopes.. Our analysis based on first-principles calculations confirms stability of *3R* phase around 9 GPa only after incorporation of spin-polarized calculations to account for the Hubbard correction with $U_{eff} = U - J = 8$ eV. The present DFT calculations predict the *C2/m* to be the ground state structure of the VSe_2 system at $P = 0$ GPa. The inadequacy of the present DFT results in capturing the experimental *1T* structure at $P = 0$ GPa needs further insights to resolve in future. Also, our DFT calculations are unable to capture a transition from *1T* to a monoclinic superstructure phase above 15.5 GPa in the system using a sparse $\boldsymbol{k}$-mesh as used in [302] as well as using a more appropriate and denser mesh of $\boldsymbol{k}$-points.

Chapter 8

CDW-induced low thermal conductivity in $GdTe_3$

8.1 Introduction

Rare earth tellurides with general formula $R\text{Te}_3$ (R = rare earth element and Te = tellurium), among several CDW materials have gained enormous attention in the field of chemistry and condensed matter physics due their structural diversity [311], exotic magnetic properties [312] and pressure induced superconductivity [313]. Depending upon the rare earth element present in $R\text{Te}_3$, the CDW transition temperature (T_{CDW}) can vary from 244 K (TmTe_3) [314] to 500 K (LaTe_3) [315]. Application of external pressure can also tune this transition temperature significantly [313, 316]. It is worth mentioning here that the heavy rare earth element (Tb−Tm) based $R\text{Te}_3$ system undergoes a second CDW transition at lower temperature [315]. Though several physical properties of $R\text{Te}_3$ system have already been studied, the thermoelectric properties remain unexplored. Recently,

$GdTe_3$, a member of RTe_3 family has drawn huge attraction due to very high carrier mobility. The electron mobility is beyond 60,000 $cm^2V^{-1}s^{-1}$ [317], which is the highest among all known layered materials. So, we chose to study $GdTe_3$ as a potential candidate for thermoelectric research.

Materials with high thermal conductivity are useful in microelectronic devices due to their efficient heat dissipation, whereas low thermal conductive materials are widely used in thermoelectrics [318–321] and thermal barrier coatings [322]. In a nonmagnetic material, the thermal conductivity (κ) is composed of two parts, namely (i) electronic thermal conductivity (κ_{ele}) which is determined by the electrical conductivity (σ) of the material via the Wiedemann–Franz law, $\kappa_{ele} = L\sigma T$ (L = Lorenz number, and T = absolute temperature), and (ii) lattice thermal conductivity (κ_l) which is primarily controlled by phonon (quantum of lattice vibration) transport. To determine the efficiency of a thermoelectric material, κ_l plays a pivotal role because it is a relatively independent parameter and can be tuned easily. After years of effort, researchers have developed several extrinsic and intrinsic strategies to minimize κ_l by enhancing phonon scattering. Extrinsic approaches like incorporation of point defects and nano/meso structures into a thermoelectric matrix are found to be effective in lowering down the κ_l [323–327]. However, these extrinsic strategies may hamper the carrier mobility to some extent which in turn can decrease the efficiency of a thermoelectric material. So, to design new materials with intrinsically low κ_l is an important task in thermoelectric research. Several inherent properties associated with crystal structure and chemical bonding such as presence of lattice anharmonicity in two dimensional (2D) layered structure [328–332], stereochemically active lone pairs [332,333], complex crystal structures [334,335], bonding heterogeneity [336,337], and resonant bonding [338] are found to be effective for achieving intrinsically low κ_l. In addition to this, materials with ferroelectric instability [339, 340], rattler atoms [341–343] and liquid-like cationic motion [344, 345] are found to show intrinsically low values of κ_l.

When the charge carrier concentration of a material is not high, phonon-phonon interactions (PPI) by three-phonon and four-phonon process is the most dominant phonons scattering mechanism determining lattice thermal conductivity at high temperature [346]. However, recent studies indicate that the electron-phonon interaction (EPI) starts to play a crucial role in determining the lattice thermal conductivity when the carrier concentration is above 10^{19} cm^{-3} [347]. Theoretical calculations performed by Liao *et al.* have shown that EPI can reduce the lattice thermal conductivity of *p*-type silicon up to 45% at room temperature by decreasing the phonon lifetime, when the carrier concentration is at around 10^{21} cm^{-3} [348]. So, materials having strong EPI may show intrinsically low κ_l. In this context, charge density wave (CDW) materials hosting strong electron phonon coupling may be a good candidate for low lattice thermal conductivity. CDW materials in general have layered structure where strong EPI breaks the translation symmetry of the lattice and induces lattice distortion into the system [349]. Recently, Chiritescu *et al.* have obtained an ultralow κ_l of around 0.05 Wm^{-1}K^{-1} at room temperature in disordered thin films of 2D layered WSe_2 [350]. Realizing this idea of layered and disordered crystal structure, one can expect a low κ_l value in CDW materials.

$GdTe_3$ exhibits fascinating hierarchical bonding environments where one corrugated GdTe slab is sandwiched between two Te sheets. From our first-principles DFT calculations, we have verified that charge transfer takes place from the GdTe slab to the adjacent Te sheets. Thus, the structure can be considered as a natural heterostructure of charged and vdW layers which gives rise to large degree of anharmonicity in the crystal lattice of $GdTe_3$ that provides significant phonon damping. The presence of unstable phonon modes arising from the displacements of Te-bilayers, strong electron-phonon coupling, and Fermi surface nesting constitute the origin of CDW transition ($T_{CDW} \sim 380$ K) in $GdTe_3$ as corroborated from the DFT studies.

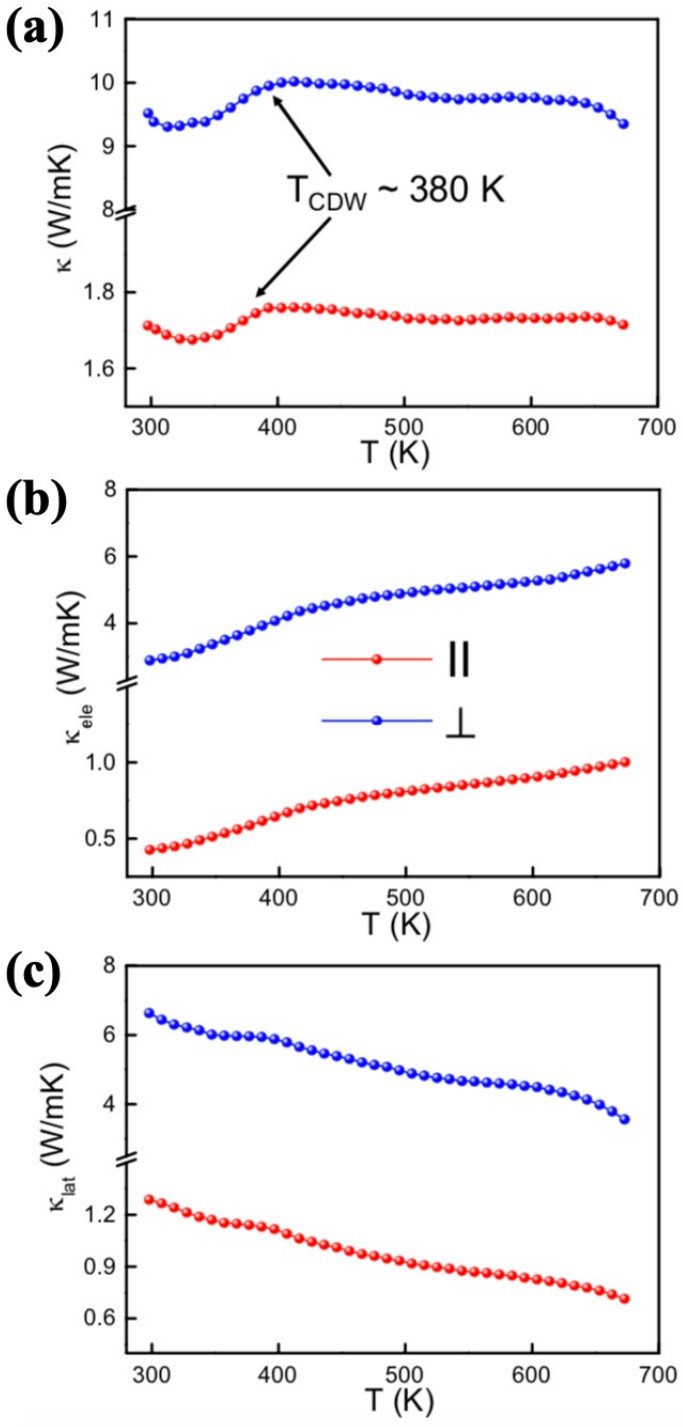

Figure 8.1: Experimentally measured (by Dr. Sushmita Chandra from Prof. Kanishka Biswas's lab at JNCASR) temperature dependent (a) κ, (b) κ_{ele}, and (c) κ_l of $GdTe_3$ measured along parallel and perpendicular to SPS pressing direction. The charge density wave transition temperature is marked by the black arrows in (a).

8.2 Experimental observations

Our experimental collaborators (Sushmita Chandra and Prof. Kanishka Biswas, Jawaharlal Nehru Centre For Advanced Scientific Research) have synthesized a simple binary charge density wave material $GdTe_3$ which shows intrinsically low lattice thermal conductivity of 0.7 $Wm^{-1}K^{-1}$ at 673 K along parallel to the SPS pressing direction (Fig. 8.1). Interestingly, our experimental collaborators have observed large anisotropy in the electrical and thermal conductivity data of $GdTe_3$ when measured along parallel and perpendicular to the SPS pressing, which is quite unusual in polycrystalline materials. To comprehend the origin of low κ_l and its relationship with the charge density wave transition, we have performed temperature dependent Raman spectroscopy and augmented our observations with density functional theoretical (DFT) calculations. Raman spectroscopy reveals the existence of low-lying optical phonon modes which also effectively enhance the phonon scattering in the system.

8.3 Computational details

Our first-principles calculations are based on density functional theory as implemented in Quantum ESPRESSO [137], and ultrasoft pseudopotentials to model interactions between electrons and the ionic cores. We used a generalized-gradient approximation (GGA) [138] of the exchange-correlation energy with functional parameterized by Perdew, Burke and Ernzerhof (PBE) [139]. We include van der Waals (vdW) interaction with the parametrization given in Grimme scheme [140]. Electronic wave functions and charge density expansions in plane wave basis sets were truncated at cut-off energies of 50 Ry and 400 Ry respectively. Brillouin Zone (BZ) integrations were sampled on a uniform 12x12x4 mesh of k-points. We used conventional unit cell of $GdTe_3$ with 16 atoms as the periodic unit for our theoretical analysis. Electronic spectrum was determined at Bloch wave vectors along high symmetry lines ($\Gamma-S-X-Y-\Gamma-Z-R-U-T-Z$) in the Brillouin

Zone with and without inclusion of spin-orbit coupling (SOC) in our calculations. Lattice-dynamical properties were determined within the framework of self-consistent density functional perturbation theory (DFPT) as implemented within the QE code [137]. We corroborated these using a 4×4×1 supercell of $GdTe_3$ in calculations with PHONOPY [351] and Vienna Ab-initio Simulation Package (VASP) [305, 306]. We determined the mode Grüneisen parameters using finite difference method and phonon dispersion calculated at volumes, $0.98\times V_0$ and $1.02\times V_0$ (where V_0 is the equilibrium volume of the ground state structure), employing the formula $\gamma_{q\nu} = -\frac{dln\omega_{q\nu}}{dlnV}$, where $\gamma_{q\nu}$, V and $\omega_{q\nu}$ denote Grüneisen parameter, unit cell volume, and frequency of a phonon mode at wavevector q for branch ν, respectively.

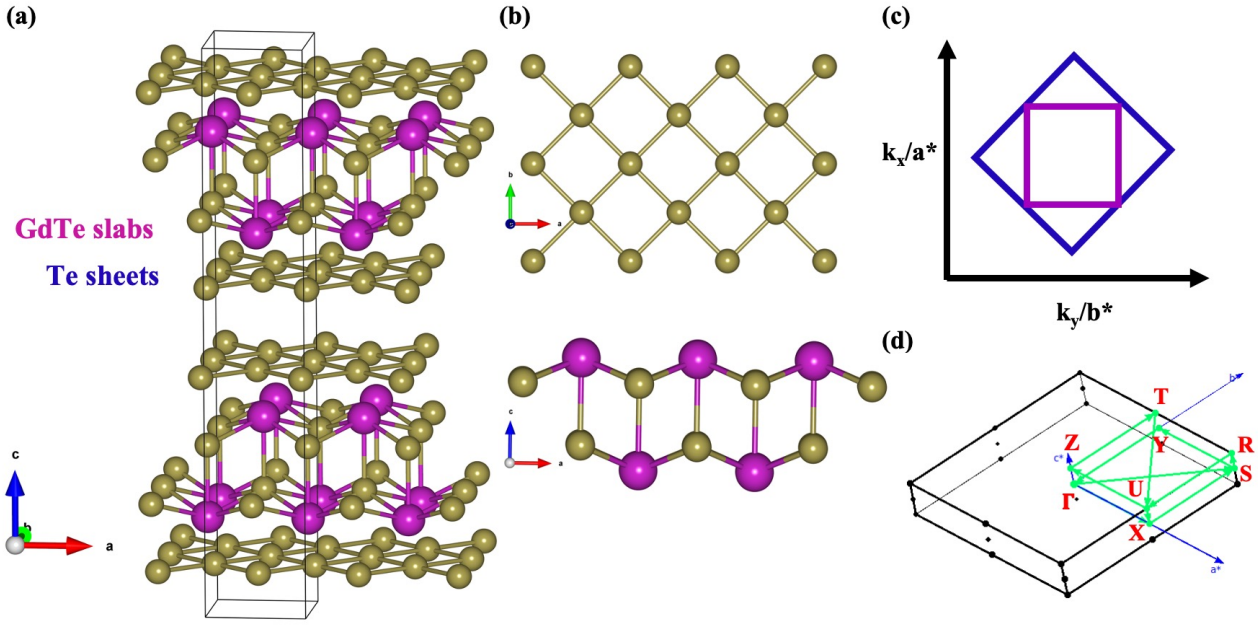

Figure 8.2: (a) The layered, undistorted structure of $GdTe_3$ where GdTe corrugated slabs and Te sheets are stacked along z-axis and held together by weak van der Waals interaction. (b) The Te sheets are planar with two Te atoms per square unit cell rotated by 45^o with respect to a and b. Ionic $[Gd_2^{3+}Te_2^{2-}]^{2+}$ layers are sandwiched between double layers of Te sheets. (c) The presence of two different structural motifs gives rise to two different Brillouin zones (BZ): a two-dimensional BZ of periodic bilayer of Te (blue) and another of the periodic GdTe slab (pink). (d) Brillouin zone of the orthorhombic unit cell of $GdTe_3$ in *Cmcm* space group where the green lines mark the path connecting the high symmetry points (in red) used in our calculations of electronic structure and phonon dispersion.

8.4 Results and Discussion

$GdTe_3$ belongs to a family of quasi-2D metals [317], RTe_3 (R = rare-earth element) in which Te atoms are arranged in square-net planar sheets and stacked between corrugated GdTe layers (Fig. 8.2(a) and Fig. 8.2(b)). The Te sheets with square unit cell of half the area (as of the basal unit of crystal) is rotated by 45^o with respect to GdTe layers. This results in two different Brillouin zones (BZ) [352]: a square BZ of the periodic Te square-net sheets and another square BZ of the periodic GdTe slab (Fig. 8.2(c)). Our optimized lattice parameters (without considering charge density wave (CDW) modulation), a, b and c are 4.32 Å, 4.35 Å and 25.6 Å respectively, within 1% of the respective experimental values [317]. The oxidation state of Gd is 3^+ and that of Te is 2^- achieved with a transfer of two electrons per cell from GdTe slab to Te sheets containing two planar sheets of Te. To derive insight into this charge transfer, we obtained difference in charge density between $GdTe_3$ crystal and its 2D building blocks;

$$\Delta\rho = \rho(GdTe_3) - [\rho(GdTe) + \rho(Te)] \tag{8.1}$$

where $\rho(GdTe_3)$, $\rho(GdTe)$ and $\rho(Te)$ are the charge densities of $GdTe_3$, GdTe slab and Te sheets calculated using the same periodic cell (a, b, c). Accumulation of electronic charge (yellow) in Te sheets and charge depletion in GdTe slab (cyan) show electrons transfer (Fig. 8.3(a)). Macroscopic average of $\Delta\rho$ (Fig. 8.3(b)) confirms electronic charge transfer from Gd atoms in GdTe slab to Te sheets.

We next obtain the electronic structure of orthorhombic $GdTe_3$, analyzing the effects of spin-orbit coupling (SOC) through the use of relativistic pseudopotentials (Fig. 8.3(c)). Undistorted $GdTe_3$ is metallic with linearly dispersed steep bands crossing Fermi energy (E_F). The linear bands describe electrons with large group velocity and small effective mass (m^*) giving rise to a high mobility. In another study, Lei *et al.* [317] reported very

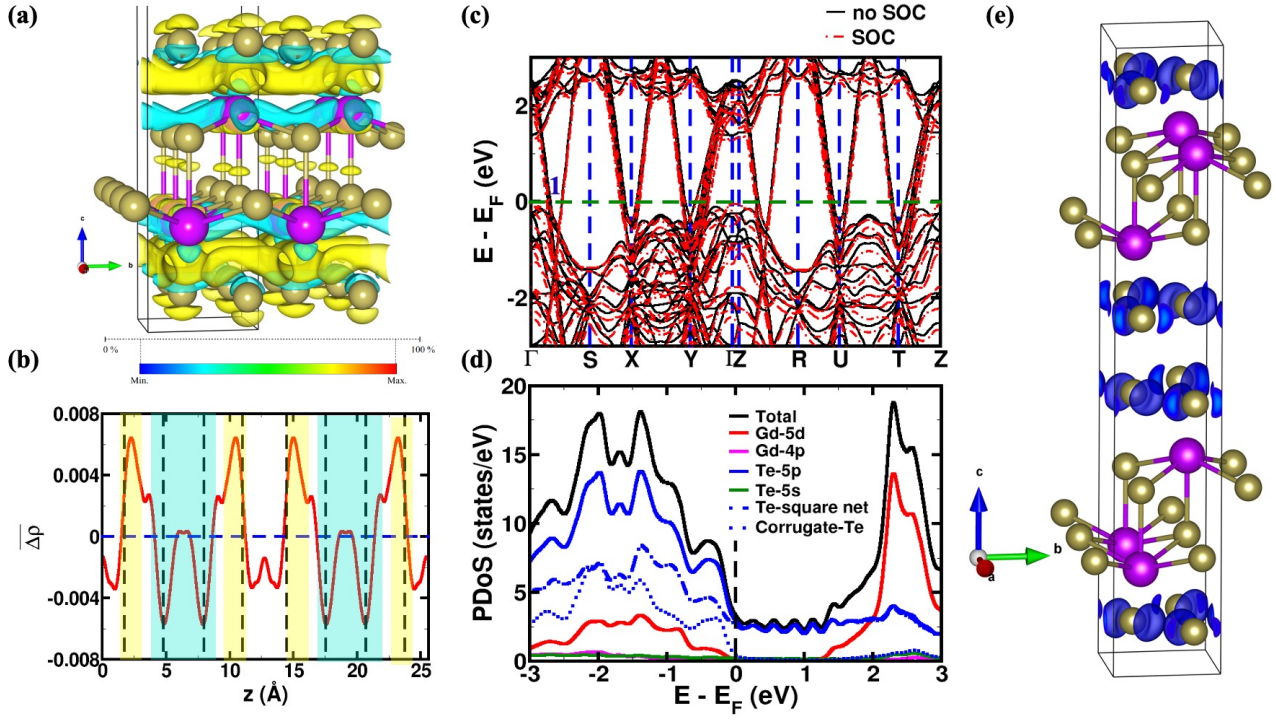

Figure 8.3: (a) Difference in charge densities of $GdTe_3$ crystal and its building blocks of GdTe slab and Te sheets, and its (b) macroscopic average between $GdTe_3$ and taking GdTe slab and Te sheets individually. The yellow regions (positive values in (b)) show regions of electronic charge accumulation and cyan regions (negative values in (b)) indicate charge depletion, showing an overall charge transfer from GdTe slab to Te sheets. (c) Electronic structure of $GdTe_3$ calculated with (red color lines) and without (black color lines) inclusion of effects of SOC show that it is a metal with linearly dispersive bands crossing Fermi energy (E_F). (d) As seen from projected density of states (PDOS) (without SOC), states near E_F have contributions primarily from $5p$ orbitals of Te. (e) Visualization of wave functions of states along $\Gamma-S$ with energy $= E_F$ (marked as 1 in (c)) show significant contributions from p-orbitals of Te atoms of bilayers.

high electron mobility of 60,000 $cm^2V^{-1}S^{-1}$ in $GdTe_3$, which is the highest among all layered materials. Inclusion of SOC leads to splitting of bands but these effects are more pronounced on the states deeper in energy, away from E_F. Since changes in the behaviour of bands near E_F due to inclusion of SOC are small, we have not included SOC in further calculations. From projected density of states of $GdTe_3$ (calculated without SOC), it is evident that the valence bands (VB) have contributions primarily from Te $5p$, with weak component of Gd $4d$ states whereas the states in conduction bands (CB) comprise largely of d-orbitals of Gd (Fig. 8.3(d)). Visualization of wave functions of the linear

bands crossing E_F along Γ−S show significant contributions from p-orbitals of Te atoms belonging to layered Te planar sheets (Fig. 8.3(e)).

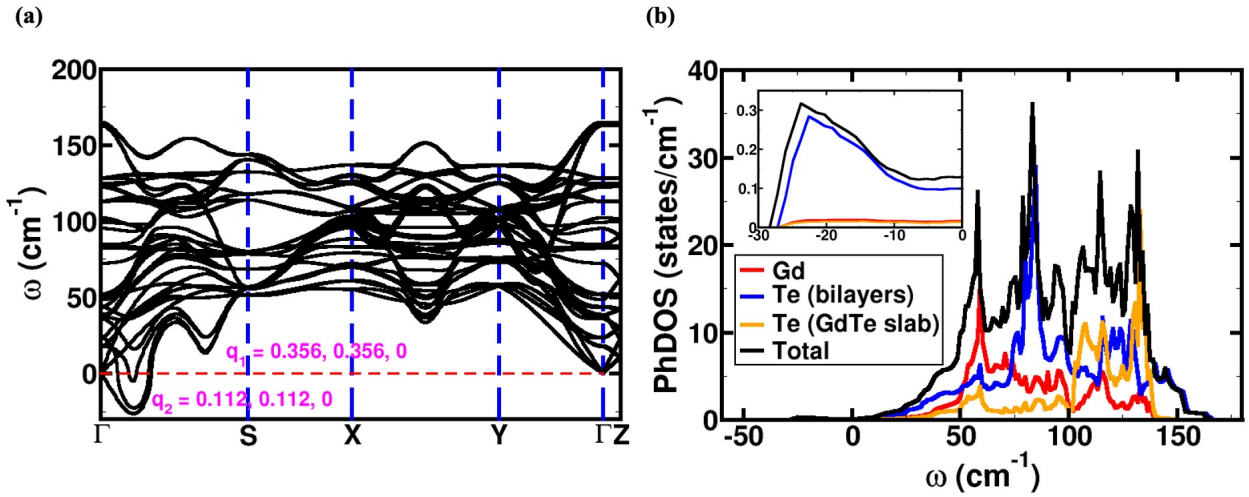

Figure 8.4: (a) Phonon dispersion of $GdTe_3$ along high symmetry directions in BZ shows instability at wavevectors only along Γ−S direction in the Brillouin zone. (b) Atom projected phonon density of states reveal that the unstable and low-frequencies optical modes involve vibrations of Te atoms in the planar sheets of Te.

We obtain vibrational spectrum of $GdTe_3$ to assess its structural stability. Our calculated phonon dispersion exhibits modes with imaginary frequencies ($\omega^2 < 0$) along Γ−S direction of the Brillouin zone and stable modes along all the other directions (Fig. 8.4(a)). An interesting thing to note in the phonon spectrum is the softening of a phonon branch or Kohn anomaly again along Γ−S and renormalization of the acoustic phonon branch which is a characteristic of CDW or Peierls instability [353]. To get insight into the atomic contributions to phonons, we examine the atom-projected phonon density of states (PhDOS) (Fig. 8.4(b)), which shows dominant contributions of Te bilayer to the modes with imaginary frequencies. It is clearly seen from PhDOS that there exist several low-frequency optical phonon branches below 50 cm^{-1} which have major contributions from the Te bilayers. This is also confirmed by visualization of eigen-displacements of these low-frequency modes. The origin of this lattice instability can be traced to the Fermi

surface (FS) which is quasi two-dimensional due to two layered structural motifs (GdTe slab and Te sheets). Linearly dispersed bands crossing E_F, are principally constituted of Te p-orbitals of Te sheets and result in a diamond-shaped FS (Fig. 8.5(a)), which exhibits strong nesting (nontrivial measure of electronic states on the FS coupled by a phonon with nesting wave vector to other states on the FS) and perturbation modulated with nesting wave vector destabilizes the structure driving it to lower energy, similar to Peierls instability, in $GdTe_3$. The nesting wave vectors (q_1 and q_2) along $\Gamma-S$ direction are also the nesting wave vectors corresponding to the instability and Kohn anomaly, respectively in phonon spectrum (Fig. 8.5(b) and Fig. 8.5(c)). Distortion of the structure by freezing of eigen-displacements of unstable modes would lead to structure with lower energy, opening up a gap in band structure. However, with periodicity of $2\pi/q$, this structure will involve a supercell of $8\times8\times1$, and its simulation is computationally expensive. The unstable modes and Kohn anomaly involve displacements of Te atoms arranged in square-net sheets (Fig. 8.5(d)), which also constitute the origin of CDW in $GdTe_3$. Thus, electronic and lattice instabilities in $GdTe_3$ are driven by the Fermi Surface Nesting.

We now investigate the origin of low lattice thermal conductivity (κ_l) of 1.25 W/mK at 300 K and further decreasing to 0.7 W/mK at 673 K in $GdTe_3$. Phenomenological relation between κ_l and phonon group velocity (v) is given by $\kappa_l = 1/3C_v vl$, where C_v is the heat capacity at constant volume and l is the phonon mean-free path [354]. With low cut-off frequencies (~ 50 cm^{-1}) of acoustic modes of $GdTe_3$, its sound velocities are rather low contributing to low κ_l. The average sound velocities determined from the slope of the linear region of acoustic phonon branches along in-plane ($\Gamma-S$) and out-of-plane ($\Gamma-Z$) are 2135 m/s and 1643 m/s respectively, consistent with experimental finding that κ_l is lower along the $SPS_{||}$ direction. Thermal conductivity of a solid is also affected by anharmonic interactions between phonons [354]. In $GdTe_3$, interactions between the low-energy optical phonons and acoustic phonons are significant, causing

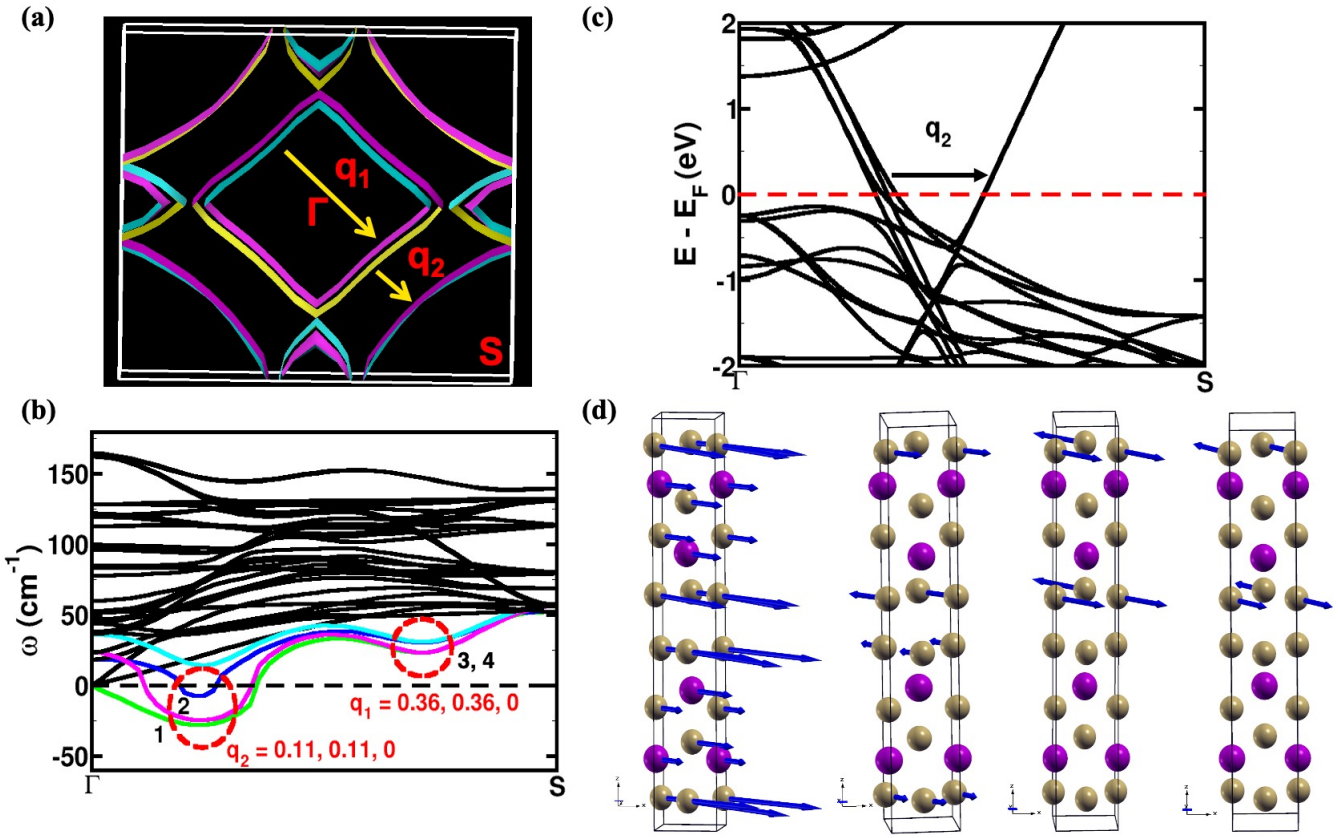

Figure 8.5: (a) The diamond-shaped Fermi Surface (FS) exhibits nesting by wave vectors (q_1 and q_2) along Γ−S direction leading to Peierls-like instability in $GdTe_3$. The wave vectors, q_1 and q_2 are also the wave vectors of Kohn anomaly and instability, respectively in (b) phonon dispersion. The nesting vector q_2 shown in band structure (c) reveals coupling between linearly dispersed bands. (d) Atomic displacements of unstable modes at q_2 corresponding to (1) $27i$ cm^{-1} and (2) $23i$ cm^{-1} and Kohn anomaly at q_1 with frequencies at (3) 13 cm^{-1} and (4) 14 cm^{-1} involve displacements of Te atoms in the planar sheets of Te.

strong scattering of heat carrier acoustic modes resulting in low κ_l. To quantify the strength of this anharmonicity, we determined the mode Grüneisen parameters ($\gamma_{q\nu}$), from changes of phonon frequencies with strain i.e., (acoustic phonon = strain)-phonon coupling (Fig. 8.6). Acoustic phonons and low-energy optical phonons exhibit anomalously high $\gamma_{q\nu}$ ~ 50 (peak in $\gamma_{q\nu}$ concentrated in the frequency range of acoustic modes), indicating strong phonon-phonon coupling. Similarly, rather high estimated for the phonon branches along Γ−S associated with CDW instability and Kohn anomaly arising from modes localized in Te bilayers, reducing κ_l. The phonon scattering rate is inversely proportional to phonon

lifetime and increases with inverse square of $\gamma_{q\nu}$, indicating that large contributors to low κ_l in $GdTe_3$ are the anomalous CDW-related modes along Γ−S.

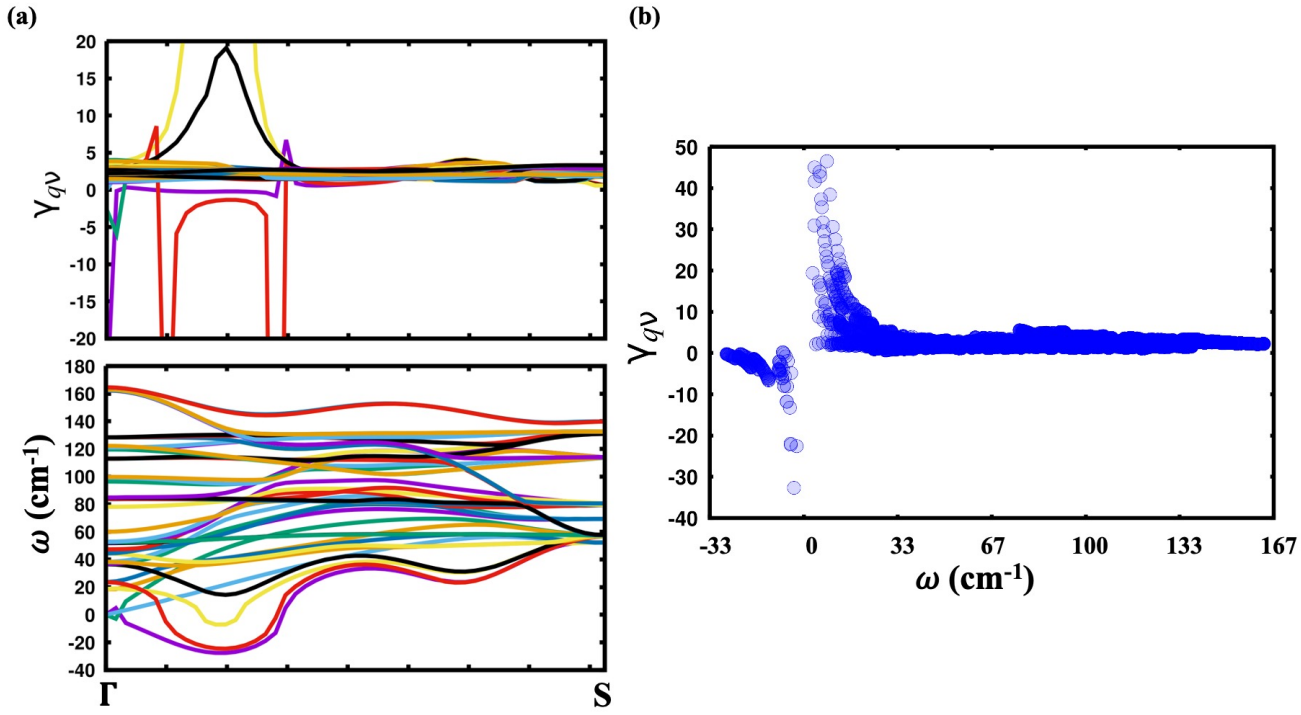

Figure 8.6: (a) Calculated mode Grüneisen parameters ($\gamma_{q\nu}$) of phonons along Γ−S directions in the Brillouin zone. Very high $\gamma_{q\nu}$ is exhibited by phonon modes associated with the CDW instability, (b) Grüneisen parameters of phonons at q on a uniform mesh of k-points in reciprocal space as a function of frequency clearly show strong coupling between acoustic and low-frequency optical phonon modes. Anomalously high $\gamma_{q\nu}$ indicates strong lattice anharmonicity induced by lattice distortion in Te bilayer.

8.5 Conclusion

In conclusion, using first-principles calculations based on density functional theory we show a charge transfer from GdTe layers to Te sheets of $GdTe_3$. The undistorted phase of $GdTe_3$ is metallic, with a strongly nested Fermi Surface leading to instability and Kohn anomalies in phonon dispersion. The unstable phonon modes involve displacements of Te atoms in bilayers constituting the origin of CDW in $GdTe_3$. Charge transfer from GdTe slab to Te bilayers means the interlayer interaction involves weak (van der Waals)

and strong (electrostatic) forces. The lattice instability involving Te bilayers is of 'sliding nature' and is still understandable despite the strong electrostatic interaction. We establish a strong anharmonicity in terms of high Grüneisen parameters of the CDW-related phonon modes along $\Gamma-$S direction, which is responsible in making acoustic phonons ineffective in transporting heat and causing low κ_l in $GdTe_3$.

Chapter 9

Low thermal conductivity in charge density wave Weyl semi-metal $(TaSe_4)_2I$

9.1 Introduction

Physics of low-dimensional materials is fascinating due to their peculiar electronic and elastic properties and have been the subject of intense research in the last decade [355]. In particular, interactions between metal ions strongly enhance electron-electron, spin-phonon, and electron-phonon (e-ph) coupling strengths which, under suitable conditions of temperature, pressure, magnetic field, etc., result in the partial or complete condensation of the free carriers by formation of a charge or spin density wave (CDW or SDW) [356]. It was pointed out by Peierls that metallic state of one-dimensional (1D) compounds is unstable, and they undergo a structural phase transition or Peierls distortion [357]. Strong

electron-phonon interaction leads to coupling of carriers on the Fermi surface through a perturbing field of nesting wavevector $\pm k_F$ resulting in softening of the $2k_F$ phonon mode (also known as Kohn anomaly). This is also accompanied by opening up of electronic band gap marking a metal to insulator transition at transition temperature T_c. CDW has been widely studied in quasi-one-dimensional (quasi-1D) metallic systems. Quasi-1D metallic systems like transition metal chalcogenides such as MX_3 (M = Nb and Ta, X = S, Se and Te) [358], blue bronzes $A_{0.3}MoO_3$ (A = K and Rb) [359], and Krogmann's salt $K_2Pt(CN)_4Br_{0.3}$-$3.2H_2O$ [360,361] have been studied extensively over the last few decades and most of their electrical and structural properties are now relatively well understood.

Recently, there has been a renewed interest in a new family of halogen transition metal tetrachalcogenides with the general formula $(MX_4)_nY$ where M = Nb, Ta, X = S, Se, Y = Cl, Br, I and n = 2, 3 and 4 [362, 363]. $(TaSe_4)_2I$ is a typical paradigmatic quasi-1D material which has been studied extensively for three decades now [364–366]. $(TaSe_4)_2I$ crystallizes in the tetragonal $I422$ chiral space group and consists of $TaSe_4$ chains running parallel to the c-axis and separated by iodine atoms located between the chains providing a quais-1D character to the crystal [363]. It undergoes a charge density wave transition at T_{CDW} = 263 K accompanied by an incommensurate structural distortion [367]. A Weyl semimetal is a type of material that has a special kind of energy band structure, characterized by the presence of Weyl points. A Weyl point is a point in the momentum space of the material where two energy bands touch and cross each other, forming a Weyl cone. The energy dispersion relation of electrons in a Weyl semimetal is linear and asymmetric, with the left and right-handed electrons having different energies and dispersions. Interestingly, $(TaSe_4)_2I$ is a type-III Weyl semi-metal classified according to the geometry of the Fermi surface [368]. Fermi surface of $(TaSe_4)_2I$ consists of two electron or two hole pockets touching at the Weyl points (WPs) [368]. In this work, we present first-principles calculations of the electronic structure of $(TaSe_4)_2I$. Our theoretical results

show that $(TaSe_4)_2I$ is infact a Weyl semi-metal with a strongly anisotropic electronic structure for the non-CDW (undistorted) phase, corresponding to its quasi-1D geometry. We show through our calculations that Fermi surface nesting (FSN) is *not* the origin of CDW in $(TaSe_4)_2I$. It has a more complex origin involving momentum dependent electron-phonon coupling. We also demonstrate how CDW-linked strong electron-phonon coupling and associated anharmonic interactions of phonons result in low thermal conductivity in $(TaSe_4)_2I$.

9.2 Experimental observations

Our experimental collaborators (Paribesh Acharyya and Prof. Kanishka Biswas, Jawaharlal Nehru Centre For Advanced Scientific Research) have measured the lattice thermal conductivity (κ_l) along the layered direction as well as the perpendicular direction (Fig. 9.1(a)). In both the directions κ_l is very low due to combined effect of bonding heterogeneity (ionic and covalent) in $(TaSe_4)_2I$ and of charge density wave (electron-phonon coupling) which can strongly scatter the heat carrying acoustic phonons. The κ_l along the direction perpendicular to the layers (parallel to the SPS direction) is lower compared to the layered direction (Fig. 9.1(a)). At room temperature, measured κ_l is 0.5 W/mK which decreases with the temperature similar to typical crystalline material and become $\sim$ 0.4 W/mK at 423 K which is very close to the theoretical κ_{min} (0.3 W/mK). κ_l of $(TaSe_4)_2I$ is very low compared to the state-of-the-art low thermal conductive materials as shown in Fig. 9.1(b).

9.3 Computational details

Our first-principles calculations are based on density functional theory as implemented in Quantum ESPRESSO [137], and ultrasoft pseudopotentials to model interactions between

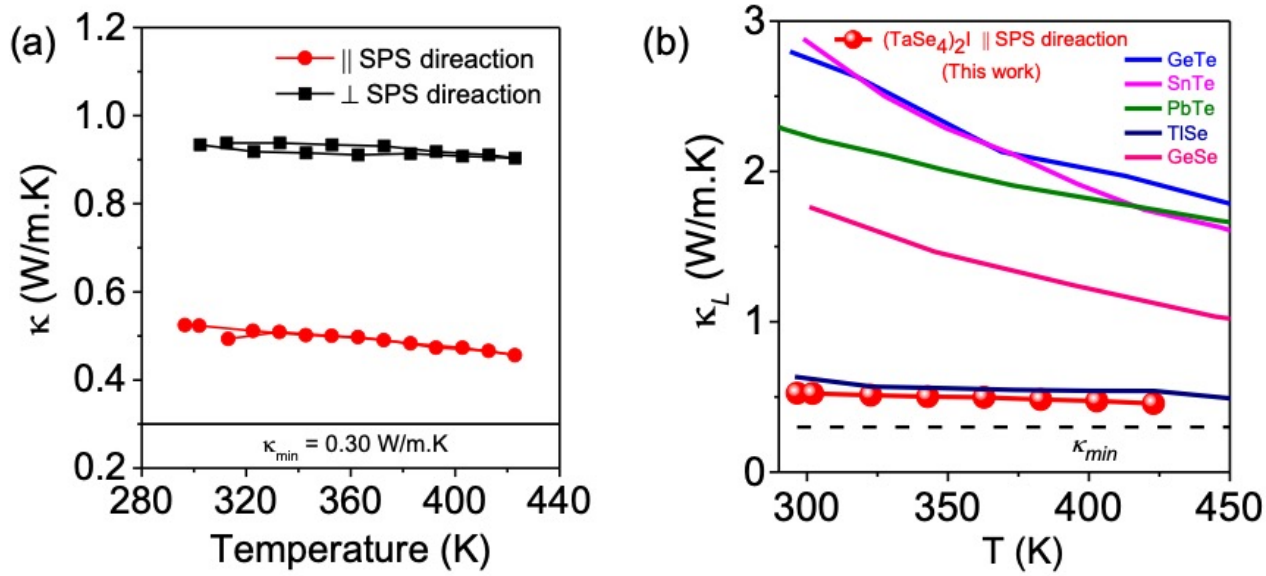

Figure 9.1: (a) Experimentally measured (by Dr. Paribesh Acharyya from Prof. Kanishka Biswas's lab at JNCASR)temperature dependent lattice thermal conductivity of $(TaSe_4)_2I$ measured parallel (||) and perpendicular ($\perp$) to the spark plasma sintering (SPS) directions. (b) Comparison of temperature-dependent thermal conductivity of $(TaSe_4)_2I$ polycrystal with well-known ultralow thermal conductivity materials.

electrons and ionic cores. We used a generalized-gradient approximation (GGA) [138] of the exchange-correlation energy with a functional parameterized by Perdew, Burke and Ernzerhof (PBE) [139]. We include van der Waals (vdW) interaction with the parametrization given in Grimme scheme [140]. We used an energy cutoff of 45 Ry to truncate the plane wave basis used in representing Kohn-Sham wave functions, and energy cutoff of 360 Ry for the basis set to represent charge density. We used a primitive unit cell of $(TaSe_4)_2I$ with 22 atoms as the periodic unit for our theoretical analysis. Brillouin Zone (BZ) integrations were sampled on a uniform 6×6×6 mesh of k-points. Electronic spectrum was determined at Bloch wave vectors along high symmetry lines ($\Gamma-Z-\Sigma-N-P-X$) in the BZ with and without inclusion of spin-orbit coupling (SOC) in our calculations. Lattice-dynamical properties were determined within the framework of self-consistent density functional perturbation theory (DFPT) as implemented within the QE code [137]. We corroborated these using a 2×2×2 supercell of $(TaSe_4)_2I$ in calcula-

tions with PHONOPY [351] and Vienna Ab-initio Simulation Package (VASP) [305,306]. We determined the mode Grüneisen parameters using finite difference method and phonon dispersion calculated at volumes, $0.98\times V_0$ and $1.02\times V_0$ (where V_0 is the equilibrium volume of the ground state structure), employing the formula $\gamma_{q\nu} = -\frac{dln\omega_{q\nu}}{dlnV}$, where $\gamma_{q\nu}$, V and $\omega_{q\nu}$ denote Grüneisen parameter, unit cell volume, and frequency of a phonon mode at wavevector q for branch ν, respectively. We analyzed bond-length distribution using the MAISE package [369].

9.4 Results and Discussion

$(TaSe_4)_2I$ crystallizes in a quasi-1D, body-centered tetragonal chiral structure with space group *I422* (D_4 point group). The conventional unit cell contains two $TaSe_4$ chains parallel to c-axis held together by weak vdW interaction and the iodine atoms are at interstitial sites located between the chains (Fig. 9.2(a)). In each $TaSe_4$ chain, Ta and Se atoms are arranged alternately with Se atoms forming a helical arrangement along c-axis. Volume of a primitive unit cell is half of the volume of conventional unit cell. Our optimized lattice parameters of the undistorted or non-CDW phase, a and c are 9.42 Å and 12.91 Å respectively, within 1% of the respective experimental values [363].

$(TaSe_4)_2I$ is a type-III Weyl semi-metal with strongly anisotropic electronic structure. Its electronic structure calculated ignoring the effects of spin-orbit coupling (SOC) shows dispersive bands along $\Gamma-Z$ (c-axis) and weak dispersion along $N-P$ (Fig. 9.2(d)), which is understandable from the structure of $TaSe_4$ chains along c-axis. It is interesting to note that there exists two sets of Weyl points, one along Γ to Z and the other along N to P directions in the Brillouin Zone. We next obtain electronic structure of $(TaSe_4)_2I$ including the effects of SOC through use of relativistic pseudopotentials, and find weak splitting of bands (Fig. 9.2(d)), consistent with an earlier report [370]. Visualization of iso-surface of

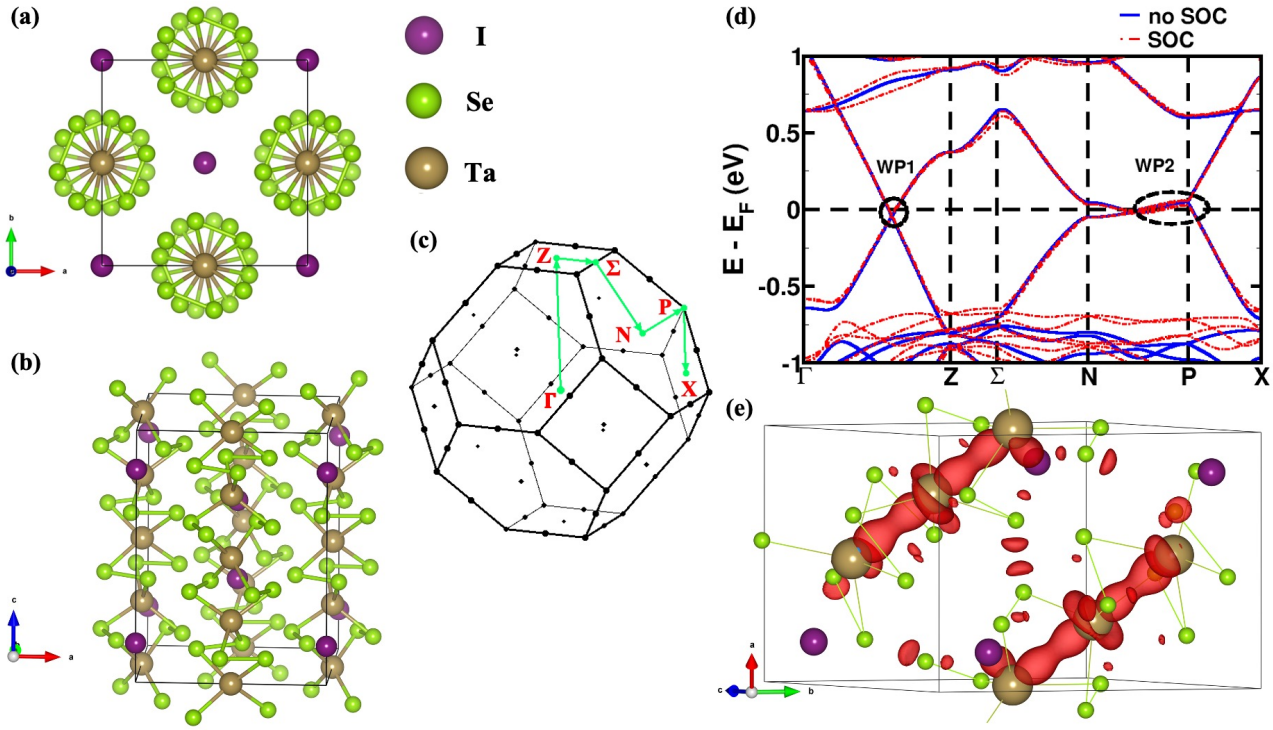

Figure 9.2: Crystal structure and the conventional unit cell of $(TaSe_4)_2I$ viewed along (a) c-axis (001) direction and (b) bc plane [(100) direction], containing two $TaSe_4$ chains aligned along c-axis, with the iodine atoms located between the chains. (c) Brillouin zone (BZ) of the primitive unit cell in $I422$ space group where the green lines mark the paths connecting the high symmetry points (in red) used in our calculations of electronic structure and phonon dispersion. (d) Electronic structure of $(TaSe_4)_2I$ calculated with (red) and without (black) inclusion of spin-orbit coupling (SOC), shows it is a Weyl semimetal with two sets of Weyl points. (e) Iso-surface of wavefunctions of states at the Weyl point along $\Gamma-Z$, revealing contributions of Ta-d_{z^2} orbitals and p-orbitals of Se.

wavefunctions of the states at the Weyl point along $\Gamma-Z$, clearly reveals the contributions of Ta-d_{z^2} orbitals and the Se-p orbitals (also seen in the atom-projected band structure) (Fig. 9.2(e) and Fig. 9.3(a)). Electron localization function analysis (ELF) is a measure of the degree of electron localization in a molecule or a solid with information about local influence of the Pauli repulsion. Our analysis of ELF in $(TaSe_4)_2I$ shows a lobe-shaped electron localization around I^- atoms which is due to hybridized $5s^2-5p^6$ lone-pair of I^- and another localized electron cloud on Se^{2-} which constitutes the partially hybridized $4s^2$ lone-pair of Se (Fig. 9.3(b)).

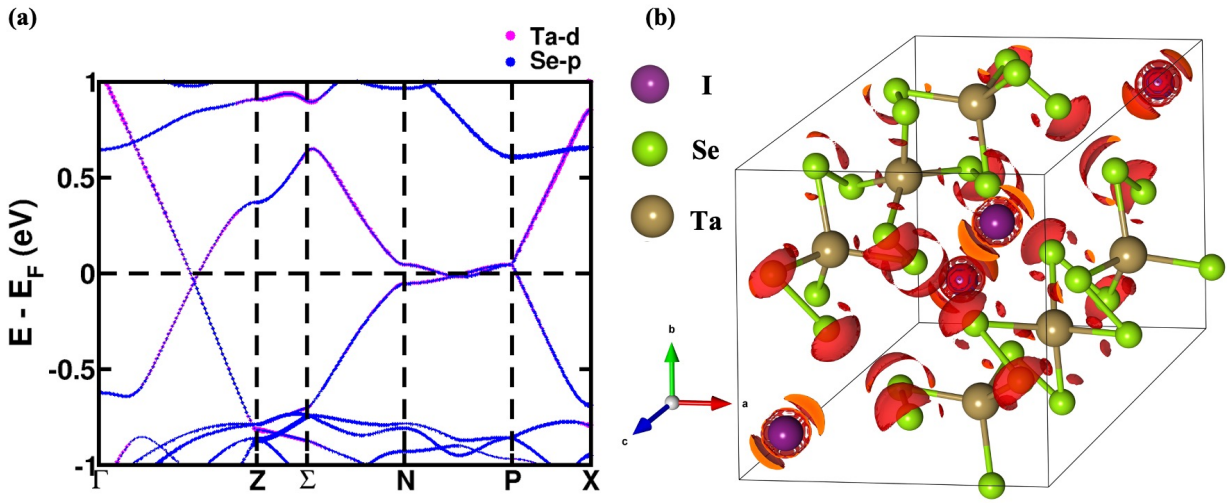

Figure 9.3: (a) Atom-resolved electronic structure calculated without spin-orbit interactions. (b) Iso-surface of electron localization function (value = 0.875), reveals hybridised $5s^2$-$5p^6$ lone-pair around I^- anion, whereas a lobe-shaped electron cloud around Se arises from the $4s^2$ lone-pair of Se.

Phonon dispersion of $(TaSe_4)_2I$ reveals weakly unstable modes with imaginary frequencies ($\omega^2 < 0$) at the Γ ($22i$ cm^{-1}), Σ ($13i$ cm^{-1}) and X ($9i$ cm^{-1}) points of the BZ (Fig. 9.4(a)). The instability at Γ is of an optical phonon mode involving displacements of Ta atoms (in $TaSe_4$ chains) along the chain direction (c-axis) (Fig. 9.4(c)) leading to tetramerization of Ta atoms, analogous to Peierls distortion in one-dimensional metal. Atom-projected phonon DOS (Fig. 9.4(b)) shows collective contributions of displacements of Ta, Se and I atoms to soft optical modes having $\omega < 50$ cm^{-1}. To trace the electronic origin of the lattice instability, we calculate Fermi surface (FS) of $(TaSe_4)_2I$, which is weakly nested along Z′ − Γ−Z by nesting wave vector, q_{CDW} (Fig. 9.5(a). This nesting vector connects the hole pockets resulting from crossing of the two bands below Fermi energy (along Γ to Z in the electronic structure) (Fig. 9.5(c). On a closer look, the FS also exhibits weak nesting in the $k_z = 2\pi/c$ plane (containing Z, Σ and X points of the BZ). However, the instability in phonon dispersion along Z′ − Γ−Z, Z−Σ−N directions and at X point is not along the nesting wavevector, q_{CDW} (Fig. 9.5(a) and Fig. 9.5(b)). If Fermi surface nesting (FSN) is the cause for CDW, as in Peierls picture, at least one of the phonon modes with

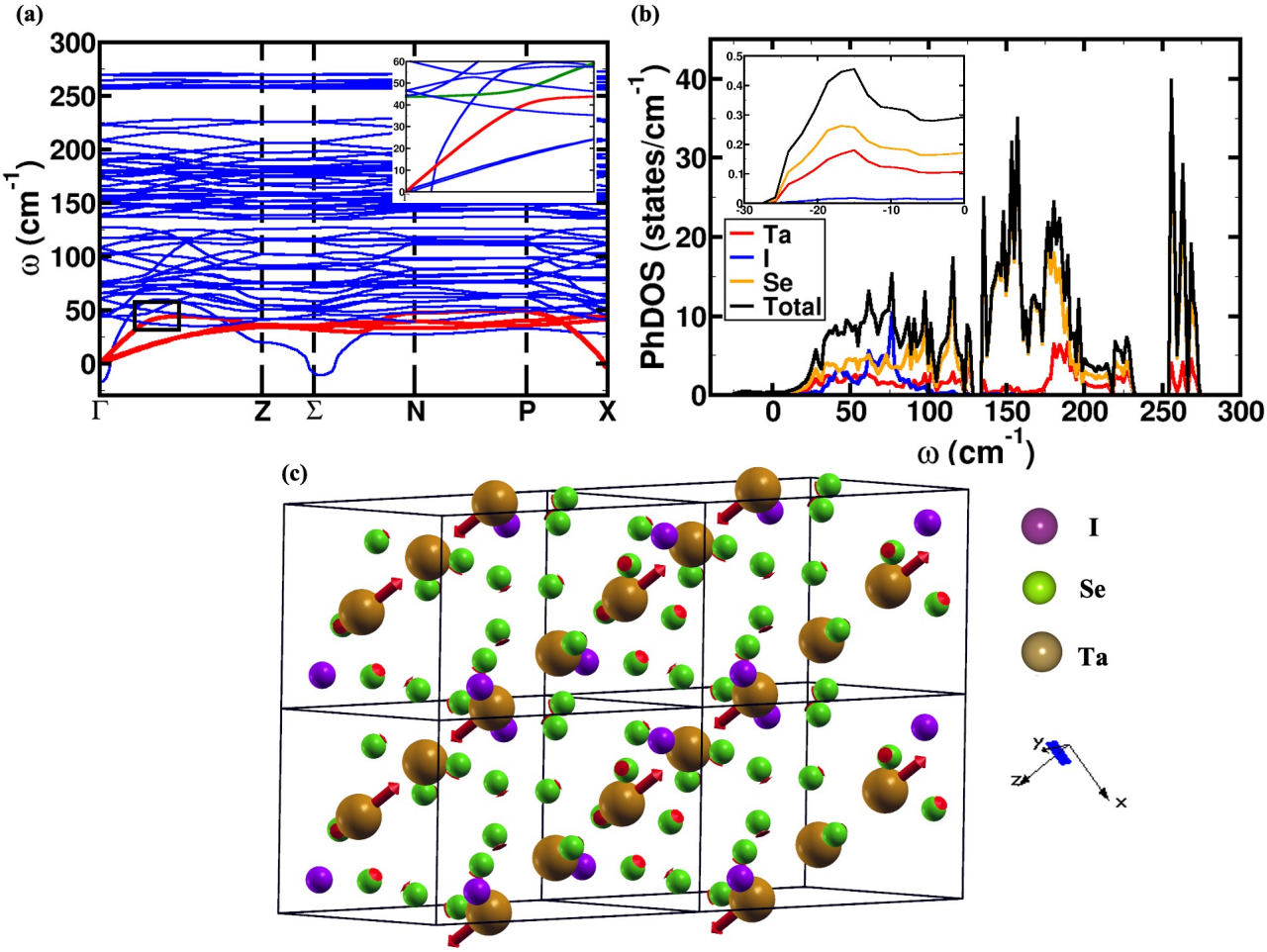

Figure 9.4: (a) Phonon dispersion of $(TaSe_4)_2I$ exhibiting unstable modes (modes with $\omega^2 < 0$) at the Γ ($22i$ cm^{-1}), Σ ($13i$ cm^{-1}) and X ($9i$ cm^{-1}) points of the BZ. Acoustic phonons have been shown in red. Large avoided-crossing is evident between phonon branches (region within the box), highlighted in green and red color zoomed in the inset. It is clear from total and atom projected phonon density of states (PhDOS) (b) that the dominant contribution to unstable and low-frequency optical modes (< 50 cm^{-1}) comes from displacements of Ta and Se atoms. (c) Visualization of eigen-displacements of unstable mode at Γ reveals displacements of Ta atoms along c-axis leading to Ta-tetramerization.

the wavevector q_{CDW} must soften or become imaginary, instead the instability is at Γ in $(TaSe_4)_2I$. So, FSN in $(TaSe_4)_2I$ is not quite related to CDW.

The non-CDW structure of $(TaSe_4)_2I$ is thus locally unstable, and structural distortion through atomic displacements in the strongest instability at Γ leads to lowering of symme-

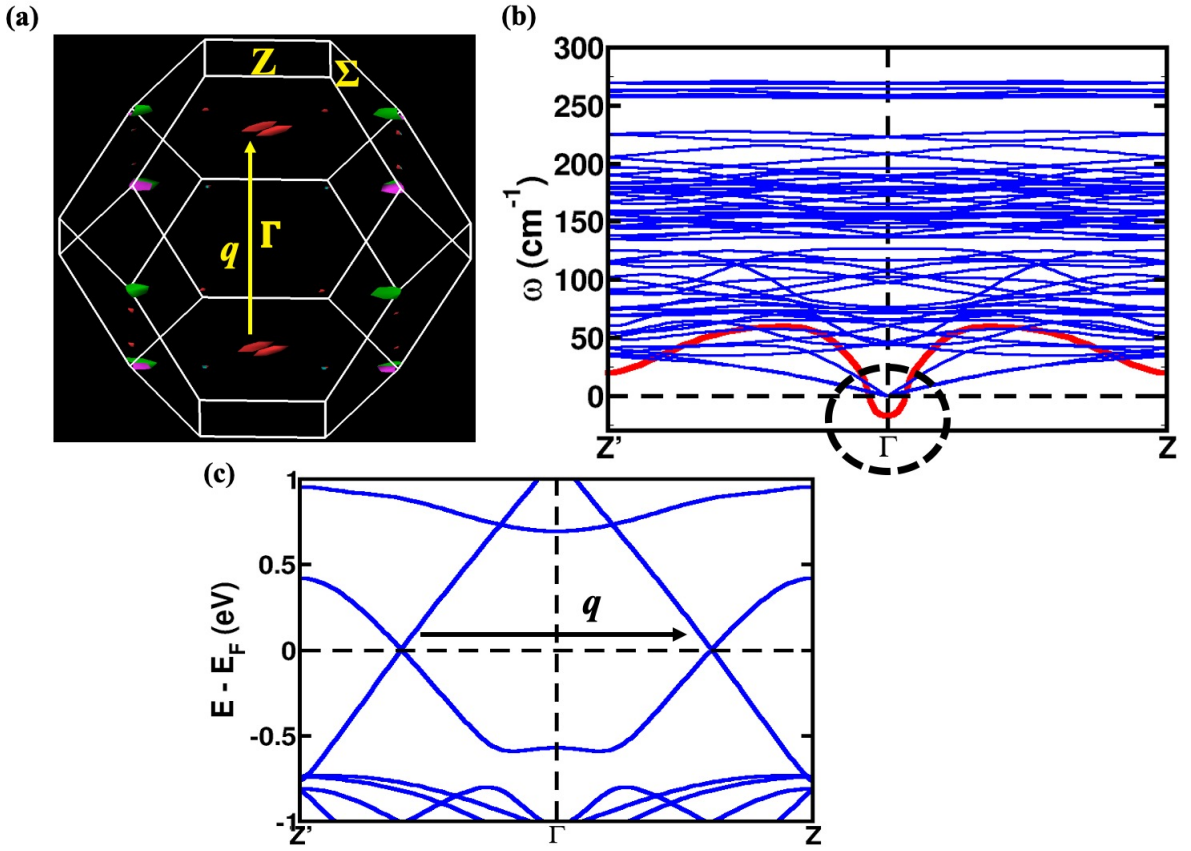

Figure 9.5: (a) Fermi surface of $(TaSe_4)_2I$ exhibits weak nesting by q along $Z' - \Gamma - Z$ direction. (b) Phonon dispersion along $Z' - \Gamma - Z$, revealing a negative phonon branch with frequency $22i$ cm^{-1} at Γ. The nesting vector q has been shown (c) in electronic structure. However, Fermi surface nesting is not the origin of CDW in $(TaSe_4)_2I$ since the instability in phonon dispersion is not located at q.

try and energy with changes in Ta-Ta bond lengths (Fig. 9.6(a)). Analysis of bond-length distribution of the distorted (CDW) phase using MAISE package revealed two Ta-Ta bond-lengths of 3.20 Å and 3.25 Å in the CDW phase compared to a nearest-neighbor Ta-Ta distance of 3.24 Å in non-CDW phase (Fig. 9.6(b)). The CDW phase has a space group of $F222$ (D_2 point group), and symmetry analysis shows that the distortion has the symmetry of a $B_1 + B_2$ representation. Structural distortion driven by unstable mode at Γ associated with CDW is accompanied by lifting of degeneracies of states at the fermi surface particularly at the nested parts and opening of band gap in the electronic structure, marking a metal to semiconductor transition. Our estimated band gap of CDW

phase is approximately 0.12 eV at the Y point of the BZ of distorted phase (Fig. 9.6(c)).

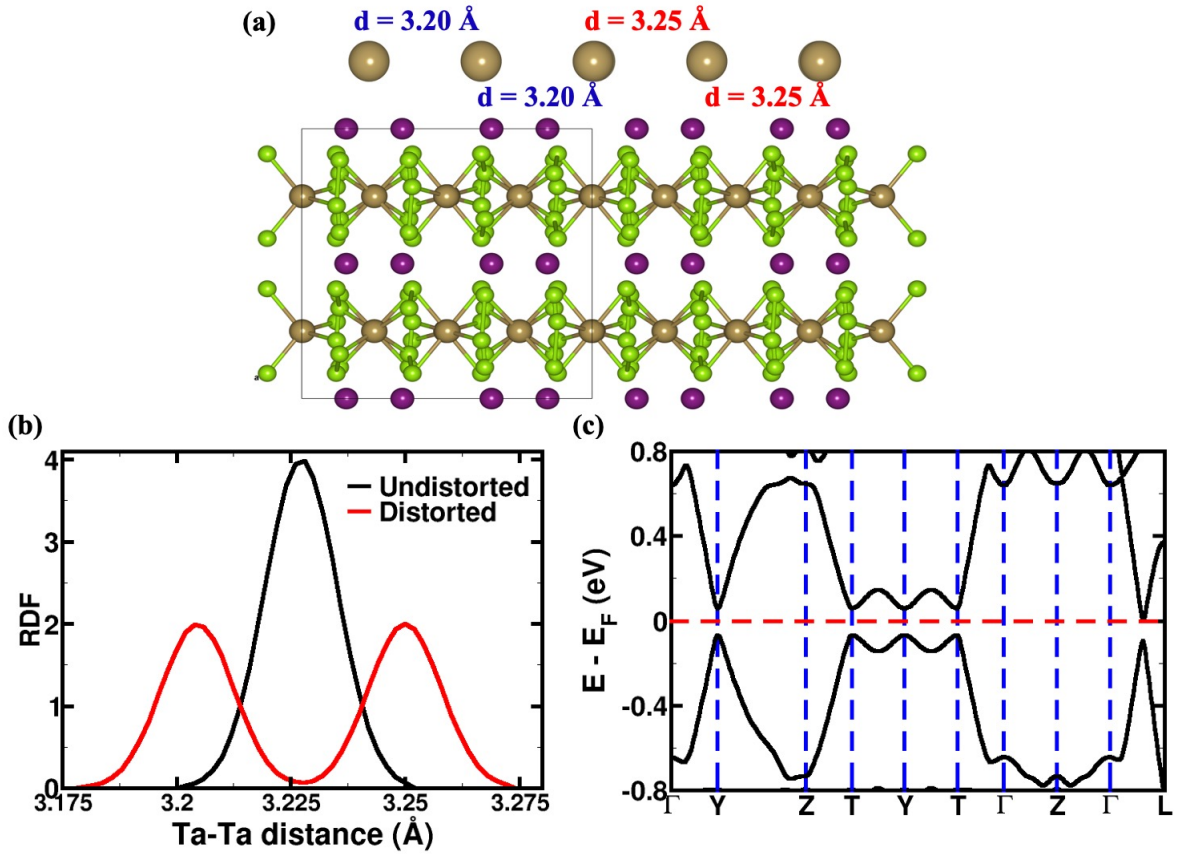

Figure 9.6: (a) Distorted structure (CDW phase) of $(TaSe_4)_2I$ with distinct Ta-Ta distances of 3.20 Å and 3.25 Å, contrary to equidistant arrangement Ta atoms along the chain in the parent structure. (b) The radial distribution function (RDF) showing nearest neighbor Ta-Ta distances of undistorted and distorted phase. (c) Calculated electronic structure of CDW phase of $(TaSe_4)_2I$ with space group $F222$, reveals a band gap (E_g) of 0.12 eV at the Y point of BZ.

In order to understand the origin of CDW, we next calculate electron-phonon coupling (EPC or λ) of a mode ν at momentum $\boldsymbol{q}$ (with frequency $\omega_{\boldsymbol{q}\nu}$) using [371]

$$\lambda_{\boldsymbol{q}\nu} = \frac{2}{\hbar\omega_{\boldsymbol{q}\nu}N(\epsilon_f)} \sum_k \sum_{mn} |g^{q\nu,\,ij}_{k+q,k}|^2 \times \delta(\epsilon_{\boldsymbol{k+q},i} - \epsilon_f) \times \delta(\epsilon_{\boldsymbol{k},j} - \epsilon_f), \tag{9.1}$$

where ω and $N(\epsilon_f)$ are the phonon frequency and electronic density of states at the Fermi

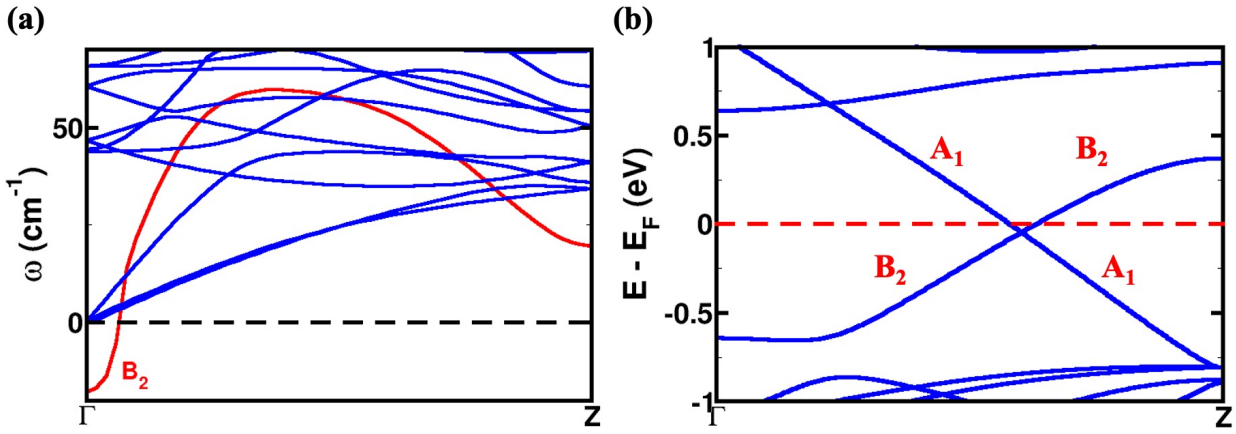

Figure 9.7: (a) The optical phonon branch (highlighted in red) with symmetry B_2 exhibits instability at Γ and is associated with CDW or Peierls-like instability in $(TaSe_4)_2I$. (b) The linearly dispersive bands at the Weyl point along Γ−Z has a symmetry of A_1 and B_2.

energy, respectively. The EPC matrix element is given by

$$g^{q\nu\,,\,ij}_{k+q,k} = (\frac{\hbar}{2M\omega_{q\nu}})^{\frac{1}{2}} < \psi_{k+q,i}|\Delta V_{q\nu}|\psi_{k,j} >, \tag{9.2}$$

where $\psi_{k,j}$ is the electronic wave function with wave vector $\boldsymbol{k}$ and energy eigenvalue $\epsilon_{k,j}$ for band j, and M is the ionic mass. $\Delta V_{q\nu}$ is the change in the self-consistent potential associated with a phonon of wavevector q, branch ν and frequency $\omega_{q\nu}$. Our estimate of λ of the unstable mode at Γ associated with CDW instability (symmetry B_2) is 4.27, as shown in Fig. 9.7(a), in contrast to EPC of $\lambda = 0.07$ for other phonon modes at Γ. We also use symmetry analysis to show that electronic states of linearly dispersed bands at Weyl point along Γ−Z (WP1) (symmetries A_1 and B_2) have a non-zero matrix element (EPC coupling matrix given by Eq. 9.2) for the perturbation of B_2 mode, giving rise to a large electron-phonon coupling in $(TaSe_4)_2I$. We thus conclude that intrinsic mechanism of electronic and lattice instabilities (CDW) in $(TaSe_4)_2I$ is dictated by strong electron-phonon coupling at the Weyl points along Γ−Z.

We now investigate the origin of low lattice thermal conductivity (κ_l) of 0.51 W/mK at

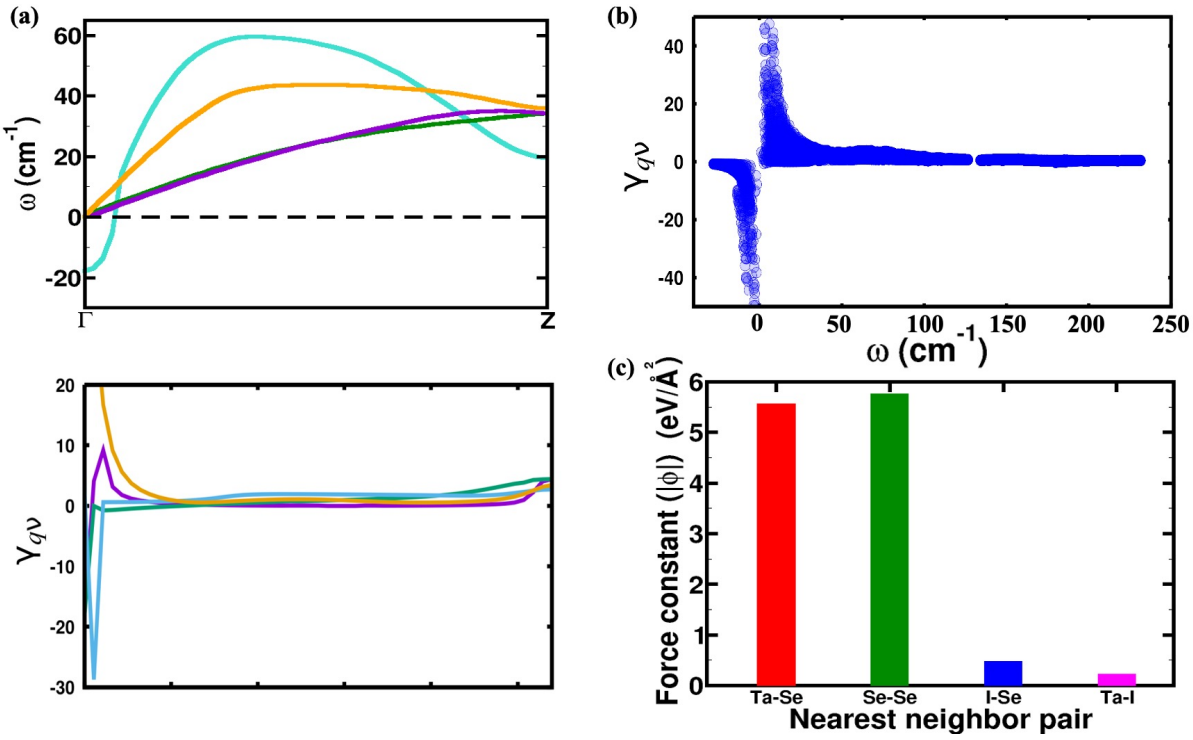

Figure 9.8: Calculated mode Grüneisen parameters ($\gamma_{q\nu}$) of the (a) four lowest frequency phonon branches along Γ−Z direction and (b) all modes at q-points on a uniform mesh in the Brillouin zone. Very high $\gamma_{q\nu}$ exhibited by the optical phonon branch exhibiting instability at Γ (highlighted in cyan) and bonding inhomogeneity in (c) interatomic force constants (IFCs) play a synergistic role in reducing κ_l.

300 K and its further reduction to 0.46 W/mK at 420 K in $(TaSe_4)_2I$. κ_l is related to heat capacity at constant volume, C_v, through the relation $\kappa_l = 1/3C_v v l$, where v is the phonon group velocity and l are the phonon mean-free path [372]. The cut-off frequencies of acoustic phonons of $(TaSe_4)_2I$ are low (< 45 cm^{-1}), suggesting rather low sound velocities, contributing to low thermal conductivity (κ_l) of $(TaSe_4)_2I$. Our estimates of average sound velocities calculated from the slopes of linearly dispersed acoustic phonon branches (near Γ) are 1425 m/s and 1279 m/s along the along chain (c-axis) and layer directions respectively, consistent with experimental finding that κ_l is lower along the $SPS_{||}$ direction. A large difference in bond strengths is reflected in our calculated interatomic force constants (IFCs). IFCs of nearest Ta-Se and Se-Se neighbours have the highest values of 5.56 and 5.78 eV/Å^2, respectively, indicating them to be the stiffest bonds. On the

other hand, very small values of IFCs for the nearest neighbour I-Se (0.48 eV/Å^2) and I-Ta (0.22 eV/Å^2) atomic pairs imply relatively weak interatomic bonding of I atoms in the lattice (Fig. 9.8(c)). This bonding heterogeneity possibly contributes to low κ_l in $(TaSe_4)_2I$ [373]. Large avoided-crossing seen in the phonon spectrum (inset of Fig. 9.4(a)) is indicative of strong optic-acoustic phonon coupling, that causes scattering of heat carrying acoustic modes by the low frequency optical modes, resulting in low κ_l. It is known that lattice anharmonicity is responsible for low thermal conductivity of a solid [372]. To quantitatively assess the strength of lattice anharmonicity, we estimate mode Grüneisen parameters ($\gamma_{q\nu}$ is the third order interaction between typical optic phonons and strain), from changes of phonon frequencies with strain. Anomalously high values of $|\gamma_{q\nu}| \sim 40$ of the modes crowded in the low frequency region (< 50 cm-1) (Fig. 9.8(b)) and reasonably high $|\gamma_{q\nu}| \sim 30$ of the optical mode associated with CDW instability around the Γ point (Fig. 9.8(a)) indicates strong coupling between acoustic and low-frequency optical modes. In the high temperature regime where the Umklapp phonon scattering is dominant, κ_l decays as $\gamma_{q\nu}^2$. Therefore, such a high value of $\gamma_{q\nu}$ indeed is a characteristic of strong anharmonicity and phonon-phonon scattering, further reducing κ_l.

9.5 Conclusion

In conclusion, we used first-principles calculations based on density functional theory to show that $(TaSe_4)_2I$ is Weyl semi-metal with a weakly nested Fermi surface. Strong electron-phonon coupling of electronic states that are weakly nested by q_{CDW} drives CDW in $(TaSe_4)_2I$. The EPC-driven CDW is accompanied by a structural rearrangement of Ta atoms (CDW phase) leading to opening of a gap in the electronic structure. We establish that (a) bonding inhomogeneity, (b) large optical-acoustic coupling (avoided-crossing), (c) low sound velocities, and (d) strong lattice anharmonicity (in terms of exceptionally high mode Grüneisen parameters of CDW-related phonons) synergistically result in low

κ_l in $(TaSe_4)_2I$.

Chapter 10

Summary

The central theme of this dissertation is to elucidate the role of external fields (twist, electric field, pressure and CDW) in modifications of physical properties of layered materials and 2D heterostructures. These materials, of both technological and fundamental importance, have provided a novel breakthrough for numerous applications in electronic industry that can benefit the society. Additionally, stacking 2D materials on top of each other also gives rise to van der Waals heterostructures with new functionalities which is otherwise absent in the pristine structure. We have employed first-principles density functional theoretical calculations and modeling in our analysis to demonstrate how external fields can be used to alter electronic, structural and vibrational properties of materials.

Due to weak vdW interactions between the layers, 2D layered materials can be stacked on top of each other with a relative twist between the successive layers. The interlayer twist destroys the allignment and breaks translational symmetry which dramatically alters the electronic properties of 2D materials and their heterostructures by modulating the crystal

symmetry. Our first-principles calculations provide an understanding of a chemical route to generation of interlayer twist through cross-linking by organic molecules like L_1 = trans-1,4-diaminocyclohexane, L_2 = 1-5-diaminonaphthalene and L_3 = oxalic acid, in graphene (G) and h-BN bilayer. The theoretical twist angles in G-L_1-G, G-L_2-G and h-BN-L_3-h-BN are 17.98^o, 9.43^o and 13.78^o, respectively. We show that in contrast to the electronic structure of monolayer graphene exhibiting Dirac cones at the K-point, the graphene complex exhibits energy bands with a gap at the K-point. Electronic structure of h-BN complex shows a much smaller band gap of 0.3 eV compared to pristine h-BN monolayer band gap of 6.08 eV. Another interesting thing to note in the electronic structure is the presence of nearly flat bands at Fermi energy (E_F).

Our experimental collaborators find hysteresis in longitudinal voltage (V^{ω}_{xx}) in twisted double bilayer graphene (TDBG) with a small twist angle $\sim 1.1^o$ encapsulated between h-BN as a function of charge density (n) (or filling factor, ν) using a dual gate geometry. We have used a combination of modeling and first-principles density functional theoretical calculations to analyze the response of TDBG to gating electric field. With broken inversion symmetry, TDBG is expected to exhibit spontaneous electric polarization that can couple with electric field perpendicular to its planar structure. We note that the encapsulating h-BN sheets do impact properties of TDBG and have not been included in any analysis so far. We have determined the effects of gate electrodes and consequent doping in TDBG on its polarization with suitable electrostatic boundary conditions in our first-principles calculations, using TDBG with a twist angle $\sim 21.8^o$ as a model system, noting that it too has a broken inversion symmetry. We clearly establish inhomogeneous doping across the layers due to differences in the top and bottom gate electrodes, which is also expected in TDBG with magic angle of twisting. Such inhomogeneity is relevant to distinctive coupling of the TDBG sheets (at all angles) with perpendicular electric field and is relevant in understanding hysteresis in V^{ω}_{xx}.

We have presented the vibrational properties of bilayer *2H*-$MoTe_2$, demonstrating the effect of hole doping on the renormalization of Raman modes. We show that *2H*-$MoTe_2$ is an indirect band gap semiconductor with the valence band maxima (VBM) at the K-point and conduction band minima (CBM) at $Q^{'}$ point (along Γ to M direction). The importance of spin-orbit coupling in accurate description of its electronic structure particularly near the E_F is highlighted in this work. We demonstrated that while hole doping in bilayer *2H*-MoTe2 results in significant softening of Raman-active E_{2g} and B_{2g} phonons, A_{1g} mode shows relatively small softening. Interestingly, this behaviour is in sharp contrast to the trends obtained in electron doped monolayer MoS_2 where the A_{1g} mode shows softening, whereas E^1_{2g} mode remains essentially inert. From first-principles theoretical calculations and group theory analysis, we show that the contrast between behaviour of MoS_2 and $MoTe_2$ arises from the difference in symmetry of their frontier states relevant to electron and hole doping. Understanding of electron–phonon coupling (EPC) in two-dimensional (2D) materials manifesting as phonon renormalization is essential to their possible applications in nanoelectronics.

Electrostriction is a second-order electromechanical response of a material involving strain/stress induced quadratically by an electric field/polarization field. In this work, we determine electrostrictive response of *1T* and *2H* polymorphs of TMS_2 (TM = Mo and Hf) from calculations of changes in dielectric susceptibilty, χ, arising in response to applied stress. We uncover dependence of electronic and phononic contributions to electrostrictive coefficients of TMS_2 on the structure, chemical composition and the number of layers in their 2D forms. We find that composition has a singular impact on the electronic part of electrostriction: M^{elec} is positive for MoS_2 and is negative for HfS_2. While electrostrictive response of transition metal dichalcogenides (TMDs) in the *2H* form is dominated by electronic contribution, it is largely phononic in the *1T* form. Lastly, we demonstrate that the phononic part, M^{ionic}, shows weak sensitivity to reduction in dimensionality, whereas

M^{elec} decreases with decrease in the number of layers (as the band gap increases) in the stable polymorphs of TMS_2. We analyze contributions of IR-active modes in terms of their mode effective charges and oscillator strengths to understand the contrast between the phononic contributions to electrostriction of *2H*-MoS_2 and *1T*-HfS_2.

We have analyzed pressure-induced structural phase transitions in VSe_2, highlighting the structural, electronic and vibrational properties of various polytypes of VSe_2. Our first-principles calculations reveal anomalies in c/a ratio, signaling isostructural transition in *1T* phase (ground state of VSe_2). Interestingly, we show a first-order structural transition from *1T* (space group $P\bar{3}m1$) to *3R* (space group $R\bar{3}m$) phase at $P \sim 9$ GPa through sliding of Se-V-Se layers in our spin-polarized calculations based on Hubbard parameter correction GGA + U, ($E_{eff} = U - J = 8$ eV). We also establish through our work that results for relative stability of various phases of VSe_2 are quite sensitive to k-point sampling, magnetic order and Hubbard parameter (U) used in calculations.

Our work on $GdTe_3$ and $(TaSe_4)_2I$, highlights strong coupling between electronic and structural degrees of freedom. We investigate the mechanism of CDW formation in both the compounds. In $GdTe_3$, strong nesting in the Fermi surface leads to instability (longitudinal acoustic mode which is a characterestics of Peierls distortion in 1D) and Kohn anomaly in the phonon dispersion and hence, the origin of CDW. Further, we demonstrate that momentum-dependent electron-phonon coupling (mostly due to optical modes rather than longitudinal acoustic modes) drives CDW instability in $(TaSe_4)_2I$. We also find significant lattice anharmonicity, as revealed by the high values of Grüneisen parameters, in these compounds and uncover other factors that are responsible in the reduction of lattice thermal conductivity.

Finally, we present a thematic summary of the thesis that brings out the commonality

and the central theme of the topics covered in this dissertation (see Fig. 10.1). We have highlighted how the effect of twist, electric field, pressure and CDW on the coupled degrees of freedom gives rise to exotic and fascinating properties in layered materials and 2D heterostructures.

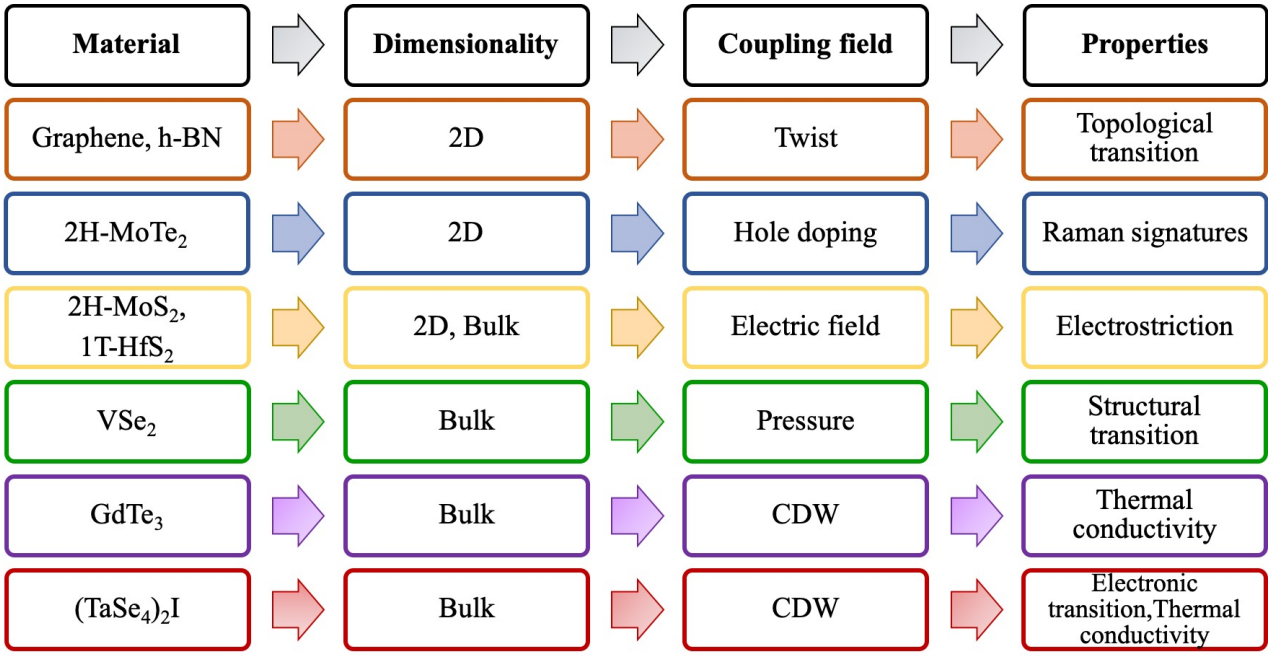

Figure 10.1: Schematic summarizing our work presented in the thesis.

References

[1] Guillaume Froehlicher, Etienne Lorchat, François Fernique, Chaitanya Joshi, Alejandro Molina-Sánchez, Ludger Wirtz, and Stéphane Berciaud. Unified description of the optical phonon modes in n-layer mote2. *Nano Letters*, 15(10):6481–6489, 2015.

[2] Olexandr Isayev, Corey Oses, Cormac Toher, Eric Gossett, Stefano Curtarolo, and Alexander Tropsha. Universal fragment descriptors for predicting properties of inorganic crystals. *Nature Communications*, 8(1), jun 2017.

[3] Steven G Louie, Yang-Hao Chan, Felipe H da Jornada, Zhenglu Li, and Diana Y Qiu. Discovering and understanding materials through computation. *Nature materials*, 20(6):728—735, June 2021.

[4] Richard M Martin. *Electronic structure: basic theory and practical methods*. Cambridge university press, 2020.

[5] P. Hohenberg and W. Kohn. Inhomogeneous electron gas. *Phys. Rev.*, 136:B864–B871, Nov 1964.

[6] Nicola Marzari, Andrea Ferretti, and Chris Wolverton. Electronic-structure methods for materials design. *Nature materials*, 20(6):736—749, June 2021.

[7] Richard Van Noorden, Brendan Maher, and Regina Nuzzo. The top 100 papers. *Nature News*, 514(7524):550, 2014.

[8] Maarten de Jong, Wei Chen, Thomas Angsten, Anubhav Jain, Randy Notestine, Anthony Gamst, Marcel Sluiter, Chaitanya Krishna Ande, Sybrand van der Zwaag, Jose J. Plata, Cormac Toher, Stefano Curtarolo, Gerbrand Ceder, Kristin A. Persson, and Mark Asta. Charting the complete elastic properties of inorganic crystalline compounds. *Scientific Data*, 2(1), 3 2015.

[9] Nicola Marzari. The frontiers and the challenges. *Nature materials*, 15(4):381–382, 2016.

[10] Paul Adrien Maurice Dirac. Quantum mechanics of many-electron systems. *Proceedings of the Royal Society of London. Series A, Containing Papers of a Mathematical and Physical Character*, 123(792):714–733, 1929.

[11] Anubhav Jain, Yongwoo Shin, and Kristin A Persson. Computational predictions of energy materials using density functional theory. *Nature Reviews Materials*, 1(1):1–13, 2016.

[12] Scott M Woodley and Richard Catlow. Crystal structure prediction from first principles. *Nature materials*, 7(12):937–946, 2008.

[13] Pierre Hohenberg and Walter Kohn. Inhomogeneous electron gas. *Physical review*, 136(3B):B864, 1964.

[14] W Kohn and LJ Sham. Self-consistent equations including exchange and correlation effects physical review. 140. *A1133*, 1965.

[15] Stefano Curtarolo, Gus LW Hart, Marco Buongiorno Nardelli, Natalio Mingo, Stefano Sanvito, and Ohad Levy. The high-throughput highway to computational materials design. *Nature materials*, 12(3):191–201, 2013.

[16] Pulickel Ajayan, Philip Kim, and Kaustav Banerjee. van der waals materials. *Phys. Today*, 69(9):38, 2016.

[17] Manish Chhowalla, Hyeon Suk Shin, Goki Eda, Lain-Jong Li, Kian Ping Loh, and Hua Zhang. The chemistry of two-dimensional layered transition metal dichalcogenide nanosheets. *Nature chemistry*, 5(4):263–275, 2013.

[18] Andre K Geim and Irina V Grigorieva. Van der waals heterostructures. *Nature*, 499(7459):419–425, 2013.

[19] Andre Konstantin Geim. Graphene: status and prospects. *science*, 324(5934):1530–1534, 2009.

[20] SUPARNA DUTTASINHA and Kostya S. Novoselov. The rise of graphene. *Nature materials*, 6 3:183–91, 2007.

[21] In Edwin Abbott's. Graphene: exploring carbon flatland. *Phys. Today*, 60(8):35, 2007.

[22] Frank Schwierz. Graphene transistors. *Nature nanotechnology*, 5(7):487–496, 2010.

[23] FHL Koppens, T Mueller, Ph Avouris, AC Ferrari, MS Vitiello, and M Polini. Photodetectors based on graphene, other two-dimensional materials and hybrid systems. *Nature nanotechnology*, 9(10):780–793, 2014.

[24] Kin Fai Mak and Jie Shan. Photonics and optoelectronics of 2d semiconductor transition metal dichalcogenides. *Nature Photonics*, 10(4):216–226, 2016.

[25] Xiaodong Xu, Wang Yao, Di Xiao, and Tony F Heinz. Spin and pseudospins in layered transition metal dichalcogenides. *Nature Physics*, 10(5):343–350, 2014.

[26] Kostya S Novoselov, D Jiang, F Schedin, TJ Booth, VV Khotkevich, SV Morozov, and Andre K Geim. Two-dimensional atomic crystals. *Proceedings of the National Academy of Sciences*, 102(30):10451–10453, 2005.

[27] KS Novoselov, o A Mishchenko, o A Carvalho, and AH Castro Neto. 2d materials and van der waals heterostructures. *Science*, 353(6298):aac9439, 2016.

[28] Qing Hua Wang, Kourosh Kalantar-Zadeh, Andras Kis, Jonathan N Coleman, and Michael S Strano. Electronics and optoelectronics of two-dimensional transition metal dichalcogenides. *Nature nanotechnology*, 7(11):699–712, 2012.

[29] Agnieszka Kuc, Nourdine Zibouche, and Thomas Heine. Influence of quantum confinement on the electronic structure of the transition metal sulfide t s 2. *Physical Review B*, 83(24):245213, 2011.

[30] Sajedeh Manzeli, Adrien Allain, Amirhossein Ghadimi, and Andras Kis. Piezoresistivity and strain-induced band gap tuning in atomically thin mos2. *Nano letters*, 15(8):5330–5335, 2015.

[31] Zongyou Yin, Hai Li, Hong Li, Lin Jiang, Yumeng Shi, Yinghui Sun, Gang Lu, Qing Zhang, Xiaodong Chen, and Hua Zhang. Single-layer mos2 phototransistors. *ACS nano*, 6(1):74–80, 2012.

[32] Branimir Radisavljevic, Aleksandra Radenovic, Jacopo Brivio, Valentina Giacometti, and Andras Kis. Single-layer mos2 transistors. *Nature nanotechnology*, 6(3):147–150, 2011.

[33] Wanxiang Feng, Yugui Yao, Wenguang Zhu, Jinjian Zhou, Wang Yao, and Di Xiao. Intrinsic spin hall effect in monolayers of group-vi dichalcogenides: A first-principles study. *Physical Review B*, 86(16):165108, 2012.

[34] Alessandro David, Péter Rakyta, Andor Kormányos, and Guido Burkard. Induced spin-orbit coupling in twisted graphene–transition metal dichalcogenide heterobilayers: Twistronics meets spintronics. *Physical Review B*, 100(8):085412, 2019.

[35] Juan F Sierra, Jaroslav Fabian, Roland K Kawakami, Stephan Roche, and Sergio O Valenzuela. Van der waals heterostructures for spintronics and opto-spintronics. *Nature Nanotechnology*, 16(8):856–868, 2021.

[36] Hong-Xin Yang, A Hallal, D Terrade, Xavier Waintal, Stephan Roche, and Mairbek Chshiev. Proximity effects induced in graphene by magnetic insulators: first-principles calculations on spin filtering and exchange-splitting gaps. *Physical review letters*, 110(4):046603, 2013.

[37] RC Myers, AC Gossard, and DD Awschalom. Tunable spin polarization in iii-v quantum wells with a ferromagnetic barrier. *Physical Review B*, 69(16):161305, 2004.

[38] Kyle L Seyler, Pasqual Rivera, Hongyi Yu, Nathan P Wilson, Essance L Ray, David G Mandrus, Jiaqiang Yan, Wang Yao, and Xiaodong Xu. Signatures of moiré-trapped valley excitons in mose2/wse2 heterobilayers. *Nature*, 567(7746):66–70, 2019.

[39] Kha Tran, Galan Moody, Fengcheng Wu, Xiaobo Lu, Junho Choi, Kyounghwan Kim, Amritesh Rai, Daniel A Sanchez, Jiamin Quan, Akshay Singh, et al. Evidence for moiré excitons in van der waals heterostructures. *Nature*, 567(7746):71–75, 2019.

[40] Ding Zhong, Kyle L Seyler, Xiayu Linpeng, Ran Cheng, Nikhil Sivadas, Bevin Huang, Emma Schmidgall, Takashi Taniguchi, Kenji Watanabe, Michael A McGuire, et al. Van der waals engineering of ferromagnetic semiconductor heterostructures for spin and valleytronics. *Science advances*, 3(5):e1603113, 2017.

[41] Rebeca Ribeiro-Palau, Changjian Zhang, Kenji Watanabe, Takashi Taniguchi, James Hone, and Cory R Dean. Twistable electronics with dynamically rotatable heterostructures. *Science*, 361(6403):690–693, 2018.

[42] Tao Jiang, Hengrui Liu, Di Huang, Shuai Zhang, Yingguo Li, Xingao Gong, Yuen-Ron Shen, Wei-Tao Liu, and Shiwei Wu. Valley and band structure engineering of folded mos2 bilayers. *Nature nanotechnology*, 9(10):825–829, 2014.

[43] Wei-Ting Hsu, Zi-Ang Zhao, Lain-Jong Li, Chang-Hsiao Chen, Ming-Hui Chiu, Pi-Shan Chang, Yi-Chia Chou, and Wen-Hao Chang. Second harmonic generation from artificially stacked transition metal dichalcogenide twisted bilayers. *ACS nano*, 8(3):2951–2958, 2014.

[44] Zhiren Zheng, Qiong Ma, Zhen Bi, Sergio de La Barrera, Ming-Hao Liu, Nannan Mao, Yang Zhang, Natasha Kiper, Kenji Watanabe, Takashi Taniguchi, et al. Unconventional ferroelectricity in moiré heterostructures. *Nature*, 588(7836):71–76, 2020.

[45] Y Cao, JY Luo, V Fatemi, S Fang, JD Sanchez-Yamagishi, K Watanabe, T Taniguchi, E Kaxiras, and Pablo Jarillo-Herrero. Superlattice-induced insulating states and valley-protected orbits in twisted bilayer graphene. *Physical review letters*, 117(11):116804, 2016.

[46] Fuyi Yang, Wenshen Song, Fanhao Meng, Fuchuan Luo, Shuai Lou, Shuren Lin, Zilun Gong, Jinhua Cao, Edward S Barnard, Emory Chan, et al. Tunable second harmonic generation in twisted bilayer graphene. *Matter*, 3(4):1361–1376, 2020.

[47] Kenji Yasuda, Xirui Wang, Kenji Watanabe, Takashi Taniguchi, and Pablo Jarillo-Herrero. Stacking-engineered ferroelectricity in bilayer boron nitride. *Science*, 372(6549):1458–1462, 2021.

[48] R Suzuki, M Sakano, YJ Zhang, R Akashi, D Morikawa, A Harasawa, K Yaji, K Kuroda, K Miyamoto, T Okuda, et al. Valley-dependent spin polarization in bulk mos2 with broken inversion symmetry. *Nature nanotechnology*, 9(8):611–617, 2014.

[49] Giovanni Scuri, Trond I Andersen, You Zhou, Dominik S Wild, Jiho Sung, Ryan J Gelly, Damien Bérubé, Hoseok Heo, Linbo Shao, Andrew Y Joe, et al. Electrically tunable valley dynamics in twisted wse 2/wse 2 bilayers. *Physical Review Letters*, 124(21):217403, 2020.

[50] Kyounghwan Kim, Matthew Yankowitz, Babak Fallahazad, Sangwoo Kang, Hema CP Movva, Shengqiang Huang, Stefano Larentis, Chris M Corbet, Takashi Taniguchi, Kenji Watanabe, et al. van der waals heterostructures with high accuracy rotational alignment. *Nano letters*, 16(3):1989–1995, 2016.

[51] Kyounghwan Kim, Ashley DaSilva, Shengqiang Huang, Babak Fallahazad, Stefano Larentis, Takashi Taniguchi, Kenji Watanabe, Brian J LeRoy, Allan H MacDonald, and Emanuel Tutuc. Tunable moiré bands and strong correlations in small-twist-angle bilayer graphene. *Proceedings of the National Academy of Sciences*, 114(13):3364–3369, 2017.

[52] Nathan R Finney, Matthew Yankowitz, Lithurshanaa Muraleetharan, K Watanabe, T Taniguchi, Cory R Dean, and James Hone. Tunable crystal symmetry in graphene–boron nitride heterostructures with coexisting moiré superlattices. *Nature nanotechnology*, 14(11):1029–1034, 2019.

[53] Matthew Yankowitz, Qiong Ma, Pablo Jarillo-Herrero, and Brian J LeRoy. van der waals heterostructures combining graphene and hexagonal boron nitride. *Nature Reviews Physics*, 1(2):112–125, 2019.

[54] Kazuyuki Uchida, Shinnosuke Furuya, Jun-Ichi Iwata, and Atsushi Oshiyama. Atomic corrugation and electron localization due to moiré patterns in twisted bilayer graphenes. *Physical Review B*, 90(15):155451, 2014.

[55] Pilkyung Moon and Mikito Koshino. Energy spectrum and quantum hall effect in twisted bilayer graphene. *Physical Review B*, 85(19):195458, 2012.

[56] Lede Xian, ZF Wang, and Mei-Yin Chou. Coupled dirac fermions and neutrino-like oscillations in twisted bilayer graphene. *Nano letters*, 13(11):5159–5164, 2013.

[57] G Gruner. Density waves in solids addison-wesley pub, 1994.

[58] Rudolf Peierls and Rudolf Ernst Peierls. *Quantum theory of solids*. Oxford University Press, 1955.

[59] W Kohn. Image of the fermi surface in the vibration spectrum of a metal. *Physical Review Letters*, 2(9):393, 1959.

[60] MD Johannes and II Mazin. Fermi surface nesting and the origin of charge density waves in metals. *Physical Review B*, 77(16):165135, 2008.

[61] B Renker, H Rietschel, L Pintschovius, W Gläser, P Brüesch, D Kuse, and MJ Rice. Observation of giant kohn anomaly in the one-dimensional conductor k 2 pt (cn) 4 br 0.3· 3 h 2 o. *Physical Review Letters*, 30(22):1144, 1973.

[62] JP Pouget, B Hennion, C Escribe-Filippini, and M Sato. Neutron-scattering investigations of the kohn anomaly and of the phase and amplitude charge-density-wave excitations of the blue bronze k 0.3 moo 3. *Physical Review B*, 43(10):8421, 1991.

[63] JA Wilson, FJ Di Salvo, and S Mahajan. Charge-density waves in metallic, layered, transition-metal dichalcogenides. *Physical review letters*, 32(16):882, 1974.

[64] Jl A Wilson, FJ Di Salvo, and S Mahajan. Charge-density waves and superlattices in the metallic layered transition metal dichalcogenides. *Advances in Physics*, 24(2):117–201, 1975.

[65] Serguei Brazovskii, Christophe Brun, Zhao-Zhong Wang, and Pierre Monceau. Scanning-tunneling microscope imaging of single-electron solitons in a material with incommensurate charge-density waves. *Physical review letters*, 108(9):096801, 2012.

[66] E DiMasi, MC Aronson, JF Mansfield, B Foran, and S Lee. Chemical pressure and charge-density waves in rare-earth tritellurides. *Physical Review B*, 52(20):14516, 1995.

[67] N Ru and IR Fisher. Thermodynamic and transport properties of y te 3, la te 3, and ce te 3. *Physical Review B*, 73(3):033101, 2006.

[68] A Sacchetti, CL Condron, SN Gvasaliya, F Pfuner, M Lavagnini, M Baldini, MF Toney, M Merlini, M Hanfland, J Mesot, et al. Pressure-induced quenching of the charge-density-wave state in rare-earth tritellurides observed by x-ray diffraction. *Physical Review B*, 79(20):201101, 2009.

[69] A Sacchetti, E Arcangeletti, A Perucchi, L Baldassarre, P Postorino, S Lupi, N Ru, IR Fisher, and L Degiorgi. Pressure dependence of the charge-density-wave gap in rare-earth tritellurides. *Physical review letters*, 98(2):026401, 2007.

[70] Christos Malliakas, Simon JL Billinge, Hyun Jeong Kim, and Mercouri G Kanatzidis. Square nets of tellurium: rare-earth dependent variation in the charge-density wave of rete3 (re= rare-earth element). *Journal of the American Chemical Society*, 127(18):6510–6511, 2005.

[71] Christos D Malliakas and Mercouri G Kanatzidis. Divergence in the behavior of the charge density wave in re te3 (re= rare-earth element) with temperature and re element. *Journal of the American Chemical Society*, 128(39):12612–12613, 2006.

[72] F Weber, S Rosenkranz, J-P Castellan, R Osborn, R Hott, R Heid, K-P Bohnen, T Egami, AH Said, and D Reznik. Extended phonon collapse and the origin of the charge-density wave in 2 h- nbse 2. *Physical Review Letters*, 107(10):107403, 2011.

[73] Bahadur Singh, Chuang-Han Hsu, Wei-Feng Tsai, Vitor M Pereira, and Hsin Lin. Stable charge density wave phase in a 1 t–tise 2 monolayer. *Physical Review B*, 95(24):245136, 2017.

[74] Xuetao Zhu, Yanwei Cao, Jiandi Zhang, EW Plummer, and Jiandong Guo. Classification of charge density waves based on their nature. *Proceedings of the National Academy of Sciences*, 112(8):2367–2371, 2015.

[75] Hans-Martin Eiter, Michela Lavagnini, Rudi Hackl, Elizabeth A Nowadnick, Alexander F Kemper, Thomas P Devereaux, Jiun-Haw Chu, James G Analytis, Ian R Fisher, and Leonardo Degiorgi. Alternative route to charge density wave formation in multiband systems. *Proceedings of the National Academy of Sciences*, 110(1):64–69, 2013.

[76] Anna F Kusmartseva, B Sipos, H Berger, Laszlo Forro, and Eduard Tutiš. Pressure induced superconductivity in pristine 1 t- tise 2. *Physical review letters*, 103(23):236401, 2009.

[77] Emilia Morosan, Henny W Zandbergen, BS Dennis, JWG Bos, Y Onose, Tomasz Klimczuk, AP Ramirez, NP Ong, and Robert J Cava. Superconductivity in cuxtise2. *Nature Physics*, 2(8):544–550, 2006.

[78] Xuetao Zhu, Yanwei Cao, Jiandi Zhang, EW Plummer, and Jiandong Guo. Classification of charge density waves based on their nature. *Proceedings of the National Academy of Sciences*, 112(8):2367–2371, 2015.

[79] Yao Li, Karel-Alexander N Duerloo, Kerry Wauson, and Evan J Reed. Structural semiconductor-to-semimetal phase transition in two-dimensional materials induced by electrostatic gating. *Nature communications*, 7(1):1–8, 2016.

[80] Chenxi Zhang, Santosh Kc, Yifan Nie, Chaoping Liang, William G Vandenberghe, Roberto C Longo, Yongping Zheng, Fantai Kong, Suklyun Hong, Robert M Wallace, et al. Charge mediated reversible metal–insulator transition in monolayer mote2 and w x mo1–x te2 alloy. *ACS nano*, 10(8):7370–7375, 2016.

[81] Eduardo V Castro, KS Novoselov, SV Morozov, NMR Peres, JMB Lopes Dos Santos, Johan Nilsson, F Guinea, AK Geim, and AH Castro Neto. Biased bilayer graphene: semiconductor with a gap tunable by the electric field effect. *Physical review letters*, 99(21):216802, 2007.

[82] Edward McCann and Vladimir I Fal'ko. Landau-level degeneracy and quantum hall effect in a graphite bilayer. *Physical review letters*, 96(8):086805, 2006.

[83] Jeroen B Oostinga, Hubert B Heersche, Xinglan Liu, Alberto F Morpurgo, and Lieven MK Vandersypen. Gate-induced insulating state in bilayer graphene devices. *Nature materials*, 7(2):151–157, 2008.

[84] R Thomas Weitz, Monica T Allen, Benjamin E Feldman, Jens Martin, and Amir Yacoby. Broken-symmetry states in doubly gated suspended bilayer graphene. *Science*, 330(6005):812–816, 2010.

[85] Taisuke Ohta, Aaron Bostwick, Thomas Seyller, Karsten Horn, and Eli Rotenberg. Controlling the electronic structure of bilayer graphene. *Science*, 313(5789):951–954, 2006.

[86] Bevin Huang, Genevieve Clark, Efrén Navarro-Moratalla, Dahlia R Klein, Ran Cheng, Kyle L Seyler, Ding Zhong, Emma Schmidgall, Michael A McGuire, David H

Cobden, et al. Layer-dependent ferromagnetism in a van der waals crystal down to the monolayer limit. *Nature*, 546(7657):270–273, 2017.

[87] Cheng Gong, Lin Li, Zhenglu Li, Huiwen Ji, Alex Stern, Yang Xia, Ting Cao, Wei Bao, Chenzhe Wang, Yuan Wang, et al. Discovery of intrinsic ferromagnetism in two-dimensional van der waals crystals. *Nature*, 546(7657):265–269, 2017.

[88] Yujun Deng, Yijun Yu, Yichen Song, Jingzhao Zhang, Nai Zhou Wang, Zeyuan Sun, Yangfan Yi, Yi Zheng Wu, Shiwei Wu, Junyi Zhu, et al. Gate-tunable room-temperature ferromagnetism in two-dimensional fe3gete2. *Nature*, 563(7729):94–99, 2018.

[89] Kenneth S Burch, David Mandrus, and Je-Geun Park. Magnetism in two-dimensional van der waals materials. *Nature*, 563(7729):47–52, 2018.

[90] Shengwei Jiang, Jie Shan, and Kin Fai Mak. Electric-field switching of two-dimensional van der waals magnets. *Nature materials*, 17(5):406–410, 2018.

[91] Ying Wang, Jun Xiao, Hanyu Zhu, Yao Li, Yousif Alsaid, King Yan Fong, Yao Zhou, Siqi Wang, Wu Shi, Yuan Wang, et al. Structural phase transition in monolayer mote2 driven by electrostatic doping. *Nature*, 550(7677):487–491, 2017.

[92] Biswanath Chakraborty, Achintya Bera, DVS Muthu, Somnath Bhowmick, Umesh V Waghmare, and AK Sood. Symmetry-dependent phonon renormalization in monolayer mos 2 transistor. *Physical Review B*, 85(16):161403, 2012.

[93] Zhen-Hua Chi, Xiao-Miao Zhao, Haidong Zhang, Alexander F Goncharov, Sergey S Lobanov, Tomoko Kagayama, Masafumi Sakata, and Xiao-Jia Chen. Pressure-induced metallization of molybdenum disulfide. *Physical review letters*, 113(3):036802, 2014.

[94] Feng Xiao, Wen Lei, Wei Wang, Carmine Autieri, Xiaojun Zheng, Xing Ming, and Jianlin Luo. Pressure-induced structural transition, metallization, and topological superconductivity in pdsse. *Physical Review B*, 105(11):115110, 2022.

[95] P Hohenberg and W Kohn. Physical review, 136. *B864*, 1964.

[96] Enrico Fermi. A statistical method for the determination of some priorieta dell'atome. *Rend. Accad. Nat. Lincei*, 6(602-607):32, 1927.

[97] P. A. M. Dirac. Note on exchange phenomena in the thomas atom. *Mathematical Proceedings of the Cambridge Philosophical Society*, 26(3):376–385, 1930.

[98] Eugene Wigner. Effects of the electron interaction on the energy levels of electrons in metals. *Transactions of the Faraday Society*, 34:678–685, 1938.

[99] Paolo Giannozzi, Stefano Baroni, Nicola Bonini, Matteo Calandra, Roberto Car, Carlo Cavazzoni, Davide Ceresoli, Guido L Chiarotti, Matteo Cococcioni, Ismaila Dabo, et al. Quantum espresso: a modular and open-source software project for quantum simulations of materials. *Journal of physics: Condensed matter*, 21(39):395502, 2009.

[100] Xavier Gonze, J-M Beuken, Razvan Caracas, F Detraux, M Fuchs, G-M Rignanese, Luc Sindic, Matthieu Verstraete, G Zerah, F Jollet, et al. First-principles computation of material properties: the abinit software project. *Computational Materials Science*, 25(3):478–492, 2002.

[101] PO Widmark. Malmqvist and bo roos, t heor. chim. p. *Aé. Acta*, 77:291, 1990.

[102] Steven G Louie, Kai-Ming Ho, and Marvin L Cohen. Self-consistent mixed-basis approach to the electronic structure of solids. *Physical Review B*, 19(4):1774, 1979.

[103] Jorge Kohanoff. *Electronic structure calculations for solids and molecules: theory and computational methods*. Cambridge university press, 2006.

[104] John P Perdew and Alex Zunger. Self-interaction correction to density-functional approximations for many-electron systems. *Physical Review B*, 23(10):5048, 1981.

[105] John P Perdew and Yue Wang. Accurate and simple analytic representation of the electron-gas correlation energy. *Physical review B*, 45(23):13244, 1992.

[106] Seymour H Vosko, Leslie Wilk, and Marwan Nusair. Accurate spin-dependent electron liquid correlation energies for local spin density calculations: a critical analysis. *Canadian Journal of physics*, 58(8):1200–1211, 1980.

[107] John P Perdew. Unified theory of exchange and correlation beyond the local density approximation. *Electronic structure of solids' 91*, 11, 1991.

[108] John P Perdew, Kieron Burke, and Matthias Ernzerhof. Generalized gradient approximation made simple. *Physical review letters*, 77(18):3865, 1996.

[109] DR Hamann, M Schlüter, and C Chiang. Norm-conserving pseudopotentials. *Physical Review Letters*, 43(20):1494, 1979.

[110] David Vanderbilt. Soft self-consistent pseudopotentials in a generalized eigenvalue formalism. *Physical review B*, 41(11):7892, 1990.

[111] Pavel Hobza, Jiří šponer, and Tomáš Reschel. Density functional theory and molecular clusters. *Journal of computational chemistry*, 16(11):1315–1325, 1995.

[112] Mark J Allen and David J Tozer. Helium dimer dispersion forces and correlation potentials in density functional theory. *The Journal of chemical physics*, 117(24):11113–11120, 2002.

[113] Igor E Dzyaloshinskii, Efrat M Lifshitz, and Lev P Pitaevskii. The general theory of van der waals forces. *Advances in Physics*, 10(38):165–209, 1961.

[114] Stefan Grimme. Semiempirical gga-type density functional constructed with a long-range dispersion correction. *Journal of computational chemistry*, 27(15):1787–1799, 2006.

[115] Alexandre Tkatchenko and Matthias Scheffler. Accurate molecular van der waals interactions from ground-state electron density and free-atom reference data. *Physical review letters*, 102(7):073005, 2009.

[116] Aditi Saraswat, K Pramoda, Koyendrila Debnath, Swaraj Servottam, Umesh V Waghmare, and CNR Rao. Chemical route to twisted graphene, graphene oxide and boron nitride. *Chemistry–A European Journal*, 26(29):6499–6503, 2020.

[117] CNR Rao, AK Sood, Rakesh Voggu, and KS Subrahmanyam. Some novel attributes of graphene. *The Journal of Physical Chemistry Letters*, 1(2):572–580, 2010.

[118] Chintamani Nagesa Ramachandra Rao and Umesh Vasudeo Waghmare. *2D inorganic materials beyond graphene*. World Scientific, 2017.

[119] Pratap Vishnoi, K Pramoda, and CNR Rao. 2d elemental nanomaterials beyond graphene. *ChemNanoMat*, 5(9):1062–1091, 2019.

[120] HSS Ramakrishna Matte, A Gomathi, Arun K Manna, Dattatray J Late, Ranjan Datta, Swapan K Pati, and CNR Rao. Mos2 and ws2 analogues of graphene. *Angewandte Chemie International Edition*, 49(24):4059–4062, 2010.

[121] Muharrem Acerce, Damien Voiry, and Manish Chhowalla. Metallic 1t phase mos2 nanosheets as supercapacitor electrode materials. *Nature nanotechnology*, 10(4):313–318, 2015.

[122] Andre K Geim and Irina V Grigorieva. Van der waals heterostructures. *Nature*, 499(7459):419–425, 2013.

[123] Matthew Yankowitz, Qiong Ma, Pablo Jarillo-Herrero, and Brian J LeRoy. van der waals heterostructures combining graphene and hexagonal boron nitride. *Nature Reviews Physics*, 1(2):112–125, 2019.

[124] CNR Rao and K Pramoda. Borocarbonitrides, bxcynz, 2d nanocomposites with novel properties. *Bulletin of the Chemical Society of Japan*, 92(2):441–468, 2019.

[125] CNR Rao, K Pramoda, and Ram Kumar. Covalent cross-linking as a strategy to generate novel materials based on layered (2d) and other low d structures. *Chemical Communications*, 53(73):10093–10107, 2017.

[126] K Pramoda, Ram Kumar, and CNR Rao. Graphene/single-walled carbon nanotube composites generated by covalent cross-linking. *Chemistry–An Asian Journal*, 10(10):2147–2152, 2015.

[127] Yuan Cao, Valla Fatemi, Shiang Fang, Kenji Watanabe, Takashi Taniguchi, Efthimios Kaxiras, and Pablo Jarillo-Herrero. Unconventional superconductivity in magic-angle graphene superlattices. *Nature*, 556(7699):43–50, 2018.

[128] JMB Lopes Dos Santos, NMR Peres, and AH Castro Neto. Graphene bilayer with a twist: electronic structure. *Physical review letters*, 99(25):256802, 2007.

[129] Rafi Bistritzer and Allan H MacDonald. Transport between twisted graphene layers. *Physical Review B*, 81(24):245412, 2010.

[130] Lola Brown, Robert Hovden, Pinshane Huang, Michal Wojcik, David A Muller, and Jiwoong Park. Twinning and twisting of tri-and bilayer graphene. *Nano letters*, 12(3):1609–1615, 2012.

[131] Tobias Stauber, Tony Low, and G Gómez-Santos. Chiral response of twisted bilayer graphene. *Physical review letters*, 120(4):046801, 2018.

[132] Sabina Simon, Elena Voloshina, Julia Tesch, Felix Förschner, Vivien Enenkel, Charlotte Herbig, Timo Knispel, Alexander Tries, Jörg Kröger, Yuriy Dedkov, et al. Layer-by-layer decoupling of twisted graphene sheets epitaxially grown on a metal substrate. *Small*, 14(13):1703701, 2018.

[133] Xu-Dong Chen, Wei Xin, Wen-Shuai Jiang, Zhi-Bo Liu, Yongsheng Chen, and Jian-Guo Tian. High-precision twist-controlled bilayer and trilayer graphene. *Advanced Materials*, 28(13):2563–2570, 2016.

[134] CC Lu, YC Lin, Z Liu, CH Yeh, K Suenaga, and PW Chiu. Acs nano 7, 2587 (2013).

[135] Y Cao, JY Luo, V Fatemi, S Fang, JD Sanchez-Yamagishi, K Watanabe, T Taniguchi, E Kaxiras, and Pablo Jarillo-Herrero. Superlattice-induced insulating states and valley-protected orbits in twisted bilayer graphene. *Physical review letters*, 117(11):116804, 2016.

[136] Umesha Mogera, Radhakrishnan Dhanya, Rajashekhar Pujar, Chandrabhas Narayana, and Giridhar U Kulkarni. Highly decoupled graphene multilayers: turbostraticity at its best. *The journal of physical chemistry letters*, 6(21):4437–4443, 2015.

[137] Paolo Giannozzi, Stefano Baroni, Nicola Bonini, Matteo Calandra, Roberto Car, Carlo Cavazzoni, Davide Ceresoli, Guido L Chiarotti, and Matteo Cococcioni *et al.* QUANTUM ESPRESSO: a modular and open-source software project for quantum simulations of materials. *Journal of Physics: Condensed Matter*, 21(39):395502, sep 2009.

[138] Xinlei Hua, Xiaojie Chen, and W. A. Goddard. Generalized generalized gradient approximation:an improved density-functional theory for accurate orbital eigenvalues. *Phys. Rev. B*, 55:16103–16109, Jun 1997.

[139] J. P. Perdew, K. Burke, and M. Ernzerhof. Perdew, burke, and ernzerhof reply:. *Phys. Rev. Lett.*, 80:891–891, Jan 1998.

[140] Stefan Grimme. Accurate description of van der waals complexes by density functional theory including empirical corrections. *Journal of Computational Chemistry*, 25(12):1463–1473, 2004.

[141] Kazuyuki Uchida, Shinnosuke Furuya, Jun-Ichi Iwata, and Atsushi Oshiyama. Atomic corrugation and electron localization due to moiré patterns in twisted bilayer graphenes. *Physical Review B*, 90(15):155451, 2014.

[142] Rafi Bistritzer and Allan H MacDonald. Moiré bands in twisted double-layer graphene. *Proceedings of the National Academy of Sciences*, 108(30):12233–12237, 2011.

[143] Shiang Fang and Efthimios Kaxiras. Electronic structure theory of weakly interacting bilayers. *Physical Review B*, 93(23):235153, 2016.

[144] Subhajit Sinha, Pratap Chandra Adak, Atasi Chakraborty, Kamal Das, Koyendrila Debnath, LD Sangani, Kenji Watanabe, Takashi Taniguchi, Umesh V Waghmare, Amit Agarwal, et al. Berry curvature dipole senses topological transition in a moiré superlattice. *Nature Physics*, pages 1–6, 2022.

[145] Yuan Cao, Valla Fatemi, Shiang Fang, Kenji Watanabe, Takashi Taniguchi, Efthimios Kaxiras, and Pablo Jarillo-Herrero. Unconventional superconductivity in magic-angle graphene superlattices. *Nature*, 556(7699):43–50, 2018.

[146] Xiaobo Lu, Petr Stepanov, Wei Yang, Ming Xie, Mohammed Ali Aamir, Ipsita Das, Carles Urgell, Kenji Watanabe, Takashi Taniguchi, Guangyu Zhang, et al. Superconductors, orbital magnets and correlated states in magic-angle bilayer graphene. *Nature*, 574(7780):653–657, 2019.

[147] Aaron L Sharpe, Eli J Fox, Arthur W Barnard, Joe Finney, Kenji Watanabe, Takashi Taniguchi, MA Kastner, and David Goldhaber-Gordon. Emergent ferromagnetism near three-quarters filling in twisted bilayer graphene. *Science*, 365(6453):605–608, 2019.

[148] M Serlin, CL Tschirhart, H Polshyn, Y Zhang, J Zhu, K Watanabe, T Taniguchi, L Balents, and AF Young. Intrinsic quantized anomalous hall effect in a moiré heterostructure. *Science*, 367(6480):900–903, 2020.

[149] Kyounghwan Kim, Ashley DaSilva, Shengqiang Huang, Babak Fallahazad, Stefano Larentis, Takashi Taniguchi, Kenji Watanabe, Brian J LeRoy, Allan H MacDonald, and Emanuel Tutuc. Tunable moiré bands and strong correlations in small-twist-angle bilayer graphene. *Proceedings of the National Academy of Sciences*, 114(13):3364–3369, 2017.

[150] Yuan Cao, Valla Fatemi, Ahmet Demir, Shiang Fang, Spencer L Tomarken, Jason Y Luo, Javier D Sanchez-Yamagishi, Kenji Watanabe, Takashi Taniguchi, Efthimios

Kaxiras, et al. Correlated insulator behaviour at half-filling in magic-angle graphene superlattices. *Nature*, 556(7699):80–84, 2018.

[151] Stephen Carr, Daniel Massatt, Shiang Fang, Paul Cazeaux, Mitchell Luskin, and Efthimios Kaxiras. Twistronics: Manipulating the electronic properties of two-dimensional layered structures through their twist angle. *Physical Review B*, 95(7):075420, 2017.

[152] Rebeca Ribeiro-Palau, Changjian Zhang, Kenji Watanabe, Takashi Taniguchi, James Hone, and Cory R Dean. Twistable electronics with dynamically rotatable heterostructures. *Science*, 361(6403):690–693, 2018.

[153] Ipsita Das, Xiaobo Lu, Jonah Herzog-Arbeitman, Zhi-Da Song, Kenji Watanabe, Takashi Taniguchi, B Andrei Bernevig, and Dmitri K Efetov. Symmetry-broken chern insulators and rashba-like landau-level crossings in magic-angle bilayer graphene. *Nature Physics*, 17(6):710–714, 2021.

[154] Di Xiao, Ming-Che Chang, and Qian Niu. Berry phase effects on electronic properties. *Reviews of modern physics*, 82(3):1959, 2010.

[155] Naoto Nagaosa, Jairo Sinova, Shigeki Onoda, Allan H MacDonald, and Nai Phuan Ong. Anomalous hall effect. *Reviews of modern physics*, 82(2):1539, 2010.

[156] Inti Sodemann and Liang Fu. Quantum nonlinear hall effect induced by berry curvature dipole in time-reversal invariant materials. *Physical review letters*, 115(21):216806, 2015.

[157] Alexandr I. Cocemasov, Denis L. Nika, and Alexander A. Balandin. Phonons in twisted bilayer graphene. *Phys. Rev. B*, 88:035428, Jul 2013.

[158] Kenji Yasuda, Xirui Wang, Kenji Watanabe, Takashi Taniguchi, and Pablo Jarillo-Herrero. Stacking-engineered ferroelectricity in bilayer boron nitride. *Science*, 372(6549):1458–1462, 2021.

[159] Subhadip Das, Koyendrila Debnath, Biswanath Chakraborty, Anjali Singh, Shivani Grover, DVS Muthu, UV Waghmare, and AK Sood. Symmetry induced phonon renormalization in few layers of 2h-mote2 transistors: Raman and first-principles studies. *Nanotechnology*, 32(4):045202, 2020.

[160] D. Puotinen and R. E. Newnham. The crystal structure of $MoTe_2$. *Acta Crystallographica*, 14(6):691–692, Jun 1961.

[161] B. E. Brown. The crystal structures of WTe_2 and high-temperature $MoTe_2$. *Acta Crystallographica*, 20(2):268–274, Feb 1966.

[162] Yanpeng Qi, Pavel G Naumov, Mazhar N Ali, Catherine R Rajamathi, Walter Schnelle, Oleg Barkalov, Michael Hanfland, Shu-Chun Wu, Chandra Shekhar, Yan Sun, et al. Superconductivity in weyl semimetal candidate mote 2. *Nature communications*, 7(1):1–7, 2016.

[163] Claudia Ruppert, Ozgur Burak Aslan, and Tony F. Heinz. Optical properties and band gap of single- and few-layer mote2 crystals. *Nano Letters*, 14(11):6231–6236, 2014.

[164] Dong Hoon Keum, Suyeon Cho, Jung Ho Kim, Duk-Hyun Choe, Ha-Jun Sung, Min Kan, Haeyong Kang, Jae-Yeol Hwang, Sung Wng Kim, Heejun Yang, et al. Bandgap opening in few-layered monoclinic mote 2. *Nature Physics*, 11(6):482–486, 2015.

[165] J. L. Verble and T. J. Wieting. Lattice mode degeneracy in mos_2 and other layer compounds. *Phys. Rev. Lett.*, 25:362–365, Aug 1970.

[166] Seunghyun Song, Dong Hoon Keum, Suyeon Cho, David Perello, Yunseok Kim, and Young Hee Lee. Room temperature semiconductor–metal transition of mote2 thin films engineered by strain. *Nano Letters*, 16(1):188–193, 2016.

[167] Wenhui Hou, Ahmad Azizimanesh, Arfan Sewaket, Tara Peña, Carla Watson, Ming Liu, Hesam Askari, and Stephen M Wu. Strain-based room-temperature non-volatile mote 2 ferroelectric phase change transistor. *Nature nanotechnology*, 14(7):668–673, 2019.

[168] Suyeon Cho, Sera Kim, Jung Ho Kim, Jiong Zhao, Jinbong Seok, Dong Hoon Keum, Jaeyoon Baik, Duk-Hyun Choe, K. J. Chang, Kazu Suenaga, Sung Wng Kim, Young Hee Lee, and Heejun Yang. Phase patterning for ohmic homojunction contact in mote2. *Science*, 349(6248):625–628, 2015.

[169] Yuan Tan, Fang Luo, Mengjian Zhu, Xiaolong Xu, Yu Ye, Bing Li, Guang Wang, Wei Luo, Xiaoming Zheng, Nannan Wu, Yayun Yu, Shiqiao Qin, and Xue-Ao Zhang. Controllable 2h-to-1t phase transition in few-layer mote2. *Nanoscale*, 10:19964–19971, 2018.

[170] Dante Zakhidov, Daniel A. Rehn, Evan J. Reed, and Alberto Salleo. Reversible electrochemical phase change in monolayer to bulk-like mote2 by ionic liquid gating. *ACS Nano*, 14(3):2894–2903, 2020.

[171] Rui Ma, Huairuo Zhang, Youngdong Yoo, Zachary Patrick Degregorio, Lun Jin, Prafful Golani, Javad Ghasemi Azadani, Tony Low, James E. Johns, Leonid A. Bendersky, Albert V. Davydov, and Steven J. Koester. Mote2 lateral homojunction field-effect transistors fabricated using flux-controlled phase engineering. *ACS Nano*, 13(7):8035–8046, 2019.

[172] Thomas Brumme, Matteo Calandra, and Francesco Mauri. First-principles theory of field-effect doping in transition-metal dichalcogenides: Structural properties, electronic structure, hall coefficient, and electrical conductivity. *Phys. Rev. B*, 91:155436, Apr 2015.

[173] A. Conan, D. Delaunay, A. Bonnet, A. G. Moustafa, and M. Spiesser. Temperature dependence of the electrical conductivity and thermoelectric power in mote2 single crystals. *physica status solidi (b)*, 94(1):279–286, 1979.

[174] A J Grant, T M Griffiths, G D Pitt, and A D Yoffe. The electrical properties and the magnitude of the indirect gap in the semiconducting transition metal dichalcogenide layer crystals. *Journal of Physics C: Solid State Physics*, 8(1):L17–L23, jan 1975.

[175] Kun Zhang, Xin Fang, Yilun Wang, Yi Wan, Qingjun Song, Wenhao Zhai, Yanping Li, Guangzhao Ran, Yu Ye, and Lun Dai. Ultrasensitive near-infrared photodetectors based on a graphene–mote2–graphene vertical van der waals heterostructure. *ACS Applied Materials & Interfaces*, 9(6):5392–5398, 2017.

[176] Manabendra Kuiri, Biswanath Chakraborty, Arup Paul, Subhadip Das, A. K. Sood, and Anindya Das. Enhancing photoresponsivity using mote2-graphene vertical heterostructures. *Applied Physics Letters*, 108(6):063506, 2016.

[177] Yongzhuo Li, Jianxing Zhang, Dandan Huang, Hao Sun, Fan Fan, Jiabin Feng, Zhen Wang, and Cun-Zheng Ning. Room-temperature continuous-wave lasing from monolayer molybdenum ditelluride integrated with a silicon nanobeam cavity. *Nature nanotechnology*, 12(10):987, 2017.

[178] Ya-Qing Bie, Gabriele Grosso, Mikkel Heuck, Marco M Furchi, Yuan Cao, Jiabao Zheng, Darius Bunandar, Efren Navarro-Moratalla, Lin Zhou, Dmitri K Efetov, et al. A mote 2-based light-emitting diode and photodetector for silicon photonic integrated circuits. *Nature nanotechnology*, 12(12):1124, 2017.

[179] Nihar R. Pradhan, Daniel Rhodes, Simin Feng, Yan Xin, Shahriar Memaran, Byoung-Hee Moon, Humberto Terrones, Mauricio Terrones, and Luis Balicas. Field-effect transistors based on few-layered -mote2. *ACS Nano*, 8(6):5911–5920, 2014.

[180] Shu Nakaharai, Mahito Yamamoto, Keiji Ueno, Yen-Fu Lin, Song-Lin Li, and Kazuhito Tsukagoshi. Electrostatically reversible polarity of ambipolar -mote2 transistors. *ACS Nano*, 9(6):5976–5983, 2015.

[181] Sikandar Aftab, Muhammad Farooq Khan, Praveen Gautam, Hwayong Noh, and Jonghwa Eom. Mote2 van der waals homojunction p–n diode with low resistance metal contacts. *Nanoscale*, 11:9518–9525, 2019.

[182] Qikun Li, Sheng Bi, Kyeiwaa Asare-Yeboah, Jin Na, Yun Liu, Chengming Jiang, and Jinhui Song. High performance vertical resonant photo-effect-transistor with an all-around oled-gate for ultra-electromagnetic stability. *ACS Nano*, 13(7):8425–8432, 2019.

[183] Sheng Bi, Qikun Li, Kyeiwaa Asare-Yeboah, Jin Na, Yeqing Sun, and Chengming Jiang. Ultra-high-responsivity vertical nanowire-based phototransistor under standing-wave plasmon mode interaction induced by near-field circular oled. *The Journal of Physical Chemistry Letters*, 11(10):3947–3954, 2020.

[184] Kyeiwaa Asare-Yeboah, Qikun Li, Chengming Jiang, Zhengran He, Sheng Bi, Yun Liu, and Chuan Liu. High performance and efficiency resonant photo-effect-transistor by near-field nano-strip-controlled organic light emitting diode gate. *The Journal of Physical Chemistry Letters*, 11(16):6526–6534, 2020.

[185] Hocheon Yoo, Seongin Hong, Sungmin On, Hyungju Ahn, Han-Koo Lee, Young Ki Hong, Sunkook Kim, and Jae-Joon Kim. Chemical doping effects in multilayer mos2 and its application in complementary inverter. *ACS Applied Materials & Interfaces*, 10(27):23270–23276, 2018.

[186] Zhen Yao, Charles L. Kane, and Cees Dekker. High-field electrical transport in single-wall carbon nanotubes. *Phys. Rev. Lett.*, 84:2941–2944, Mar 2000.

[187] Dmitri K. Efetov and Philip Kim. Controlling electron-phonon interactions in graphene at ultrahigh carrier densities. *Phys. Rev. Lett.*, 105:256805, Dec 2010.

[188] Biswanath Chakraborty, Achintya Bera, D. V. S. Muthu, Somnath Bhowmick, U. V. Waghmare, and A. K. Sood. Symmetry-dependent phonon renormalization in monolayer mos_2 transistor. *Phys. Rev. B*, 85:161403, Apr 2012.

[189] Biswanath Chakraborty, Satyendra Nath Gupta, Anjali Singh, Manabendra Kuiri, Chandan Kumar, D V S Muthu, Anindya Das, U V Waghmare, and A K Sood. Electron-hole asymmetry in the electron-phonon coupling in top-gated phosphorene transistor. *2D Materials*, 3(1):015008, feb 2016.

[190] Hongtao Yuan, Hidekazu Shimotani, Atsushi Tsukazaki, Akira Ohtomo, Masashi Kawasaki, and Yoshihiro Iwasa. High-density carrier accumulation in zno field-effect transistors gated by electric double layers of ionic liquids. *Advanced Functional Materials*, 19(7):1046–1053, 2009.

[191] Chenguang Lu, Qiang Fu, Shaoming Huang, and Jie Liu. Polymer electrolyte-gated carbon nanotube field-effect transistor. *Nano Letters*, 4(4):623–627, 2004.

[192] Matthew A. Gebbie, Howard A. Dobbs, Markus Valtiner, and Jacob N. Israelachvili. Long-range electrostatic screening in ionic liquids. *Proceedings of the National Academy of Sciences*, 112(24):7432–7437, 2015.

[193] L. Andres Jurado and Rosa M. Espinosa-Marzal. Insight into the electrical double layer of an ionic liquid on graphene. *Scientific Reports*, 7(1):4225, Jun 2017.

[194] Yu Xia, Wei Xie, P. Paul Ruden, and C. Daniel Frisbie. Carrier localization on surfaces of organic semiconductors gated with electrolytes. *Phys. Rev. Lett.*, 105:036802, Jul 2010.

[195] Patrick Gallagher, Menyoung Lee, Trevor A Petach, Sam W Stanwyck, James R Williams, Kenji Watanabe, Takashi Taniguchi, and David Goldhaber-Gordon. A high-mobility electronic system at an electrolyte-gated oxide surface. *Nature communications*, 6(1):1–5, 2015.

[196] K. Ueno, S. Nakamura, H. Shimotani, A. Ohtomo, N. Kimura, T. Nojima, H. Aoki, Y. Iwasa, and M. Kawasaki. Electric-field-induced superconductivity in an insulator. *Nature Materials*, 7(11):855–858, Nov 2008.

[197] J. T. Ye, S. Inoue, K. Kobayashi, Y. Kasahara, H. T. Yuan, H. Shimotani, and Y. Iwasa. Liquid-gated interface superconductivity on an atomically flat film. *Nature Materials*, 9(2):125–128, Feb 2010.

[198] Bhupendra Karki, Byron Freelon, Manthila Rajapakse, Rajib Musa, S M Shah Riyadh, Blake Morris, Usman Abu, Ming Yu, Gamini Sumanasekera, and Jacek B Jasinski. Strain-induced vibrational properties of few layer black phosphorus and MoTe2 via raman spectroscopy. *Nanotechnology*, 31(42):425707, jul 2020.

[199] M Grzeszczyk, K Gołasa, M Zinkiewicz, K Nogajewski, M R Molas, M Potemski, A Wysmołek, and A Babiński. Raman scattering of few-layers MoTe 2. *2D Materials*, 3(2):025010, apr 2016.

[200] Guillaume Froehlicher, Etienne Lorchat, François Fernique, Chaitanya Joshi, Alejandro Molina-Sánchez, Ludger Wirtz, and Stéphane Berciaud. Unified description of the optical phonon modes in n-layer mote2. *Nano Letters*, 15(10):6481–6489, 2015.

[201] Qingjun Song, Haifeng Wang, Xingchen Pan, Xiaolong Xu, Yilun Wang, Yanping Li, Fengqi Song, Xiangang Wan, Yu Ye, and Lun Dai. Anomalous in-plane anisotropic raman response of monoclinic semimetal 1 t´-mote2. *Scientific Reports*, 7(1):1758, May 2017.

[202] Manabendra Kuiri, Subhadip Das, D. V. S. Muthu, Anindya Das, and A. K. Sood. Thickness dependent transition from the 1t to weyl semimetal phase in ultrathin mote2: electrical transport, noise and raman studies. *Nanoscale*, 12:8371–8378, 2020.

[203] Achintya Bera, Anjali Singh, D V S Muthu, U V Waghmare, and A K Sood. Pressure-dependent semiconductor to semimetal and lifshitz transitions in 2h-MoTe2: Raman and first-principles studies. *Journal of Physics: Condensed Matter*, 29(10):105403, feb 2017.

[204] Xiao-Miao Zhao, Han-yu Liu, Alexander F. Goncharov, Zhi-Wei Zhao, Viktor V. Struzhkin, Ho-Kwang Mao, Alexander G. Gavriliuk, and Xiao-Jia Chen. Pressure effect on the electronic, structural, and vibrational properties of layered $2h-\mathrm{mote}_2$. *Phys. Rev. B*, 99:024111, Jan 2019.

[205] Andrea Splendiani, Liang Sun, Yuanbo Zhang, Tianshu Li, Jonghwan Kim, Chi-Yung Chim, Giulia Galli, and Feng Wang. Emerging photoluminescence in monolayer mos2. *Nano Letters*, 10(4):1271–1275, 2010.

[206] Gheorghe Stan, Cristian V. Ciobanu, Sri Ranga Jai Likith, Asha Rani, Siyuan Zhang, Christina A. Hacker, Sergiy Krylyuk, and Albert V. Davydov. Doping

of mote2 via surface charge transfer in air. *ACS Applied Materials & Interfaces*, 12(15):18182–18193, 2020.

[207] Deshun Qu, Xiaochi Liu, Ming Huang, Changmin Lee, Faisal Ahmed, Hyoungsub Kim, Rodney S. Ruoff, James Hone, and Won Jong Yoo. Carrier-type modulation and mobility improvement of thin mote2. *Advanced Materials*, 29(39):1606433, 2017.

[208] J. Ribeiro-Soares, R. M. Almeida, E. B. Barros, P. T. Araujo, M. S. Dresselhaus, L. G. Cançado, and A. Jorio. Group theory analysis of phonons in two-dimensional transition metal dichalcogenides. *Phys. Rev. B*, 90:115438, Sep 2014.

[209] Mahito Yamamoto, Sheng Tsung Wang, Meiyan Ni, Yen-Fu Lin, Song-Lin Li, Shinya Aikawa, Wen-Bin Jian, Keiji Ueno, Katsunori Wakabayashi, and Kazuhito Tsukagoshi. Strong enhancement of raman scattering from a bulk-inactive vibrational mode in few-layer mote2. *ACS Nano*, 8(4):3895–3903, 2014.

[210] Andrea Dal Corso and Adriano Mosca Conte. Spin-orbit coupling with ultrasoft pseudopotentials: Application to au and pt. *Phys. Rev. B*, 71:115106, Mar 2005.

[211] Thomas Brumme, Matteo Calandra, and Francesco Mauri. Electrochemical doping of few-layer zrncl from first principles: Electronic and structural properties in field-effect configuration. *Phys. Rev. B*, 89:245406, Jun 2014.

[212] Stefano Baroni, Stefano de Gironcoli, Andrea Dal Corso, and Paolo Giannozzi. Phonons and related crystal properties from density-functional perturbation theory. *Rev. Mod. Phys.*, 73:515–562, Jul 2001.

[213] Osvald Knop and Roderick D. MacDonald. Chalkogenides of the transition elements: Iii. molybdenum ditelluride. *Canadian Journal of Chemistry*, 39(4):897–904, 1961.

[214] A. K. Geim. Graphene: Status and prospects. *Science*, 324(5934):1530–1534, 2009.

[215] Kin Fai Mak, Changgu Lee, James Hone, Jie Shan, and Tony F. Heinz. Atomically thin MoS_2: A new direct-gap semiconductor. *Phys. Rev. Lett.*, 105:136805, Sep 2010.

[216] Changgu Lee, Hugen Yan, Louis E. Brus, Tony F. Heinz, James Hone, and Sunmin Ryu. Anomalous lattice vibrations of single- and few-layer mos2. *ACS Nano*, 4(5):2695–2700, 2010.

[217] Frank Schwierz. Graphene transistors. *Nature Nanotechnology*, 5(7):487–496, Jul 2010.

[218] K. S. Novoselov, D. Jiang, F. Schedin, T. J. Booth, V. V. Khotkevich, S. V. Morozov, and A. K. Geim. Two-dimensional atomic crystals. *Proceedings of the National Academy of Sciences*, 102(30):10451–10453, 2005.

[219] K. S. Novoselov, A. Mishchenko, A. Carvalho, and A. H. Castro Neto. 2D materials and van der waals heterostructures. *Science*, 353(6298):aac9439, 2016.

[220] K. K. Kam and B. A. Parkinson. Detailed photocurrent spectroscopy of the semiconducting group vib transition metal dichalcogenides. *The Journal of Physical Chemistry*, 86(4):463–467, 1982.

[221] A. Kuc, N. Zibouche, and T. Heine. Influence of quantum confinement on the electronic structure of the transition metal sulfide TS_2. *Phys. Rev. B*, 83:245213, Jun 2011.

[222] Qing Hua Wang, Kourosh Kalantar-Zadeh, Andras Kis, Jonathan N. Coleman, and Michael S. Strano. Electronics and optoelectronics of two-dimensional transition metal dichalcogenides. *Nature Nanotechnology*, 7(11):699–712, Nov 2012.

[223] Yi Ding, Yanli Wang, Jun Ni, Lin Shi, Siqi Shi, and Weihua Tang. First principles study of structural, vibrational and electronic properties of graphene-like MX_2 (M=Mo, Nb, W, Ta; X=S, Se, Te) monolayers. *Physica B: Condensed Matter*, 406(11):2254–2260, 2011.

[224] T.E. Kidd, D. Klein, T.A. Rash, and L.H. Strauss. Dopant based electron beam lithography in Cu_xTiSe_2. *Applied Surface Science*, 257(8):3812–3816, 2011.

[225] Nobuyuki Takei, Christian Sommer, Claudiu Genes, Guido Pupillo, Haruka Goto, Kuniaki Koyasu, Hisashi Chiba, Matthias Weidemüller, and Kenji Ohmori. Direct observation of ultrafast many-body electron dynamics in an ultracold rydberg gas. *Nature Communications*, 7(1):13449, Nov 2016.

[226] Chenxi Zhang, Santosh KC, Yifan Nie, Chaoping Liang, William G. Vandenberghe, Roberto C. Longo, Yongping Zheng, Fantai Kong, Suklyun Hong, Robert M. Wallace, and Kyeongjae Cho. Charge mediated reversible metal–insulator transition in monolayer $MoTe_2$ and $W_xMo_{1-x}Te_2$ alloy. *ACS Nano*, 10(8):7370–7375, 2016. PMID: 27415610.

[227] R. R. Nair, P. Blake, A. N. Grigorenko, K. S. Novoselov, T. J. Booth, T. Stauber, N. M. R. Peres, and A. K. Geim. Fine structure constant defines visual transparency of graphene. *Science*, 320(5881):1308–1308, 2008.

[228] Peng Lu, Xiaojun Wu, Wanlin Guo, and Xiao Cheng Zeng. Strain-dependent electronic and magnetic properties of MoS_2 monolayer, bilayer, nanoribbons and nanotubes. *Phys. Chem. Chem. Phys.*, 14:13035–13040, 2012.

[229] C. Ataca, H. Şahin, E. Aktürk, and S. Ciraci. Mechanical and electronic properties of MoS_2 nanoribbons and their defects. *The Journal of Physical Chemistry C*, 115(10):3934–3941, 2011.

[230] Changgu Lee, Xiaoding Wei, Jeffrey W. Kysar, and James Hone. Measurement of the elastic properties and intrinsic strength of monolayer graphene. *Science*, 321(5887):385–388, 2008.

[231] Simone Bertolazzi, Jacopo Brivio, and Andras Kis. Stretching and breaking of ultrathin MoS_2. *ACS Nano*, 5(12):9703–9709, 2011. PMID: 22087740.

[232] Ryan C. Cooper, Changgu Lee, Chris A. Marianetti, Xiaoding Wei, James Hone, and Jeffrey W. Kysar. Nonlinear elastic behavior of two-dimensional molybdenum disulfide. *Phys. Rev. B*, 87:035423, Jan 2013.

[233] Wenzhuo Wu, Lei Wang, Yilei Li, Fan Zhang, Long Lin, Simiao Niu, Daniel Chenet, Xian Zhang, Yufeng Hao, Tony F Heinz, et al. Piezoelectricity of single-atomic-layer mos2 for energy conversion and piezotronics. *Nature*, 514(7523):470–474, 2014.

[234] Sung Kyun Kim, Ravi Bhatia, Tae-Ho Kim, Daehee Seol, Jung Ho Kim, Hyun Kim, Wanchul Seung, Yunseok Kim, Young Hee Lee, and Sang-Woo Kim. Directional dependent piezoelectric effect in cvd grown monolayer mos2 for flexible piezoelectric nanogenerators. *Nano Energy*, 22:483–489, 2016.

[235] Kenji Uchino, Shoichiro Nomura, Leslie E Cross, SJ Jang, and RE Newnham. Electrostrictive effect in lead magnesium niobate single crystals. *Journal of Applied Physics*, 51(2):1142–1145, 1980.

[236] Kenji Uchino, Shoichiro Nomura, Leslie E Cross, Robert E Newnham, and Sei J Jang. Electrostrictive effect in perovskites and its transducer applications. *Journal of Materials science*, 16(3):569–578, 1981.

[237] L. E. Cross, S. J. Jang, R. E. Newnham, S. Nomura, and K. Uchino. Large electrostrictive effects in relaxor ferroelectrics. *Ferroelectrics*, 23(1):187–191, 1980.

[238] S. Nomura, J. Kuwata, S.J. Jang, L.E. Cross, and R.E. Newnham. Electrostriction in $Pb(Zn_{1/3}Nb_{2/3})O_3$. *Materials Research Bulletin*, 14(6):769–774, 1979.

[239] SJ Jang, K Uchino, S Nomura, and L_ E Cross. Electrostrictive behavior of lead magnesium niobate based ceramic dielectrics. *Ferroelectrics*, 27(1):31–34, 1980.

[240] K. Uchino, L. E. Cross, R. E. Newnham, and S. Nomura. Electrostrictive effects in non-polar perovskites. *Phase Transitions*, 1(4):333–341, 1980.

[241] Daniel S. P. Tanner, Eric Bousquet, and Pierre-Eymeric Janolin. Optimized methodology for the calculation of electrostriction from first-principles. *Small*, 17(50):2103419, 2021.

[242] Paolo Giannozzi, Stefano Baroni, Nicola Bonini, Matteo Calandra, Roberto Car, Carlo Cavazzoni, Davide Ceresoli, Guido L. Chiarotti, Matteo Cococcioni, Ismaila Dabo, Andrea Dal Corso, Stefano De Gironcoli, Stefano Fabris, Guido Fratesi, Ralph Gebauer, Uwe Gerstmann, Christos Gougoussis, Anton Kokalj, Michele Lazzeri, Layla Martin-Samos, Nicola Marzari, Francesco Mauri, Riccardo Mazzarello, Stefano Paolini, Alfredo Pasquarello, Lorenzo Paulatto, Carlo Sbraccia, Sandro Scandolo, Gabriele Sclauzero, Ari P. Seitsonen, Alexander Smogunov, Paolo Umari, and Renata M. Wentzcovitch. QUANTUM ESPRESSO: A modular and open-source software project for quantum simulations of materials. *Journal of physics. Condensed matter : an Institute of Physics journal*, 21(39), 2009.

[243] Xinlei Hua, Xiaojie Chen, and W. A. Goddard. Generalized generalized gradient approximation: An improved density-functional theory for accurate orbital eigenvalues. *Phys. Rev. B*, 55:16103–16109, Jun 1997.

[244] John P. Perdew, Kieron Burke, and Matthias Ernzerhof. Generalized Gradient Approximation made simple [phys. rev. lett. 77, 3865 (1996)]. *Phys. Rev. Lett.*, 78:1396–1396, Feb 1997.

[245] Ryky Nelson, Christina Ertural, Janine George, Volker L. Deringer, Geoffroy Hautier, and Richard Dronskowski. LOBSTER: Local orbital projections, atomic charges, and chemical-bonding analysis from projector-augmented-wave-based density-functional theory. *Journal of Computational Chemistry*, 41(21):1931–1940, 2020.

[246] Richard Dronskowski and Peter E. Bloechl. Crystal orbital Hamilton populations (COHP): energy-resolved visualization of chemical bonding in solids based on

density-functional calculations. *The Journal of Physical Chemistry*, 97(33):8617–8624, 1993.

[247] Volker L. Deringer, Andrei L. Tchougréeff, and Richard Dronskowski. Crystal Orbital Hamilton Population (COHP) Analysis As Projected from Plane-Wave Basis Sets. *The Journal of Physical Chemistry A*, 115(21):5461–5466, 2011. PMID: 21548594.

[248] X. Gonze, F. Jollet, F. Abreu Araujo, D. Adams, B. Amadon, T. Applencourt, C. Audouze, J.-M. Beuken, J. Bieder, A. Bokhanchuk, E. Bousquet, F. Bruneval, D. Caliste, M. Côté, F. Dahm, F. Da Pieve, M. Delaveau, M. Di Gennaro, B. Dorado, C. Espejo, G. Geneste, L. Genovese, A. Gerossier, M. Giantomassi, Y. Gillet, D.R. Hamann, L. He, G. Jomard, J. Laflamme Janssen, S. Le Roux, A. Levitt, A. Lherbier, F. Liu, I. Lukačević, A. Martin, C. Martins, M.J.T. Oliveira, S. Poncé, Y. Pouillon, T. Rangel, G.-M. Rignanese, A.H. Romero, B. Rousseau, O. Rubel, A.A. Shukri, M. Stankovski, M. Torrent, M.J. Van Setten, B. Van Troeye, M.J. Verstraete, D. Waroquiers, J. Wiktor, B. Xu, A. Zhou, and J.W. Zwanziger. Recent developments in the ABINIT software package. *Computer Physics Communications*, 205:106–131, 2016.

[249] Michiel J van Setten, Matteo Giantomassi, Eric Bousquet, Matthieu J Verstraete, Don R Hamann, Xavier Gonze, and G-M Rignanese. The pseudodojo: Training and grading a 85 element optimized norm-conserving pseudopotential table. *Computer Physics Communications*, 226:39–54, 2018.

[250] RE Newnham, V Sundar, R Yimnirun, J Su, and QM Zhang. Electrostriction: nonlinear electromechanical coupling in solid dielectrics. *The Journal of Physical Chemistry B*, 101(48):10141–10150, 1997.

[251] A.F. Devonshire. Theory of ferroelectrics. *Advances in Physics*, 3(10):85–130, 1954.

[252] Akash Laturia, Maarten L. Van de Put, and William G. Vandenberghe. Dielectric properties of hexagonal boron nitride and transition metal dichalcogenides: from monolayer to bulk. *npj 2D Materials and Applications*, 2(1):6, Mar 2018.

[253] C. Ataca, M. Topsakal, E. Aktürk, and S. Ciraci. A comparative study of lattice dynamics of three- and two-dimensional MoS_2. *The Journal of Physical Chemistry C*, 115(33):16354–16361, 2011.

[254] N. Wakabayashi, H. G. Smith, and R. M. Nicklow. Lattice dynamics of hexagonal MoS_2 studied by neutron scattering. *Phys. Rev. B*, 12:659–663, Jul 1975.

[255] Th. Böker, R. Severin, A. Müller, C. Janowitz, R. Manzke, D. Voß, P. Krüger, A. Mazur, and J. Pollmann. Band structure of MoS_2, $MoSe_2$, and $\alpha - MoTe_2$: angle-resolved photoelectron spectroscopy and ab initio calculations. *Phys. Rev. B*, 64:235305, Nov 2001.

[256] David T. Hodul and Angelica M. Stacy. Anomalies in the properties of $Hf(S_{2-x}Te_x)_{1-y}$ and $Hf(Se_{2-x}Te_x)_{1-y}$ near the metal-insulator transition. *Journal of Solid State Chemistry*, 54(3):438–446, 1984.

[257] Stefana Anais Colibaba, Sabine Körbel, Carlo Motta, Fedwa El-Mellouhi, and Stefano Sanvito. Interlayer dielectric function of a type-II van der waals semiconductor: The HfS_2/PtS_2 heterobilayer. *Phys. Rev. Materials*, 3:124002, Dec 2019.

[258] Larbi Roubi and Cosmo Carlone. Resonance raman spectrum of HfS_2 and ZrS_2. *Phys. Rev. B*, 37:6808–6812, Apr 1988.

[259] Toshiki Iwasaki, Noritaka Kuroda, and Yuichiro Nishina. Anisotropy of lattice dynamical properties in ZrS_2 and HfS_2. *Journal of the Physical Society of Japan*, 51(7):2233–2240, 1982.

[260] Sharmila N. Shirodkar and Umesh V. Waghmare. Emergence of ferroelectricity at a metal-semiconductor transition in a $1T$ monolayer of MoS_2. *Phys. Rev. Lett.*, 112:157601, Apr 2014.

[261] Max Born and Kun Huang. Dynamical theory of crystal lattices oxford university press. *London, New York*, 1954.

[262] Srishti Pal, Koyendrila Debnath, Satyendra Nath Gupta, Luminita Harnagea, DVS Muthu, Umesh V Waghmare, and AK Sood. Pressure-induced 1 t to 3 r structural phase transition in metallic vse 2: X-ray diffraction and first-principles theory. *Physical Review B*, 104(1):014108, 2021.

[263] Yuki Umemoto, Katsuaki Sugawara, Yuki Nakata, Takashi Takahashi, and Takafumi Sato. *Nano Res.*, 12(1):165, 2019.

[264] Zhepeng Zhang, Yue Gong, Xiaolong Zou, Porun Liu, Pengfei Yang, Jianping Shi, Liyun Zhao, Qing Zhang, Lin Gu, and Yanfeng Zhang. *ACS Nano*, 13:885, 2019.

[265] Ganbat Duvjir, Byoung Ki Choi, Iksu Jang, Søren Ulstrup, Soonmin Kang, Trinh Thi Ly, Sanghwa Kim, Young Hwan Choi, Chris Jozwiak, Aaron Bostwick, Eli Rotenberg, Je-Geun Park, Raman Sankar, Ki-Seok Kim, Jungdae Kim, , and Young Jun Chang. *Nano Lett.*, 18:5432, 2018.

[266] Qing Hua Wang, Kourosh Kalantar-Zadeh, Andras Kis, Jonathan N. Coleman, and Michael S. Strano. *Nat. Nanotechnol.*, 7:699, 2012.

[267] Goki Eda, Takeshi Fujita, Hisato Yamaguchi, Damien Voiry, Mingwei Chen, and Manish Chhowalla. *ACS Nano*, 6:7311, 2012.

[268] A. A. Balchin. Physics and chemistry of materials with layered structures. *Crystallography and Crystal Chemistry of Materials with Layered Structures*, 2:1–50, 1976. (F. Levy, Ed.).

[269] H. Katzke, P. Tolèdano, and W. Depmeier. *Phys. Rev. B*, 69:134111, 2004.

[270] Yan Sun, Shu-Chun Wu, Mazhar N. Ali, Claudia Felser, and Binghai Yan. *Phys. Rev. B*, 92:161107(R), 2015.

[271] Bruce E. Bwnro. *Acta Cryst.*, 20:268, 1966.

[272] J. Augustin, V. Eyert, Th. Böker, W. Frentrup, H. Dwelk, C. Janowitz, and R. Manzke. *Phys. Rev. B*, 62:10812, 2000.

[273] Erling Rost and Liv Gjertsen. *ZAAC*, 328:299, 1964.

[274] Michel Bayard and M. J. Sienko. *J. Solid State Chem.*, 19:325, 1976.

[275] Fengyu Li, Kaixiong Tu, and Zhongfang Chen. *J. Phys. Chem. C*, 118:21264, 2014.

[276] H. W. Myron. *Physica*, 99B:243, 1980.

[277] Alex Zunger and A. J. Freeman. *Phys. Rev. B*, 19:6001, 1979.

[278] Wouter Jolie, Timo Knispel, Niels Ehlen, Konstantin Nikonov, Carsten Busse, Alexander Grüneis, and Thomas Michely. *Phys. Rev. B*, 99:115417, 2019.

[279] Sourabh Barua, M. Ciomaga Hatnean, M. R. Lees, and G. Balakrishnan. *Sci. Rep.*, 7:10964, 2017.

[280] K. Terashima, T. Sato, H. Komatsu, and T. Takahashi. *Phys. Rev. B*, 68:155108, 2003.

[281] Vladimir N. Strocov, Ming Shi, Masaki Kobayashi, Claude Monney, Xiaoqiang Wang, Juraj Krempasky, Thorsten Schmitt, Luc Patthey, Helmuth Berger, and Peter Blaha. *Phys. Rev. Lett.*, 109:086401, 2012.

[282] K. Tsutsumi. *Phys. Rev. B*, 26:5756, 1982.

[283] P. M. Williams. Physics and chemistry of materials with layered structures. *Crystallography and Crystal Chemistry of Materials with Layered Structures*, 2:51–92, 1976. (F. Levy, Ed.).

[284] Yuki Umemoto, Katsuaki Sugawara, Yuki Nakata1, Takashi Takahashi, and Takafumi Sato. *Nano Res.*, 12:165, 2019.

[285] P. Chen, Woei Wu Pai, Y.-H. Chan, V. Madhavan, M. Y. Chou, S.-K. Mo, A.-V. Fedorov, and T.-C. Chiang. *Phys. Rev. Lett.*, 121:196402, 2018.

[286] A. H. M. Abdul Wasey, Soubhik Chakrabarty, and G. P. Das. *J. Appl. Phys.*, 117:064313, 2015.

[287] Jiyong Yang, Weike Wang, Yan Liu, Haifeng Du, Wei Ning, Guolin Zheng, Chiming Jin, Yuyan Han, Ning Wang, Zhaorong Yang, Mingliang Tian, and Yuheng Zhang. *Appl. Phys. Lett.*, 105:063109, 2014.

[288] Ganbat Duvjir, Byoung Ki Choi, Iksu Jang, Søren Ulstrup, Soonmin Kang, Trinh Thi Ly, Sanghwa Kim, Young Hwan Choi, Chris Jozwiak, Aaron Bostwick, Eli Rotenberg, Je-Geun Park, Raman Sankar, Ki-Seok Kim, Jungdae Kim, and Young Jun Chang. *Nano Lett.*, 18:5432, 2018.

[289] H. E. Brauer, H. I. Starnberg, L. J. Holleboom, V. N. Strocov, and H. P. Hughes. *Phys. Rev. B*, 58:10031, 1998.

[290] H. I. Starnberg, H. E. Brauer, L. J. Holleboom, and H. P. Hughes. *Phys. Rev. Lett.*, 70:3111, 1993.

[291] Inger Ekvall, Hans E. Brauer, Erik Wahlström, and Håkan Olin. *Phys. Rev. B*, 59:7751, 1999.

[292] F. J. DiSalvo and J. V. Waszczak. *Phys. Rev. B*, 23:457, 1981.

[293] Avinash P. Nayak, Swastibrata Bhattacharyya, Jie Zhu, Jin Liu, Xiang Wu, Tribhuwan Pandey, Changqing Jin, Abhishek K. Singh, Deji Akinwande, and Jung-Fu Lin. *Nat. Comm.*, 5:3731, 2014.

[294] Zhen-Hua Chi, Xiao-Miao Zhao, Haidong Zhang, Alexander F. Goncharov, Sergey S. Lobanov, Tomoko Kagayama, Masafumi Sakata, and Xiao-Jia Chen. *Phys. Rev. Lett.*, 113:036802, 2014.

[295] Zhao Zhao, Haijun Zhang, Hongtao Yuan, Shibing Wang, Yu Lin, Qiaoshi Zeng, Gang Xu, Zhenxian Liu, G. K. Solanki, K. D. Patel, Yi Cui, Harold Y. Hwang, and Wendy L. Mao. *Nat. Comm.*, 6:7312, 2015.

[296] Xuefei Wang, Xuliang Chen, Yonghui Zhou, Changyong Park, Chao An an Ying Zhou, Ranran Zhang, Chuanchuan Gu, Wenge Yang, and Zhaorong Yang. *Sci. Rep.*, 7:46694, 2017.

[297] F. Yu, J.-X. Sun, and Y.-H. Zhou. *Solid State Sci.*, 12:1786, 2010.

[298] T. Chattopadhyay, H. G. V. Schnering, and W. A. Grosshans. *Physica*, 139 & 140B:305, 1986.

[299] J. M. Lègera, A. S. Pereiraa, J. Hainesa, S. Jobicb, and R. Brec. *J. Phys. Chem. Solids*, 61:27, 2000.

[300] R. H. Friend, D. Jèrome, D. M. Schleich, and P. Moliniè. *Solid State Comm.*, 27:169, 1978.

[301] S. Sahoo, U. Dutta, L. Harnagea, A. K. Sood, and S. Karmakar. *Phys. Rev. B*, 101:014514, 2020.

[302] Raimundas Sereika, Changyong Park, Curtis Kenney-Benson, Sateesh Bandaru, Niall J. English, Qiangwei Yin, Hechang Lei, Ning Chen, Cheng-Jun Sun, Steve M. Heald, Jichang Ren, Jun Chang, Yang Ding, and Ho kwang Mao. *J. Phys. Chem. Lett.*, 11:380, 2020.

[303] P. E. Blöchl. Projector augmented-wave method. *Phys. Rev. B*, 50:17953–17979, Dec 1994.

[304] G. Kresse and D. Joubert. From ultrasoft pseudopotentials to the projector augmented-wave method. *Phys. Rev. B*, 59:1758–1775, Jan 1999.

[305] G. Kresse and J. Furthmüller. Efficient iterative schemes for ab initio total-energy calculations using a plane-wave basis set. *Phys. Rev. B*, 54:11169–11186, Oct 1996.

[306] G. Kresse and J. Furthmüller. Efficiency of ab-initio total energy calculations for metals and semiconductors using a plane-wave basis set. *Computational Materials Science*, 6(1):15 – 50, 1996.

[307] S. L. Dudarev, G. A. Botton, S. Y. Savrasov, C. J. Humphreys, and A. P. Sutton. Electron-energy-loss spectra and the structural stability of nickel oxide: An lsda+u study. *Phys. Rev. B*, 57:1505, 1998.

[308] S. Lutfalla, V. Shapovalov, and A. T. Bell. Calibration of the DFT/GGA+U Method for Determination of Reduction Energies for Transition and Rare Earth Metal Oxides of Ti, V, Mo, and Ce. *J. Chem. Theory Comput.*, 7:2218, 2011.

[309] Marco Esters, Richard G. Hennig, and David C. Johnson. Dynamic instabilities in strongly correlated vse_2 monolayers and bilayers. *Phys. Rev. B*, 96:235147, Dec 2017.

[310] C. Ataca, H. Sahin, and S. Ciraci. *J. Phys. Chem. C*, 116:8983, 2012.

[311] Christos Malliakas, Simon JL Billinge, Hyun Jeong Kim, and Mercouri G Kanatzidis. Square nets of tellurium: rare-earth dependent variation in the charge-density wave of rete3 (re= rare-earth element). *Journal of the American Chemical Society*, 127(18):6510–6511, 2005.

[312] N Ru, J-H Chu, and IR Fisher. Magnetic properties of the charge density wave compounds r te 3 (r= y, la, ce, pr, nd, sm, gd, tb, dy, ho, er, and tm). *Physical Review B*, 78(1):012410, 2008.

[313] DA Zocco, JJ Hamlin, K Grube, J-H Chu, H-H Kuo, IR Fisher, and MB Maple. Pressure dependence of the charge-density-wave and superconducting states in gdte 3, tbte 3, and dyte 3. *Physical Review B*, 91(20):205114, 2015.

[314] N Ru, CL Condron, GY Margulis, KY Shin, J Laverock, SB Dugdale, MF Toney, and IR Fisher. Effect of chemical pressure on the charge density wave transition in rare-earth tritellurides r te 3. *Physical Review B*, 77(3):035114, 2008.

[315] Alfred Zong, Pavel E Dolgirev, Anshul Kogar, Emre Ergeçen, Mehmet B Yilmaz, Ya-Qing Bie, Timm Rohwer, I-Cheng Tung, Joshua Straquadine, Xirui Wang, et al. Dynamical slowing-down in an ultrafast photoinduced phase transition. *Physical review letters*, 123(9):097601, 2019.

[316] A Sacchetti, CL Condron, SN Gvasaliya, F Pfuner, M Lavagnini, M Baldini, MF Toney, M Merlini, M Hanfland, J Mesot, et al. Pressure-induced quenching of the charge-density-wave state in rare-earth tritellurides observed by x-ray diffraction. *Physical Review B*, 79(20):201101, 2009.

[317] Shiming Lei, Jingjing Lin, Yanyu Jia, Mason Gray, Andreas Topp, Gelareh Farahi, Sebastian Klemenz, Tong Gao, Fanny Rodolakis, Jessica L McChesney, et al. High mobility in a van der waals layered antiferromagnetic metal. *Science advances*, 6(6):eaay6407, 2020.

[318] Gangjian Tan, Li-Dong Zhao, and Mercouri G Kanatzidis. Rationally designing high-performance bulk thermoelectric materials. *Chemical reviews*, 116(19):12123–12149, 2016.

[319] Yu Xiao and Li-Dong Zhao. Seeking new, highly effective thermoelectrics. *Science*, 367(6483):1196–1197, 2020.

[320] Subhajit Roychowdhury, Tanmoy Ghosh, Raagya Arora, Manisha Samanta, Lin Xie, Niraj Kumar Singh, Ajay Soni, Jiaqing He, Umesh V Waghmare, and Kanishka Biswas. Enhanced atomic ordering leads to high thermoelectric performance in agsbte2. *Science*, 371(6530):722–727, 2021.

[321] LD Zhao. Energy environ. sci., 2014, 7, 251–268;(c) j. he, mg kanatzidis and vp dravid. *Mater. Today*, 16:166–176, 2013.

[322] Nitin P Padture, Maurice Gell, and Eric H Jordan. Thermal barrier coatings for gas-turbine engine applications. *Science*, 296(5566):280–284, 2002.

[323] Kanishka Biswas, Jiaqing He, Ivan D Blum, Chun-I Wu, Timothy P Hogan, David N Seidman, Vinayak P Dravid, and Mercouri G Kanatzidis. High-performance bulk thermoelectrics with all-scale hierarchical architectures. *Nature*, 489(7416):414–418, 2012.

[324] Liangwei Fu, Meijie Yin, Di Wu, Wei Li, Dan Feng, Li Huang, and Jiaqing He. Large enhancement of thermoelectric properties in n-type pbte via dual-site point defects. *Energy & Environmental Science*, 10(9):2030–2040, 2017.

[325] Bed Poudel, Qing Hao, Yi Ma, Yucheng Lan, Austin Minnich, Bo Yu, Xiao Yan, Dezhi Wang, Andrew Muto, Daryoosh Vashaee, et al. High-thermoelectric performance of nanostructured bismuth antimony telluride bulk alloys. *Science*, 320(5876):634–638, 2008.

[326] J Ma, Olivier Delaire, AF May, CE Carlton, MA McGuire, LH VanBebber, DL Abernathy, G Ehlers, Tao Hong, A Huq, et al. Glass-like phonon scattering from a spontaneous nanostructure in agsbte2. *Nature nanotechnology*, 8(6):445–451, 2013.

[327] Sushmita Chandra and Kanishka Biswas. Realization of high thermoelectric figure of merit in solution synthesized 2d snse nanoplates via ge alloying. *Journal of the American Chemical Society*, 141(15):6141–6145, 2019.

[328] Manisha Samanta, Tanmoy Ghosh, Sushmita Chandra, and Kanishka Biswas. Layered materials with 2d connectivity for thermoelectric energy conversion. *Journal of Materials Chemistry A*, 8(25):12226–12261, 2020.

[329] Li-Dong Zhao, Shih-Han Lo, Yongsheng Zhang, Hui Sun, Gangjian Tan, Ctirad Uher, Christopher Wolverton, Vinayak P Dravid, and Mercouri G Kanatzidis. Ultralow thermal conductivity and high thermoelectric figure of merit in snse crystals. *nature*, 508(7496):373–377, 2014.

[330] Cheng Chang, Minghui Wu, Dongsheng He, Yanling Pei, Chao-Feng Wu, Xuefeng Wu, Hulei Yu, Fangyuan Zhu, Kedong Wang, Yue Chen, et al. 3d charge and 2d phonon transports leading to high out-of-plane zt in n-type snse crystals. *Science*, 360(6390):778–783, 2018.

[331] Chongjian Zhou, Yong Kyu Lee, Yuan Yu, Sejin Byun, Zhong-Zhen Luo, Hyungseok Lee, Bangzhi Ge, Yea-Lee Lee, Xinqi Chen, Ji Yeong Lee, et al. Polycrystalline snse with a thermoelectric figure of merit greater than the single crystal. *Nature materials*, 20(10):1378–1384, 2021.

[332] Eric J Skoug and Donald T Morelli. Role of lone-pair electrons in producing minimum thermal conductivity in nitrogen-group chalcogenide compounds. *Physical review letters*, 107(23):235901, 2011.

[333] Michele D Nielsen, Vidvuds Ozolins, and Joseph P Heremans. Lone pair electrons minimize lattice thermal conductivity. *Energy & Environmental Science*, 6(2):570–578, 2013.

[334] G Jeffrey Snyder and Eric S Toberer. Complex thermoelectric materials. In *Materials for sustainable energy: a collection of peer-reviewed research and review articles from Nature Publishing Group*, pages 101–110. World Scientific, 2011.

[335] Xiyang Li, Peng-Fei Liu, Enyue Zhao, Zhigang Zhang, Tatiana Guidi, Manh Duc Le, Maxim Avdeev, Kazutaka Ikeda, Toshiya Otomo, Maiko Kofu, et al. Ultralow thermal conductivity from transverse acoustic phonon suppression in distorted crystalline α-mgagsb. *Nature communications*, 11(1):1–9, 2020.

[336] Moinak Dutta, Koushik Pal, Umesh V Waghmare, and Kanishka Biswas. Bonding heterogeneity and lone pair induced anharmonicity resulted in ultralow thermal conductivity and promising thermoelectric properties in n-type agpbbise 3. *Chemical science*, 10(18):4905–4913, 2019.

[337] Paribesh Acharyya, Tanmoy Ghosh, Koushik Pal, Kaushik Kundu, Kewal Singh Rana, Juhi Pandey, Ajay Soni, Umesh V Waghmare, and Kanishka Biswas. Intrinsically ultralow thermal conductivity in ruddlesden–popper 2d perovskite cs2pbi2cl2: localized anharmonic vibrations and dynamic octahedral distortions. *Journal of the American Chemical Society*, 142(36):15595–15603, 2020.

[338] Sangyeop Lee, Keivan Esfarjani, Tengfei Luo, Jiawei Zhou, Zhiting Tian, and Gang Chen. Resonant bonding leads to low lattice thermal conductivity. *Nature communications*, 5(1):1–8, 2014.

[339] Debattam Sarkar, Tanmoy Ghosh, Subhajit Roychowdhury, Raagya Arora, Sandra Sajan, Goutam Sheet, Umesh V Waghmare, and Kanishka Biswas. Ferroelectric

instability induced ultralow thermal conductivity and high thermoelectric performance in rhombohedral p-type gese crystal. *Journal of the American Chemical Society*, 142(28):12237–12244, 2020.

[340] Ananya Banik, Tanmoy Ghosh, Raagya Arora, Moinak Dutta, Juhi Pandey, Somnath Acharya, Ajay Soni, Umesh V Waghmare, and Kanishka Biswas. Engineering ferroelectric instability to achieve ultralow thermal conductivity and high thermoelectric performance in sn 1- x ge x te. *Energy & Environmental Science*, 12(2):589–595, 2019.

[341] Moinak Dutta, Manisha Samanta, Tanmoy Ghosh, David J Voneshen, and Kanishka Biswas. Evidence of highly anharmonic soft lattice vibrations in a zintl rattler. *Angewandte Chemie*, 133(8):4305–4311, 2021.

[342] DJ Voneshen, K Refson, E Borissenko, M Krisch, A Bosak, A Piovano, E Cemal, M Enderle, MJ Gutmann, M Hoesch, et al. Suppression of thermal conductivity by rattling modes in thermoelectric sodium cobaltate. *Nature materials*, 12(11):1028–1032, 2013.

[343] Manoj K Jana, Koushik Pal, Avinash Warankar, Pankaj Mandal, Umesh V Waghmare, and Kanishka Biswas. Intrinsic rattler-induced low thermal conductivity in zintl type tlinte2. *Journal of the American Chemical Society*, 139(12):4350–4353, 2017.

[344] Huili Liu, Xun Shi, Fangfang Xu, Linlin Zhang, Wenqing Zhang, Lidong Chen, Qiang Li, Ctirad Uher, Tristan Day, and G Jeffrey Snyder. Copper ion liquid-like thermoelectrics. *Nature materials*, 11(5):422–425, 2012.

[345] B Li, H Wang, Y Kawakita, Qijing Zhang, M Feygenson, HL Yu, D Wu, K Ohara, T Kikuchi, K Shibata, et al. Liquid-like thermal conduction in intercalated layered crystalline solids. *Nature materials*, 17(3):226–230, 2018.

[346] Qian Xu, Jiawei Zhou, Te-Huan Liu, and Gang Chen. Effect of electron-phonon interaction on lattice thermal conductivity of sige alloys. *Applied Physics Letters*, 115(2):023903, 2019.

[347] X Shi, YZ Pei, GJ Snyder, and LD Chen. Energy environ. sci. 4, 4086 (2011).

[348] Bolin Liao, Bo Qiu, Jiawei Zhou, Samuel Huberman, Keivan Esfarjani, and Gang Chen. Significant reduction of lattice thermal conductivity by the electron-phonon interaction in silicon with high carrier concentrations: A first-principles study. *Physical review letters*, 114(11):115901, 2015.

[349] George Grüner. *Density waves in solids*. CRC press, 2018.

[350] RM Costescu, DG Cahill, FH Fabreguette, ZA Sechrist, and SM George. Ultra-low thermal conductivity in w/al2o3 nanolaminates. *Science*, 303(5660):989–990, 2004.

[351] Atsushi Togo, Fumiyasu Oba, and Isao Tanaka. First-principles calculations of the ferroelastic transition between rutile-type and cacl 2-type sio 2 at high pressures. *Physical Review B*, 78(13):134106, 2008.

[352] JS Liu, SC Huan, ZH Liu, WL Liu, ZT Liu, XL Lu, Z Huang, ZC Jiang, X Wang, N Yu, et al. Electronic structure of the high-mobility two-dimensional antiferromagnetic metal gd te 3. *Physical Review Materials*, 4(11):114005, 2020.

[353] G Grüner. Density waves in solids addison-wesley. *Reading, Massachusetts*, 1994.

[354] DT Morelli, V Jovovic, and JP Heremans. Intrinsically minimal thermal conductivity in cubic i- v- vi 2 semiconductors. *Physical review letters*, 101(3):035901, 2008.

[355] George Grüner. *Density waves in solids*. CRC press, 2018.

[356] Pierre Monceau. Electronic crystals: an experimental overview. *Advances in Physics*, 61(4):325–581, 2012.

[357] RE Peierls. Quantum theory of solids p. 108, clarendon, 1975.

[358] J_ Chaussy, P Haen, JC Lasjaunias, P Monceau, G Waysand, A Waintal, A Meerschaut, Po Molinie, and J Rouxel. Phase transitions in nbse3. *Solid State Communications*, 20(8):759–763, 1976.

[359] M Sato, H Fujishita, S Sato, and S Hoshino. Neutron inelastic scattering and x-ray structural study of the charge-density-wave state in k0. 3moo3. *Journal of Physics C: Solid State Physics*, 18(13):2603, 1985.

[360] K Krogmann and H-D Hausen. Strukturen mit pt-ketten, i.violettes" kaliumtetracyanoplatinat, k2 [pt (cn) 4] x0, 3· 2, 5 h2o (x= cl, br). *Zeitschrift für anorganische und allgemeine Chemie*, 358(1-2):67–81, 1968.

[361] B Renker, L Pintschovius, W Gläser, H Rietschel, R Comes, L Liebert, and W Drexel. Neutron-scattering study of the structural phase transition in the one-dimensional conductor k 2 pt (cn) 4 br 0.3· 3 d 2 o. *Physical Review Letters*, 32(15):836, 1974.

[362] P Gressier, A Meerschaut, L Guemas, J Rouxel, and P Monceau. Characterization of the new series of quasi one-dimensional compounds (mx4) ny (m= nb, ta; x= s, se; y= br, i). *Journal of Solid State Chemistry*, 51(2):141–151, 1984.

[363] Pascal Gressier, Louisette Guemas, and Alain Meerschaut. Preparation and structure of ditantalum iodide octaselenide, ta2ise8. *Acta Crystallographica Section B: Structural Crystallography and Crystal Chemistry*, 38(11):2877–2879, 1982.

[364] H Fujishita, M Sato, and S Hoshino. Incommensurate superlattice reflections in quasi one dimensional conductors,(mse4) 2i (m= ta and nb). *Solid state communications*, 49(4):313–316, 1984.

[365] V Favre-Nicolin, S Bos, JE Lorenzo, JL Hodeau, JF Berar, P Monceau, R Currat, F Levy, and H Berger. Structural evidence for ta-tetramerization displacements in the charge-density-wave compound (tase 4) 2 i from x-ray anomalous diffraction. *Physical Review Letters*, 87(1):015502, 2001.

[366] Sander van Smaalen, Erwin J Lam, and Jens Lüdecke. Structure of the charge-density wave in (tase4) 2i. *Journal of Physics: Condensed Matter*, 13(44):9923, 2001.

[367] Zo Z Wang, MC Saint-Lager, P Monceau, M Renard, P Gressier, A Meerschaut, L Guemas, and J Rouxel. Charge density wave transport in (tase4) 2i. *Solid state communications*, 46(4):325–328, 1983.

[368] Xiao-Ping Li, Ke Deng, Botao Fu, YongKai Li, Da-Shuai Ma, JunFeng Han, Jianhui Zhou, Shuyun Zhou, and Yugui Yao. Type-iii weyl semimetals:(tase 4) 2 i. *Physical Review B*, 103(8):L081402, 2021.

[369] Samad Hajinazar, Aidan Thorn, Ernesto D Sandoval, Saba Kharabadze, and Aleksey N Kolmogorov. Maise: Construction of neural network interatomic models and evolutionary structure optimization. *Computer Physics Communications*, 259:107679, 2021.

[370] Yang Zhang, Ling-Fang Lin, Adriana Moreo, Shuai Dong, and Elbio Dagotto. First-principles study of the low-temperature charge density wave phase in the quasi-one-dimensional weyl chiral compound (tase 4) 2 i. *Physical Review B*, 101(17):174106, 2020.

[371] Claudio Attaccalite, Ludger Wirtz, Michele Lazzeri, Francesco Mauri, and Angel Rubio. Doped graphene as tunable electron- phonon coupling material. *Nano letters*, 10(4):1172–1176, 2010.

[372] DT Morelli, V Jovovic, and JP Heremans. Intrinsically minimal thermal conductivity in cubic i- v- vi 2 semiconductors. *Physical review letters*, 101(3):035901, 2008.

[373] Moinak Dutta, Koushik Pal, Umesh V Waghmare, and Kanishka Biswas. Bonding heterogeneity and lone pair induced anharmonicity resulted in ultralow thermal conductivity and promising thermoelectric properties in n-type agpbbise 3. *Chemical science*, 10(18):4905–4913, 2019.